UNIVERSITY OF CALIFORNIA,
IRVINE

Inertial Radio SLAM: Standalone and Collaborative Architectures

DISSERTATION

submitted in partial satisfaction of the requirements
for the degree of

DOCTOR OF PHILOSOPHY

in Electrical Engineering and Computer Science

by

Joshua J. Morales

Dissertation Committee:
Professor Zak Kassas, Chair
Professor Andrei Skhel
Professor Solmaz Kia

2020

TABLE OF CONTENTS

LIST OF FIGURES

LIST OF TABLES

LIST OF ALGORITHMS

ACKNOWLEDGMENTS

I would like to thank my Ph.D. advisor Dr. Zak Kassas for the guidance and support during this journey. I am grateful for the opportunity to help build ASPIN lab along with my great colleagues. His support has allowed me to freely explore the research topics that I was interested in and to conduct and demonstrate my research findings experimentally and present them at conferences.

I also thank Professor Jay Farrell for his motivational conversations during the early stages of my studies and supporting my graduate school applications with letters of recommendations.

I thank Dr. Phu Tran who taught a very rigorous physics series. Dr. Tran continuously pushed his students to be the best they could be, both inside and outside of school. If it were not for his courses and his push early in my studies, I would not have been disciplined into a student ready for the Ph.D. journey.

I would like to thank my Ph.D. committee members Prof. Andrei Shkel and Prof. Solmaz Kia for taking time to serve on the committee and for their helpful advice and feedback throughout my Qualifying Exam and Ph.D. Defense.

I appreciate the generous funding from the Office of Naval Research (ONR), the National Science Foundation (NSF), and the National Center for Sustainable Transportation (NCST), which is funded by the U.S. Department of Transportation (USDOT).

I thank my friends and colleagues: Joe, Kimia, Mahdi, and Ali for their support, helpful discussions, and help with collecting experimental data.

I thank my best friends: Frank, Keith, and Jason who have been brothers to me and have stuck by my side, even though I was not always able to be around during this busy Ph.D. journey.

A special thanks to my family: Mom, Dad, Jennifer, Eric, Caitlin, Lauren, Sierra, Mike, Brandon, Uncle Jim, Aunt Cindy, Uncle Mick, Aunt Kim, Grandma Donna, and Tim. My family has been so supportive and understanding of my busy schedule. Their love and support has kept me going during the challenging times encountered during the pursuit of this Ph.D.

Lastly, but very importantly, I thank my grandparents Nana and Tata. Tata has always been my role model in my life and one of my strongest motivations during my Ph.D. studies. I can only hope to be as good of a role model to the next family generation as he is to us. Everyone who knows Nana knows she can literally bring tears of joy with her warm and loving personality. Nana and Tata have always been the anchor to our family and were my anchor during this Ph.D. journey. I can not emphasize this enough: I could not have done this without your continuous love, support, and life advice.

VITA

Joshua J. Morales

EDUCATION

Doctor of Philosophy in Electrical Engineering **2020**
University of California, Irvine *Irvine, California*

Bachelor of Science in Electrical Engineering **2014**
University of California, Riverside *Riverside, California*

RESEARCH EXPERIENCE

Graduate Research Assistant **2019–2020**
University of California, Irvine *Irvine, California*

Graduate Research Assistant **2014–2019**
University of California, Riverside *Riverside, California*

TEACHING EXPERIENCE

Teaching Assistant **2016–2017**
University of California, Riverside *Riverside, California*

HONORS & AWARDS

Best Presentation Award **2018**
ION GNSS+ Conference *Miami, Florida*

NCST Outstanding Student of the Year **2017**
U.S. Department of Transportation (USDOT) *Washington D.C.*

Best Presentation Award **2017**
ION GNSS+ Conference *Portland, Oregon*

Best Presentation Award **2016**
ION GNSS+ Conference *Portland, Oregon*

NCST Graduate Fellowship **2016**
National Center for Sustainable Transportation (NCST) *Riverside, California*

NSF Honorable Mention **2016**
National Science Foundation (NSF) *Riverside, California*

Best Paper Award **2015**
ION GNSS+ Conference *Tampa, Florida*

JOURNAL PUBLICATIONS

[J7] **Morales**, **J**. & Kassas, Z. (2020). Communication and information fusion strategies for collaborative inertial navigation with signals of opportunity aiding Part II: simulation and experimental results. *IEEE Transactions on Intelligent Transportation Systems*. (In preparation)

[J6] **Morales**, **J**. & Kassas, Z. (2020). Communication and information fusion strategies for collaborative inertial navigation with signals of opportunity aiding Part I: theory and algorithms. *IEEE Transactions on Intelligent Transportation Systems*. (In preparation)

[J5] **Morales**, **J**. & Kassas, Z. (2019). Tightly-coupled inertial navigation system with signals of opportunity aiding. *IEEE Transactions on Aerospace and Electronic Systems*. (Submitted).

[J4] Kassas, Z., Maaref, M., **Morales**, **J**, Khalife, J., & Shamaei, K. (2019). Robust vehicular navigation and map-matching in urban environments with IMU, GNSS, and cellular signals. *IEEE Intelligent Transportation Magazine*. (Accepted).

[J3] **Morales**, **J**. & Kassas, Z. (2019, April). Stochastic observability and uncertainty characterization in simultaneous receiver and transmitter localization. *IEEE Transactions on Aerospace and Electronic Systems*, 55(2), 1021–1031.

[J2] **Morales**, **J**. & Kassas, Z. (2018, April). Optimal collaborative mapping of terrestrial transmitters: receiver placement and performance characterization. *IEEE Transactions on Aerospace and Electronic Systems*, 54(2), 992–1007.

[J1] Kassas, Z., Khalife, J., Shamaei, K., & **Morales**, **J**. (2017, September). I hear, therefore I know where I am: compensating for GNSS limitations with cellular signals. *IEEE Signal Processing Magazine*, 34(5), 111–124. (*Invited*).

CONFERENCE PUBLICATIONS

[C14] **Morales**, **J**., Khalife, J., Santa Cruz, U., & Kassas, Z. (2019, September). Orbit modeling for simultaneous tracking and navigation using LEO satellite signals. *In Proceedings of ION Global Navigation Satellite Systems Conference*, pp. 2090–2099.

[C13] **Morales**, **J**., Khalife, J., & Kassas, Z. (2019, April). Simultaneous tracking of Orbcomm LEO satellites and inertial navigation system aiding using Doppler measurements. *In Proceedings of IEEE Vehicular Technology Conference*, pp. 1–6.

[C12] Shamaei, K., **Morales**, **J**., & Kassas, Z. (2019, April). A framework for navigation with LTE time-correlated pseudorange errors in multipath environments. *In Proceedings of IEEE Vehicular Technology Conference*, pp. 1–6.

[C11] Ardito, C., **Morales**, **J**., Khalife, J., Abdalla, A., & Kassas, Z. (2019, January). Per-

formance evaluation of navigation using LEO satellite signals with periodically transmitted satellite positions. *In Proceedings of ION International Technical Meeting*, pp. 306–318.

[C10] **Morales**, **J**. & Kassas, Z. (2018, October). Event-based communication strategy for collaborative navigation with signals of opportunity. *In Proceedings of Asilomar Conference on Signals, Systems and Computers*, pp. 548–553. (*Invited*).

[C9] **Morales**, **J**., Khalife, J., Abdallah, A., Ardito, C., & Kassas, Z. (2018, September). Inertial navigation system aiding with Orbcomm LEO satellite Doppler measurements. *In Proceedings of ION Global Navigation Satellite Systems Conference*, pp. 2718–2725.

[C8] Shamaei, K., **Morales**, **J**., & Kassas, Z. (2018, September). Positioning performance of LTE signals in Rician fading environments exploiting antenna motion. *In Proceedings of ION Global Navigation Satellite Systems Conference*, pp. 24–28.

[C7] **Morales**, **J**. & Kassas, Z. (2018, June). A low communication rate distributed inertial navigation architecture with cellular signal aiding. *In Proceedings of IEEE Vehicular Technology Conference*, pp. 1–6.

[C6] **Morales**, **J**. & Kassas, Z. (2018, April). Information fusion strategies for collaborative radio SLAM. *In Proceedings of IEEE/ION Position, Location, and Navigation Symposium*, pp. 1445–1454.

[C5] **Morales**, **J**. & Kassas, Z. (2017, September). Distributed signals of opportunity aided inertial navigation with intermittent communication. *In Proceedings of ION Global Navigation Satellite Systems Conference*, pp. 2519–2530.

[C4] **Morales**, **J**., Khalife, J., & Kassas, Z. (2017, January). Collaborative autonomous vehicles with signals of opportunity aided inertial navigation systems. *In Proceedings of ION International Technical Meeting*, pp. 805–818.

[C3] **Morales**, **J**., Roysdon, P., & Kassas, Z. (2016, September). Signals of opportunity aided inertial navigation. *In Proceedings of ION Global Navigation Satellite Systems Conference*, pp. 1256–1268.

[C2] **Morales**, **J**., Khalife, J., & Kassas, Z. (2016, January). GNSS vertical dilution of precision reduction using terrestrial signals of opportunity. *In Proceedings of ION International Technical Meeting*, pp. 664–669.

[C1] **Morales**, **J**. & Kassas, Z. (2015, September). Optimal receiver placement for collaborative mapping of signals of opportunity. *In Proceedings of ION Global Navigation Satellite Systems Conference*, pp. 2362–2368.

MAGAZINE PUBLICATIONS

[M3] Kassas, Z., **Morales**, **J**., & Khalife, J. (2019, August). New-age satellite-based naviga-

tion STAN: simultaneous tracking and navigation with LEO satellite signals. *Inside GNSS*. (*Cover article*).

[M2] Kassas, Z., **Morales**, **J**., Shamaei, K., & Khalife, J. (2017, April). LTE steers UAV. *GPS World Magazine*, 28(4), 1825. (*Cover article*).

[M1] **Morales**, **J**., Khalife, J., & Kassas, Z. (2016, March). Opportunity for accuracy. *GPS World Magazine*, 27(3), 22–29. (*Cover article*).

COINVENTED PATENTS

[P4] Receiver design for Doppler positioning with low Earth orbit satellites. U.S. Patent Application No. 62/834,317, Filed: April. 15, 2019.

[P3] Low Earth orbit satellite signal aided inertial navigation system. U.S. Patent Application No. 62/834,313, Filed: April 15, 2019.

[P2] Crowdsourced signals of opportunity aided inertial navigation system. U.S. Patent Application No. 62/561,026, Filed: September 20, 2017.

[P1] Signals of opportunity aided inertial navigation system. U.S. Patent Application No. 62/398,413, Filed: September 22, 2016.

SOFTWARE

MATLAB, Python, C++

ABSTRACT OF THE DISSERTATION

Inertial Radio SLAM: Standalone and Collaborative Architectures

By

Joshua J. Morales

Doctor of Philosophy in Electrical Engineering and Computer Science

University of California, Irvine, 2020

Professor Zak Kassas, Chair

Autonomous vehicles are promised to share the road, sea, and sky alongside human-operated vehicles. Full autonomy requires an accurate and tamper-proof navigation system that operates robustly in all settings. To meet this requirement, vehicles must fuse redundant position information from various sources. The state of the art is to fuse position information from a suite of diverse and complementary onboard sensors (e.g., a global navigation satellite system (GNSS) receiver provides stable absolute position information and an inertial measurement unit (IMU) and other dead reckoning (DR) sensors provide short-term accurate DR-type information). Relying on GNSS alone to provide absolute positioning poses an alarming vulnerability: GNSS signals could become unavailable or unreliable in deep urban canyons or locations experiencing a malicious attack (e.g., jamming or spoofing). After prolonged GNSS signal unavailability, the position solution degrades to unsafe levels as error-corrupted DR-type information is integrated without correction from an absolute positioning source. Recently, ambient radio frequency signals of opportunity (SOPs), such as AM/FM, cellular, digital television, and low Earth orbit (LEO) satellites, have emerged as an effective backup or alternative source of absolute positioning information in the absence of GNSS signals.

SOPs posses several desirable characteristics as sources of positioning information: (i) ubiquitous in most environments of interest, (ii) signal diversity in frequency and direction,

(iii) higher signal reception strength compared to GNSS signals, (iv) they are free to use, since their infrastructure is already operational and maintained by service providers. However, SOPs were never intended as sources for positioning information, which gives rise to a number of challenges. First, unlike GNSS satellites, the positions of SOP emitters may be unknown. Second, the clocks equipped on different SOP emitters are not tightly synchronized with each other and are driven by lower quality oscillators compared to atomic oscillators on GNSS satellites. Third, unavailability of navigation architectures for fusing SOP information with other commonly used navigation sensors, such as IMUs.

This dissertation addresses the aforementioned challenges by developing and studying an inertial radio simultaneous localization and navigation (inertial radio SLAM) architecture, in which vehicles exploit SOPs to aid their INSs while simultaneously mapping unknown states of SOPs in space and time. Theoretical and practical questions are addressed. Throughout the dissertation, simulation and experimental demonstrations evaluate the established theorems and answers to the practical questions.

Chapter 1

Introduction

The last decade has seen a dramatic increase in the research and development of fully autonomous navigating vehicles. In 2019 alone, the private sector saw record-breaking funding numbers to develop self-driving cars, autonomous package delivery, and other autonomous services of-the-like [1]. Besides the private sector, the U.S. Department of Defense requested $9.39 billion in 2019 for unmanned systems and associated technologies [2]. As these navigating vehicle's begin to operate alongside human-operated vehicles, requirements on their equipped navigation system's robustness and the accuracy of the produced position solution are becoming more stringent [3,4]. To meet such stringent requirements, vehicular navigation systems must draw and fuse information from various sensing modalities.

Today's navigation systems fuse absolute positioning information from a global navigation satellite system (GNSS) receiver with dead reckoning information from an inertial navigation system (INS) [5], and potentially a multitude of other information sources [6] (e.g., lasers [7,8], cameras [9,10], and maps [11]). Relying on GNSS alone to provide absolute positioning poses an alarming vulnerability: GNSS signals could become unavailable or unreliable in environments such as deep urban canyons or environments experiencing a malicious attack

(e.g., jamming or spoofing). During prolonged periods without absolute position information from GNSS, the errors in the INS (and other dead-reckoning type sensors) will inevitably diverge, compromising the vehicle's safe operation.

Consumer and small-size applications that use affordable micro-electro-mechanical systems (MEMS)-based inertial measurement units (IMUs) are particularly susceptible to large error divergence rates. While adding additional sensors may reduce the rate of error divergence, they may violate cost, size, weight, and/or power constraints. Moreover, these sensors may not properly function in all environments (e.g., fog, snow, rain, dust, nighttime, etc.), and are still susceptible to malicious attacks [12].

1.1 Exploiting Signals of Opportunity for Navigation

Recently, signals of opportunity (SOPs) have been demonstrated as an attractive source of absolute positioning information in the absence of GNSS signals [13–17]. SOPs are ambient radio frequency signals that are not intended for navigation or timing purposes, such as AM/FM radio [18–21], cellular [22–27], digital television [28–30], Wi-Fi [31–33], and low Earth orbit (LEO) satellite signals [34–42]. These SOPs are illustrated in Fig. 1.1. Even when GNSS signals are available, SOP observables can be coupled with GNSS observables to significantly improve the accuracy of the navigation solution [43]. With appropriately designed receivers and algorithms, they may be exploited for standalone navigation or absolute positioning for an aided INS [24]. In contrast to the aforementioned DR-type sensors, *absolute* position information may be extracted from SOPs to provide bounded INS errors. Moreover, SOPs are practically unaffected by dense smoke, lighting conditions, fog, rain, snow, and other poor weather conditions. SOPs enjoy several inherently desirable attributes for navigation purposes:

- **Abundance**: SOPs are collectively available in most locales of interest.
- **Diversity**: SOPs are diverse in both frequency and direction.
- **High received power**: SOPs are often available in GNSS denied environments and are received with a carrier-to-noise ratio that is commonly tens of dBs higher than that of GNSS signals.
- **Free to use**: with specialized SOP navigation receivers, their signals may be exploited without network subscriptions and their infrastructure is already operational and maintained by service providers.

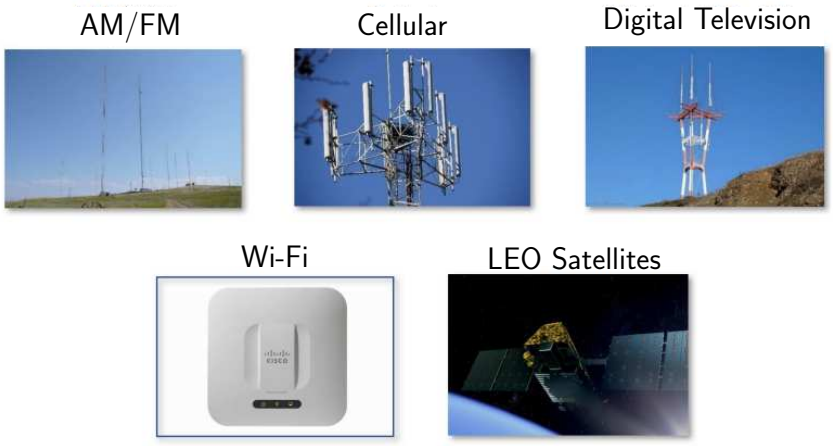

Figure 1.1: Illustration of example SOPs that may be exploited for absolute positioning.

However, unlike GNSS, whose satellites' states are known via a transmitted navigation message, the states of SOPs, namely their position and clock states, are typically unknown *a priori* and must be estimated. Furthermore, the oscillators equipped on SOP transmitters are lower quality compared to the autonomic clocks equipped on Global Positioning System (GPS) satellites, which are maintained by the U.S. Air Force. This dissertation tackles these challenges by developing a simultaneous localization and mapping (SLAM)-type architecture in order to aid a vehicle's INS using unknown SOPs in the absence of GNSS signals. This architecture is termed inertial radio SLAM. Radio SLAM is similar to the traditional SLAM problem in robotics, however in contrast to the typical SLAM map that consists of static

landmarks, the radio SLAM map consists of both static states as well as stochastic and dynamic states, which correspond to the positions of the SOPs and the clock bias and drift, respectively. This dissertation builds up an architecture that may operate in a standalone or collaborative fashion and answers a number of theoretical questions and addresses several practical concerns. The contributions of this dissertation are elaborated next.

1.2 Dissertation Contributions and Relevant Work

To begin, this dissertation first considers the case of known vehicle states and solves the problem of optimal mapping of unknown SOPs. Optimal mapping is an important objective that arises in many application domains, such as source localization [44], target tracking [45], and autonomous vehicle navigation [46]. The mapping problem can be abstracted to that of estimating desired states in the environment, given information extracted from a sensor or a sensor network. Map optimality is furnished by considering a desired performance criterion, such as minimization of uncertainty, convergence time, and computational time.

While increasing the number of mapping sensors typically improves the quality of the produced maps, introducing additional sensors may be prohibitive due to economical, physical, or computational constraints. Optimal sensor placement has been studied as an enabling tool to achieve optimal mapping by using only a subset of available sensors for source localization [47,48] and target tracking [49–52]. In autonomous vehicle navigation, environmental features are mapped *a priori* or on-the-fly, and these maps are used to estimate the vehicle's motion within the environment. These features could posses (i) a static state space, such as stationary landmarks (e.g., traffic lights, poles, buildings, etc.) or (ii) a dynamic state space, such as SOP transmitters. This dissertation considers the problem of optimal collaborative mapping of unknown terrestrial SOPs. This problem is important in two contexts: (1) unknown emitter localization and (2) opportunistic navigation.

Collaboration generally improves navigation. In collaborative opportunistic navigation, multiple receivers share their observations of SOPs in the environment to construct and continuously refine a global signal landscape map. Such signal landscape could be cloud-hosted, such that whenever GNSS signals become inaccessible or untrustworthy, the receivers continue navigating with the aid of this map [16]. The quality of the constructed map depends on the quality of the observations and the spatial geometry between the SOPs and receivers. The quality of the constructed map could be improved by prescribing the receivers' motion to minimize the uncertainty about the SOPs' together with the receivers' states assuming the initial states of all receivers to be unknown [53]. This motion planning could be generated in a greedy [54] or a receding horizon fashion [55].

This dissertation makes two contributions associated with mapping SOPs. First, the optimal receiver placement problem is extended to environments comprising *multiple* SOPs. To this end, a novel optimization criterion, namely, the product of areas maximization is derived. This optimization criterion is intimately related to the classical geometric dilution of precision (GDOP) minimization and determinant of the inverse of the GDOP matrix maximization criteria, making it a good alternative for optimal receiver placement. The proposed optimization criterion yields a family of parallelizable convex programs and is computationally cheaper compared to the classical optimization criteria, which do not yield convex programs. Second, the optimal mapping performance in an environment comprising N mobile receivers estimating the states of one unknown terrestrial SOP is characterized as a function of time and N. This dissertation presents a rigourous proof for the optimal mapping performance together with simulation and experimental results illustrating various receiver trajectories versus the optimal mapping performance. The experimental results demonstrate collaborative mapping of an unknown cellular code division multiple access (CDMA) SOP transmitter to an unprecedented degree of accuracy. It is important to note that while this dissertation focuses on mapping SOPs for opportunistic navigation purposes, the developed techniques are widely applicable to other application domains involving range-type sensors.

This dissertation considers the following two problems for the mapping problem. The first problem assumes that multiple receivers with random initial states are dropped in a planar environment comprising multiple unknown terrestrial SOPs with a random configuration. Each receiver has *a priori* knowledge about its own states (e.g., from GNSS observables). The receivers draw pseudorange observations from each SOP, which are fused through a centralized estimator that estimates the states of all SOPs. It is desired to reduce the uncertainty of the produced state estimates. However, in many practical scenarios, the receivers may be prevented from moving to more favorable locations to achieve the best reduction in uncertainty, e.g., if their motion is constrained or moving to new locations would consume a considerable amount of time or energy. Instead, it may be more efficient to deploy an additional collaborating receiver. Where should this additional receiver be placed to minimize the uncertainty about the SOPs' states?

The second problem considers a planar environment comprising N *mobile* receivers with knowledge about their own states, making pseudorange observations on *one* unknown terrestrial SOP, and fusing their observations through a centralized estimator. What is the optimal mapping performance as a function of time and N? The answer to this question would enable one to determine the minimum number of receivers that must be deployed in an environment to achieve a desired estimation uncertainty within a specified period of time.

Similar questions to the first problem this dissertation considers have arisen in other contexts, such as optimal GNSS space vehicle (SV) distribution and selection [56–59] and optimal sensor placement for target localization and tracking [52, 60, 61]. Common metrics to assess the quality of the spatial geometry of GNSS SVs and range-based sensors are the geometric dilution of precision (GDOP) [62] and the determinant of the inverse of the GDOP matrix [56]. The GDOP is related to the sum of the variances of a position estimate. Therefore, smaller GDOP values (or larger determinants of the inverse of the GDOP matrix) correspond to more favorable geometries for localization. It was demonstrated in [57] that the GDOP at

the center of an N-sided polygon is minimized when the sensors' locations form the vertices of a regular polygon. In [63], this sensor configuration was also shown to achieve the upper bound of the determinant of the Fisher information matrix (FIM), which is proportional to the inverse of the GDOP matrix. In [64], the area of a polygon inscribed in the unit circle whose vertices are the line of sight (LOS) vectors from the receiver (target) to the SVs (sensors) was presented as an alternative optimization function for selecting the best SVs.

While previous work considered optimizing the location of a constellation of SVs or a group of sensors with respect to a specified criterion, this dissertation assumes that N of the receivers are *arbitrarily* placed, and treats the problem of optimal placement of an *additional* $(N+1)^{\text{st}}$ receiver to improve the estimate of the SOPs' states. This introduces two main challenges when compared to optimizing the location of *all* available sensors. First, the optimal placement of the $(N+1)^{\text{st}}$ sensor is dependent on the distribution of the pre-deployed sensors, whereas the optimal placement of all available sensors is only dependent on the number of sensors whose optimal configuration is a regular polygon. Second, the optimal placement of the $(N+1)^{\text{st}}$ sensor is dependent on the optimization criterion employed, whereas the optimal placement of all available sensors is invariant to the optimization criterion (GDOP minimization, determinant of the inverse of the GDOP matrix maximization, and area maximization).

A preliminary study comparing the problems of (1) GDOP minimization, (2) determinant of the inverse of the GDOP matrix maximization, and (3) area maximization, for optimal placement of an additional $(N+1)^{\text{st}}$ receiver was conducted in [65]. It was demonstrated that these three optimization problems are comparable and that the area maximization problem is piecewise-concave with a simple analytical solution. However, only an environment comprising a *single* SOP was considered. Optimal sensor placement for multiple target positioning was considered in [66] by maximizing the determinant of the FIM. However, the optimization was performed over the entire set of sensors.

Next, the SOP mapping problem is extended by considering the scenario when the states of the receiver are also unknown. These states may be *simultaneously* estimated alongside the SOPs' states, which provide a self-contained solution that does not require the installation of additional infrastructure [17, 54]. Localizing unknown radio frequency (RF) transmitters in general is important in applications ranging from identifying rogue transmitters, such as jammers and spoofers [67, 68], to radionavigation via signals of opportunity [13, 16].

This estimation problem is referred to as radio simultaneous localization and mapping (radio SLAM) and is analogous to the SLAM problem in robotics [69]. However, in contrast to the *static* feature map of the typical SLAM problem which consists of static states (e.g., positions of buildings, walls, poles, trees, etc.), the radio SLAM signal landscape map consists of static states (e.g., positions of terrestrial transmitters) and dynamic stochastic states (e.g., clock bias and drift).

Observability of the SLAM problem in robotics has been extensively studied [70–73]. In [74], observability of the radio SLAM problem was thoroughly analyzed through a linearized deterministic observability framework, deriving conditions on the minimal *a priori* knowledge about the receivers' and/or transmitters' states for observability. In [55], a nonlinear deterministic observability framework was utilized to show that receiver-controlled maneuvers reduce the *a priori* knowledge needed to establish observability. This dissertation studies the observability of the radio SLAM problem in a stochastic framework to characterize the evolution of the estimation error covariance produced by an extended Kalman filter (EKF) estimating the stochastic dynamic states.

Classic deterministic observability tests do not include the statistics of the: (i) process noise, (ii) measurement noise, or (iii) initial state estimate. The EKF Riccati equation, however, which governs the time evolution of the estimation error covariance, is a function of such statistics. Therefore, a system may pass deterministic observability tests, while there may exist a combination of system statistics for which an EKF would yield estimates with

unbounded estimation error variances [75]. For this reason, studying observability via a stochastic framework is of considerable importance to characterize the time evolution of the EKF's estimation error covariance.

Several stochastic observability notions have been defined in the literature. In [75, 76], a system was said to be stochastically observable if there exists a time such that an estimator could produce a finite estimation error covariance, when no prior information about the system's state vector is available. In [77], a system was said to be estimable if in estimating its states from measurements, the posterior estimation error covariance matrix is strictly smaller than the prior state covariance matrix. In [78] and [79], the stochastic stability of the discrete-time (DT) and continuous-time EKF were studied and conditions on the initial estimation error and disturbing noise terms were specified that will guarantee bounded estimation error. In [80], stochastic observability (or estimability) was defined as an assessment of the "degree of observability." Thus, in contrast to Boolean deterministic observability tests, stochastic observability was defined as a measure to whether an observable system is poorly estimable due to the gradient vectors comprising the Fisher information matrix being nearly collinear. In [81], stochastic observability was used to describe the ability of the estimator to reduce the entropy of any non-trivial function of its initial state by using the measurements.

In this dissertation, the stochastic observability of the radio SLAM problem is studied by directly analyzing the time evolution of the estimation error covariance through the Riccati equation. The radio SLAM problem is found to be stochastically unobservable when both the receiver's and transmitters' clock biases are simultaneously estimated by showing divergence of their individual variances. The stochastic observability analysis in this dissertation allows for the initial estimation error covariance to be finite, unlike other existing approaches that assume infinite initial uncertainty [75,76]. This dissertation makes three contributions. First, a closed-form expression for a lower bound on the time evolution of the estimation error variances of the stochastically unobservable states is derived. Second, the lower bound's

divergence rate is characterized. Third, numerical and experimental results are presented demonstrating an unmanned aerial vehicle (UAV)-mounted receiver, navigating in a radio SLAM fashion by fusing pseudoranges made on unknown terrestrial signals of opportunity transmitters. It is worth noting that for the stochastic observability study, this dissertation focuses on a planer environment to simplify the analysis. Extensions to three-dimensional environments is expected to follow straightforwardly.

Next, this dissertation extends the radio SLAM problem that uses a vehicular dynamic model to the case when the vehicle is equipped with an IMU. Specifically, an EKF-based inertial radio SLAM architecture is developed, where the states of *unknown* terrestrial SOPs are simultaneously estimated along with the states of the navigating vehicle. Terrestrial SOP pseudoranges are used to aid a vehicle's INS and simultaneously map unknown SOPs.

Radio SLAM-type frameworks have been adopted to exploit unknown SOPs for navigation as a standalone alternative to GNSS [82]. However, the unknown SOPs were estimated in a batch filter over the entire traversed trajectory, which is not suitable for realtime applications. EKF-based SOP-aided INS frameworks that operate recursively on incoming measurements were developed and studied in [37, 83]. In contrast to prior work presenting EKF-based SOP-aided INS frameworks, this dissertation provides a self-contained treatment of an aided INS, with sufficient details for the interested reader to implement an SOP-aided INS that operates both when GNSS is available and when GNSS becomes unavailable or unreliable. To evaluate the performance of the developed SOP-aided INS framework, the dissertation presents a performance sensitivity study conducted through numerical simulations, by varying the quantity and quality of exploited SOPs. Moreover, the article presents experimental results demonstrating an unmanned aerial vehicle (UAV) using terrestrial cellular SOPs to aid its onboard consumer-grade IMU in the absence of GNSS signals. It is demonstrated that the final position error of a traditional tightly-coupled GNSS-aided INS after 30 seconds of GNSS cutoff was 57.30 m, while the final position error of the tightly-coupled SOP-aided

INS was 9.59 m.

Finally, this dissertation extends the inertial radio SLAM problem to the case when multiple navigating vehicles are working together as a team. Future navigating vehicles will demand a reliable and accurate navigation system. To meet such stringent requirements, vehicular navigation systems must draw and fuse information from various sensing modalities and, if available, other vehicles in their vicinity. Fortunately, advances of autonomous features on cars have driven the development of vehicle-to-vehicle (V2V) communication technologies. These technologies enable current and future navigating vehicles to share information with other navigating vehicles, which will boost situational awareness and navigation performance altogether [84, 85].

To address this estimation problem, this dissertation develops a collaborative inertial radio SLAM (inertial CoRSLAM) architecture, in which multiple vehicles estimate the *unknown* states of SOPs along with the states of navigating vehicles using shared SOP and INS information. Despite the more complex stochastic and dynamic map of radio SLAM, this architecture provides an absolute position source for INS aiding in the absence of GNSS signals, preventing INS drift during prolonged GNSS unavailability periods [86].

In EKF-based inertial CoRSLAM, collaborating vehicles can improve their state estimates over single-vehicle inertial radio SLAM by communicating and fusing mutual measurements made on SOPs along with all vehicles' INS information [87]. However, V2V communication of inertial data comes with a large communication bourdon due to the substantial amount of IMU data produced by each vehicle, which is required to maintain proper inter-vehicle correlations for consistent EKF-produced estimates. This dissertation answers three practical and theoretical questions to determine how to extract the most information from the SOP measurements and how to deal with the communication bourdon. First, the estimation uncertainties of two information fusion strategies in a CoRSLAM framework are compared: (i) time-of-arrival (TOA) and (ii) time-difference-of-arrival (TDOA) taken with reference

to selected SOPs. Second, an efficient method to package and communicate INS and SOP information is developed. Third, an event-based communication scheme governing when information should be communicated is developed.

The use of TOA and TDOA for positioning have been compared in other contexts. In [88], it was determined that using GPS pseudoranges as TOA and TDOA produced identical positing results. In [89], the Cramér-Rao lower bound (CRLB) was shown to be identical for receivers with *known states* that are using either TOA or TDOA to localize multiple transmitters. In [90], the same conclusion was found for single emitter localization and was shown to be independent of the TDOA reference selection when the receivers were *stationary* and *time-synchronized*, with the measurement noise being independent and identically-distributed. These conclusions do not extend to the CoRSLAM architecture studied in this dissertation due to three reasons. The first pertains to the nature of radio SLAM, which is the unavailability of the SOPs' states that are simultaneously estimated along with the navigating vehicles' states. The second arises because the vehicle-mounted receivers' and SOPs' clocks are practically unsynchronized. The third is because the measurement noise can not be assumed to be independent and identically-distributed. A preliminary study was conducted in [91], which determined that TOA produces less than or equal estimation error covariance compared to TDOA. However, the communication bourdon of sharing the large amount of IMU data was not addressed.

In [92], transmission of IMU data was avoided by communicating state estimates and covariances between collaborators and then using covariance intersection to fuse estimates with unknown inter-vehicle correlations. In [93], estimated Euler angles and positions were shared between collaborators instead of IMU data. Then, computations of estimation error covariances were avoided by fusing estimates using the inverse of the measurement period as a weight. In contrast to [92,93], this dissertation maintains inter-vehicle correlations and deals with the communication bourdon by determining the minimal sufficient INS information

that must be communicated to maintain consistent estimates. Then, an event-based communication scheme is developed, which minimizes the amount of communicated information by transmitting data only if an event of interest is triggered.

In recent years, a number of studies in other contexts have been reported for event-based communication; see [94], and references therein. These studies have lead to different event-triggering tests, such as: level-triggering, which compares the amplitude of a signal versus a pre-defined threshold [95]; average estimation error covariance, which checks the average of the time-history of the trace of the estimation error covariance [96]; state difference, which uses the difference between a vehicle's current state and the last transmitted state; residual-based, which checks the difference between the actually and predicted measurement [97]; and innovation variance-based tests [98]. While several event-triggering tests have been developed, the development of event-based tests in the context of distributed estimation has not been adequately addressed. In [99], an event-based scheme was developed for a distributed filter, however was studied using a simplified linear dynamics model. In this dissertation, an event-based scheme is developed and studied for inertial CoRSLAM, where vehicles only exchange information if the norm of the estimation error will violate a threshold with a user-specified probability. Two norms important for vehicular navigation are considered: two-norm, which tests absolute positioning error and infinity-norm, which tests the largest error in any coordinate direction.

The contributions in this dissertations have resulted in the refereed publications: [J2], [J3], [J5], [J6], [J7], [C1], [C2], [C3], [C4], [C6], [C7], [C9], and [C10], which are listed above in the Curriculum Vitae.

1.3 Dissertation Outline

This dissertation is organized as follow:

- **Chapter 2: Optimal Receiver Placement for Mapping Terrestrial SOPs.** This chapter introduces the dynamics model of the SOPs and the pseudorange measurement model made on the SOPs by a receiver. A novel computationally efficient optimization criterion, that is based on area-maximization, to optimally place an additional receiver into the environment for mapping unknown SOPs is derived. The optimal mapping performance as a function of time and number of receivers in the environment is presented.

- **Chapter 3: Optimal Receiver Placement for Mapping Terrestrial SOPs.** This chapter analyzes the stochastic observability of radio SLAM. It is shown that the receiver's and transmitters' clock biases are stochastically unobservable and that their estimation error variances will diverge. A lower bound on the divergence rate of the estimation error variances of the receiver's and transmitters' clock biases is derived and demonstrated numerically. Simulation and experimental results are presented for an unmanned aerial vehicle (UAV) navigating without GPS signals, using pseudoranges made on unknown terrestrial transmitters. It is demonstrated that despite the receiver's and transmitters' clock biases being stochastically unobservable, the EKF produces bounded *localization* errors.

- **Chapter 4: Tightly-Coupled SOP-Aided Inertial Navigation.** This chapter provides a self-contained treatment of an aided INS, with sufficient details for the interested reader to implement an SOP-aided INS that operates both when GNSS is available and when GNSS becomes unavailable or unreliable. The SOP-aided INS is studied by varying the number of available SOPs and the quality of the oscillators equipped on the SOPs.

- **Chapter 5: Information Fusion and Communication Strategies for Collaborative SOP-Aided Inertial Navigation.** This chapter extends the SOP-aided INS concept to multiple collaborating vehicles and studies communication and information fusion strategies for collaborators sharing and fusing SOP and INS data to aid their INSs. This chapter is concerned with answering three questions: what SOP and INS information should shared between collaborators and when should it be shared?

- **Chapter 6: Dissertation Conclusions and Main Takeaways.** This chapter summarizes the contributions of this dissertation and highlights the major discoveries.

Chapter 2

Optimal Receiver Placement for Mapping Terrestrial SOPs

This chapter is organized as follows. Section 2.1 describes the SOPs' dynamics and receivers' observation model. Section 2.2 formulates the optimal receiver placement problem for an arbitrary number of SOPs in the environment as GDOP minimization and determinant of the inverse of the GDOP matrix maximization. The placement problem is reformulated as an area maximization for the single SOP case and a product of areas maximization for the multiple SOP case. The area and product of areas optimization problems are compared against the GDOP optimization problems and their optimal solution is specified. Section 2.3 derives the optimal mapping performance as a function of time and number of receivers. Section 2.4 presents experimental results for collaboratively mapping an unknown SOP.

2.1 Model Description

The following nomenclature and conventions will be used throughout this chapter. Vectors will be column and represented by lower-case, italicized, and bold characters, e.g., $\boldsymbol{x}$. Matrices will be represented by upper-case bold characters, e.g., $\mathbf{A}$. The following notation is use only in this chapter.

2.1.1 SOP Dynamics Model

The SOP clock error dynamics will be modeled according to the two-state model composed of the clock bias δt_s and clock drift $\dot{\delta t}_s$. The clock error states $\boldsymbol{x}_{\text{clk},s}$ evolve according to

$$\dot{\boldsymbol{x}}_{\text{clk},s}(t) = \mathbf{A}_{\text{clk}}\, \boldsymbol{x}_{\text{clk},s}(t) + \tilde{\boldsymbol{w}}_{\text{clk},s}(t),$$

$$\boldsymbol{x}_{\text{clk},s} = \begin{bmatrix} \delta t_s \\ \dot{\delta t}_s \end{bmatrix}, \quad \tilde{\boldsymbol{w}}_{\text{clk},s} = \begin{bmatrix} \tilde{w}_{\delta t_s} \\ \tilde{w}_{\dot{\delta t}_s} \end{bmatrix}, \quad \mathbf{A}_{\text{clk}} = \begin{bmatrix} 0 & 1 \\ 0 & 0 \end{bmatrix},$$

where the elements of $\tilde{\boldsymbol{w}}_{\text{clk},s}$ are modeled as zero-mean, mutually independent white noise sequences, and the power spectral density of $\tilde{\boldsymbol{w}}_{\text{clk},s}$ is given by $\tilde{\mathbf{Q}}_{\text{clk},s} = \text{diag}\left[S_{\tilde{w}_{\delta t_s}}, S_{\tilde{w}_{\dot{\delta t}_s}}\right]$, where $\text{diag}\,[a, b]$ is an appropriately sized square matrix with diagonal elements a and b and zeros elsewhere. The power spectra $S_{\tilde{w}_{\delta t_s}}$ and $S_{\tilde{w}_{\dot{\delta t}_s}}$ can be related to the power-law coefficients $\{h_\alpha\}_{\alpha=-2}^{2}$, which have been shown through laboratory experiments to be adequate to characterize the power spectral density of the fractional frequency deviation $y(t)$ of an oscillator from nominal frequency, which takes the form $S_y(f) = \sum_{\alpha=-2}^{2} h_\alpha f^\alpha$ [100]. It is common to approximate the clock error dynamics by considering only the frequency random walk coefficient h_{-2} and the white frequency coefficient h_0, which lead to $S_{\tilde{w}_{\delta t_s}} \approx \frac{h_0}{2}$ and $S_{\tilde{w}_{\dot{\delta t}_s}} \approx 2\pi^2 h_{-2}$ [80].

The SOP will be assumed to emanate from a spatially-stationary terrestrial transmitter, and

its state vector will consist of its planar position states $\boldsymbol{r}_s \triangleq [x_s,\, y_s]^{\mathsf{T}}$ and $c\,\boldsymbol{x}_{\mathrm{clk},s}$, where c is the speed of light. Hence, the SOP's dynamics can be described by the state space model

$$\dot{\boldsymbol{x}}_s(t) = \mathbf{A}_s\,\boldsymbol{x}_s(t) + \mathbf{D}_s\tilde{\boldsymbol{w}}_s(t), \tag{2.1}$$

where $\boldsymbol{x}_s \triangleq \left[\boldsymbol{r}_s^{\mathsf{T}},\, c\,\boldsymbol{x}_{\mathrm{clk},s}^{\mathsf{T}}\right]^{\mathsf{T}}$, $\tilde{\boldsymbol{w}}_s \triangleq \tilde{\boldsymbol{w}}_{\mathrm{clk},s}$,

$$\mathbf{A}_s = \begin{bmatrix} \mathbf{0}_{2\times2} & \mathbf{0}_{2\times2} \\ \mathbf{0}_{2\times2} & \mathbf{A}_{\mathrm{clk}} \end{bmatrix}, \quad \mathbf{D}_s = \begin{bmatrix} \mathbf{0}_{2\times2} \\ \mathbf{I}_{2\times2} \end{bmatrix}.$$

Discretizing the SOP's dynamics (2.1) at a constant sampling interval T yields the discrete-time (DT)-equivalent model

$$\boldsymbol{x}_s\,(k+1) = \mathbf{F}_s\,\boldsymbol{x}_s(k) + \boldsymbol{w}_s(k), \quad k = 1, 2, \ldots, \tag{2.2}$$

where $\boldsymbol{w}_s \triangleq \left[w_{x_s}, w_{y_s}, w_{\delta t_s}, w_{\delta \dot{t}_s}\right]^{\mathsf{T}}$ is a zero-mean white noise sequence with covariance $\mathbf{Q}_s$, and

$$\mathbf{F}_s = \mathrm{diag}\left[\mathbf{I}_{2\times2},\, \mathbf{F}_{\mathrm{clk}}\right], \quad \mathbf{Q}_s = \mathrm{diag}\left[\mathbf{0}_{2\times2},\, c^2\mathbf{Q}_{\mathrm{clk},s}\right],$$

$$\mathbf{F}_{\mathrm{clk}} = \begin{bmatrix} 1 & T \\ 0 & 1 \end{bmatrix}, \; \mathbf{Q}_{\mathrm{clk},s} = \begin{bmatrix} S_{\tilde{w}_{\delta t_s}} T + S_{\tilde{w}_{\delta \dot{t}_s}} \frac{T^3}{3} & S_{\tilde{w}_{\delta \dot{t}_s}} \frac{T^2}{2} \\ S_{\tilde{w}_{\delta \dot{t}_s}} \frac{T^2}{2} & S_{\tilde{w}_{\delta \dot{t}_s}} T \end{bmatrix}.$$

2.1.2 Observation Model

The pseudorange observation made by the n^{th} receiver on the SOP, after discretization and mild approximations discussed in [74], is related to the SOP's states by

$$z_n(k) = \|\boldsymbol{r}_{r_n}(k) - \boldsymbol{r}_s\| + c \cdot [\delta t_{r_n}(k) - \delta t_s(k)] + v_n(k), \tag{2.3}$$

where $\|\cdot\|$ is the Euclidean norm, $\boldsymbol{r}_{r_n} \triangleq [x_{r_n},\, y_{r_n}]^{\mathsf{T}}$ and δt_{r_n} are the position and clock bias of the receiver, respectively, and v_n is the measurement noise, which is modeled as a DT zero-mean white Gaussian sequence with variance σ_n^2.

2.2 Optimal Receiver Placement

This section answers the question: where to optimally place a receiver in an environment comprising N randomly pre-deployed receivers and M unknown SOPs with an arbitrary configuration? The following subsection will formulate and compare three optimization problems: GDOP minimization, determinant maximization, and area maximization. Subsequently, the convexity of these problems is analyzed. Finally, an analytical solution to the area maximization problem is derived for two cases: single ($M = 1$) and multiple ($M > 1$) SOPs.

2.2.1 Problem Formulation

Consider a planar environment comprising M unknown SOPs and N arbitrarily placed receivers with knowledge about their own states. The receivers draw pseudorange observations from each SOP, denoted $\{{}^m z_n\}_{n=1}^N$, for $m = 1, \ldots, M$. These observations are fused through a centralized estimator whose role is to estimate the augmented state vector $\boldsymbol{x}'$ defined as

$$\boldsymbol{x}' \triangleq \left[\boldsymbol{x}_{s_1}'^{\mathsf{T}},\, \cdots,\, \boldsymbol{x}_{s_M}'^{\mathsf{T}}\right]^{\mathsf{T}}, \quad \boldsymbol{x}_{s_m}' \triangleq [\,\boldsymbol{r}_{s_m}, c\delta t_{s_m}\,]^{\mathsf{T}}.$$

It is desired to deploy an additional receiver to a location that will result in the maximum improvement of the estimate of $\boldsymbol{x}'$, denoted as $\hat{\boldsymbol{x}}'$. The measurement residual computed by the centralized estimator has a first-order approximation of its Taylor series expansion about

$\hat{\boldsymbol{x}}'$, which is given by

$$\boldsymbol{\Delta z} = \mathbf{H}' \, \boldsymbol{\Delta x}' + \boldsymbol{v}, \tag{2.4}$$

where $\boldsymbol{\Delta z} \triangleq \boldsymbol{z} - \hat{\boldsymbol{z}}$, i.e., the difference between the observation vector

$$\boldsymbol{z} \triangleq \left[{}^1z_1, \ldots, {}^1z_{N+1}, {}^2z_1, \ldots, {}^2z_{N+1}, \ldots, {}^Mz_{N+1} \right]^{\mathsf{T}}$$

and its estimate $\hat{\boldsymbol{z}}$; $\boldsymbol{\Delta x}' \triangleq \boldsymbol{x}' - \hat{\boldsymbol{x}}'$, i.e., the difference between $\boldsymbol{x}'$ and its estimate $\hat{\boldsymbol{x}}'$; $\boldsymbol{v} \triangleq \left[{}^1\boldsymbol{v}^{\mathsf{T}}, \ldots, {}^M\boldsymbol{v}^{\mathsf{T}} \right]^{\mathsf{T}}$, where ${}^m\boldsymbol{v} \triangleq [{}^mv_1, \ldots, {}^mv_{N+1}]^{\mathsf{T}}$; and $\mathbf{H}'$ is the Jacobian matrix evaluated at the estimate $\hat{\boldsymbol{x}}'$, which is given by $\mathbf{H}' = \text{diag}\,[\mathbf{H}'_1, \ldots, \mathbf{H}'_M]$, where

$$\mathbf{H}'_m = -\begin{bmatrix} {}^m\hat{\mathbf{1}}_1^{\mathsf{T}} & 1 \\ \vdots & \vdots \\ {}^m\hat{\mathbf{1}}_{N+1}^{\mathsf{T}} & 1 \end{bmatrix} = -\begin{bmatrix} \cos({}^m\phi_1) & \sin({}^m\phi_1) & 1 \\ \vdots & \vdots & \vdots \\ \cos({}^m\phi_{N+1}) & \sin({}^m\phi_{N+1}) & 1 \end{bmatrix}.$$

Without loss of generality, assume an East-North coordinate frame, denoted $\{f_m\}$, centered at the m^{th} SOP's position estimate $\hat{\boldsymbol{r}}_{s_m}$. The vector ${}^m\hat{\mathbf{1}}_n \triangleq [\cos({}^m\phi_n), \sin({}^m\phi_n)]^{\mathsf{T}} = \frac{\boldsymbol{r}_{r_n} - \hat{\boldsymbol{r}}_{sm}}{\|\boldsymbol{r}_{r_n} - \hat{\boldsymbol{r}}_{sm}\|}$ is geometrically a unit LOS vector expressed in $\{f_m\}$ to the n^{th} receiver position $\boldsymbol{r}_{r_n}$. The bearing angle ${}^m\phi_n$ will be measured counterclockwise with respect to the East axis of $\{f_m\}$ and $\boldsymbol{r}_{r_n}$ will be expressed in $\{f_1\}$. The observation noise for the set of measurements is assumed to be independent and identically-distributed (i.i.d.) across all channels, i.e., $\{\sigma_n^2\}_{n=1}^N \equiv \sigma^2$ and $\text{cov}\,(\boldsymbol{v}) = \sigma^2 \mathbf{I}_{M(N+1)\times M(N+1)}$. The weighted least-squares solution to (2.4) and associated estimation error covariance $\mathbf{P}'$ are given by

$$\boldsymbol{\Delta}\hat{\boldsymbol{x}}' = \left(\mathbf{H}'^{\mathsf{T}}\mathbf{H}'\right)^{-1}\mathbf{H}'^{\mathsf{T}}\boldsymbol{\Delta z}, \quad \mathbf{P}' = \sigma^2 \left(\mathbf{H}'^{\mathsf{T}}\mathbf{H}'\right)^{-1}. \tag{2.5}$$

The matrix $\left(\mathbf{H}'^{\mathsf{T}}\mathbf{H}'\right)^{-1}$ is known as the geometric dilution of precision (GDOP) matrix. Hence, the quality of the estimate depends on the receiver-to-SOP geometry and the pseu-

dorange observation noise variance σ^2. The GDOP is defined as GDOP $\triangleq \sqrt{\mathrm{tr}\left[\left(\mathbf{H}'^{\mathsf{T}}\mathbf{H}'\right)^{-1}\right]}$, where $\mathrm{tr}\left[\cdot\right]$ is the matrix trace. The GDOP provides a simple scalar characterization of the receiver-to-SOP geometry– the lower the GDOP, the more favorable the geometry [62]. Therefore, the receiver placement problem can be cast as the GDOP minimization problem

$$\underset{\boldsymbol{r}_{r_{N+1}}}{\text{minimize}} \quad \sqrt{\mathrm{tr}\left[\left[\,\mathbf{H}'^{\mathsf{T}}(\boldsymbol{r}_{r_{N+1}})\mathbf{H}'(\boldsymbol{r}_{r_{N+1}})\,\right]^{-1}\right]}, \tag{2.6}$$

where $\boldsymbol{r}_{r_{N+1}}$ is the location of the $(N+1)^{\text{st}}$ receiver. The GDOP is approximately minimized when the determinant $\det\left(\mathbf{H}'^{\mathsf{T}}\mathbf{H}'\right)$ is maximized, since $\left(\mathbf{H}'^{\mathsf{T}}\mathbf{H}'\right)^{-1} = \mathrm{adj}\left(\mathbf{H}'^{\mathsf{T}}\mathbf{H}'\right)/\det\left(\mathbf{H}'^{\mathsf{T}}\mathbf{H}'\right)$ and the adjoint $\mathrm{adj}\left(\mathbf{H}'^{\mathsf{T}}\mathbf{H}'\right)$ varies less with the geometry of the receiver placement than $\det\left(\mathbf{H}'^{\mathsf{T}}\mathbf{H}'\right)$ [62]. Therefore, an alternative optimization problem to (2.6) is

$$\underset{\boldsymbol{r}_{r_{N+1}}}{\text{maximize}} \quad \det\left[\,\mathbf{H}'^{\mathsf{T}}(\boldsymbol{r}_{r_{N+1}})\mathbf{H}'(\boldsymbol{r}_{r_{N+1}})\,\right]. \tag{2.7}$$

The optimization problems (2.6) and (2.7) are equivalent to the so-called A- and D-optimality criteria, respectively [101]. In (2.6), the average variance of the estimates are minimized, whereas (2.7) is equivalent to minimizing the volume of the uncertainty ellipsoid, which has a useful geometric interpretation for receiver placement. This interpretation gives rise to an alternative optimization problem to both (2.6) and (2.7), which is formulated and compared in Subsections 2.2.2 and 2.2.3 for $M = 1$ and $M > 1$, respectively.

2.2.2 Case One: Single SOP

For planar environments comprising a single SOP, (2.6) and (2.7) may be reparameterized over ${}^1\phi_{N+1}$, since $\mathbf{H}'$ is completely determined by the SOP-to-receiver bearing angles. Since the environment consists of only a single SOP, the superscript will be dropped to simplify notation for the remainder of this subsection, i.e., ${}^1\phi_n \equiv \phi_n$. It can be shown that $\det\left(\mathbf{H}'^{\mathsf{T}}\mathbf{H}'\right)$

is related to the area of the polytope inscribed in a unit circle, whose vertices are defined by the SOP-to-receiver unit LOS vector endpoints [56]. Hence, the optimization problem can be reformulated as a polytope area maximization problem over ϕ_{N+1}. In a planar scenario composed of three receivers, the relationship is exact, i.e., maximizing $\det\left(\mathbf{H}'^{\mathsf{T}}\mathbf{H}'\right)$ simultaneously maximizes the area of the triangle whose vertices are defined by the unit LOS vectors. This is due to the fact that $\mathbf{H}'$ is now a square matrix. With the exception of the scenario when all receivers are collinear with an SOP, $\mathbf{H}'$ is an invertible matrix and the area is $A = \frac{1}{2}\sqrt{\det(\mathbf{H}'^{\mathsf{T}}\mathbf{H}')} = \frac{1}{2}\det(\mathbf{H}')$. For more than three receivers, the relationship is exact for regular polygons, but approximate for non-regular polygons. Specifically, a polygon inscribed in the unit circle that simultaneously maximizes the determinant and maximizes the area is a regular polygon [64].

For non-regular polygons, the relationship is "almost exact" and the discrepancy is minimal. To see this, $N+1$ receivers were placed randomly around an SOP, where the n^{th} receiver position was chosen such that $\phi_n \sim \mathcal{U}(0, 2\pi)$, for $n = 2, \ldots, N+1$, and $\phi_1 = 0$, for a total of 10^5 random configurations, where $\mathcal{U}(a, b)$ is the uniform distribution over (a, b). For each configuration, the corresponding GDOP and area were calculated, which are plotted in Fig. 2.1(a)–(d) for $N = 2, \ldots, 5$, respectively. Subsequently, for each of the configurations, the first N receivers' positions were fixed and the $(N+1)^{\text{st}}$ receiver was placed so to optimize the GDOP then to optimize the area. The resulting optimal GDOP versus optimal area are plotted in Fig. 2.1(e)–(h) for $N = 2, \ldots, 5$, respectively.

The following can be concluded from the plots in Fig. 2.1. First, placing the $(N+1)^{\text{st}}$ receiver to optimize the area simultaneously optimizes the GDOP only for $N = 2$. Second, for $N > 2$, placing the $(N+1)^{\text{st}}$ receiver to optimize the area approximately optimizes the GDOP. Third, the voids in the "point cloud" in the optimal area versus optimal GDOP plot (Fig. 2.1(e)–(h)) compared to the area versus GDOP plot (Fig. 2.1(a)–(d)) are due to optimizing the placement of the $(N+1)^{\text{st}}$ receiver, which effectively increases the area

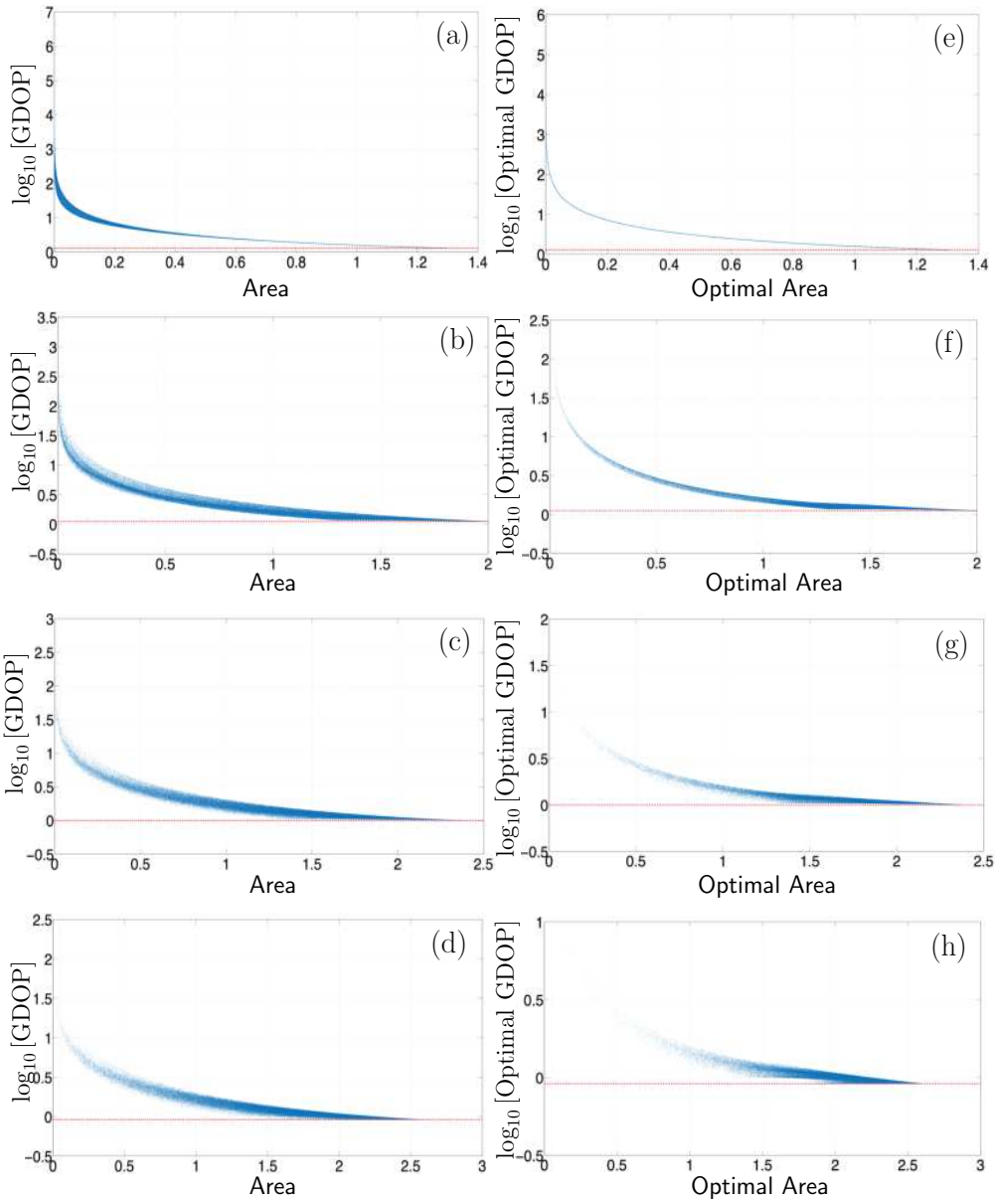

Figure 2.1: $N+1$ receivers were randomly placed around an SOP for a total of 10^5 configurations. Fig. (a)–(d) correspond to $N = 2, \ldots, 5$, respectively, and Fig. (e)–(h) correspond to $N = 2, \ldots, 5$, respectively. For each configuration, the resulting area and the resulting GDOP were computed and plotted in Fig. (a)–(d). Each point in the point cloud represents the area and corresponding GDOP for a particular configuration. Then, for each previous configuration, the first N receiver locations were fixed and the $(N+1)^{\text{st}}$ receiver was optimally placed to optimize the GDOP and then to optimize the area. Each point in the point cloud plotted in Fig. (e)–(h) represents the optimal area versus optimal GDOP for a particular configuration. Dotted red line corresponds to the theoretical minimum achievable GDOP.

(decreases the GDOP), pushing the "point cloud" towards the right (bottom). Fourth, when $N+1$ receivers are arranged so that the end-point's of the unit LOS vectors form a regular polygon configuration, the theoretical minimum GDOP, given by $\text{GDOP}_{\min} = \sqrt{5/(N+1)}$ is achieved (dotted red line in Fig. 2.1) [57] and the area simultaneously achieves its maximum value.

Motivated by these results, an alternative optimization problem to (2.6) and (2.7) is proposed, which aims to maximize the area A of the polygon over the angle of the unit LOS vector of the $(N+1)^{\text{st}}$ receiver, namely

$$\underset{\phi_{N+1}}{\text{maximize}} \quad A\left(\phi_{N+1}\right) = A_N + \Delta A\left(\phi_{N+1}\right), \tag{2.8}$$

where A_N is the total area for N pre-deployed receivers. The area A_N can be derived from the the sum of triangle areas as

$$A_N = \sum_{n=1}^{N} \frac{1}{2}\sin(\theta_n), \tag{2.9}$$

where $\theta_n \triangleq \phi_{n+1} - \phi_n$ for $n = 1, \ldots, N-1$; $\theta_N \triangleq 2\pi - \phi_N$; and $\Delta A\left(\phi_{N+1}\right)$ is the change in area resulting from placing the $(N+1)^{\text{st}}$ receiver at ϕ_{N+1}, where $\phi_n \leq \phi_{N+1} \leq \phi_{n+1} < 2\pi$. The change in area $\Delta A\left(\phi_{N+1}\right)$ is given by

$$\Delta A\left(\phi_{N+1}\right) = \frac{1}{2}\left[\sin(\phi_{N+1} - \phi_n) + \sin(\theta_n - \phi_{N+1} + \phi_n) - \sin(\theta_n)\right]. \tag{2.10}$$

A depiction of $A\left(\phi_{N+1}\right)$ is illustrated in Fig. 2.2.

Next, it will be shown that while the optimization functions in (2.6) and (2.7) are neither

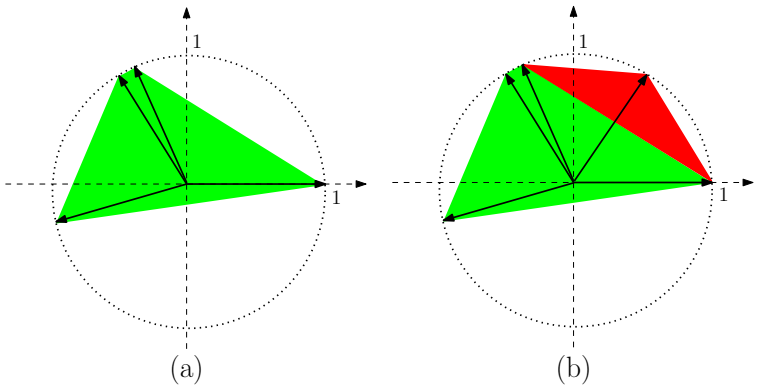

Figure 2.2: (a) Polygon inscribed in the unit circle formed by the endpoints of the unit LOS vectors from the SOP to four randomly-deployed receivers for the configuration depicted in Fig. 2.3(a). The area A_N is highlighted in green. (b) Resulting polygon due to introducing an additional fifth receiver depicted in Fig. 2.3(a). The change in area $\Delta A\left(\phi_{N+1}\right)$ due to introducing the $(N+1)^{\text{st}}$ receiver is highlighted in red.

convex nor concave, necessitating a general-purpose numerical nonlinear optimization solver, the optimization function in (2.8) is piecewise-concave with a simple analytical solution.

Convexity Analysis

The term $\mathbf{H}'^{\mathsf{T}}\mathbf{H}'$ in the optimization problems (2.6) and (2.7) can be readily shown to be

$$\mathbf{H}'^{\mathsf{T}}\mathbf{H}' = \sum_{n=1}^{N+1} \begin{bmatrix} \cos^2\phi_n & \cos\phi_n \sin\phi_n & \cos\phi_n \\ \sin\phi_n \cos\phi_n & \sin^2\phi_n & \sin\phi_n \\ \cos\phi_n & \sin\phi_n & 1 \end{bmatrix}.$$

It is obvious that the optimization functions in (2.6) and (2.7) are neither convex nor concave. However, while the optimization function (2.8) is neither convex nor concave, it is piecewise-concave, and the "zero-crossings" occur when the additional receiver is introduced at the same bearing angle as a pre-deployed receiver. A depiction of these functions is illustrated in Fig. 2.3.

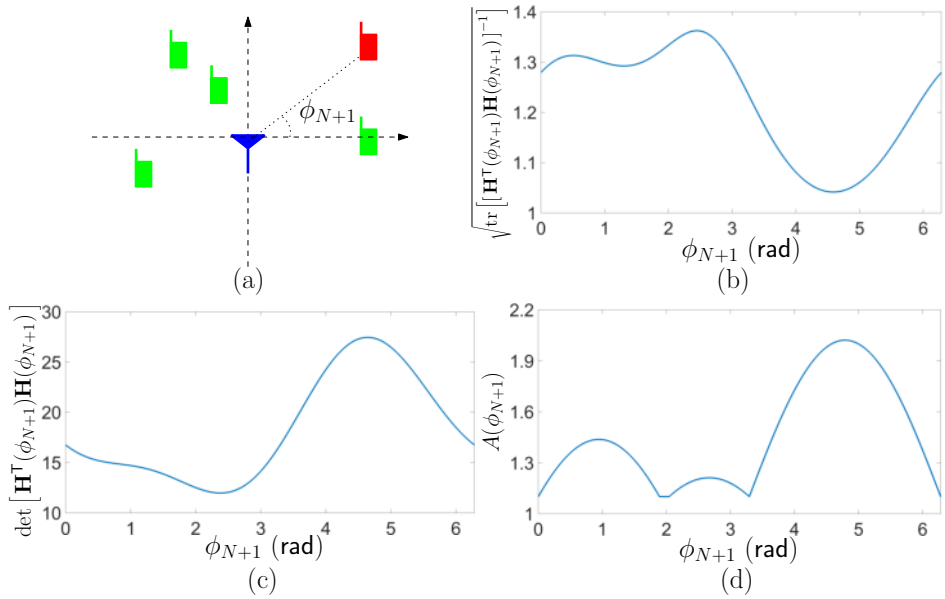

Figure 2.3: (a) Four randomly placed receivers (green) with respective angles given by $\phi_n \in \{\,0,\,1.892,\,2.043,\,3.295\,\}$ rad estimating the state vector of an unknown SOP (blue). The optimal receiver placement problem is to place an additional receiver (red) at an angle ϕ_{N+1} that will minimize the GDOP (2.6), maximize the determinant of the inverse of the GDOP matrix (2.7), or maximize the area of the polygon (2.8). The corresponding GDOP, determinant, and area optimization functions, respectively, due to sweeping $0 \leq \phi_{N+1} \leq 2\pi$ of the additional receiver, are plotted in (b)–(d).

Optimal Solution to Area Maximization

The special property of piecewise-concavity of the area maximization problem (2.8) allows for a simple analytical solution for the receiver placement problem. This is summarized in the following theorem.

Theorem 2.2.1. *The optimal placement with respect to the area maximization criterion (2.8) of a receiver to an environment comprising N arbitrarily placed receivers and one SOP is anywhere on a LOS vector from the SOP at an angle $\phi^{\star}_{N+1} = \frac{1}{2}\max_n \theta_n$, for $n = 1, \ldots, N-1$, where $\theta_n \triangleq \phi_{n+1} - \phi_n$ and $\theta_N \triangleq 2\pi - \phi_N$.*

Proof. First, it will be shown that in a particular $\theta_n \in [0, 2\pi)$, the angle that maximizes the change in area is at $\phi^{\star(n)}_{N+1}$, where $\phi^{\star(n)}_{N+1} \triangleq \phi_n + \alpha^{\star}_n$ and $\alpha^{\star}_n = \frac{1}{2}\theta_n$, where α_n is defined as the angle sweeping θ_n, i.e., $\alpha_n \triangleq \phi_{N+1} - \phi_n$ for $0 \leq \alpha_n \leq \theta_n$.

Parameterizing $\Delta A\left(\phi_{N+1}\right)$ by α_n in (2.10) yields

$$\Delta A\left(\alpha_n\right) = \frac{1}{2}\left[\sin(\alpha_n) + \sin(\theta_n - \alpha_n) - \sin(\theta_n)\right], \tag{2.11}$$

and applying the first-order necessary condition for optimality yields

$$\begin{aligned}\frac{d\Delta A\left(\alpha_n\right)}{d\alpha_n} &= \frac{1}{2}\cos(\alpha_n) - \frac{1}{2}\cos(\theta_i - \alpha_n) \equiv 0 \\ \Rightarrow \alpha_n^\star &= \frac{1}{2}\,\theta_n + \pi k.\end{aligned}$$

Substituting $\alpha^\star$ into the definition of $0 \leq \alpha_n \leq \theta_n$ yields $-\frac{1}{2}\theta_n \leq \pi k \leq \frac{1}{2}\theta_n$. Since the angle between any two known receivers is $0 \leq \theta_n < 2\pi$, k is bounded by $-\pi < \pi k < \pi$. The only value of k that satisfies this inequality is $k = 0$. Therefore, $\alpha_n^\star = \frac{1}{2}\theta_n$ is the only critical angle in θ_n.

Furthermore, since $0 \leq \theta_n < 2\pi$, the critical angle is $0 \leq \alpha_n^\star < \pi$. The second-order necessary condition for optimality, evaluated at this critical angle is

$$\begin{aligned}\frac{d^2\Delta A_n}{d\alpha_n^2} &= -\frac{1}{2}\sin(\alpha_n) - \frac{1}{2}\sin(\theta_n - \alpha_n) \\ &= -\frac{1}{2}\sin(\alpha_n^\star) - \frac{1}{2}\sin(2\alpha_n^* - \alpha_n^*) \\ &= -\sin(\alpha_n^\star).\end{aligned} \tag{2.12}$$

Since (2.12) is always negative, the change in area in (2.10) is concave over $\phi_n + \theta_n$, and $\alpha^\star$ is the global maximizer. The above analysis holds $\forall\theta_n$, and the change in area over $[0, 2\pi)$ is piecewise-concave with N concave regions, where each region corresponds to $\{\theta_n\}_{n=1}^N$.

Next, it will be shown that the largest change in area $\Delta A\left(\phi_{N+1}\right)$ is achieved when the largest region θ_n is chosen, i.e., the receiver is positioned at $\phi_{N+1}^\star = \phi_{n_{\max}} + \alpha_{n_{\max}}^\star$, where

$\phi_{n_{\max}} = \phi_{n_{\max+1}} - \theta_{n_{\max}}$, $\theta_{n_{\max}} \triangleq \max_n\{\theta_n\}$, $\alpha^\star_{n_{\max}} = \frac{1}{2}\theta_{n_{\max}}$, where $n = 1, \ldots, N$.

Substituting for $\alpha^\star_n = \frac{1}{2}\theta_n$ into (2.11) yields

$$\Delta A\left(\alpha^\star_n\right) = \sin\left(\frac{1}{2}\theta_n\right) - \frac{1}{2}\sin\left(\theta_n\right).$$

Taking the derivative with respect to θ_n yields

$$\frac{d\Delta A\left(\alpha_n\right)}{d\theta_n} = \frac{1}{2}\cos\left(\frac{1}{2}\theta_n\right) - \frac{1}{2}\cos(\theta_n). \tag{2.13}$$

Equation (2.13) is non-negative from $\left[0,\ \frac{4\pi}{3}\right]$, i.e., increasing the region $\theta_n \in \left[0,\ \frac{4\pi}{3}\right]$ increases the resulting area. Hence, choosing $\theta_{n_{\max}}$ in this range guarantees the largest change in area. In $\left(\frac{4\pi}{3},\ 2\pi\right)$, (2.13) is negative; therefore, the change in area begins to decrease as θ_n sweeps $\left(\frac{4\pi}{3},\ 2\pi\right)$. To verify that choosing $\theta_{n_{\max}}$ is the optimal choice, it is shown that $\Delta A\left(\theta_n\right) < \Delta A\left(\theta_{n_{\max}}\right)$, when $\theta_n \in [0, 2\pi - \Gamma]$, where $\Gamma = \theta_{n_{\max}} = \frac{4\pi}{3} + \varepsilon$, $0 < \varepsilon < \frac{2\pi}{3}$. Hence,

$$\begin{aligned}
\Delta A\left(\theta_{n_{\max}}\right) &> \Delta A\left(\theta_n\right) \\
\sin\left(\frac{1}{2}\Gamma\right) - \frac{1}{2}\sin(\Gamma) &> \sin\left[\frac{1}{2}(2\pi - \Gamma)\right] - \frac{1}{2}\sin(2\pi - \Gamma) \\
-\frac{1}{2}\sin(\Gamma) &> \frac{1}{2}\sin(\Gamma).
\end{aligned}$$

Since $\sin(\Gamma) < 0$, $\forall\, \varepsilon \in \left(0, \frac{2\pi}{3}\right)$, the above inequality holds and $\Delta A\left(\theta_{n_{\max}}\right) > \Delta A\left(\theta_n\right)$. □

Theorem 2.2.1 provides a simple recipe for the placement problem, which is summarized in Algorithm 1.

It is worth noting that several approaches have been developed in the literature specifying the optimal configuration of *all* available sensors to map a single target. In contrast, Theorem 2.2.1 specifies the optimal placement of *one* additional receiver into an environment comprising *arbitrarily* placed, pre-deployed receivers. While these two problems are not di-

Algorithm 1 Optimal Receiver Placement for One SOP

Given: Positions of all pre-deployed receivers and an estimate of the SOP's position.
Calculate the angles $\{\theta_n\}_{n=1}^{N}$ sandwiched between every two consecutive receivers.
Halve the largest of these angles.
Place the $(N+1)^{\text{st}}$ receiver anywhere on a ray with the angle calculated in the previous step.

rectly comparable, in what follows, it is easy to verify that the optimal GDOP for the 2D environments found in [102] and [57] and the maximum logarithm of the FIM determinant in [66] is achieved by Algorithm 1 when the pre-deployed receivers reside at N of the vertices of an $(N+1)$-sided regular polygon. Specifically, there will be $N-1$ angles sandwiched between consecutive receivers equal to $360/(N+1)$ and one angle equal to $2\times 360/(N+1)$. The largest angle $2\times 360/(N+1)$ is halved, which places the receiver anywhere on a ray passing through the remaining vertex of the regular polygon.

2.2.3 Case Two: Multiple SOPs

For planar environments comprising multiple SOPs, it is obvious that (2.6) and (2.7) can not be reparameterized over ${}^1\phi_{N+1}$ as was done in Subsection 2.2.2. As such, the optimization functions in (2.6) and (2.7) are over $\boldsymbol{r}_{N+1}$, and are neither convex nor concave. To see this, an environment comprising three pre-deployed receivers, a candidate receiver position, and two terrestrial SOPs is illustrated in Fig. 2.4(a). The resulting $\text{GDOP}(\boldsymbol{r}_{r_{N+1}})$ and $\det\left[\,\mathbf{H}'^{\mathsf{T}}(\boldsymbol{r}_{r_{N+1}})\mathbf{H}'(\boldsymbol{r}_{r_{N+1}})\,\right]$ for placing an additional receiver at candidate positions on a grid sampled at one meter intervals in $[-1500,-1000]^{\mathsf{T}} \leq \boldsymbol{r}_{r_{N+1}} \leq [1500,1500]^{\mathsf{T}}$ are plotted in Fig. 2.4(b)–(c), respectively. The bounds on the grid $[-1500,-1000]^{\mathsf{T}}$ and $[1500,1500]^{\mathsf{T}}$ were chosen to center the environment for illustration purposes. In general, arbitrary bounds may be chosen. It is clear from these surfaces that (2.6) and (2.7) do not posses any useful convexity properties. In the following, the area maximization problem will be generalized and shown to yield a family of convex programs.

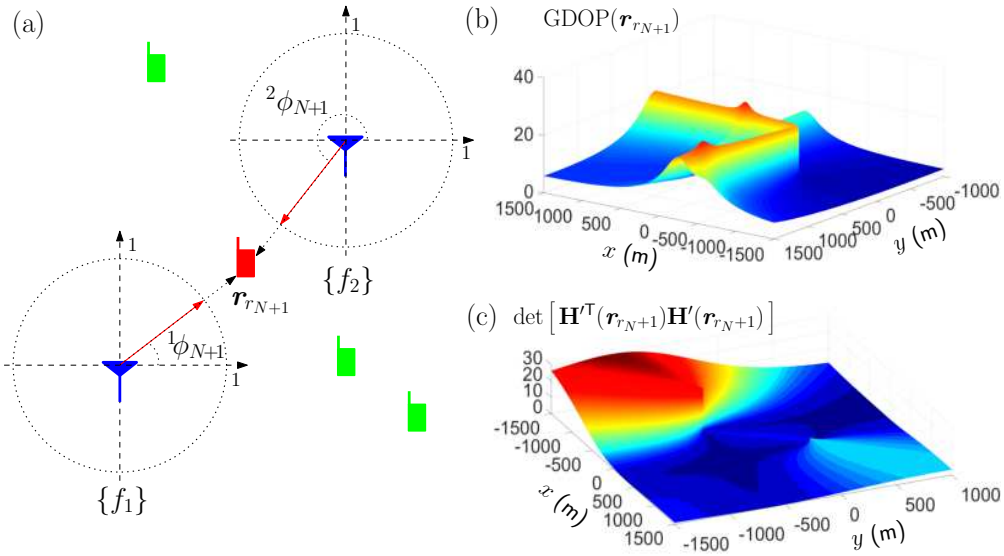

Figure 2.4: (a) Environment comprised of 3 pre-deployed receivers (green) estimating the states of 2 unknown SOPs (blue). The optimal receiver placement problem is to place an additional receiver (red) at a position $\boldsymbol{r}_{r_{N+1}}$ that will minimize the GDOP (b) or maximize the determinant (c).

Product of Areas Maximization

Recall the block diagonal structure of the measurement Jacobian $\mathbf{H}' = \text{diag}\left[\mathbf{H}'_1, \ldots, \mathbf{H}'_M\right]$ for environments comprising multiple SOPs. From this structure, it is readily seen that

$$\mathbf{H}'^{\mathsf{T}}\mathbf{H}' = \begin{bmatrix} \mathbf{H}'^{\mathsf{T}}_1\mathbf{H}'_1 & \mathbf{0}_{3\times3} & \cdots & \mathbf{0}_{3\times3} \\ \mathbf{0}_{3\times3} & \mathbf{H}'^{\mathsf{T}}_2\mathbf{H}'_2 & \cdots & \mathbf{0}_{3\times3} \\ \vdots & \vdots & \ddots & \vdots \\ \mathbf{0}_{3\times3} & \mathbf{0}_{3\times3} & \cdots & \mathbf{H}'^{\mathsf{T}}_M\mathbf{H}'_M \end{bmatrix}.$$

By exploiting the block diagonal structure of $\mathbf{H}'^{\mathsf{T}}\mathbf{H}'$, the optimization problem in (2.7) can be rewritten as

$$\underset{\boldsymbol{r}_{r_{N+1}}}{\text{maximize}} \quad \prod_{m=1}^{M} \det\left[\mathbf{H}'^{\mathsf{T}}_m({}^m\phi_{r_{N+1}})\mathbf{H}'_m({}^m\phi_{r_{N+1}})\right]. \tag{2.14}$$

Note that the optimization problem in (2.7) for the single SOP case generalized to product of determinants in (2.14) for the multiple SOP case. As such, a natural extension of the area maximization problem in (2.8) to the multiple SOP case is to consider the product of each area ${}^{m}A$ of the polygon formed by the unit LOS vector endpoints pointing from the m^{th} SOP to each receiver. To compare this optimization criterion with (2.6), $N+1$ receivers were placed randomly around multiple SOPs, where the n^{th} receiver position was chosen according to $\boldsymbol{r}_{r_n} \sim \mathcal{U}([-1500,-1500]^{\mathsf{T}},[1500,1500]^{\mathsf{T}})$, for $n=1,\ldots,N$, for a total of 10^5 random configurations. For each configuration, the first N receivers were fixed. Next, the $(N+1)^{\text{st}}$ receiver was placed so to first optimize the GDOP then to optimize the product of areas. The corresponding GDOP and product of areas are plotted for $M=2$ in Fig. 2.5(a)–(c) for $N=2,\ldots,4$, respectively, and for $M=3$ in Fig. 2.5(d)–(f) for $N=2,\ldots,4$, respectively.

The following can be concluded from these plots. First, placing the $(N+1)^{\text{st}}$ receiver to optimize the product of areas approximately optimizes the GDOP and the loss in optimality is minimal, which is captured by the thickness of the "point cloud." The loss in optimality is defined as the increase incurred in the GDOP from the optimal GDOP value due to optimizing the product of areas $\prod_{m=1}^{M} {}^{m}A$. Second, when $N+1$ receivers are arranged so the endpoints of the LOS vectors approach the formation of regular polygons for each SOP, the theoretical minimum GDOP, given by $\text{GDOP}_{\min} = \sqrt{5M/(N+1)}$ (dotted red line in Fig. 2.5), and maximum product of areas, given by $[(N+1)\sin[2\pi/(N+1)]/2]^M$ are simultaneously approached. Third, the potential loss in optimality is greater at smaller values of $\prod_{m=1}^{M} {}^{m}A$, which is attributed only to cases when all pre-deployed receivers are approximately collinear with an SOP.

Motivated by these results, an alternative optimization problem to (2.6) and (2.7) is proposed for $M>1$, which aims to maximize the product of areas A_M over the position of the $(N+1)^{\text{st}}$

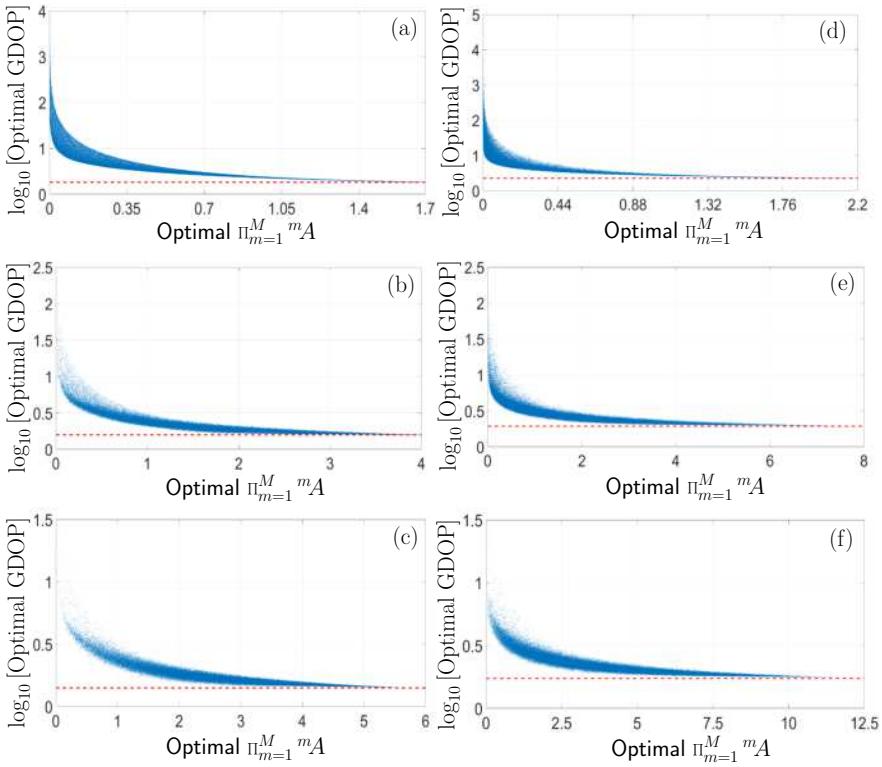

Figure 2.5: N receivers were randomly placed around M SOPs for a total of 10^5 configurations. Next, the $(N+1)^{\text{st}}$ receiver was optimally placed so to first optimize the GDOP then to optimize the product of areas. Each point in the point cloud plotted in Fig. (a)–(f) represent the optimal product of areas versus optimal GDOP for a particular configuration. Fig. (a)–(c) correspond to $N = 2, \ldots, 4$, respectively, for $M = 2$, and Fig. (d)–(f) correspond to $N = 2, \ldots, 4$, respectively, for $M = 3$. The minimum possible GDOP is plotted for each case (red dotted line).

receiver, namely

$$\underset{\boldsymbol{r}_{r_{N+1}}}{\text{maximize}} \quad A_M\left(\boldsymbol{r}_{r_{N+1}}\right) = \prod_{m=1}^{M} {}^{m}A\left({}^{m}\phi_{N+1}\right). \tag{2.15}$$

Although (2.15) is not a convex optimization problem, it can be re-cast as a family of convex optimization problems by noting the following. First, by exploiting the preserving property of the logarithm, an equivalent optimization function is given by $\sum_{m=1}^{M} \log\left[{}^{m}A\left({}^{m}\phi_{N+1}\right)\right]$. Second, recall from Fig. 2.2 that ${}^{m}A\left({}^{m}\phi_{N+1}\right)$ is concave over ${}^{m}\phi_{N+1}$ in ${}^{m}\phi_n \leq {}^{m}\phi_{N+1} \leq {}^{m}\phi_{n+1}, n = 1, \ldots, N-1$. Third, the composition of a non-decreasing concave function, the logarithm, and a concave function, ${}^{m}A\left({}^{m}\phi_{N+1}\right)$, is concave [103]. Fourth, the sum of concave

functions is concave. Therefore, (2.15) can be re-cast as K convex optimization problems, each of which is the maximization of a concave function over a polyhedron S_k, specifically,

$$\begin{aligned} &\underset{\boldsymbol{r}_{r_{N+1}}}{\text{maximize}} \quad \mathcal{J}_k\left(\boldsymbol{r}_{r_{N+1}}\right) = \sum_{m=1}^{M} \log\left[{}^{m}A\left({}^{m}\phi_{N+1}\right)\right] \\ &\text{subject to} \quad \mathrm{S}_k = \{\boldsymbol{r}_{r_{N+1}} \mid \mathbf{P}_k \boldsymbol{r}_{r_{N+1}} \preceq \boldsymbol{q}_k\}, \end{aligned} \tag{2.16}$$

for $\{\mathrm{S}_k\}_{k=1}^{K}$, where

$$\mathbf{P}_k = \begin{bmatrix} \boldsymbol{p}_{1,k}^{\mathsf{T}} \\ \vdots \\ \boldsymbol{p}_{L,k}^{\mathsf{T}} \end{bmatrix}, \ \boldsymbol{q}_k = \begin{bmatrix} q_{1,k} \\ \vdots \\ q_{L,k} \end{bmatrix}.$$

It can be shown that K is upper-bounded by a classical equation related to the number of regions formed by intersecting lines, namely $K \leq \left([NM]^2 + [NM] + 2\right)/2$ [104]. The polyhedron S_k is formed by the intersection of L halfspaces, where $3 \leq L \leq NM$, and its geometry is determined by the positions of the receivers and SOPs [105]. The direction of the l^{th} halfspace forming S_k is given by $-\boldsymbol{p}_{l,k}$, whereas $q_{l,k}$ accounts for the halfspace's offset from the origin of $\{f_1\}$. The inequality $\preceq$ denotes vector (componentwise) inequality. Fig. 2.6(a) is an illustration of these relationships for the same environment in Fig. 2.4(a). The resulting $\sum_{m=1}^{M} \log\left[{}^{m}A\left({}^{m}\phi_{N+1}\right)\right]$ for this environment is plotted in Fig. 2.6(b). The family of K convex programs in (2.16) yields K receiver positions that are optimal over each S_k. Therefore, the global optimal solution $\mathcal{J}^\star$ is given by

$$\mathcal{J}^\star\left(\boldsymbol{r}^\star_{r_{N+1}}\right) = \arg\max_{k} \left[\mathcal{J}_k^\star(\boldsymbol{r}_{r^\star_{N+1},k})\right], \tag{2.17}$$

where the optimizer $\boldsymbol{r}^\star_{r_{N+1}}$ is the global optimal receiver position, and $\mathcal{J}_k^\star$ and $\boldsymbol{r}_{r^\star_{N+1},k}$ are the optimal value and the corresponding optimizer in the k^{th} set. The above analysis provides a simple recipe for the optimal placement of an additional receiver into an environment

comprising multiple, arbitrarily deployed SOPs, which is summarize in Algorithm 2.

Algorithm 2 Optimal Receiver Placement for Multiple SOPs

Given: Positions of N pre-deployed receivers and estimates of M SOPs' positions
for $m = 1, \ldots, M$

- **Place** the origin of a cartesian coordinate frame at the position of the m^{th} SOP.
- **Calculate** the angles $\{{}^m\theta_n\}_{n=1}^N$ sandwiched between vectors pointing from the m^{th} SOP to each receiver.
- **Parameterize** the area ${}^mA$ for the m^{th} SOP by the candidate receiver position $\boldsymbol{r}_{N+1}$ using (A.4) in Appendix A.

end for
Divide the environment into K polyhedra using (A.5) and (A.6) in Appendix B.
for $k = 1, \ldots, K$

- **Initialize** receiver placement guess anywhere in set k.
- **Solve** the convex optimization problem (2.16) numerically.
- **Save** the optimal value $\mathcal{J}_k^\star$ and its optimizer $\boldsymbol{r}_{r_{N+1}^\star,k}$.

end for
Place the additional receiver at $\boldsymbol{r}_{r_{N+1}}^\star$ according to (2.17).

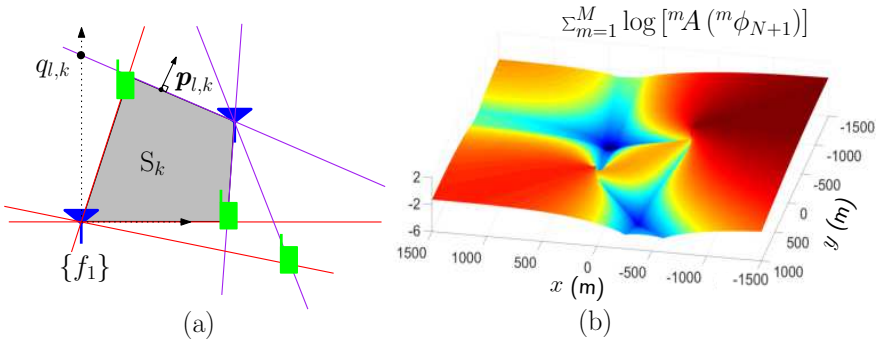

(a) (b)

Figure 2.6: (a) Environment comprising 3 pre-deployed receivers (green) estimating the states of 2 unknown SOPs (blue). The polyhedron set S_k (gray) is formed by the intersection of $L = 4$ halfspaces. The direction of the l^{th} halfspace forming S_k is given by $-\mathbf{p}_{l,k}$. Each halfspace boundary is the line (purple and red) through each SOP to each receiver. For SOPs other than the reference frame SOP $\{f_1\}$, the resulting halfspace may not pass through the origin, which is captured by $q_{l,k}$. (b) The resulting $\sum_{m=1}^{M} \log\left[{}^mA\,({}^m\phi_{N+1})\right]$ for placing an additional receiver at positions on a grid sampled at one meter intervals in $[-1500, -1000]^\mathsf{T} \leq \boldsymbol{r}_{r_{N+1}} \leq [1500, 1500]^\mathsf{T}$ into an environment comprised of 3 pre-deployed receivers and 2 SOPs.

Convergence Analysis

To solve the GDOP optimization problem, a nonlinear numerical optimization solver must be relied on. Due to the shape of the GDOP function in (2.6), the solver will often undesirably converge to a local optimal solution. To demonstrate this behavior, the environment in Fig. 2.4(a) was simulated and MATLAB's numerical nonlinear optimization function `fmincon` was used.

The solver's initial guess was drawn according to $\boldsymbol{r}_{r_{N+1}} \sim \mathcal{U}([-1500, -1000]^{\mathsf{T}}, [1500, 1500]^{\mathsf{T}})$ and the optimization problem was solved $10,000$ times. In addition, the environment was gridded with a resolution $\Delta x = \Delta y = 1$ and the optimazation problem was solved through exhaustive search to find the global minimum. The solution obtained through the numerical solver failed to converge to the global minimum 44.1% of the time.

The proposed optimization criterion (2.16)-(2.17), while not directly optimizing GDOP, posses the following advantages. First, it decomposes the optimization problem into a family of independent convex programs, which may be executed in parallel. Second, the optimal solution of the optimization criterion (2.16)-(2.17) is the global optimum to which the solver would converge in a faster fashion. Third, the obtained solution from (2.16)-(2.17) is very "close" to the global solution of (2.6).

The global optimizer for the GDOP problem (2.6) turned out to be $\boldsymbol{r}^{\star}_{N+1} = [-1500, -630]^{\mathsf{T}}$, while the optimizer for (2.16)-(2.17) turned out to be $\boldsymbol{r}^{\star}_{N+1} = [-1500, -657]^{\mathsf{T}}$. The GDOP associated with the optimizer of (2.6) was 2.5517, while the GDOP evaluated at the optimizer of (2.16)-(2.17) was 2.5518. It is worth noting that one could use the optimal solution from (2.16)-(2.17) as a good initial guess that is close to the optimal solution of the GDOP problem (2.6).

2.3 Optimal Mapping Performance Characterization

This section characterizes the optimal mapping performance of an SOP as a function of the number of mobile receivers in the environment and time. The objective of this characterization is to prescribe the optimal achievable mapping performance of an SOP within a specified time and for a certain number of receivers.

2.3.1 Problem Formulation

The following problem is considered. A set of N mobile receivers with knowledge about their own states are making pseudorange observations on an unknown terrestrial SOP. Assuming that these observations are fused through a dynamic centralized estimator, specifically an extended Kalman filter (EKF), to estimate the state vector of the SOP $\boldsymbol{x}_s$ with dynamics (2.1), what is the optimal mapping performance as a function of N and time?

In contrast to Section 2.2, which analyzed the optimal placement of the $(N+1)^{\text{st}}$ receiver, given a set of N randomly-distributed receivers, the optimal mapping performance for the problem considered here is a function of the simultaneous placement of all the receivers. Specifically, the optimization is over all the receiver angles $\{{}^1\phi_n\}_{n=1}^N$. This optimization enables an off-line characterization of the optimal achievable mapping performance, which is summarized in Theorem 2.3.1.

Theorem 2.3.1. *The optimal mapping performance for N mobile receivers with knowledge of their own states collaboratively estimating the state vector of one terrestrial SOP with dynamics (2.2) using pseudorange observations (2.3) with independent noise with identical measurement noise variance σ^2 is: (i) independent of the SOP's state vector estimate and (ii) solvable off-line. The optimal mapping performance is given by the solution to the discrete-*

time Riccati equation

$$\begin{aligned}\mathbf{P}(k+1|k) = \mathbf{F}_s\big\{&\mathbf{P}(k|k-1) - \mathbf{P}(k|k-1)\mathbf{H}^{\star\mathsf{T}} \\ &\cdot \Big[\mathbf{H}^{\star}\mathbf{P}(k|k-1)\mathbf{H}^{\star\mathsf{T}} + \mathbf{R}\Big]^{-1} \\ &\cdot \mathbf{H}^{\star}\mathbf{P}(k|k-1)\big\}\mathbf{F}_s^{\mathsf{T}} + \mathbf{Q}_s,\end{aligned} \tag{2.18}$$

with initial value $\mathbf{P}(0|-1)$*, where* $\mathbf{P}$ *is the prediction error covariance,*

$$\mathbf{H}^{\star} = \begin{bmatrix} -\cos\frac{2\pi 0}{N} & -\sin\frac{2\pi 0}{N} & -1 & 0 \\ -\cos\frac{2\pi}{N} & -\sin\frac{2\pi}{N} & -1 & 0 \\ \vdots & \vdots & \vdots & \vdots \\ -\cos\frac{2\pi(N-1)}{N} & -\sin\frac{2\pi(N-1)}{N} & -1 & 0 \end{bmatrix}, \tag{2.19}$$

the matrix $\mathbf{R}$ *is the measurement noise covariance, and* $\mathbf{F}_s$ *and* $\mathbf{Q}_s$ *are the SOP's state dynamics and process noise covariance, respectively, which are defined in Subsection 2.1.1.*

Proof. Assuming the receivers' observation noise to be i.i.d., i.e., $\{\sigma_n^2\}_{n=1}^N \equiv \sigma^2$ and $\mathbf{R} = \sigma^2\mathbf{I}_{N\times N}$, the optimal achieved performance is essentially determined by the geometric placement of the receivers. The lowest GDOP is achieved when the unit LOS vectors pointing from the SOP to the receivers reside at the vertices of a regular polygon [57]. Therefore, an environment consisting of N optimally-placed receivers, each drawing pseudorange observations on the same SOP modifies the observation Jacobian matrix for (2.3) to take the form of (2.19).

Next, consider the estimation error covariance update equation of the EKF in the information form

$$\mathbf{P}^{-1}(k+1|k+1) = \mathbf{P}^{-1}(k+1|k) + \frac{1}{\sigma^2}\mathbf{H}^{\mathsf{T}}(k+1)\mathbf{H}(k+1),$$

where $\mathbf{P}(k+1|k+1)$ is the estimation error covariance and $\mathbf{P}(k+1|k)$ is the prediction error covariance. The information associated with the latest observation (at time step $k+1$) is $\boldsymbol{\Upsilon}(k+1) \triangleq \frac{1}{\sigma^2}\mathbf{H}^{\mathsf{T}}(k+1)\mathbf{H}(k+1)$. If the receivers are placed optimally, plugging (2.19) into $\boldsymbol{\Upsilon}(k+1)$ yields

$$\boldsymbol{\Upsilon}(k+1) = \frac{1}{\sigma^2}\sum_{n=0}^{N-1}\begin{bmatrix} \cos^2\frac{2\pi n}{N} & \cos\frac{2\pi n}{N}\sin\frac{2\pi n}{N} & \cos\frac{2\pi n}{N} & 0 \\ \sin\frac{2\pi n}{N}\cos\frac{2\pi n}{N} & \sin^2\frac{2\pi n}{N} & \sin\frac{2\pi n}{N} & 0 \\ \cos\frac{2\pi n}{N} & \sin\frac{2\pi n}{N} & 1 & 0 \\ 0 & 0 & 0 & 0 \end{bmatrix}. \tag{2.20}$$

By using the Fourier equations

$$\sum_{n=0}^{N-1}\cos^2\frac{2\pi n}{N} = \frac{N}{2}, \quad \sum_{n=0}^{N-1}\sin^2\frac{2\pi n}{N} = \frac{N}{2},$$

$$\sum_{n=0}^{N-1}\cos\frac{2\pi n}{N}\sin\frac{2\pi n}{N} = 0,$$

and the summation equations

$$\sum_{n=0}^{N-1}\cos\frac{2\pi n}{N} = 0, \quad \sum_{n=0}^{N-1}\sin\frac{2\pi n}{N} = 0,$$

the information (2.20) becomes

$$\boldsymbol{\Upsilon}(k+1) = \frac{1}{\sigma^2}\mathrm{diag}\left[\frac{N}{2}, \frac{N}{2}, N, 0\right],$$

which is independent of the SOP's state vector estimate. Noting that the SOP's dynamics are linear, the prediction error covariance, given by

$$\mathbf{P}(k+1|k) = \mathbf{F}_s\mathbf{P}(k|k)\mathbf{F}_s^{\mathsf{T}} + \mathbf{Q}_s,$$

is also independent of the SOP's state vector estimate. Therefore, if the receivers maintain their optimal distribution around the latest SOP's position estimate $\hat{\boldsymbol{r}}_s$ at the time instants when new observations are taken, the estimation error covariance can be computed without knowledge of the SOP's state vector estimates. This allows for solving the Riccati equation (2.18) governing the evolution of the estimation error covariance off-line, and the resulting estimation error covariance time history is the optimal mapping performance as a function of time and number of receivers N. □

2.3.2 Simulation Results

This subsection presents simulation results demonstrating the optimal mapping performance as a function of time and N. Moreover, the estimation error due to random receiver trajectories is compared with the optimal mapping performance. The simulation settings are summarized in Table 2.1.

Table 2.1: Simulation Settings for Optimal Mapping Performance of an Unknown SOP

Parameter	**Value**
$\boldsymbol{x}_s(0)$	$[0,\ 0,\ 1,\ 0.1]^{\mathsf{T}}$
$\mathbf{P}_s(0\|-1)$	$(10^3)\cdot \mathrm{diag}\,[1, 1, 3, 0.3]$
$\hat{\boldsymbol{x}}_s(0\|-1)$	$\sim \mathcal{N}\,[\boldsymbol{x}_s(0), \mathbf{P}_s(0\|-1)]$
$\{h_{0,\mathrm{s}},\ h_{-2,\mathrm{s}}\}$	$\{8.0\times 10^{-20},\ 4.0\times 10^{-23}\}$
σ^2	$100\,\mathrm{m}^2$
T	$0.1\,\mathrm{s}$

Fig. 2.7 illustrates the logarithm of the determinant of the posterior estimation error covariance, $\log\{\det[\mathbf{P}^{\star}(k+1|k+1)]\}$, which is related to the volume of the estimation uncertainty ellipsoid [53], as a function of time and N. This plot provides the minimum achievable uncertainty of the states of an unknown SOP as a function of time and N. This plot can be utilized to determine the minimum number of receivers that must be deployed in an environment to

achieve a desired estimation uncertainty within a specified period of time.

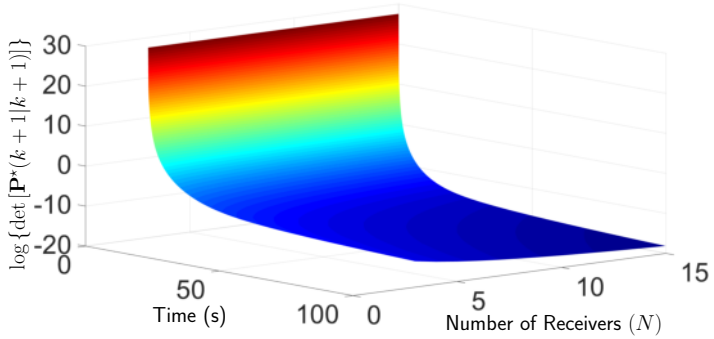

Figure 2.7: The logarithm of the determinant of the optimal posterior estimation error covariance $\log\{\det[\mathbf{P}^\star(k+1|k+1)]\}$ expressed as a function of time and $N \in \{3, 4, \ldots 15\}$ receivers.

To compare the optimal mapping performance versus random receiver trajectories that do not maintain the optimal receiver placement around the SOP's position estimate, four receivers were randomly placed around the SOP. The initial state vector of the n^{th} receiver was set to $\boldsymbol{x}_{r_n}(0) = \left[\boldsymbol{r}_{r_n}^{\mathsf{T}}(0), \dot{\boldsymbol{r}}_{r_n}^{\mathsf{T}}(0), c\delta t_{r_n}(0), c\dot{\delta} t_{r_n}(0)\right]^{\mathsf{T}}$, where $\dot{\boldsymbol{r}}_{r_n}(0) = [0, 0]^{\mathsf{T}}$, $c\delta t_{r_n}(0) = 10$, and $c\dot{\delta} t_{r_n}(0) = 1$. The receivers' initial positions $\boldsymbol{r}_{r_n}(0)$ are specified in Table 2.2. The receivers' initial positions were varied across three simulation runs, by varying an offset $\{\boldsymbol{b}_j\}_{j=1}^{3}$ to create varying GDOP quality. Subsequently, the receivers moved according to a velocity random walk motion with an acceleration process noise power spectral density $\tilde{q}_x = \tilde{q}_y = 0.1\,(\text{m/s}^2)^2$ [17]. The receivers' trajectories across the three simulation runs (corresponding to $j = 1, 2, 3$) were the same in order to analyze the effect of the initial GDOP. The time history of the resulting $\log\{\det[\mathbf{P}^j(k+1|k+1)]\}$ corresponding to $j = 1, 2, 3$ versus the optimal $\log\{\det[\mathbf{P}^\star(k+1|k+1)]\}$ are plotted in Fig. 2.8(a) for the trajectories traversed plotted in Fig. 2.8(b)–(d).

It can be seen from Fig. 2.8 that although the shape of the trajectories were the same between each run, the initial GDOP quality greatly influenced the resulting estimation uncertainty. Also note that although the trajectories in (b) corresponded to the lowest initial GDOP out of all the runs, the resulting estimation uncertainty for these trajectories never violated the

optimal $\log\{\det[\mathbf{P}^{\star}(k+1|k+1)]\}$.

Table 2.2: Simulation Settings for the Receivers' Initial Position

Parameter	**Value**
$\boldsymbol{r}_{r_1}^j(0)$	$[-150.8,\ 169.3]^{\mathsf{T}} + \boldsymbol{b}_j$
$\boldsymbol{r}_{r_2}^j(0)$	$[24.6,\ -13.7]^{\mathsf{T}} + \boldsymbol{b}_j$
$\boldsymbol{r}_{r_3}^j(0)$	$[-25.6,\ -45.5]^{\mathsf{T}} + \boldsymbol{b}_j$
$\boldsymbol{r}_{r_4}^j(0)$	$[105.7,\ -29.6]^{\mathsf{T}} + \boldsymbol{b}_j$
$\boldsymbol{b}_1, \boldsymbol{b}_2, \boldsymbol{b}_3$	$[0,\ 0]^{\mathsf{T}}, [125,\ 0]^{\mathsf{T}}, [200,\ 0]^{\mathsf{T}}$

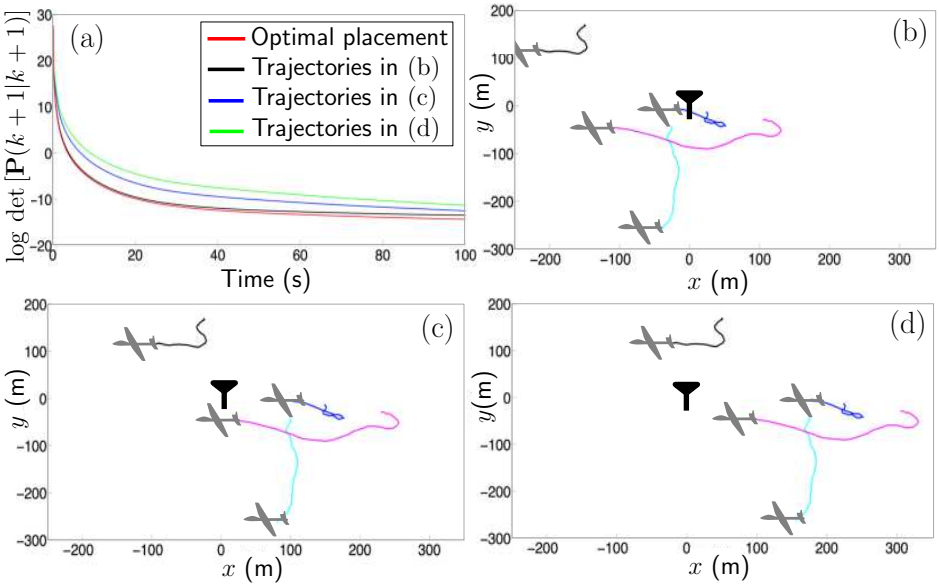

Figure 2.8: The logarithm of the determinant of the optimal posterior estimation error covariance $\log\{\det[\mathbf{P}^{\star}(k+1|k+1)]\}$ versus the posterior estimation error covariance due to three simulation runs corresponding to the receiver trajectories in (b)–(d). The receivers' trajectories in (b)–(d) are the same. The receivers' initial positions in (b)–(d) were varied according to an offset $\boldsymbol{b}_j$ to yield different initial GDOP quality: (b) low GDOP with $\boldsymbol{b}_1$, (c) medium GDOP with $\boldsymbol{b}_2$, and (d) high GDOP with $\boldsymbol{b}_3$.

2.4 Experimental Results

This section demonstrates collaborative mapping of a terrestrial SOP emanating from a cellular CDMA base transceiver station (BTS). This section consists of two subsections. In

the first subsection, the dynamics and observation models presented in Section 2.1 are validated to be suitable models in a real-world setting. Such model validation is crucial, since these models were used in deriving the optimal collaborative mapping performance of the EKF in Theorem 2.3.1. In the second subsection, collaborative mapping results demonstrate the bound derived in Theorem 2.3.1. To this end, three vehicles were equipped with two antennas each, to acquire and track multiple GPS signals and a cellular BTS whose signal was modulated through CDMA. The GPS and cellular signals were simultaneously downmixed and synchronously sampled via two National Instruments® universal software radio peripherals (USRPs). These front-ends fed their data to the Generalized Radionavigation Interfusion Device (GRID) software-defined radio (SDR) [106] and the Multichannel Adaptive TRansceiver Information eXtractor (MATRIX) SDR [107], which produced pseudorange observables from all GPS L1 C/A signals in view and the cellular BTS, respectively, at $1/T = 5$Hz. Fig. 2.10 depicts the experimental hardware setup.

The MATRIX SDR produced pseudorange observables to the BTS, modeled according to (2.3), by exploiting the cellular CDMA signal structure as described in detail in [107]. The produced pseudoranges are unambiguous in the sense that they were associated with a particular BTS by decoding the BTS's identification number from the cellular CDMA paging channel. For this field experiment, the SOP's signal structure was known to be cellular CDMA. If the signal structure is unknown, several SDR modules (e.g., CDMA, LTE, FM, etc.) may be run in parallel until a LOS signal is acquired and tracked and data association for the produced pseudorange and the SOP transmitter is performed. If the receiver is in an environment subject to multipath, one of several multipath mitigation methods can first be employed to improve the LOS time-of-arrival (TOA) estimate, e.g., estimation of signal parameters via rotational invariance (ESPRIT) [108] and space-alternating generalized expectation maximization (SAGE) [109].

2.4.1 Model Verification

The symbol ρ_n will be used to denote the n^{th} receiver's produced pseudorange measurement (i.e., data by the MATRIX SDR) to contrast the pseudorange model z_n in (2.3). Consider the n^{th} receiver's clock bias-compensated pseudorange observation model

$$z'_n(k) \triangleq z_n(k) - c\delta t_r(k) = d_n(k) - c\delta t_s(k) + v_n(k), \tag{2.21}$$

where $d_n(k) \triangleq \|\boldsymbol{r}_{r_n}(k) - \boldsymbol{r}_s\|$. According to (2.21), the MATRIX SDR's clock bias-compensated pseudorange $\rho'_n(k) \triangleq \rho_n(k) - c\delta t_{r_n}(k)$ should consist of d_n, $c\delta t_s$, and v_n. To analyze this, a vehicle traversed a trajectory for 28 seconds while producing ρ_1 to a single BTS. The receiver's states $c\delta t_{r_1}$ and $\boldsymbol{r}_{r_1}$ were estimated by a least-squares solver using the available GPS pseudoranges and the position $\boldsymbol{r}_s$ was surveyed from the BTS's true location. The true data ρ'_1 and the distance d_1 are plotted in Fig. 2.9(a). The initial value $\rho'_1(0)$ was aligned with $d_1(0)$ to compensate for $c\delta t_s(0)$.

From Fig. 2.9(a) it can be noted that the profiles of the curves closely match, indicating that the trend of ρ_1 is mainly due to d_1. The receiver's clock bias-compensated observation model (2.21) suggests that the deviation of ρ'_1 from d_1 is attributed to v_n and the dynamics of $c\delta t_s$. To verify this deviation, the measurement noise v_n and the process noise terms $w_{\delta t_s}$ and $w_{\dot{\delta} t_s}$ driving $c\delta t_s$ and $c\dot{\delta} t_s$ are studied next by applying the following steps commonly used in time-series analysis [110]. First, the data is de-trended by subtracting d_n and applying a transformation to obtain stationary residuals, specifically, a linear combination of $w_{\delta t_s}$, $w_{\dot{\delta} t_s}$, and v_n. Second, the sample autocorrelation function (ACF) is computed for the resulting sequence. Third, an appropriate model is identified by using key attributes from the sample ACF and is compared with the model presented in this chapter.

The transformation applied is a double-difference in time defined by $\lambda_n(k+1) \triangleq \gamma_n(k+1) - \gamma_n(k)$, where $\gamma_n(k+1) \triangleq \bar{z}(k+1) - \bar{z}(k)$ and $\bar{z}(k) \triangleq d_n(k) - z'_n(k)$. It is shown in appendix

C that $\lambda_n(k)$ has the form

$$\lambda_n(k) = \lambda_{n,1}(k) + \lambda_{n,2}(k) + \lambda_{n,3}(k), \tag{2.22}$$

where $\lambda_{n,1}(k) \triangleq w_{\delta t_s}(k) - w_{\delta t_s}(k-1)$, $\lambda_{n,2}(k) \triangleq -[v_n(k) - 2v_n(k-1) + v_n(k-2)]$, and $\lambda_{n,3}(k) \triangleq Tw_{\dot{\delta} t_s}(k)$. The sequences $\lambda_{n,1}$ and $\lambda_{n,2}$ are first-order and second-order moving averages (MAs), respectively, which have the form

$$\xi_i(k) = \sum_{j=0}^{q_i} \beta_j e(k-j), \quad \beta_0 = 1,$$

where β_j is a constant, e is a DT zero-mean white noise sequence, and q_i is the MA order [111]. The sequence $\lambda_{n,3}$ is a DT zero-mean white noise sequence, which can be generalized as an MA with order $q_3 = 0$. It follows that λ_n itself is an MA, since the sum of MAs is also an MA with order $q \leq \max\{q_1, q_2, q_3\} = 2$, where q_i is the order of $\lambda_{n,i}$ [112].

The sample ACF of a q^{th} order MA will have significant values up to lag q, and will become effectively zero thereafter. Effectively zero implies that the sample ACF values should be approximately zero-mean and obey the 95^{th} percentile confidence bounds ($\pm\sigma_{95\%} \approx \pm 1.96/\sqrt{L}$), where L is the total number of samples [111]. To check if the collected data agrees with this hypothesis, z'_n was replaced with ρ'_1 to produce λ_1, which is plotted in Fig. 2.9(b). The sample ACF of λ_1 and the corresponding $\pm\sigma_{95\%}$ bounds are plotted in Fig. 2.9(c)-(d) for $L = 400$ samples.

The following conclusions about the underlying sequences can be noted from Fig. 2.9(c)-(d). First, since the last significant ACF value is at the second lag, a second order MA model is appropriate, as hypothesized. Second, since an MA model is appropriate, the driving process noise $w_{\delta t_s}$ and $w_{\dot{\delta} t_s}$ and the measurement noise v_n are appropriately modeled as white sequences. Third, since a double-difference in time was required to de-trend the data, a double-integrator SOP clock model is appropriate. Fourth, since λ_n is a stationary MA

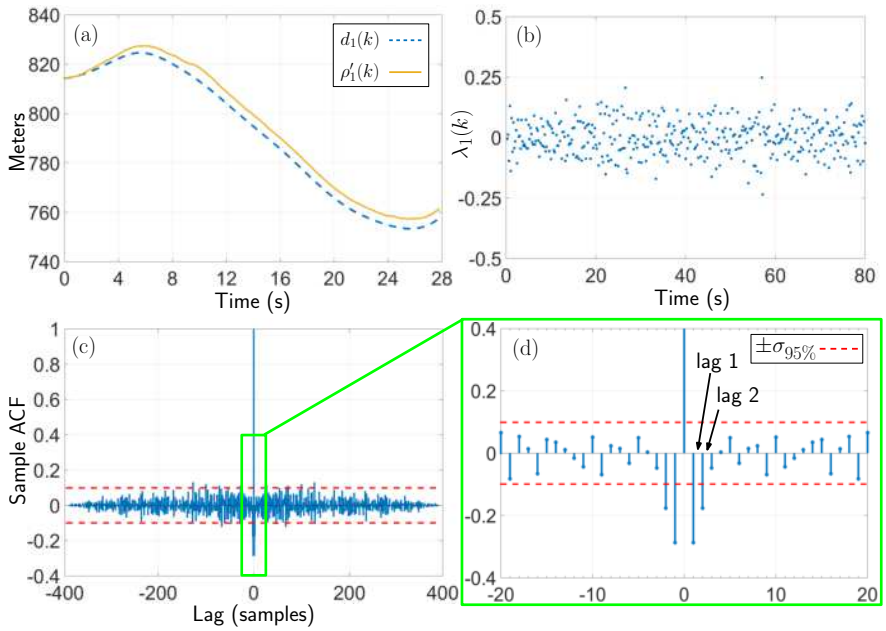

Figure 2.9: Measurement analysis. (a) Comparison of the true data produced by the MATRIX SDR, ρ_1', and the distance from the receiver to the BTS, d_1. (b) The sequence (2.22) computed by replacing z_n' with the true data ρ_1'. (c) Resulting sample ACF of the sequence in (b) with the corresponding $\pm\sigma_{95\%}$ confidence bounds. (d) Zoom of (c) illustrating that only values up to the first two lags of the sample ACF are significant.

and by invoking a second-order ergodicity assumption, the measurement noise variance σ_n^2 can be computed from the data, as is shown in Appendix D, to be

$$\sigma_n^2 = \frac{1}{6}\text{var}_L\left(\lambda_n\right) - \frac{1}{3}c^2(S_{\tilde{w}_{\delta t_s}}T + S_{\tilde{w}_{\delta \dot{t}_s}}\frac{T^3}{3}), \tag{2.23}$$

where $\text{var}_L\left(\lambda_n\right)$ is the sample variance of λ_n using L samples.

2.4.2 Mapping Results

Three separate runs were conducted. In the first run, the vehicle-mounted receivers began their trajectories in positions that resulted in a low GDOP. The receivers began estimating the states of the cellular BTS $\boldsymbol{x}_s$ by fusing their pseudorange observables through a centralized EKF. The network implementation to fuse these pseudoranges could be inte-

grated into developing communication standards, such as the IEEE802.11p Dedicated Short Range Communication (DSRC), which is designed to support future vehicle-to-vehicle and vehicle-to-infrastructure communication [113].

The EKF was initialized with an initial estimate given by $\hat{\boldsymbol{x}}_s(0|-1) \sim \mathcal{N}\left[\boldsymbol{x}_s(0), \mathbf{P}_s(0|-1)\right]$, where $\boldsymbol{x}_s(0) = \left[\boldsymbol{r}_s^{\mathsf{T}}(0), c\delta t_s(0), c\dot{\delta t}_s(0)\right]^{\mathsf{T}}$, where $\boldsymbol{r}_s(0)$ is the projection of the BTS's true position in the Earth-Centered Earth-Fixed (ECEF) coordinate frame to a planar system, $c\delta t_s(0) \equiv d_1(0) + c\delta t_{r_1}(0) - \rho_1(0)$, $c\dot{\delta t}_s(0) \equiv [c\delta t_s(1) - c\delta t_s(0)]/T$, and $\mathbf{P}_s(0|-1) \equiv (10^4) \cdot \mathrm{diag}\left[1, 1, 3, 0.3\right]$. This initialization scheme is customary in EKFs in which the prior, uncertain information is utilized. Other initialization schemes are also possible. For example, a batch nonlinear least-squares-type approach could be employed in which a batch of initial measurements are used to produce an initial guess $\hat{\boldsymbol{x}}_s(0|-1)$ and associated $\mathbf{P}_s(0|-1)$. Alternatively, a particle filter operating on a batch of measurements could be employed to produce $\hat{\boldsymbol{x}}_s(0|-1)$ and $\mathbf{P}_s(0|-1)$. The particles could be initialized by drawing positions from a polar coordinate system fixed at each receiver with an angle drawn uniformly between 0 and 2π and a radius drawn uniformly between 0 and the maximum operating range of the cellular BTS. The initial clock bias for each particle may be computing using the initial measurements and the drawn position, while the clock drift for each particle could be initialized to zero. It is worth noting that since three non-collinear receivers were collaboratively mapping the two-dimensional position of a BTS, there will be no local observability issues with the EKF and the estimates will be unambiguous.

The process noise covariance for the BTS's oscillator $\mathbf{Q}_{\mathrm{clk},s}$ was assumed to correspond to a typical oven-controlled crystal oscillator (OCXO), which is usually the case for cellular CDMA BTSs [15]. Any mismatch between the true $\mathbf{Q}_{\mathrm{clk},s}$ and the assumed one will be small and will be included in the measurement noise variances $\{\sigma_n^2\}_{n=1}^3$. Alternatively, $\mathbf{Q}_{\mathrm{clk},s}$ could be estimated off-line through a batch estimator or on-line adaptively [114]. The measurement noise variances $\{\sigma_n^2\}_{n=1}^3$ were calculated using equation (2.23) as described in Subsection

2.4.1. These values were found to be very similar, i.e., $\{\sigma_n^2\}_{n=1}^3 \approx \sigma^2$. Moreover, the receivers were placed sufficiently far from each other to assume independent channels between the BTS and each receiver. Therefore, the measurement noise covariance was set to $\mathbf{R} \equiv \sigma^2 \mathbf{I}_{3\times 3}$.

The final two-dimensional estimation error of the BTS's position was within 3 meters from the true BTS position after 70 seconds. Fig. 2.11 is an illustration of the receivers' trajectories, the true and estimated BTS position, and the initial and final 95^{th}-percentile estimation uncertainty ellipses of $\hat{\boldsymbol{r}}_s$ for the low GDOP run. Note from Fig. 2.11 the significant reduction in the size of estimation uncertainty ellipse from the initial to the final uncertainty with only three receivers. The black curve in Fig. 2.12 illustrates the corresponding time history of $\log\{\det[\mathbf{P}(k+1|k+1)]\}$ plotted against the theoretical lower bound that was found in Section 2.3. In the second and third runs, the receivers were initialized in positions that resulted in a medium and high GDOP, respectively. A summary of the mapping errors for each run are tabulated in Table 2.3. The 3 meter localization is dependent on many factors (e.g., type of transmitter being mapped, noise statistics, number of receivers and corresponding trajectories, elapsed time, etc.). The resulting time history of $\log\{\det[\mathbf{P}(k+1|k+1)]\}$ are plotted as the blue and green curves in Fig. 2.12. Comparable results were noted upon running the EKF with different initial estimates. These experimental results demonstrate the expected behavior of: (i) a worse quality mapping performance for receiver positions yielding higher GDOP and (ii) none of the traversed trajectories resulted in an estimation uncertainty which violated the theoretical optimal mapping performance (lower-bound).

Table 2.3: Final BTS Position Errors

Initial GDOP	Low (3.8)	Medium (8.5)	High (12.4)
Mapping Error (m)	3.0	4.7	6.9

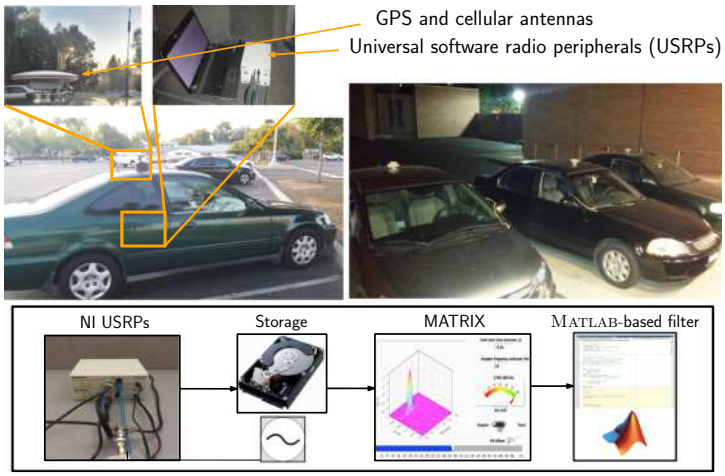

Figure 2.10: Experiment hardware setup.

Figure 2.11: Experimental results for low GDOP run. Image: Google Earth.

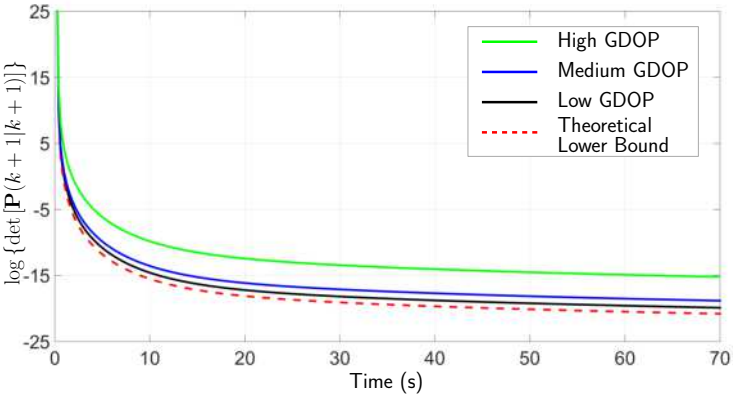

Figure 2.12: The resulting $\log\{\det[\mathbf{P}(k+1|k+1)]\}$ produced by the EKF for each of the three experimental runs plotted against the theoretical lower bound (red dotted curve), which was found using Theorem 2.3.1. The black curve corresponds to low GDOP calculated from the receiver positions illustrated in Fig. 2.11. The blue and green curves correspond to medium and high GDOP, respectively, which were calculated from the second and third experimental runs, respectively.

Chapter 3

Radio SLAM: Stochastic Observability

Next, this chapter will extend the SOP mapping problem by introducing a layer of complexity. In this chapter, the state of the receiver is also unknown and the problem of simultaneously mapping unknown SOP transmitters while navigating using pseudoranges drawn from their signals is considered. This chapter is organized as follows. Section 3.1 introduces new notation for the system dynamics and measurement models. Section 3.2 studies the stochastic observability of the simultaneous receiver and transmitter localization problem. Section 3.3 presents simulation results to validate the findings of Section 3.2. Section 3.4 provides experimental results.

3.1 Model Description

The notation defined is confined within this chapter.

3.1.1 RF Transmitter Dynamics Model

Each RF signal will be assumed to emanate from a spatially-stationary terrestrial transmitter, and its state vector will consist of its planar position states $\boldsymbol{r}_{s_m} \triangleq [x_{s_m},\, y_{s_m}]^{\mathsf{T}}$ and clock error states $\boldsymbol{x}_{\text{clk},s_m} \triangleq c\left[\delta t_{s_m},\, \dot{\delta t}_{s_m}\right]^{\mathsf{T}}$, where c is the speed of light, δt_{s_m} and $\dot{\delta t}_{s_m}$ are the clock bias and drift of the m^{th} RF transmitter, respectively, and $m = 1, \ldots, M$, where M is the total number of RF transmitters.

The discretized RF transmitters' dynamics are given by

$$\boldsymbol{x}_{s_m}(k+1) = \mathbf{F}_s\, \boldsymbol{x}_{s_m}(k) + \boldsymbol{w}_{s_m}(k), \quad k = 1, 2, \ldots,$$

where

$$\boldsymbol{x}_{s_m} = \left[\boldsymbol{r}_{s_m}^{\mathsf{T}},\, \boldsymbol{x}_{\text{clk},s_m}^{\mathsf{T}}\right]^{\mathsf{T}},$$

$$\mathbf{F}_s = \text{diag}\left[\mathbf{I}_{2\times 2},\, \mathbf{F}_{\text{clk}}\right], \quad \mathbf{F}_{\text{clk}} = \begin{bmatrix} 1 & T \\ 0 & 1 \end{bmatrix},$$

T is the constant sampling interval and $\boldsymbol{w}_{s_m}$ is the process noise, which is modeled as a DT white noise sequence with covariance $\mathbf{Q}_{s_m} = \text{diag}\left[\mathbf{0}_{2\times 2},\, c^2\mathbf{Q}_{\text{clk},s_m}\right]$, where

$$\mathbf{Q}_{\text{clk},s_m} = \begin{bmatrix} S_{\tilde{w}_{\delta t_{s,m}}} T + S_{w_{\dot{\delta} t_{s,m}}} \frac{T^3}{3} & S_{\tilde{w}_{\dot{\delta} t_{s,m}}} \frac{T^2}{2} \\ S_{\tilde{w}_{\dot{\delta} t_{s,m}}} \frac{T^2}{2} & S_{\tilde{w}_{\dot{\delta} t_{s,m}}} T \end{bmatrix}.$$

The terms $S_{\tilde{w}_{\delta t_{s,m}}}$ and $S_{\tilde{w}_{\dot{\delta} t_{s,m}}}$ are the clock bias and drift process noise power spectra, respectively, which can be related to the power-law coefficients, $\{h_{\alpha,s_m}\}_{\alpha=-2}^{2}$, which have been shown through laboratory experiments to characterize the power spectral density of the fractional frequency deviation of an oscillator from nominal frequency according to $S_{\tilde{w}_{\delta t_{s,m}}} \approx \frac{h_{0,s_m}}{2}$ and $S_{\tilde{w}_{\dot{\delta} t_{s,m}}} \approx 2\pi^2 h_{-2,s_m}$ [100].

3.1.2 Receiver Dynamics Model

The receiver's planar position $\boldsymbol{r}_r \triangleq [x_r,\, y_r]^{\mathsf{T}}$ and velocity $\dot{\boldsymbol{r}}_r$ will be assumed to evolve according to an arbitrary, but known, continuous-time dynamics model $\tilde{\boldsymbol{f}}_{\text{pv}}$ (e.g., velocity random walk or constant turn rate [115]). The receiver's state vector $\boldsymbol{x}_r$ is defined by augmenting the receiver's position and velocity states $\boldsymbol{x}_{\text{pv}} \triangleq \left[\boldsymbol{r}_r^{\mathsf{T}},\, \dot{\boldsymbol{r}}_r^{\mathsf{T}}\right]^{\mathsf{T}}$ with its clock error states, $\boldsymbol{x}_{\text{clk},r} \triangleq c\left[\delta t_r,\, \dot{\delta t}_r\right]^{\mathsf{T}}$, i.e., $\boldsymbol{x}_r \triangleq \left[\boldsymbol{x}_{\text{pv}}^{\mathsf{T}},\, \boldsymbol{x}_{\text{clk},r}^{\mathsf{T}}\right]^{\mathsf{T}}$. Discretizing the receiver's dynamics at a constant sampling period T yields

$$\boldsymbol{x}_r\,(k+1) = \boldsymbol{f}_r[\,\boldsymbol{x}_r(k)\,] + \boldsymbol{w}_r(k),$$

$$\boldsymbol{f}_r[\,\boldsymbol{x}_r(k)\,] \triangleq \left[\boldsymbol{f}_{\text{pv}}^{\mathsf{T}}[\,\boldsymbol{x}_{\text{pv}}(k)\,],\, [\mathbf{F}_{\text{clk}}\boldsymbol{x}_{\text{clk},r}(k)]^{\mathsf{T}}\right]^{\mathsf{T}},$$

where $\boldsymbol{f}_{\text{pv}}$ is a vector-valued function, which is obtained by discretizing $\tilde{\boldsymbol{f}}_{\text{pv}}$ at a constant sampling interval T, $\boldsymbol{w}_r$ is the process noise vector, which is modeled as a DT zero-mean white noise sequence with covariance $\mathbf{Q}_r = \text{diag}\,[\mathbf{Q}_{\text{pv}},\, c^2\mathbf{Q}_{\text{clk},r}]$, where $\mathbf{Q}_{\text{pv}}$ is the position and velocity process noise covariance and $\mathbf{Q}_{\text{clk},r}$ is identical to $\mathbf{Q}_{\text{clk},s_m}$, except that $S_{\tilde{w}_{\delta t_{s,m}}}$ and $S_{\tilde{w}_{\dot{\delta} t_{s,m}}}$ are now replaced with receiver-specific spectra, $S_{\tilde{w}_{\delta t_r}}$ and $S_{\tilde{w}_{\dot{\delta} t_r}}$, respectively. A summary of the receiver and RF transmitter states are tabulated in Table 3.1.

Table 3.1: Receiver and RF Transmitter States

States	**Position**	**Velocity**	**Clock bias**	**Clock drift**
Receiver	$\boldsymbol{r}_r$	$\dot{\boldsymbol{r}}_r$	δt_r	$\dot{\delta} t_r$
RF Transmitter m	$\boldsymbol{r}_{s_m}$	-	δt_{s_m}	$\dot{\delta} t_{s_m}$

3.1.3 Measurement Model

The pseudorange measurement made by the receiver on the m^{th} RF transmitter, after discretization and mild approximations discussed in [74], is related to the receiver's and RF transmitter's states by

$$z_{s_m}(k) = \|\boldsymbol{r}_r(k) - \boldsymbol{r}_{s_m}\| + c \cdot [\delta t_r(k) - \delta t_{s_m}(k)] + v_{s_m}(k), \tag{3.1}$$

where $\|\cdot\|$ is the Euclidean norm and v_{s_m} is the measurement noise, which is modeled as a DT zero-mean white Gaussian sequence with variance $\sigma^2_{s_m}$.

3.1.4 Augmented System

The augmented system of an environment comprising one receiver and M RF transmitters will be denoted Σ and is given by

$$\Sigma : \begin{cases} \boldsymbol{x}\,(k+1) = \boldsymbol{f}[\,\boldsymbol{x}(k)\,] + \boldsymbol{w}(k) \\ \\ \boldsymbol{z}(k) = \boldsymbol{h}\,[\,\boldsymbol{x}(k)\,] + \boldsymbol{v}(k) \end{cases} \tag{3.2}$$

where $\boldsymbol{f}[\,\boldsymbol{x}(k)\,] \triangleq \left[\boldsymbol{f}_r^{\mathsf{T}}[\,\boldsymbol{x}_r(k)\,],\, [\boldsymbol{\Phi}_s \boldsymbol{x}_s(k)]^{\mathsf{T}}\right]^{\mathsf{T}}$; $\boldsymbol{x} \triangleq \left[\boldsymbol{x}_r^{\mathsf{T}}, \boldsymbol{x}_s^{\mathsf{T}}\right]^{\mathsf{T}}$; $\boldsymbol{\Phi}_s \triangleq \text{diag}\,[\mathbf{F}_s, \ldots, \mathbf{F}_s]$; $\boldsymbol{x}_s = \left[\boldsymbol{x}_{s_1}^{\mathsf{T}}, \ldots, \boldsymbol{x}_{s_M}^{\mathsf{T}}\right]^{\mathsf{T}}$; $\boldsymbol{w} \triangleq \left[\boldsymbol{w}_r^{\mathsf{T}}, \boldsymbol{w}_{s_1}^{\mathsf{T}}, \ldots, \boldsymbol{w}_{s_M}^{\mathsf{T}}\right]^{\mathsf{T}}$; $\boldsymbol{z} \triangleq [z_{s_1}, \ldots, z_{s_M}]^{\mathsf{T}}$; and $\boldsymbol{v} \triangleq [v_{s_1}, \ldots, v_{s_M}]^{\mathsf{T}}$, with covariance $\text{cov}\,(\boldsymbol{v}) \triangleq \mathbf{R} = \text{diag}[\sigma^2_{s_1}, \ldots, \sigma^2_{s_M}]$.

3.2 Stochastic Observability Analysis

In this section, an overview of the EKF-based radio SLAM problem is presented, and the system's stochastic observability is studied according to the definition [75]:

Definition 3.2.1. *A dynamic system is stochastically observable if and only if there exists a time t_b such that the estimation error covariance $\mathbf{P}_{\boldsymbol{\xi}}(k|k)$ of the state vector $\boldsymbol{\xi}$ produced by a dynamic estimator remains upper bounded by σ_b in the sense that*

$$\sigma_{\max}\{\mathbf{P}_{\boldsymbol{\xi}}(k|k)\} \leq \sigma_b < \infty, \quad \forall\, kT \geq t_b.$$

where $\sigma_{\max}\{\mathbf{A}\}$ denotes the maximum singular value of $\mathbf{A}$.

3.2.1 EKF-based Radio SLAM Overview

The goal of radio SLAM is for a receiver to construct and continuously refine a spatiotemporal signal landscape map of the environment, within which the receiver localizes itself in space and time. In the event that GNSS signals become unavailable or untrustworthy, the receiver continues navigating with the aid of this map. In EKF-based radio SLAM, an EKF produces an estimate $\hat{\boldsymbol{x}}(k|k) \triangleq \mathbb{E}[\boldsymbol{x}(k)|\boldsymbol{Z}^k]$ of $\boldsymbol{x}(k)$, where $\mathbb{E}[\,\cdot\,|\,\cdot\,]$ is the conditional expectation and $\boldsymbol{Z}^k$ denotes all the measurements up to and including time-step k, i.e., $\boldsymbol{Z}^k \triangleq \{\boldsymbol{z}(j)\}_{j=1}^{k}$. In this chapter, it is assumed that the receiver's initial state vector $\boldsymbol{x}_r(0)$ is known, which could be obtained from the last instant a reliable GNSS solution was available. The EKF-based radio SLAM prediction (time update) and correction (measurement update) are given by:

Prediction

$$\hat{\boldsymbol{x}}(k+1|k) = \mathbf{F}(k)\hat{\boldsymbol{x}}(k|k),$$
$$\mathbf{P}_{\boldsymbol{x}}(k+1|k) = \mathbf{F}(k)\mathbf{P}_{\boldsymbol{x}}(k|k)\mathbf{F}^{\mathsf{T}}(k) + \mathbf{Q},$$

Correction

$$\hat{\boldsymbol{x}}(k+1|k+1) = \hat{\boldsymbol{x}}(k+1|k) + \mathbf{L}(k+1)\mathbf{S}^{-1}\boldsymbol{\nu}(k+1),$$

$$\mathbf{P}_{\boldsymbol{x}}(k+1|k+1) = \mathbf{P}_{\boldsymbol{x}}(k+1|k) - \mathbf{L}(k+1)\mathbf{S}^{-1}(k+1)\mathbf{L}^{\mathsf{T}}(k+1),$$

where, $\hat{\boldsymbol{x}}(k+1|k)$ and $\hat{\boldsymbol{x}}(k+1|k+1)$ are the predicted and corrected state estimates, respecitively; $\mathbf{P}_{\boldsymbol{x}}(k+1|k)$ and $\mathbf{P}_{\boldsymbol{x}}(k+1|k+1)$ are the prediction error covariance and corrected estimation error covariance, respectively; $\mathbf{F}$ is the Jacobian of $\boldsymbol{f}$ evalulated at the current state estimate $\hat{\boldsymbol{x}}(k|k)$; $\boldsymbol{\nu}(k+1) \triangleq \boldsymbol{z}(k+1) - \hat{\boldsymbol{z}}(k+1|k)$ is the innovation; $\hat{\boldsymbol{z}}(k+1|k) \triangleq \boldsymbol{h}[\hat{\boldsymbol{x}}(k+1|k)]$ is the measurement prediction; $\mathbf{L}(k+1) \triangleq \mathbf{P}_{\boldsymbol{x}}(k+1|k)\mathbf{H}^{\mathsf{T}}(k+1)$; $\mathbf{S}(k+1) \triangleq \mathbf{H}(k+1)\mathbf{L}(k+1) + \mathbf{R}$ is the innovation covariance; and $\mathbf{H}(k+1)$ is the Jacobian of $\boldsymbol{h}$ evaluated at $\hat{\boldsymbol{x}}(k+1|k)$, which has the form

$$\mathbf{H} = \begin{bmatrix} \boldsymbol{h}_{r,s_1}^{\mathsf{T}} & \boldsymbol{h}_{s_1}^{\mathsf{T}} & \cdots & \mathbf{0}_{1\times 4} \\ \vdots & \vdots & \ddots & \vdots \\ \boldsymbol{h}_{r,s_M}^{\mathsf{T}} & \mathbf{0}_{1\times 4} & \cdots & \boldsymbol{h}_{s_M}^{\mathsf{T}} \end{bmatrix},$$

$$\boldsymbol{h}_{r,s_m}^{\mathsf{T}}(k) = \left[\hat{\mathbf{1}}_m^{\mathsf{T}}(k),\, \mathbf{0}_{1\times 2},\, \boldsymbol{h}_{\text{clk}}^{\mathsf{T}}\right],$$

$$\boldsymbol{h}_{s_m}^{\mathsf{T}}(k) = \left[-\hat{\mathbf{1}}_m^{\mathsf{T}}(k),\, -\boldsymbol{h}_{\text{clk}}^{\mathsf{T}}\right], \quad \boldsymbol{h}_{\text{clk}} = \begin{bmatrix} 1 \\ \\ 0 \end{bmatrix},$$

$$\hat{\mathbf{1}}_m(k) \triangleq \frac{\hat{\boldsymbol{r}}_r(k|k-1) - \hat{\boldsymbol{r}}_{s_m}(k|k-1)}{\|\hat{\boldsymbol{r}}_r(k|k-1) - \hat{\boldsymbol{r}}_{s_m}(k|k-1)\|}, \quad m = 1, \ldots, M.$$

3.2.2 Stochastically Unobservable Clock Errors

This subsection shows that the EKF estimating the state vector of the system in (3.2) produces an estimation error covariance matrix $\mathbf{P}_{\boldsymbol{x}}(k|k)$ whose time evolution grows unboundedly.

Traditional deterministic observability tests provide a necessary, but not sufficient condition for stochastic observability [75]. They also do not incorporate *a priori* knowledge of the uncertainty about the initial state estimate $\mathbf{P}_{\boldsymbol{x}}(0|0)$, process noise covariance $\mathbf{Q}$, or measurement noise covariance $\mathbf{R}$. Moreover, since they only provide a Boolean assessment of the observability of a system, if the system is stochastically unobservable, they do not yield any characterization or the rate of divergence of unobservable states. In what follows, the time evolution of the Riccati equation is studied to show that the radio SLAM problem is stochastically unobservable and to derive a lower bound for the rate of divergence of stochastically unobservable states.

Lemma 3.2.1. *If the estimation error covariance matrix* $\mathbf{P}_{\boldsymbol{\xi}}(k|k)$ *is such that*

$$\lim_{k\to\infty} \boldsymbol{e}_i^{\mathsf{T}} \mathbf{P}_{\boldsymbol{\xi}}(k|k) \boldsymbol{e}_i = \infty, \tag{3.3}$$

where $\boldsymbol{e}_i$ *denotes the* i^{th} *standard basis vector consisting of a* 1 *in the* i^{th} *element and zeros elsewhere, then the* i^{th} *state of* $\boldsymbol{\xi} \in \mathbb{R}^n$ *is stochastically unobservable, and subsequently the system is stochastically unobservable.*

Proof. If $\lim_{k\to\infty} \boldsymbol{e}_i^{\mathsf{T}} \mathbf{P}_{\boldsymbol{\xi}}(k|k)\boldsymbol{e}_i = \infty$, then

$$\lim_{k\to\infty} \operatorname{tr}\left[\mathbf{P}_{\boldsymbol{\xi}}(k|k)\right] = \lim_{k\to\infty} \sum_{i=1}^{n} \boldsymbol{e}_i^{\mathsf{T}} \mathbf{P}_{\boldsymbol{\xi}}(k|k)\boldsymbol{e}_i = \infty,$$

where $\operatorname{tr}[\mathbf{A}]$ denotes the trace of $\mathbf{A}$. From the trace properties, $\operatorname{tr}\left[\mathbf{P}_{\boldsymbol{\xi}}(k|k)\right] = \sum_{i=1}^{n} \lambda_i[\mathbf{P}_{\boldsymbol{\xi}}(k|k)]$, where $\lambda_i[\mathbf{A}]$ denotes the i^{th} eigenvalue of $\mathbf{A}$. Since $\mathbf{P}_{\boldsymbol{\xi}}(k|k)$ is symmetric positive semi-definite, its singular values $\sigma_i[\mathbf{P}_{\boldsymbol{\xi}}(k|k)] = \lambda_i[\mathbf{P}_{\boldsymbol{\xi}}(k|k)]$. Therefore

$$\begin{aligned}\lim_{k\to\infty} \operatorname{tr}\left[\mathbf{P}_{\boldsymbol{\xi}}(k|k)\right] &= \lim_{k\to\infty} \sum_{i=1}^{n} \lambda_i[\mathbf{P}_{\boldsymbol{\xi}}(k|k)] \\ &= \lim_{k\to\infty} \sum_{i=1}^{n} \sigma_i[\mathbf{P}_{\boldsymbol{\xi}}(k|k)] = \infty.\end{aligned}$$

Since n is finite, then at least the largest singular value will grow unboundedly, i.e.,

$$\lim_{k\to\infty} \sigma_{\max}\left[\mathbf{P}_{\boldsymbol{\xi}}(k|k)\right] = \infty,$$

where $\sigma_{\max}[\mathbf{A}] = \max_i \{\sigma_i[\mathbf{A}]\}$, making the system stochastically unobservable. □

Theorem 3.2.1. *The radio SLAM problem consisting of one receiver with knowledge of its initial states and M unknown RF transmitters is stochastically unobservable regardless of the receiver's motion. Moreover, δt_r and $\{\delta t_{s_m}\}_{m=1}^{M}$ are stochastically unobservable states.*

Proof. The proof will proceed in two main steps. First, three simplified systems will be defined, denoted Σ_{I}, Σ_{II}, and Σ_{III}, where Σ_{I} is a simplified form of Σ and each subsequent system is a simplified version of the preceding one. It is shown that if the subsequent system is stochastically unobservable, then the preceding system must be stochastically unobservable as well. Second, Σ_{III} is shown to be stochastically unobservable according to Definition 3.2.1 by invoking lemma 3.2.1.

Step 1: First, define Σ_{I} as a system with (i) known RF transmitter position states $\{\boldsymbol{r}_{s_m}\}_{m=1}^{M}$

and (ii) no process noise driving the receiver's position and velocity states (i.e., $\mathbf{Q}_{\text{pv}} = \mathbf{0}$), e.g., a receiver moving with a constant velocity. From (i) and (ii), and since $\boldsymbol{r}_r(0)$ is known, it is obvious that $\{\boldsymbol{r}_{s_m}\}_{m=1}^{M}$ and $\boldsymbol{r}_r(k)$ are known $\forall\, k$ and need not be estimated by the EKF, simplifying the system to be estimated to a linear time-invariant (LTI) system, given by

$$\Sigma_{\text{I}} : \begin{cases} \boldsymbol{x}_{\text{clk}}\,(k+1) = \boldsymbol{\Phi}_{\text{clk}}\,\boldsymbol{x}_{\text{clk}}(k) + \boldsymbol{w}_{\text{clk}}(k) \\ \boldsymbol{z}_{\text{clk}}(k) = \mathbf{H}_{\text{clk}}\boldsymbol{x}_{\text{clk}}\,(k) + \boldsymbol{v}(k), \end{cases}$$

where

$$\boldsymbol{x}_{\text{clk}} \triangleq \left[\boldsymbol{x}_{\text{clk},r}^{\mathsf{T}},\, \boldsymbol{x}_{\text{clk},s_1}^{\mathsf{T}},\, \ldots,\, \boldsymbol{x}_{\text{clk},s_M}^{\mathsf{T}}\right]^{\mathsf{T}} \in \mathbb{R}^{(2+2M)},$$

$$\boldsymbol{\Phi}_{\text{clk}} \triangleq \text{diag}\left[\mathbf{F}_{\text{clk}},\, \ldots,\, \mathbf{F}_{\text{clk}}\right] \in \mathbb{R}^{[(2+2M)\times(2+2M)]},$$

$$\boldsymbol{z}_{\text{clk}} \triangleq \left[z_{\text{clk},s_1},\, \ldots,\, z_{\text{clk},s_M}\right]^{\mathsf{T}},$$

$$\mathbf{H}_{\text{clk}} = \begin{bmatrix} \boldsymbol{h}_{\text{clk}}^{\mathsf{T}} & -\boldsymbol{h}_{\text{clk}}^{\mathsf{T}} & \cdots & \mathbf{0}_{1\times 2} \\ \vdots & \vdots & \ddots & \vdots \\ \boldsymbol{h}_{\text{clk}}^{\mathsf{T}} & \mathbf{0}_{1\times 2} & \cdots & -\boldsymbol{h}_{\text{clk}}^{\mathsf{T}} \end{bmatrix},$$

where $\boldsymbol{w}_{\text{clk}}$ is a DT zero-mean white process noise vector with covariance $\mathbf{Q}_{\text{clk}} = c^2 \cdot \text{diag}\left[\mathbf{Q}_{\text{clk},r},\, \mathbf{Q}_{\text{clk},s_1}, \ldots,\, \mathbf{Q}_{\text{clk},s_M}\right]$. The measurements have the form $z_{\text{clk},s_m}(k) \triangleq z_m(k) - \|\boldsymbol{r}_r(k) - \boldsymbol{r}_{s_m}\|$ for $m = 1, \ldots, M$.

Since system Σ_{I} is LTI, a Kalman filter (KF) may be employed to estimate the state vector $\boldsymbol{x}_{\text{clk}}$. To incorporate perfect *a priori* knowledge of $\boldsymbol{x}_{\text{clk},r}(0)$ in the KF, the corresponding block of the initial estimation error covariance matrix is set to zero. Assuming the initial estimates of $\{\boldsymbol{x}_{\text{clk},s_m}\}_{m=1}^{M}$ to be uncorrelated, the initial estimation error covariance matrix is given as

$${}^{\text{I}}\mathbf{P}_{\boldsymbol{x}_{\text{clk}}}(0|0) = \text{diag}\left[\,\mathbf{0}_{2\times 2},\, {}^{\text{I}}\mathbf{P}_{\boldsymbol{x}_{\text{clk},s}}(0|0)\,\right], \tag{3.4}$$

where ${}^{\mathrm{I}}\mathbf{P}_{\boldsymbol{x}_{\mathrm{clk}}}(0|0)$ is the initial estimation error covariance of the KF associated with Σ_{I},

$$
\begin{aligned}
&{}^{\mathrm{I}}\mathbf{P}_{\boldsymbol{x}_{\mathrm{clk},s}}(0|0) \triangleq \\
&\mathrm{diag}\left[{}^{\mathrm{I}}\sigma^2_{\delta t_{s_1}}(0|0), {}^{\mathrm{I}}\sigma^2_{\dot{\delta} t_{s_1}}(0|0), \ldots, {}^{\mathrm{I}}\sigma^2_{\delta t_{s_M}}(0|0), {}^{\mathrm{I}}\sigma^2_{\dot{\delta} t_{s_M}}(0|0)\right]
\end{aligned}
$$

is the initial estimation error covariance of the state vectors $\{\boldsymbol{x}_{\mathrm{clk},s_m}\}_{m=1}^{M}$, and ${}^{\mathrm{I}}\sigma^2_{\delta t_{s_m}}$ and ${}^{\mathrm{I}}\sigma^2_{\dot{\delta} t_{s_m}}$ are the variances of the transmitters' clock bias and drift, respectively.

Define Σ_{II} to be the same as Σ_{I} with the additional simplifications that $S_{\tilde{w}_{\dot{\delta} t_r}} = 0$ and $\{S_{\tilde{w}_{\dot{\delta} t_{s,m}}}\}_{m=1}^{M} = 0$. Since Σ_{II} has less process noise than Σ_{I}, it is obvious that ${}^{\mathrm{II}}\mathbf{P}_{\boldsymbol{x}_{\mathrm{clk}}}(k+1|k) \prec {}^{\mathrm{I}}\mathbf{P}_{\boldsymbol{x}_{\mathrm{clk}}}(k+1|k), \forall\, k$, where $\mathbf{A} \prec \mathbf{B}$ denotes the difference $\mathbf{B} - \mathbf{A}$ being positive definite. Therefore, if Σ_{II} is stochastically unobservable, then Σ_{I} must be stochastically unobservable as well.

Define Σ_{III} to be the same as Σ_{II} with the additional simplification that $\mathbf{R} = \mathbf{0}_{M\times M}$. Since Σ_{III} has no measurement noise, it is obvious that ${}^{\mathrm{III}}\mathbf{P}_{\boldsymbol{x}_{\mathrm{clk}}}(k+1|k+1) \prec {}^{\mathrm{II}}\mathbf{P}_{\boldsymbol{x}_{\mathrm{clk}}}(k+1|k+1), \forall\, k$. Therefore, if Σ_{III} is stochastically unobservable, then Σ_{II} must be stochastically unobservable as well. Also, since for each k there are M perfect measurements that are linearly related to $2 + 2M$ states, the state vector order of Σ_{III} may be reduced from $2 + 2M$ to $2 + M$ and a reduced-order KF may be used. Reduced-order KFs are used in practice to avoid potential numerical issues and reduce computational complexity [116]. It turns out that the reduced-order KF lends itself to a tractable closed-form expression of the time evolution of the associated estimation error covariance; therefore, is used to evaluate the stochastic observability of Σ_{III} for the second part of this proof.

Step 2: An estimate of $\boldsymbol{x}_{\mathrm{clk}}(k)$ can be computed though

$$
\hat{\boldsymbol{x}}_{\mathrm{clk}}(k|k) = \mathbf{L}_1 \boldsymbol{z}_{\mathrm{clk}}(k) + \mathbf{L}_2 \hat{\boldsymbol{x}}_{\mathrm{ro}}(k|k), \tag{3.5}
$$

where $\hat{\boldsymbol{x}}_{\rm ro}(k|k)$ is an estimate produced by a reduced-order KF of the reduced-order state vector $\boldsymbol{x}_{\rm ro}(k) \triangleq \mathbf{G}\boldsymbol{x}_{\rm clk}(k)$; $(\mathbf{L}_1|\mathbf{L}_2) \triangleq \left(\frac{\mathbf{H}_{\rm clk}}{\mathbf{G}}\right)^{-1}$; $(\mathbf{L}_1|\mathbf{L}_2)$ is the matrix formed by augmenting the columns of $\mathbf{L}_1$ and $\mathbf{L}_2$; $\left(\frac{\mathbf{H}_{\rm clk}}{\mathbf{G}}\right)$ is the matrix formed by augmenting the rows of $\mathbf{H}_{\rm clk}$ and $\mathbf{G}$; and $\mathbf{G}$ is the design matrix which is chosen to be

$$\mathbf{G} \equiv \begin{bmatrix} \mathbf{I}_2 & \mathbf{0}_{2\times 2} & \dots & \mathbf{0}_{2\times 2} \\ \boldsymbol{g}^{\mathsf{T}} & -\boldsymbol{g}^{\mathsf{T}} & \dots & \mathbf{0}_{1\times 2} \\ \vdots & \vdots & \ddots & \vdots \\ \boldsymbol{g}^{\mathsf{T}} & \mathbf{0}_{1\times 2} & \dots & -\boldsymbol{g}^{\mathsf{T}} \end{bmatrix}, \qquad \boldsymbol{g} \triangleq \begin{bmatrix} 0 \\ 1 \end{bmatrix}, \tag{3.6}$$

so that δt_r is the first state of $\boldsymbol{x}_{\rm ro}$ and $\left(\frac{\mathbf{H}_{\rm clk}}{\mathbf{G}}\right)$ is invertible. It is important to note that although the choice of $\mathbf{G}$ and the corresponding reduced-order state vector $\boldsymbol{x}_{\rm ro}$ are non-unique, the remainder of the proof is invariant to any feasible choice of $\mathbf{G}$ that makes $\left(\frac{\mathbf{H}_{\rm clk}}{\mathbf{G}}\right)$ invertible.

A reduced-order KF produces $\hat{\boldsymbol{x}}_{\rm ro}(k+1|k+1)$ and an associated posterior estimation error covariance given by

$$\begin{aligned} &\mathbf{P}_{\boldsymbol{x}_{\rm ro}}(k+1|k+1) \\ &\quad = \left[\boldsymbol{\Psi} - \boldsymbol{\Lambda}(k)\boldsymbol{\Xi}\right] \mathbf{P}_{\boldsymbol{x}_{\rm ro}}(k|k) \left[\boldsymbol{\Psi} - \boldsymbol{\Lambda}(k)\boldsymbol{\Xi}\right]^{\mathsf{T}} \\ &\qquad + \mathbf{G}\mathbf{Q}_{\rm clk}\mathbf{G}^{\mathsf{T}} - \mathbf{G}\mathbf{Q}_{\rm clk}\mathbf{H}_{\rm clk}^{\mathsf{T}}\boldsymbol{\Lambda}^{\mathsf{T}}(k) \\ &\qquad - \boldsymbol{\Lambda}(k)\mathbf{H}_{\rm clk}\mathbf{Q}_{\rm clk}^{\mathsf{T}}\mathbf{G}^{\mathsf{T}} + \boldsymbol{\Lambda}(k)\mathbf{R}_{\rm ro}\boldsymbol{\Lambda}^{\mathsf{T}}(k), \end{aligned} \tag{3.7}$$

where $\boldsymbol{\Psi} \triangleq \mathbf{G}\boldsymbol{\Phi}_{\rm clk}\mathbf{L}_2$, $\boldsymbol{\Xi} \triangleq \mathbf{H}_{\rm clk}\boldsymbol{\Phi}_{\rm clk}\mathbf{L}_2$, $\mathbf{R}_{\rm ro} \triangleq \mathbf{H}_{\rm clk}\mathbf{Q}_{\rm clk}\mathbf{H}_{\rm clk}^{\mathsf{T}}$, and

$$\begin{aligned} \boldsymbol{\Lambda}(k) \;&=\; \left[\boldsymbol{\Psi}\mathbf{P}_{\boldsymbol{x}_{\rm ro}}(k|k)\boldsymbol{\Xi}^{\mathsf{T}} + \mathbf{G}\mathbf{Q}_{\rm clk}\mathbf{H}_{\rm clk}^{\mathsf{T}}\right] \\ &\qquad \cdot \left[\boldsymbol{\Xi}\mathbf{P}_{\boldsymbol{x}_{\rm ro}}(k|k)\boldsymbol{\Xi}^{\mathsf{T}} + \mathbf{R}_{\rm ro}\right]^{-1}. \end{aligned} \tag{3.8}$$

Note that the matrix $\boldsymbol{\Xi}\mathbf{P}_{\boldsymbol{x}_{\rm ro}}(k|k)\boldsymbol{\Xi}^{\mathsf{T}}$ is symmetric positive semi-definite $\forall\, k$ and $\mathbf{R}_{\rm ro}$ is symmetric positive definite and time-invariant; therefore, $\left[\boldsymbol{\Xi}\mathbf{P}_{\boldsymbol{x}_{\rm ro}}(k|k)\boldsymbol{\Xi}^{\mathsf{T}}+\mathbf{R}_{\rm ro}\right]$ is symmetric positive definite and invertible $\forall\, k$.

The estimate of $\hat{\boldsymbol{x}}_{\rm clk}(k{+}1|k{+}1)$ is then produced through (3.5) and its corresponding posterior estimation error covariance is

$$^{\rm III}\mathbf{P}_{\boldsymbol{x}_{\rm clk}}(k{+}1|k{+}1)=\mathbf{L}_2\mathbf{P}_{\boldsymbol{x}_{\rm ro}}(k{+}1|k{+}1)\mathbf{L}_2^{\mathsf{T}}, \tag{3.9}$$

where $\mathbf{L}_2=[\boldsymbol{e}_1,\boldsymbol{e}_2,\boldsymbol{e}_1,\boldsymbol{e}_2-\boldsymbol{e}_3,\ldots,\boldsymbol{e}_1,\boldsymbol{e}_2-\boldsymbol{e}_{M+2}]^{\mathsf{T}}$. From (3.9) and the structure of $\mathbf{L}_2$, the clock bias estimation error variances of the receiver and the RF transmitters are equal, i.e.,

$$^{\rm III}\sigma^2_{\delta t_r}(k|k)=\{^{\rm III}\sigma^2_{\delta t_{s_m}}(k|k)\}_{m=1}^{M}. \tag{3.10}$$

This equality holds for any feasible $\mathbf{G}$, since there are M perfect measurements; therefore, the biases of the receiver and RF transmitters are linearly related to each other by a deterministic quantity, given by $\delta t_r=\delta t_{s_m}+z_{{\rm clk},s_m}$, for $m=1,\ldots,M$. A closed-form expression of the time evolution of $^{\rm III}\sigma^2_{\delta t_r}(k|k)$ is found through the following two steps. First, (3.7) is recursively solved using an initial estimation error covariance given by

$$\mathbf{P}_{\boldsymbol{x}_{\rm ro}}(0|0)=\mathbf{G}^{\rm III}\mathbf{P}_{\boldsymbol{x}_{\rm clk}}(0|0)\mathbf{G}^{\mathsf{T}},$$

where $^{\rm III}\mathbf{P}_{\boldsymbol{x}_{\rm clk}}(0|0)$ has the same structure as (3.4), except I is replaced with III. Second, the element corresponding to the receiver's clock bias $\boldsymbol{e}_1^{\mathsf{T}\,\rm III}\mathbf{P}_{\boldsymbol{x}_{\rm clk}}(k|k)\boldsymbol{e}_1$ is found by substituting the right-hand side of (3.7) into (3.9), yielding

$$^{\rm III}\sigma^2_{\delta t_r}(k|k)=\frac{kq_r\prod_{m=1}^{M}\Omega_m(k)}{\det\left[k\boldsymbol{\Xi}\mathbf{P}_{\boldsymbol{x}_{\rm ro}}(0|0)\boldsymbol{\Xi}^{\mathsf{T}}+\mathbf{R}_{\rm ro}\right]},\ k=1,2,\ldots, \tag{3.11}$$

where $\Omega_m(k)\triangleq q_{s_m}+kT^2\beta_m$, $\beta_m=^{\rm III}\sigma^2_{\dot{\delta}t_{s_m}}(0|0)$, $q_r\triangleq c^2S_{\tilde{w}_{\delta t_r}}T$, and $q_{s_m}\triangleq c^2S_{\tilde{w}_{\delta t_{s_m}}}T$. Finally,

to evaluate the limit (3.3) for the first state of ${}^{\mathrm{III}}\mathbf{P}_{\boldsymbol{x}_{\mathrm{clk}}}$, the closed-form (3.11) is used, yielding

$$\begin{aligned}
&\lim_{k\to\infty} \boldsymbol{e}_1^{\mathsf{T}\,\mathrm{III}}\mathbf{P}_{\boldsymbol{x}_{\mathrm{clk}}}(k|k)\boldsymbol{e}_1 \\
&\quad= \lim_{k\to\infty} {}^{\mathrm{III}}\sigma^2_{\delta t_r}(k|k) \\
&\quad= \lim_{k\to\infty} \frac{kq_r \prod_{m=1}^{M} \Omega_m(k)}{\det\left[k\Xi\mathbf{P}_{\boldsymbol{x}_{\mathrm{ro}}}(0|0)\Xi^{\mathsf{T}}+\mathbf{R}_{\mathrm{ro}}\right]} \\
&\quad= \lim_{k\to\infty} \frac{k^{(M+1)}q_r \prod_{m=1}^{M} (\frac{1}{k}q_{s_m} + T^2\beta_m)}{k^M \det\left[\Xi\mathbf{P}_{\boldsymbol{x}_{\mathrm{ro}}}(0|0)\Xi^{\mathsf{T}}+\frac{1}{k}\mathbf{R}_{\mathrm{ro}}\right]} = \infty.
\end{aligned} \tag{3.12}$$

Therefore, stochastic unobservability follows from Lemma 3.2.1. □

Theorem 3.2.2. *The EKF estimating the receiver's state simultaneously with the states of M terrestrial transmitters, with a priori knowledge about the receiver's initial state, for the stochastically unobservable system Σ, produces corresponding estimation error variances $\sigma^2_{\delta t_r}$ and $\{\sigma^2_{\delta t_{s_m}}\}_{m=1}^{M}$, respectively, whose time evolution is lower-bounded by a diverging sequence with a divergence rate $\gamma(k)$, where $\gamma(k) \xrightarrow{k\to\infty} c^2 S_{\tilde{w}_{\delta t_r}} T$.*

Proof. From Theorem 3.2.1, system Σ is stochastically unobservable and the variances $\sigma^2_{\delta t_r}$ and $\{\sigma^2_{\delta t_{s_m}}\}_{m=1}^{M}$ produced by an EKF will diverge and their time evolutions are lower bounded by (3.11).

Define the divergence rate of the estimation error variance associated with the i^{th} state of the vector $\boldsymbol{\xi} \in \mathbb{R}^n$ as

$$\gamma(k) = \boldsymbol{e}_i^{\mathsf{T}} \left[\mathbf{U}_{\boldsymbol{\xi},\mathrm{inc}}(k) - \mathbf{U}_{\boldsymbol{\xi},\mathrm{red}}(k)\right] \boldsymbol{e}_i, \tag{3.13}$$

where

$$\mathbf{U}_{\boldsymbol{\xi},\mathrm{inc}}(k) \triangleq \mathbf{P}_{\boldsymbol{\xi}}(k+1|k) - \mathbf{P}_{\boldsymbol{\xi}}(k|k)$$

is the uncertainty increase from the EKF prediction step and

$$\mathbf{U}_{\boldsymbol{\xi},\mathrm{red}}(k) \triangleq \mathbf{P}_{\boldsymbol{\xi}}(k+1|k) - \mathbf{P}_{\boldsymbol{\xi}}(k+1|k+1)$$

is the uncertainty reduction from the EKF correction step.

Substituting (3.11) into (3.13) for the first state of ${}^{\mathrm{III}}\mathbf{P}_{\boldsymbol{x}_{\mathrm{clk}}}$ gives

$$\begin{aligned}
&\boldsymbol{e}_1^{\mathsf{T}}\left[\mathbf{U}_{\boldsymbol{x}_{\mathrm{clk}},\mathrm{inc}}(k) - \mathbf{U}_{\boldsymbol{x}_{\mathrm{clk}},\mathrm{red}}(k)\right]\boldsymbol{e}_1 \\
&\qquad = {}^{\mathrm{III}}\sigma^2_{\delta t_r}(k+1|k+1) - {}^{\mathrm{III}}\sigma^2_{\delta t_r}(k|k) \\
&\qquad = \frac{(k+1)q_r \prod_{m=1}^{M} \Omega_m(k+1)}{\det\left[(k+1)\Xi\mathbf{P}_{\boldsymbol{x}_{\mathrm{ro}}}(0|0)\Xi^{\mathsf{T}} + \mathbf{R}_{\mathrm{ro}}\right]} \\
&\qquad\quad - \frac{kq_r \prod_{m=1}^{M} \Omega_m(k)}{\det\left[k\Xi\mathbf{P}_{\boldsymbol{x}_{\mathrm{ro}}}(0|0)\Xi^{\mathsf{T}} + \mathbf{R}_{\mathrm{ro}}\right]}.
\end{aligned} \tag{3.14}$$

Evaluating the limit of (3.14) yields

$$\begin{aligned}
&\lim_{k\to\infty} \boldsymbol{e}_1^{\mathsf{T}}\left[\mathbf{U}_{\boldsymbol{x}_{\mathrm{clk}},\mathrm{inc}}(k) - \mathbf{U}_{\boldsymbol{x}_{\mathrm{clk}},\mathrm{red}}(k)\right]\boldsymbol{e}_1 \\
&\quad = \lim_{k\to\infty} \frac{[k+1]^{(M+1)} q_r \prod_{m=1}^{M} (\frac{1}{k+1} q_{s_m} + T^2\beta_m)}{[k+1]^M \det\left[\Xi\mathbf{P}_{\boldsymbol{x}_{\mathrm{ro}}}(0|0)\Xi^{\mathsf{T}} + \frac{1}{k+1}\mathbf{R}_{\mathrm{ro}}\right]} \\
&\qquad - \lim_{k\to\infty} \frac{k^{(M+1)} q_r \prod_{m=1}^{M} (\frac{1}{k} q_{s_m} + T^2\beta_m)}{k^M \det\left[\Xi\mathbf{P}_{\boldsymbol{x}_{\mathrm{ro}}}(0|0)\Xi^{\mathsf{T}} + \frac{1}{k}\mathbf{R}_{\mathrm{ro}}\right]} \\
&\quad = \frac{q_r \lim_{k\to\infty} (k+1) \prod_{m=1}^{M} (T^2\beta_m)}{\det\left[\Xi\mathbf{P}_{\boldsymbol{x}_{\mathrm{ro}}}(0|0)\Xi^{\mathsf{T}}\right]} \\
&\qquad - \frac{q_r \lim_{k\to\infty} k \prod_{m=1}^{M} (T^2\beta_m)}{\det\left[\Xi\mathbf{P}_{\boldsymbol{x}_{\mathrm{ro}}}(0|0)\Xi^{\mathsf{T}}\right]} \\
&\quad = \frac{q_r \prod_{m=1}^{M} (T^2\beta_m)}{\prod_{m=1}^{M} (T^2\beta_m)} = q_r,
\end{aligned} \tag{3.15}$$

where $q_r \triangleq c^2 S_{\tilde{w}_{\delta t_r}} T$. □

Theorem 3.2.1 shows that the radio SLAM problem with *a priori* knowledge about the

receiver's states is stochastically unobservable, since the estimation uncertainty associated with the clock biases of both the receivers and terrestrial transmitters will diverge. Theorem 3.2.2 establishes a lower bound of this divergence, which in the limit, only depends on the quality of the receiver's clock, characterized by $S_{\tilde{w}_{\delta t_r}}$. The following two sections present numerical and experimental results demonstrating radio SLAM.

3.3 Simulation Results

In this section, an environment consisting of one UAV-mounted receiver and $M = 5$ RF transmitters is simulated to demonstrate that both the receiver's clock bias δt_r and the transmitters' clock biases $\{\delta t_{s_m}\}_{m=1}^{M}$ are stochastically unobservable, as was shown in Theorem 3.2.1 and to demonstrate that the divergence rate $\gamma(k) \xrightarrow{k\to\infty} q_r$, as established in Theorem 3.2.2. To this end, two systems are simulated: (i) system Σ_{III} to demonstrate the divergence rate $\gamma(k) \xrightarrow{k\to\infty} q_r$ (3.15) and (ii) the full system Σ to demonstrate the divergence of the estimation error variances of the clock biases when the receiver's position and velocity and the transmitters' positions are also estimated.

First, an estimate $\hat{\boldsymbol{x}}_{\text{clk}}(k|k)$ of Σ_{III}'s state vector was computed through (3.5), using the design matrix (3.6) and the estimate $\hat{\boldsymbol{x}}_{\text{ro}}(k|k)$, which was produced by a reduced-order KF. The reduced-order KF was initialized according to $\hat{\boldsymbol{x}}_{\text{ro}}(0|0) \sim \mathcal{N}\left[\mathbf{G}\boldsymbol{x}_{\text{clk}}(0), \mathbf{P}_{\boldsymbol{x}_{\text{ro}}}(0|0)\right]$, where $\mathbf{P}_{\boldsymbol{x}_{\text{ro}}}(0|0) = \mathbf{G}\left[{}^{\text{III}}\mathbf{P}_{\boldsymbol{x}_{\text{clk}}}(0|0)\right]\mathbf{G}^{\mathsf{T}}$. The simulation settings are tabulated in Table 3.2. The non-zero estimation error trajectories $\tilde{\boldsymbol{x}}_{\text{ro}} \triangleq \boldsymbol{x}_{\text{ro}} - \hat{\boldsymbol{x}}_{\text{ro}}$ and their associated $\pm 2\sigma$ bounds are plotted in Figs. 3.1(a)–(b). The time evolution of $\gamma(k) = \boldsymbol{e}_1^{\mathsf{T}}\left[\mathbf{U}_{\boldsymbol{x}_{\text{ro}},\text{inc}}(k) - \mathbf{U}_{\boldsymbol{x}_{\text{ro}},\text{red}}(k)\right]\boldsymbol{e}_1$ is plotted in Fig. 3.1(c). The estimation error $\tilde{\boldsymbol{x}}_{\text{clk}} \triangleq \boldsymbol{x}_{\text{clk}} - \hat{\boldsymbol{x}}_{\text{clk}}$ was reconstructed from (3.5) and the associated posterior estimation error covariance ${}^{\text{III}}\mathbf{P}_{\boldsymbol{x}_{\text{clk}}}$ was computed by substituting the reduced-order KF's posterior estimation error covariance (3.7) into (3.9). The estimation error trajectories and corresponding $\pm 2\sigma$ bounds for δt_r, δt_{s_1}, and $\delta\dot{t}_{s_1}$ are plotted

in Figs. 3.1(d)–(f).

Table 3.2: Simulation Settings: System Σ_{III}

Parameter	**Value**
$\boldsymbol{x}_{\text{clk}_r}(0)$	$[100,\ 10]^{\mathsf{T}}$
$\{\boldsymbol{x}_{\text{clk}_{s_m}}(0)\}_{m=1}^{5}$	$[10,\ 1]^{\mathsf{T}}$
$\boldsymbol{x}_{\text{clk}}(0)$	$\left[\boldsymbol{x}_{\text{clk}_r}^{\mathsf{T}}(0),\ \boldsymbol{x}_{\text{clk}_{s_1}}^{\mathsf{T}}(0),\ \ldots,\ \boldsymbol{x}_{\text{clk}_{s_5}}^{\mathsf{T}}(0)\right]^{\mathsf{T}}$
${}^{\text{III}}\mathbf{P}_{\boldsymbol{x}_{\text{clk}}}(0\|0)$	$(10^2)\cdot\text{diag}\,[0, 0, 3, 0.3, \ldots, 3, 0.3]$
$\{h_{0,r},\ h_{-2,r}\}$	$\{9.4\times10^{-20},\ 0\}$
$\{h_{0,s_m},\ h_{-2,s_m}\}_{m=1}^{5}$	$\{8.0\times10^{-20},\ 0\}$
T	0.01 s
$\{\sigma_{s_m}^2\}_{m=1}^{5}$	0 m^2

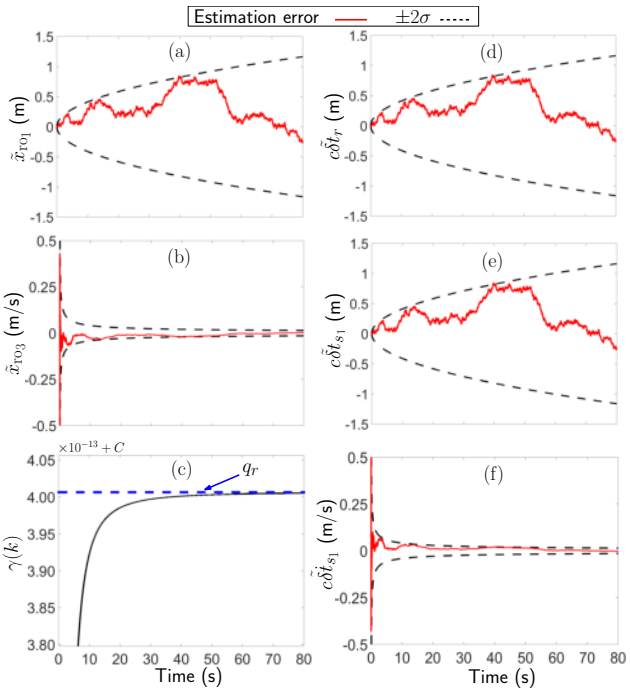

Figure 3.1: Estimation error trajectories (red) and corresponding $\pm2\sigma$ bounds (black dashed). Figs. (a) and (b) correspond to a reduced-order KF estimating $\boldsymbol{x}_{\text{ro}}$ using settings from Table 3.2, where $\boldsymbol{x}_{\text{ro}_i} \triangleq \boldsymbol{e}_i^{\mathsf{T}}\boldsymbol{x}_{\text{ro}}$. Fig. (c) illustrates the time evolution of $\gamma(k) = \boldsymbol{e}_1^{\mathsf{T}}\left[\mathbf{U}_{\boldsymbol{x}_{\text{clk}},\text{inc}}(k) - \mathbf{U}_{\boldsymbol{x}_{\text{clk}},\text{red}}(k)\right]\boldsymbol{e}_1$ (black) and the value of its limit q_r (blue dotted), where $C = 4.2241493\times10^{-5}$. Figs. (d)–(f) correspond to the clock errors of the receiver and transmitter 1, which were reconstructed through (3.5), and their corresponding $\pm2\sigma$ bounds, which were computed using (3.7) and (3.9).

The following can be concluded from these plots. First, ${}^{\text{III}}\sigma_{\delta t_r}^2(k|k) = {}^{\text{III}}\sigma_{\delta t_s}^2(k|k)\,\forall\,k$, as

expected from (3.10). Second, ${}^{\text{III}}\sigma^2_{\delta t_r}$ and ${}^{\text{III}}\sigma^2_{\delta t_{s_1}}$ are diverging, implying δt_r and δt_{s_1} are stochastically unobservable. The same behavior was observed for the variances associated with $\{\delta t_{s_m}\}_{m=2}^5$. Third, Fig. 3.1(c) illustrates that their divergence rate converges to a constant, $\gamma(k) \xrightarrow{k\to\infty} q_r$, as established in Theorem 3.2.2. The diverging errors were noted to be consistent with their $\pm 2\sigma$ bounds when the simulator was ran using different realizations of process noise and initial state estimates.

Next, the full system Σ was simulated and an EKF was employed to estimate $\boldsymbol{x}(k)$. The purpose of this simulation is to illustrate that δt_r and $\{\delta t_{s_m}\}_{m=1}^5$ are stochastically unobservable in the full system Σ and to demonstrate the behavior of the estimation errors of the receiver's position and velocity and the RF transmitters' positions, along with their corresponding variances. The receiver moved in a favorable trajectory around the RF transmitters. Specifically, the receiver's position and velocity states were set to evolve according to a constant turn rate model as described in [115], i.e.,

$$\boldsymbol{f}_{\text{pv}}[\,\boldsymbol{x}_{\text{pv}}(k)\,] \equiv \begin{bmatrix} 1 & 0 & \frac{\mathsf{s}(\omega T)}{\omega} & -\frac{1-\mathsf{c}(\omega T)}{\omega} \\ 0 & 1 & \frac{1-\mathsf{c}(\omega T)}{\omega} & \frac{\mathsf{s}(\omega T)}{\omega} \\ 0 & 0 & \mathsf{c}(\omega T) & -\mathsf{s}(\omega T) \\ 0 & 0 & \mathsf{s}(\omega T) & \mathsf{c}(\omega T) \end{bmatrix} \boldsymbol{x}_{\text{pv}}(k),$$

$$\mathbf{Q}_{\text{pv}} \equiv$$

$$S_w \begin{bmatrix} 2\frac{\omega T - \mathsf{s}(\omega T)}{\omega^3} & 0 & \frac{1-\mathsf{c}(\omega T)}{\omega^2} & \frac{\omega T - \mathsf{s}(\omega T)}{\omega^2} \\ 0 & 2\frac{\omega T - \mathsf{s}(\omega T)}{\omega^3} & -\frac{\omega T - \mathsf{s}(\omega T)}{\omega^2} & \frac{1-\mathsf{c}(\omega T)}{\omega^2} \\ \frac{1-\mathsf{c}(\omega T)}{\omega^2} & -\frac{\omega T - \mathsf{s}(\omega T)}{\omega^2} & T & 0 \\ \frac{\omega T - \mathsf{s}(\omega T)}{\omega^2} & \frac{1-\mathsf{c}(\omega T)}{\omega^2} & 0 & T \end{bmatrix},$$

where $\mathsf{s}(\cdot)$ and $\mathsf{c}(\cdot)$ denote $\sin(\cdot)$ and $\cos(\cdot)$, respectively, ω is a known constant turn rate, and S_w is the process noise power spectral density. This type of open-loop trajectory has

been demonstrated to produce better estimates than an open-loop velocity random walk trajectory [54]. The EKF initialization settings and receiver and RF transmitters' initial states are tabulated in Table 3.3. The environment layout and UAV trajectory is illustrated in Fig. 3.2. The estimation error trajectories and associated $\pm 2\sigma$ bounds are plotted in Figs. 3.3(a)–(f) and Fig. 3.3(g)–(j) for the receiver and RF transmitter 1, respectively.

Table 3.3: Simulation Settings: System Σ

Parameter	**Value**
$\boldsymbol{x}_r(0)$	$[0,\ 0,\ 10,\ 10,\ 100,\ 10]^{\mathsf{T}}$
$\mathbf{P}_r(0\|0)$	$\mathrm{diag}\,[0, 0, 0, 0, 0, 0]$
$\{h_{0,\mathrm{r}},\ h_{-2,\mathrm{r}}\}$	$\{9.4 \times 10^{-20},\ 3.8 \times 10^{-21}\}$
$\boldsymbol{r}_{s_1}(0)$	$[-110,\ 240]^{\mathsf{T}}$
$\boldsymbol{r}_{s_2}(0)$	$[-150,\ 340]^{\mathsf{T}}$
$\boldsymbol{r}_{s_3}(0)$	$[-215,\ -60]^{\mathsf{T}}$
$\boldsymbol{r}_{s_4}(0)$	$[-75,\ 105]^{\mathsf{T}}$
$\boldsymbol{r}_{s_5}(0)$	$[-5,\ 80]^{\mathsf{T}}$
$\boldsymbol{x}_{s_m}(0)$	$\left[\boldsymbol{r}_{s_m}^{\mathsf{T}},\ 10,\ 1\right]^{\mathsf{T}}$
$\mathbf{P}_{s_m}(0\|0)$	$(10^2) \cdot \mathrm{diag}\,[1, 1, 30, 3]$
$\hat{\boldsymbol{x}}_{s_m}(0\|0)$	$\sim \mathcal{N}\left[\boldsymbol{x}_{s_m}(0), \mathbf{P}_{s_m}(0\|0)\right]$
$\{h_{0,s_m},\ h_{-2,s_m}\}_{m=1}^{5}$	$\{8.0 \times 10^{-20},\ 4.0 \times 10^{-23}\}$
T	0.01 s
ω	0.1 rad/s
S_w	0.01 $\mathrm{m}^2.\mathrm{rad}^2/\mathrm{s}^3$
$\left\{\sigma_{s_m}^2\right\}_{m=1}^{5}$	20 m^2

The following can be concluded from the full system simulation plots in Fig. 3.3. First, while the variance of $c\tilde{\delta}t_{s_1}$ decreases, at some point in time, it begins to diverge unboundedly. On the other hand, the variance of $c\tilde{\delta}t_r$ starts from zero (due to the prior knowledge about the receiver's clock bias) and diverges unboundedly with time. Second, although the errors $c\tilde{\delta}t_r$ and $c\tilde{\delta}t_s$ are relatively small, their variances will continue to increase and cause the estima-

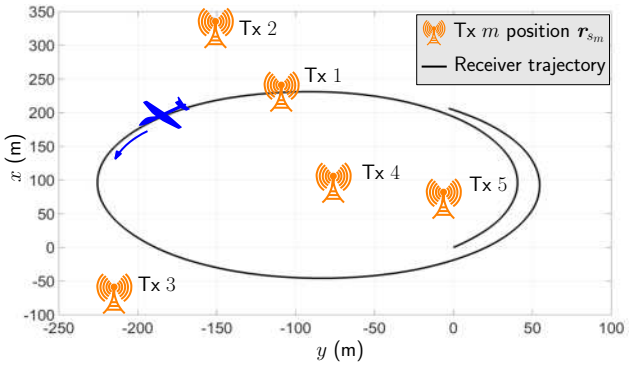

Figure 3.2: Simulated environment consisting of $M = 5$ RF transmitters (Tx) (orange) and one UAV-mounted receiver traversing a circular orbit (black).

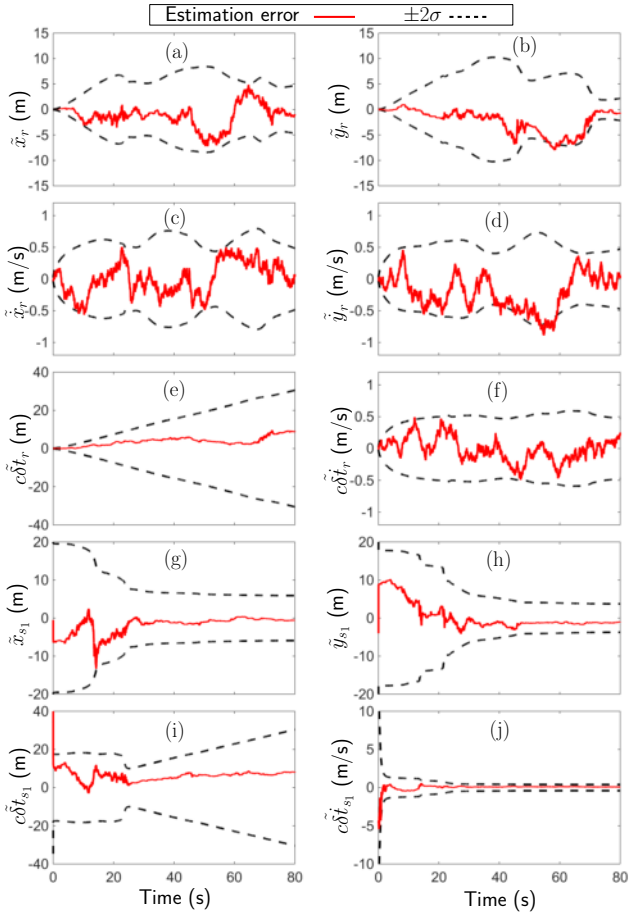

Figure 3.3: Estimation error trajectories (red) and corresponding $\pm 2\sigma$ bounds (black) for EKF-based radio SLAM with settings from Table 3.3.

tion error covariance matrix to become ill-conditioned. Note that an extended information filter (EIF) will not resolve this issue, and a similar problem will be encountered. This is because as the uncertainties of the clock states become larger, the corresponding elements

in the information matrix become smaller, causing the information matrix to also become ill-conditioned. This is evident from the fact that the condition number of the estimation error covariance matrix $\mathbf{P}$ is equal to the condition number of the corresponding information matrix $\mathbf{Y} = \mathbf{P}^{-1}$. Since the pseudorange measurements are a nonlinear function of the receivers' and the RF transmitters' positions, a conversion from the information space to the state space is required in order to compute the measurement residual and the measurement Jacobians, which are necessary for the EIF update step. This conversion requires the inversion of the information matrix which becomes ill-conditioned at the same rate as the covariance matrix. Third, despite the stochastically unobservable clock biases, the estimation error variances appear to have a finite bound for $\tilde{x}_r$, $\tilde{y}_r$, $\tilde{\dot{x}}_r$, $\tilde{\dot{y}}_r$, $c\tilde{\dot{\delta t}}_r$, $\tilde{x}_{s_1}$, $\tilde{y}_{s_1}$, and $c\tilde{\dot{\delta t}}_{s_1}$. Similar behavior was noted for the estimates associated with the other four RF transmitters.

3.4 Experimental Demonstration

A field experiment was conducted in Riverside, California, U.S.A., using a UAV to demonstrate the stochastically unobservable clock biases of both a UAV-mounted receiver and multiple cellular transmitters when an EKF-based radio SLAM framework is employed.

To this end, a UAV was equipped with a two-channel Ettus® E312 universal software radio peripheral (USRP). Two antennas were mounted to the UAV and connected to the USRP: (i) a consumer-grade patch GPS antenna and (ii) a consumer-grade omni-directional cellular antenna. The USRP was tuned to (i) 1575.42 MHz to sample GPS L1 C/A signals and (ii) 882.75 MHz to sample cellular signals which were modulated through code division multiple access (CDMA) and were transmitted from nearby cellular towers. The E312 fed the sampled data to the Multichannel Adaptive TRansceiver Information eXtractor (MATRIX) software-defined receiver (SDR) [107, 117], which produced pseudorange observables to all available GPS SVs and to four cellular towers of the U.S. cellular provider Verizon. The

GPS pseudoranges were only used to estimate the UAV-mounted receiver's initial position and clock error states. Such estimates were used to initialize the EKF, which simultaneously estimated the UAV's and the four unknown transmitters' state *before* navigation via radio SLAM began, while cellular pseudoranges were used exclusively *thereafter* as measurements in the EKF. The experimental setup is illustrated in Fig. 3.4.

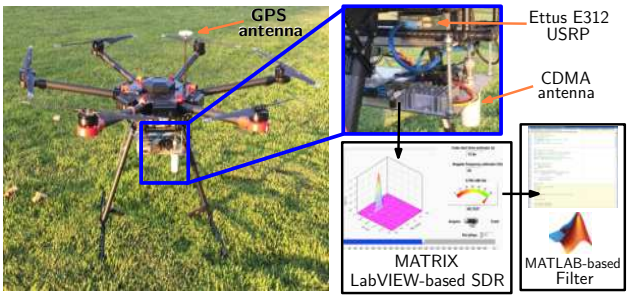

Figure 3.4: Experiment hardware setup.

The UAV traversed a commanded trajectory for 130 seconds. The "ground truth" traversed trajectory was obtained from the UAV's onboard integrated navigation system, which used a GPS, an inertial navigation system (INS), and other sensors. The UAV's trajectory was also estimated via the radio SLAM framework described in this chapter. The UAV's and cellular towers' heights were assumed to be known for the entire duration of the experiment; therefore, this is a two-dimensional radio SLAM problem which is consistent with the stochastic observability analysis conducted in Section 3.2. The EKF-based radio SLAM filter was initialized with a state estimate given by

$$\hat{\boldsymbol{x}}(0|0) = \left[\hat{\boldsymbol{x}}_r^{\mathsf{T}}(0|0), \hat{\boldsymbol{x}}_{s_1}^{\mathsf{T}}(0|0), \ldots, \hat{\boldsymbol{x}}_{s_4}^{\mathsf{T}}(0|0)\right]^{\mathsf{T}}$$

and a corresponding estimation error covariance

$$\mathbf{P}(0|0) = \operatorname{diag}\left[\mathbf{P}_r(0|0), \mathbf{P}_{s_1}(0|0), \ldots, \mathbf{P}_{s_4}(0|0)\right].$$

The UAV-mounted receiver's initial estimate $\hat{\boldsymbol{x}}_r(0|0)$ was set to the solution provided by

the UAV's onboard GPS-INS solution at the beginning of the trajectory, and was assumed to be perfectly known, i.e., $\mathbf{P}_r(0|0) \equiv \mathbf{0}_{6\times 6}$. The transmitters' initial state estimates were drawn according to $\hat{\boldsymbol{x}}_{s_m}(0|0) \sim \mathcal{N}\big(\big[\boldsymbol{r}_{s_m}^{\mathsf{T}}, \boldsymbol{x}_{\mathrm{clk},s_m}^{\mathsf{T}}(0)\big]^{\mathsf{T}}, \mathbf{P}_{s_m}(0|0)\big)$. The true transmitters' positions $\{\boldsymbol{r}_{s_m}\}_{m=1}^{4}$ were surveyed beforehand according to the framework described in [118] and verified using Google Earth. The initial clock bias and drift

$$\boldsymbol{x}_{\mathrm{clk},s_m}(0) = c\left[\delta t_{s_m}(0),\, \dot{\delta} t_{s_m}(0)\right]^{\mathsf{T}} \quad m = 1, \ldots, 4,$$

were solved for by using the initial set of cellular transmitter pseudoranges (3.1) according to

$$c\delta t_{s_m}(0) = \|\boldsymbol{r}_r(0) - \boldsymbol{r}_{s_m}\| + c\delta t_{r_1}(0) - z_{s_m}(0),$$

$$c\dot{\delta} t_s(0) = [c\delta t_s(1) - c\delta t_s(0)]/T,$$

where $c\delta t_{s_m}(1) = \|\boldsymbol{r}_r(1) - \boldsymbol{r}_{s_m}\| + c\delta t_{r_1}(1) - z_{s_m}(1)$. The initial uncertainty associated with the transmitters' states was set to $\mathbf{P}_{s_m}(0|0) \equiv 10^3 \cdot \mathrm{diag}\,[1, 1, 3, 0.3]$ for $m = 1, \ldots, 4$.

The process noise covariance of the receiver's clock $\mathbf{Q}_{\mathrm{clk},r}$ was set to correspond to a typical temperature-compensated crystal oscillator (TCXO) with $h_{0,r} = 9.4 \times 10^{-20}$ and $h_{-2,r} = 3.8 \times 10^{-21}$. The process noise covariances of the cellular transmitters' clocks were set to correspond to a typical oven-controlled crystal oscillator (OCXO) with $h_{0,s_m} = 8 \times 10^{-20}$ and $h_{-2,s_m} = 4 \times 10^{-23}$, which is usually the case for cellular transmitters [15, 114]. The UAV's position and velocity states were assumed to evolve according to velocity random walk dynamics with

$$\boldsymbol{f}_{\mathrm{pv}}[\boldsymbol{x}_{\mathrm{pv}}(k)] = \begin{bmatrix} \mathbf{I}_{2\times 2} & T\mathbf{I}_{2\times 2} \\ \mathbf{0}_{2\times 2} & \mathbf{I}_{2\times 2} \end{bmatrix} \boldsymbol{x}_{\mathrm{pv}}(k),$$

$$\mathbf{Q}_{\text{pv}} = \begin{bmatrix} \frac{T^3}{3}\mathbf{S}_{\text{pv}} & \frac{T^2}{2}\mathbf{S}_{\text{pv}} \\ \frac{T^2}{2}\mathbf{S}_{\text{pv}} & T\mathbf{S}_{\text{pv}} \end{bmatrix},$$

where $T = 0.0267$ s and $\mathbf{S}_{\text{pv}} = \text{diag}\,[0.02, 0.2]$ is the process noise power spectral density matrix, whose value was found empirically. The measurement noise variances $\{\sigma^2_{s_m}\}_{m=1}^4$ were computed beforehand according to the method described in [118], and were found to be $\sigma^2_{s_1} = 0.7$, $\sigma^2_{s_2} = 0.2$, $\sigma^2_{s_3} = 0.7$, and $\sigma^2_{s_4} = 0.1$. The trajectory produced by the UAV's onboard integrated GPS-INS and the one estimated by the radio SLAM framework are plotted in Fig. 3.5 along with the initial uncertainty ellipses of the 4 transmitters and the final east-north 99^{th}-percentile estimation uncertainty ellipses for tower 1. Similar reduction in the final uncertainty ellipses corresponding to the 3 other towers was noted.

The root mean squared error (RMSE) of the UAV's estimated trajectory was 9.5 meters and the final error was 7.9 meters. These errors were computed with respect to the GPS-INS trajectory. The resulting estimation errors and corresponding $\pm 2\sigma$ bounds of the vehicle's east and north position and the $\pm 2\sigma$ bounds of the clock bias of both the receiver and tower 1 are plotted in Fig. 3.6. Only the $\pm 2\sigma$ bounds are shown for the clock biases of both the receiver and tower 1, since the true biases are unknown; therefore, the estimation error trajectories cannot be plotted. Note that while the estimation error variances of the UAV's east and north position remained bounded, the estimation error variances of the receiver and tower 1 grew unboundedly, indicating their stochastic unobservability, which is consistent with the simulation results presented in Section 3.3 and Theorem 3.2.1.

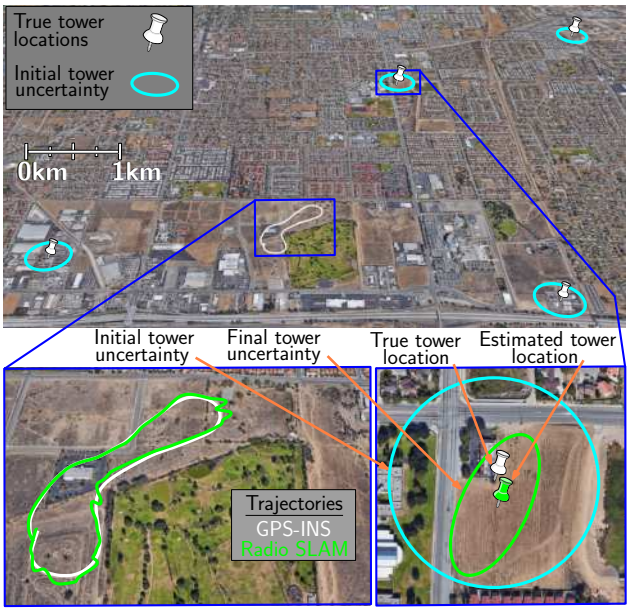

Figure 3.5: Environment layout and experimental results showing the estimated UAV trajectories from (i) its onboard GPS-INS integrated navigation system (white) and (ii) radio SLAM (green), the initial position uncertainty of each unknown tower, and tower 1 final position estimate and corresponding uncertainty ellipse. Image: Google Earth.

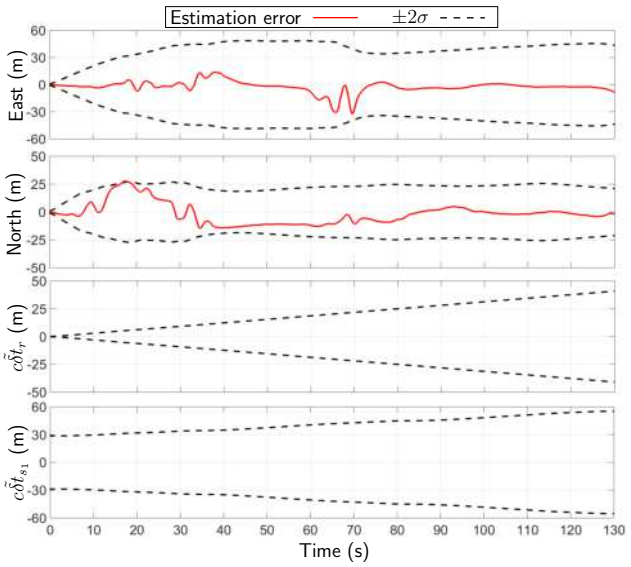

Figure 3.6: Radio SLAM experimental results: north and east errors of the UAV-mounted receiver and corresponding estimation error variances and the estimation error variances of the clock bias for both the receiver and transmitter 1.

Chapter 4

Tightly-Coupled SOP-Aided Inertial Navigation

This chapter expands on the radio SLAM problem by introducing a more complex dynamic model for the navigating vehicle. Specifically, an INS is employed and SOP pseudoranges are used to aid the INS in the absence of GNSS signals. This chapter is organized as follows. Section 4.1 provides a high-level description of the SOP-aided INS framework developed in this chapter. Section 4.2 overviews the main components of an aided INS. Section 4.3 describes the radio SLAM SOP-aided INS framework. Section 4.4 presents simulation results comparing the estimation performance of the SOP-aided INS using a consumer-grade IMU with a traditional GNSS-aided INS using a tactical-grade IMU. It also presents a performance sensitivity analysis of the SOP-aided INS framework over varying quantity and quality of exploited SOPs. Section 4.5 presents experimental results demonstrating a UAV navigating with cellular SOPs using the SOP-aided INS framework.

4.1 Problem Description

A high-level block diagram of the developed EKF-based radio SLAM framework to aid a navigating vehicle's INS with SOP pseudoranges is illustrated in Fig. 4.1(a). When GNSS signals are available, *both* GNSS and SOP receivers produce pseudoranges that are sent to an EKF update step to simultaneously aid the INS and estimate the unknown SOPs' states. When GNSS signals become unavailable, SOP pseudoranges are used *exclusively* to continue aiding the INS and refine the SOPs' state estimates. Fig. 4.1(b) is a conceptual illustration comparing the resulting position errors for a: traditional GNSS-aided INS (green), SOP-aided INS (blue), and unaided INS (red). Note that when GNSS signals are available, the SOP-aided INS is expected to produce lower position estimation errors compared to a traditional GNSS-aided INS. This is primarily due to a reduction in the vertical dilution of precision (VDOP) over using GNSS alone when terrestrial SOP pseudoranges, which have small elevation angles, are used with GNSS pseudoranges, which inherently have larger elevation angles [43]. In [24], experimental results show a UAV's position estimation uncertainty ellipsoid reduce by 84% compared to using Global Positioning System (GPS) pseudoranges alone when seven GPS satellites' and five SOPs' pseudoranges were used together to estimate the position of the UAV. When GNSS signals become unavailable, a bound can be established on the SOP-aided INS position errors, whereas the unaided INS errors expectedly diverge.

4.2 Overview of Aided Inertial Navigation

An aided inertial navigation system consists of three main components: (i) IMU, (ii) INS processor, and (iii) aiding sensors and corresponding fusion filter. This section overviews these components.

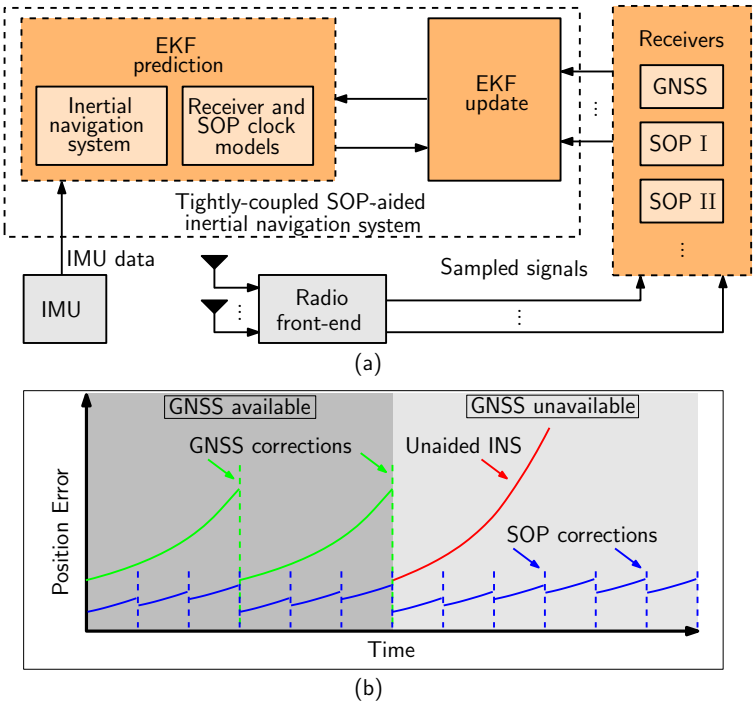

Figure 4.1: (a) A High-level diagram of an EKF-based tightly-coupled INS aided by GNSS (when available) and different SOP types, denoted SOP i, $i = \text{I, II, } \ldots$ (b) Conceptual illustration comparing the resulting position errors for a: traditional GNSS-aided INS (green), SOP-aided INS (blue), and unaided INS (red).

4.2.1 Inertial Measurement Unit

An IMU typically consist of a triad-gyroscope and triad-accelerometer, which produce rotation rate and specific force measurements, respectively, along three coordinate axes. These measurements are corrupted by noise as well as static and dynamic stochastic errors (e.g., biases, scale factors, cross-coupling, and cross-axis sensitivity). A DR-based navigation solution integrates these corrupted measurements over time, which causes the navigation solution to undesirable drift. Therefore, it is important to "clean up" these measurements, as much as possible, before they get integrated through an INS. The IMU's onboard processor removes factory-calibrated static errors; however, dynamic and stochastic error components (known as in-run errors), should be modeled and estimated online. It is within the discretion of the navigation filter designer to determine which errors should be modeled and estimated by considering the navigation system's processing power, IMU's quality, and maneuvers that

the IMU is expected to undertake. To avoid convoluting the forthcoming discussion, only random noise and the gyroscope's and accelerometer's biases are modeled. Additional details of IMU errors and methods to determine which states should be estimated are discussed in [5, 119, 120]. It is also important to mention that different INS architectures are used depending on the grade of the IMU. When navigation-grade IMUs are used, it is common that an aiding source, such is GPS, is used in order to constrain the INS error growth. In this case, INS errors are typically directly estimated. When lower quality IMUs are used, it is more common that the IMU is used to coast or interpolate between GPS updates, in which case absolute states are estimated. In this chapter, absolute states will be modeled, since lower quality IMUs are considered.

Noise-corrupted and bias-corrupted IMU measurements can be modeled in discrete-time as

$$ {}^{b}\boldsymbol{\omega}_{\text{imu}}(k) = {}^{b}\boldsymbol{\omega}_{i}(k) + \boldsymbol{b}_{\text{gyr}}(k) + \boldsymbol{n}_{\text{gyr}}(k), \;\; k = 1, 2, \ldots \tag{4.1} $$

$$ \begin{aligned} {}^{b}\mathbf{a}_{\text{imu}}(k) =& {}^{b}_{i}\mathbf{R}(k) \left[{}^{i}\mathbf{a}_{b}(k) - {}^{i}\boldsymbol{g}(k, {}^{i}\boldsymbol{r}_{b}(k)) \right] + \boldsymbol{b}_{\text{acc}}(k) \\ & + \boldsymbol{n}_{\text{acc}}(k), \end{aligned} \tag{4.2} $$

where ${}^{b}\boldsymbol{\omega}_{i} \in \mathbb{R}^3$ is the true rotation rate of a coordinate frame $\{b\}$ fixed to the body of the IMU with respect to an inertial frame $\{i\}$, such as the Earth-centered inertial (ECI) frame; $\boldsymbol{b}_{\text{gyr}} \in \mathbb{R}^3$ is the gyroscope's three-dimensional (3-D) bias; $\boldsymbol{n}_{\text{gyr}} \in \mathbb{R}^3$ is a measurement noise vector, which is modeled as a white noise sequence with covariance $\mathbf{Q}_{\boldsymbol{n}_{\text{gyr}}}$; ${}^{b}_{i}\mathbf{R} \in \mathbb{R}^{3\times3}$ is the rotation matrix, which rotates the coordinates of a vector expressed in frame $\{i\}$ into frame $\{b\}$; ${}^{i}\mathbf{a}_{b} \in \mathbb{R}^3$ is the true acceleration of $\{b\}$ expressed in $\{i\}$; ${}^{i}\boldsymbol{g} \in \mathbb{R}^3$ is the acceleration due to gravity in the inertial frame, which depends on the position of the IMU ${}^{i}\boldsymbol{r}_{b} \in \mathbb{R}^3$; $\boldsymbol{b}_{\text{acc}} \in \mathbb{R}^3$ is the accelerometer's 3-D bias; and $\boldsymbol{n}_{\text{acc}} \in \mathbb{R}^3$ is a measurement noise vector, which is modeled as a white noise sequence with covariance $\mathbf{Q}_{\boldsymbol{n}_{\text{acc}}}$. Fig. 4.2 illustrates the relationships of the

position and orientation of $\{b\}$ with respect to $\{i\}$ for an aerial vehicle-mounted IMU. The evolution of the gyroscope and accelerometer biases are modeled as random walks according to

$$\boldsymbol{b}_{\text{gyr}}(k+1) = \boldsymbol{b}_{\text{gyr}}(k) + \boldsymbol{w}_{\text{gyr}}(k), \tag{4.3}$$

$$\boldsymbol{b}_{\text{acc}}(k+1) = \boldsymbol{b}_{\text{acc}}(k) + \boldsymbol{w}_{\text{acc}}(k), \tag{4.4}$$

where $\boldsymbol{w}_{\text{gyr}}$ and $\boldsymbol{w}_{\text{acc}}$ are process noise vectors that drive the in-run bias variation (or bias instability) and are modeled as white noise sequences with covariance $\mathbf{Q}_{\boldsymbol{w}_{\text{gyr}}}$ and $\mathbf{Q}_{\boldsymbol{w}_{\text{acc}}}$, respectively. Note that other models may be used in place of (4.3) and (4.4), e.g., a common model is to use a Gauss-Markov process to model the slow varying bias, which is parameterized by a time constant and is driven by white noise [119, 120].The measurements (4.1) and (4.2) are sent to the INS to produce an orientation, velocity, and position solution, as discussed next.

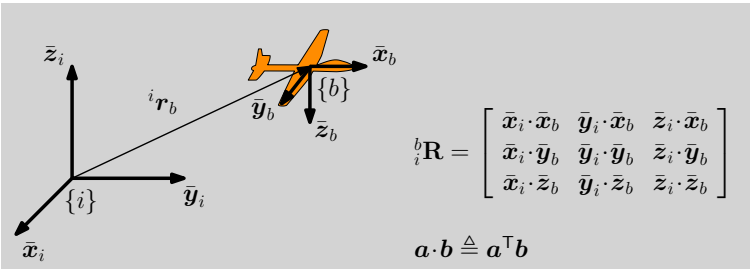

Figure 4.2: Position ${}^i\boldsymbol{r}_b$ of the origin of coordinate frame $\{b\}$ expressed in coordinate frame $\{i\}$. The rotation matrix ${}^b_i\mathbf{R}$ rotates the coordinates of a vector expressed in frame $\{i\}$ into frame $\{b\}$. The notation $\boldsymbol{a}\cdot\boldsymbol{b}$ denotes the inner product of vectors $\boldsymbol{a}$ and $\boldsymbol{b}$. The principal directions of $\{i\}$ and $\{b\}$ are represented by the unit vectors $\bar{\boldsymbol{x}}_i, \bar{\boldsymbol{y}}_i, \bar{\boldsymbol{z}}_i$ and $\bar{\boldsymbol{x}}_b, \bar{\boldsymbol{y}}_b, \bar{\boldsymbol{z}}_b$, respectively. Note that the describing frame leading superscript on these unit vectors has been omitted, since the frame used to describe these vectors is arbitrary when computing ${}^b_i\mathbf{R}$, as long as they are all described in the same frame.

4.2.2 Inertial Navigation System

There are two main INS architectures: stable platform (i.e., gimballed) and strapdown. On one hand, a stable platform INS uses a complex bulky physical structure to mechanically isolate the IMU's sensing axes from the rotational motion of the navigating vehicle. This isolation allows for direct extraction and integration of the IMU's acceleration measurements. On the other hand, a strapdown INS omits the complex bulky structure and instead uses a smaller size and lighter weight IMU, whose sensing axes are fixed to the navigating vehicle. The smaller size and lighter weight comes at the cost of additional computational complexity, which is used to resolve the IMU's sensing axes into an inertial frame before the acceleration measurements are integrated. With advances in computational power, most current navigation systems, especially those that require smaller and lighter weight sensors (e.g., small unmanned aerial vehicles (UAVs)), employ a strapdown architecture. For this reason, all subsequent equations and discussions pertain to a strapdown INS; however, the SOP-aided INS developed in this chapter can be readily applied to a stable platform architecture by replacing strapdown mechanization equations with stable platform ones.

An INS can be used as a standalone DR system or as part of an integrated navigation system, e.g., an EKF-based aided INS, as in Fig. 4.1(a). The role of the INS in the context of an EKF-based aided INS is to take the sequence of sampled IMU measurements (4.1) and (4.2), extract ${}^{b}\boldsymbol{\omega}_i$ and ${}^{i}\mathbf{a}_b$, and perform successive integrations to propagate an estimate of an IMU state vector between aiding measurement updates. It is common to directly estimate the orientation, position, and velocity of the IMU in an Earth-centered Earth-fixed (ECEF) frame $\{e\}$, since aiding sources (e.g., GPS satellites and SOP emitters) are typically represented in $\{e\}$. To this end, this chapter develops an EKF to estimate the IMU state vector $\boldsymbol{x}_{\text{imu}} \in \mathbb{R}^{16}$, given by

$$\boldsymbol{x}_{\text{imu}} = \left[{}^{b}_{e}\bar{\boldsymbol{q}}^{\mathsf{T}},\ {}^{e}\boldsymbol{r}_b^{\mathsf{T}},\ {}^{e}\dot{\boldsymbol{r}}_b^{\mathsf{T}},\ \boldsymbol{b}_{\text{gyr}}^{\mathsf{T}},\ \boldsymbol{b}_{\text{acc}}^{\mathsf{T}} \right]^{\mathsf{T}}, \tag{4.5}$$

where ${}^b_e\bar{\boldsymbol{q}} = \left[{}^b_e\boldsymbol{q}^{\mathsf{T}},\, {}^b_e q_4\right]^{\mathsf{T}} = \left[{}^b_e q_1,\, {}^b_e q_2,\, {}^b_e q_3,\, {}^b_e q_4\right]^{\mathsf{T}} \in \mathbb{R}^4$ is a four-dimensional (4-D) unit quaternion, representing the IMU's orientation (i.e., rotation from frame $\{e\}$ to $\{b\}$), and ${}^e\dot{\boldsymbol{r}}_b \in \mathbb{R}^3$ is the IMU's velocity. Out of several orientation representations, the unit quaternion is selected because it provides a minimal orientation state representation and avoids singularities that Euler angles are subject to. This quaternion is related to the rotation matrix ${}^b_e\mathbf{R}$ through,

$$ {}^b_e\mathbf{R} = \mathbf{I}_{3\times 3} - {}^b_e q_4 \lfloor {}^e_b\boldsymbol{q}\times \rfloor + 2\lfloor {}^e_b\boldsymbol{q}\times \rfloor^2, $$

where $\mathbf{I}_{3\times 3}$ denotes a 3×3 identity matrix and $\lfloor {}^e_b\boldsymbol{q}\times \rfloor$ is the skew-symmetric form of ${}^e_b\boldsymbol{q}$, which is given by

$$ \lfloor {}^e_b\boldsymbol{q}\times \rfloor = \begin{bmatrix} 0 & -{}^b_e q_3 & {}^b_e q_2 \\ {}^b_e q_3 & 0 & -{}^b_e q_1 \\ -{}^b_e q_2 & {}^b_e q_1 & 0 \end{bmatrix}. $$

A block diagram of the one-step EKF time update that propagates the estimate $\hat{\boldsymbol{x}}_{\text{imu}}(k|j)$ to $\hat{\boldsymbol{x}}_{\text{imu}}(k+1|j)$ is illustrated in Fig. 4.3, where $\hat{\boldsymbol{x}}_{\text{imu}}(k|j) \triangleq \mathbb{E}[\boldsymbol{x}_{\text{imu}}(k)|\boldsymbol{Z}^j]$, $\mathbb{E}[\,\cdot\,|\,\cdot\,]$ is the conditional expectation operator, $\boldsymbol{Z}^j \triangleq \{\boldsymbol{z}(i)\}_{i=1}^j$, $\boldsymbol{z}$ is a vector of INS-aiding measurements (e.g., from GNSS or SOPs), and $k \geq j$. GNSS aiding is discussed in the next subsection and SOP-aiding is discussed in the following section. The strapdown INS equations pertaining to each block are provided in Appendix A.5. Upon receiving an aiding measurement $z(k+1)$, the EKF performs a measurement update to produce $\boldsymbol{x}_{\text{imu}}(k+1|k+1)$, as discussed in the following subsection. If $z(k+1)$ is not available then $\boldsymbol{x}_{\text{imu}}(k+L-1|j)$ is recursively fed back to the INS to produce $\boldsymbol{x}_{\text{imu}}(k+L|j)$, where $L = 2, 3, \ldots$, until a measurement becomes available.

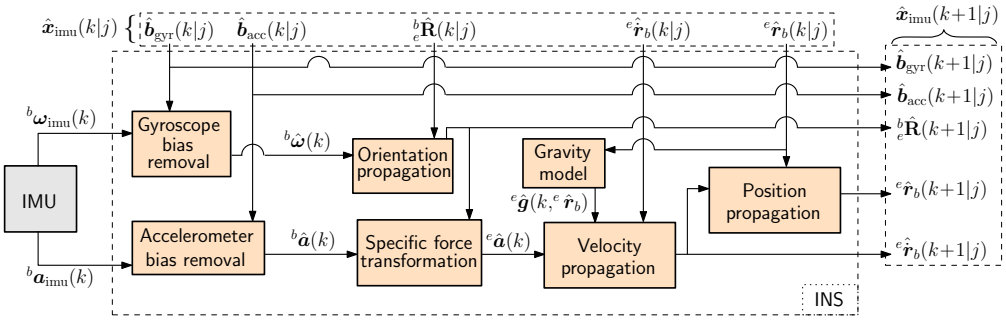

Figure 4.3: Block diagram of an INS within an EKF-based aided INS. The inputs to the INS are the current state estimate $\hat{\boldsymbol{x}}_{\text{imu}}(k|j)$ and IMU measurements ${}^{b}\boldsymbol{a}_{\text{imu}}(k)$ and ${}^{b}\boldsymbol{\omega}_{\text{imu}}(k)$. The output is the one-step time update $\hat{\boldsymbol{x}}_{\text{imu}}(k+1|j)$. The internal signals ${}^{b}\hat{\boldsymbol{\omega}}$, ${}^{e}\hat{\boldsymbol{a}}$, and ${}^{b}\hat{\boldsymbol{a}}$, are the bias-compensated rotation rate, bias-compensated transformed specific force, and bias-compensated untransformed specific force, respectively, which are computed according to (A.12), (A.14), and (A.15), respectively.

4.2.3 Traditional GNSS-Aided INS

A traditional EKF-based GNSS-aided INS couples the INS and GNSS through either: (i) loose coupling, which fuses the INS and GNSS position and velocity solutions; (ii) tight coupling, which fuses the INS solution with GNSS pseudoranges; or (iii) deep coupling, which uses the INS solution to aid the GNSS receiver's tracking-loops [121]. This dissertation considers tight coupling for four main reasons. First, in the event that less than four GNSS pseudoranges are available, tightly-coupled systems can still provide an EKF aiding update, which is not the case in a loosely-coupled system. Second, a tightly-coupled system can be implemented with most commercial off-the-shelf (COTS) components, which is not the case in a deeply coupled system, since internal GNSS tracking loops are typically required. Third, the filter will optimally deal with the geometry of the aiding measurements. Forth, the aiding source output does not have to be decimated in time in order to maintain statistical independence due to any internal filtering conducted by the aiding sensor.

To use GNSS pseudoranges in an EKF measurement update, the receiver's clock state vector $\boldsymbol{x}_{\text{clk},r} \triangleq \left[c\delta t_{\text{r}},\, c\dot{\delta} t_{\text{r}}\right]^{\mathsf{T}} \in \mathbb{R}^2$ must be estimated, where δt_{r} is the receiver's clock bias, $\dot{\delta} t_{\text{r}}$ is

the receiver's clock drift, and c is the speed of light. The clock dynamics is modeled as [122]

$$\boldsymbol{x}_{\text{clk,r}}(k+1) = \mathbf{F}_{\text{clk}}\boldsymbol{x}_{\text{clk,r}}(k) + \boldsymbol{w}_{\text{clk,r}}(k), \quad \mathbf{F}_{\text{clk}} = \begin{bmatrix} 1 & T \\ 0 & 1 \end{bmatrix}, \tag{4.6}$$

where T is the sampling interval and $\boldsymbol{w}_{\text{clk,r}}$ is the process noise, which is modeled as a discrete-time white noise sequence with covariance

$$\mathbf{Q}_{\text{clk,r}} = c^2 \cdot \begin{bmatrix} S_{\tilde{w}_{\delta t,\text{r}}} T + S_{\tilde{w}_{\dot{\delta} t,\text{r}}} \frac{T^3}{3} & S_{\tilde{w}_{\dot{\delta} t,\text{r}}} \frac{T^2}{2} \\ S_{\tilde{w}_{\dot{\delta} t,\text{r}}} \frac{T^2}{2} & S_{\tilde{w}_{\dot{\delta} t,\text{r}}} T \end{bmatrix}, \tag{4.7}$$

where $S_{\tilde{w}_{\delta t,\text{r}}}$ and $S_{\tilde{w}_{\dot{\delta} t,\text{r}}}$ are the power spectra of the continuous-time process noise $\tilde{\boldsymbol{w}}_{\text{clk,r}} \triangleq \left[\tilde{w}_{\delta t,\text{r}}, \tilde{w}_{\dot{\delta} t,\text{r}}\right]^{\mathsf{T}}$, respectively [74], which can be related to the power-law coefficients, $\{h_{\alpha,\text{r}}\}_{\alpha=-2}^{2}$, which have been shown through laboratory experiments to characterize the power spectral density of the fractional frequency deviation of an oscillator from nominal frequency according to $S_{\tilde{w}_{\delta t,\text{r}}} \approx \frac{h_{0,\text{r}}}{2}$ and $S_{\tilde{w}_{\dot{\delta} t,\text{r}}} \approx 2\pi^2 h_{-2,\text{r}}$. Augmenting $\boldsymbol{x}_{\text{clk,r}}$ with $\boldsymbol{x}_{\text{imu}}$ gives the GNSS-aided INS state vector $\boldsymbol{x}_{\text{gnss,ins}} \in \mathbb{R}^{18}$ that the EKF estimates, namely

$$\boldsymbol{x}_{\text{gnss,ins}} \triangleq \left[\, \boldsymbol{x}_{\text{imu}}^{\mathsf{T}},\, \boldsymbol{x}_{\text{clk},r}^{\mathsf{T}} \right]^{\mathsf{T}}. \tag{4.8}$$

The GNSS receiver makes pseudorange measurements $\{z'_{\text{gnss},n}\}_{n=1}^{N}$ at discrete-time instants to all N available GNSS satellites. After compensating for ionospheric and tropospheric delays $\{z'_{\text{gnss},n}\}_{n=1}^{N}$ is given by

$$\begin{aligned} z_{\text{gnss},n}(j) =& \|{}^{e}\boldsymbol{r}_b(j) - {}^{e}\boldsymbol{r}_{\text{gnss},n}(j)\|_2 \\ &+ c \cdot [\delta t_{\text{r}}(j) - \delta t_{\text{gnss},n}(j)] + v_{\text{gnss},n}(j), \end{aligned} \tag{4.9}$$

where $z_{\text{gnss},n} \triangleq z'_{\text{gnss},n} - c\delta t_{\text{iono},n} - c\delta t_{\text{tropo},n}$; $\delta t_{\text{iono},n}$ and $\delta t_{\text{tropo},n}$ are the ionospheric and

tropospheric delays, respectively; $z'_{\text{gnss},n}$ is the uncompensated pseudorange; ${}^{e}\boldsymbol{r}_{\text{gnss},n}$ is the position of the n^{th} GNSS satellite; $\delta t_{\text{gnss},n}$ is the clock bias of the n^{th} GNSS satellite; $v_{\text{gnss},n}$ is the measurement noise, which is modeled as a discrete-time zero-mean white Gaussian sequence with variance $\sigma^2_{\text{gnss},n}$; and $j \in \mathbb{N}$ represents the time index at which $\{z_{\text{gnss},n}\}_{n=1}^{N}$ is available, which could be aperiodic. These pseudoranges $\{z_{\text{gnss},n}\}_{n=1}^{N}$ are used to filter $\hat{\boldsymbol{x}}_{\text{gnss,ins}}$ through an EKF measurement update step to produce the updated estimate $\hat{\boldsymbol{x}}_{\text{gnss,ins}}(j|j)$. Note that, to simplify the forthcoming discussion, it is assumed that the number of GNSS satellites available is constant and that the ionospheric and tropospheric errors are perfectly accounted for. In practice, so-called "range bias" states may be added to the state vector $\hat{\boldsymbol{x}}_{\text{gnss,ins}}$. Such states serve two purposes. One is to estimate any residual atmospheric and multipath error for each pseudorange measurement. Second, and typically more importantly, when new or reacquired GNSS satellite measurements are added to the measurement vector, these states (along with a reset of the corresponding rows/columns of the prediction error covariance matrix) can be used to absorb the "jump" in $\hat{\boldsymbol{x}}_{\text{gnss,ins}}$ that would otherwise occur.

Whenever GNSS pseudoranges become unavailable, the INS continues to propagate in an open-loop fashion (i.e., performing only EKF time updates). This causes the position and velocity errors to grow unboundedly with time. This is largely due to integrating the estimation errors of $\boldsymbol{b}_{\text{gyr}}$ and $\boldsymbol{b}_{\text{acc}}$, denoted $\tilde{\boldsymbol{b}}_{\text{gyr}}$ and $\tilde{\boldsymbol{b}}_{\text{acc}}$, respectively. The time evolution of the velocity estimation error ${}^{e}\tilde{\dot{\boldsymbol{r}}}_b$ and position estimation error ${}^{e}\tilde{\boldsymbol{r}}_b$ after t seconds of open-loop propagation due to a constant 3-D accelerometer bias error $\tilde{\boldsymbol{b}}_{\text{acc}}$ are given by [119]

$$ {}^{e}\tilde{\dot{\boldsymbol{r}}}_b(t) \approx {}^{e}_{b}\mathbf{R}\tilde{\boldsymbol{b}}_{\text{acc}}t, \qquad {}^{e}\tilde{\boldsymbol{r}}_b(t) \approx \frac{1}{2}{}^{e}_{b}\mathbf{R}\tilde{\boldsymbol{b}}_{\text{acc}}t^2. $$

The increase of ${}^{e}\tilde{\dot{\boldsymbol{r}}}_b$ and ${}^{e}\tilde{\boldsymbol{r}}_b$ with time due to a constant gyroscope bias error $\tilde{\boldsymbol{b}}_{\text{gyr}}$ is even more significant– it is squared and cubic with time, respectively. This is caused by linearly increasing orientation errors with time due to integrating $\tilde{\boldsymbol{b}}_{\text{gyr}}$. Assuming the IMU moves at a constant velocity and is level with respect to the Earth's surface, the time evolution of ${}^{e}\tilde{\dot{\boldsymbol{r}}}_b$

and ${}^{e}\tilde{\boldsymbol{r}}_{b}$ are given by [119]

$$ {}^{e}\tilde{\dot{\boldsymbol{r}}}_{b}(t) \approx \frac{1}{2}{}^{e}_{b}\mathbf{R}\left[\tilde{\boldsymbol{b}}_{\text{gyr}}\times\right]{}^{l}\boldsymbol{g}t^{2}, \quad {}^{e}\tilde{\boldsymbol{r}}_{b}(t) \approx \frac{1}{6}{}^{e}_{b}\mathbf{R}\left[\tilde{\boldsymbol{b}}_{\text{gyr}}\times\right]{}^{l}\boldsymbol{g}t^{3}, $$

where ${}^{l}\boldsymbol{g} = [\,0,\,0,\,-\|{}^{e}\boldsymbol{g}\,\|_{2}]^{\mathsf{T}}$ is a local-level frame gravity vector. It is important to note that these relationships are approximate, since additional errors can integrate into the position and velocity due to gravity model approximations, timing errors, and orientation errors. Even if the biases are perfectly estimated before GNSS becomes unavailable, i.e., $\tilde{\boldsymbol{b}}_{\text{gyr}} = \mathbf{0}_{3\times1}$ and $\tilde{\boldsymbol{b}}_{\text{acc}} = \mathbf{0}_{3\times1}$, the integration of the white noise $\boldsymbol{n}_{\text{gyr}}$ and $\boldsymbol{n}_{\text{acc}}$ will cause the standard deviation of the position error in the i^{th} coordinate direction $\sigma\left({}^{e}\tilde{\boldsymbol{r}}_{b,i}\right)$ to grow according to

$$ \sigma\left({}^{e}\tilde{\boldsymbol{r}}_{b,i}\right) = \sqrt{\frac{1}{5}S_{\text{gyr}}t^{5}}, \quad \sigma\left({}^{e}\tilde{\boldsymbol{r}}_{b,i}\right) = \sqrt{\frac{1}{3}S_{\text{acc}}t^{3}}, \quad i = x, y, z, $$

respectively, where S_{gyr} and S_{acc} are the one-sided power spectral density (PSD) of $\boldsymbol{n}_{\text{gyr}}$ and $\boldsymbol{n}_{\text{acc}}$, respectively.

From the above relationships, it is obvious that without INS aiding corrections, the position errors and position error standard deviations grow unboundedly. The next section develops an SOP-aided INS framework, which uses pseudoranges drawn from unknown terrestrial SOPs to provide INS aiding corrections. The following sections demonstrate through simulations and an experiment that the SOP-aided INS reduces ${}^{e}\tilde{\boldsymbol{r}}_{b}$ compared to a traditional GNSS-aided INS while GNSS is available and bounds ${}^{e}\tilde{\boldsymbol{r}}_{b}$ when GNSS becomes unavailable.

4.3 SOP-Aided Inertial Navigation

The SOP-aided INS framework provides both accurate and robust navigation with and without GNSS signals by using pseudoranges drawn from ambient terrestrial SOPs to correct INS errors. This section formulates the SOP-aided INS, which operates in two modes:

- **Mapping mode:** GNSS pseudoranges are available. Here, GNSS and SOP pseudoranges are fused in the EKF to aid the INS, producing a more accurate estimate of $\boldsymbol{x}_{\text{gnss,ins}}$ while mapping the SOP radio environment (i.e., estimating the unknown states of the SOPs).

- **Radio SLAM mode:** GNSS pseudoranges are unavailable. Here, SOP pseudoranges aid the INS to simultaneously localize the vehicle-mounted INS (estimate $\boldsymbol{x}_{\text{imu}}$) while mapping the unknown states of the SOPs.

4.3.1 SOP Dynamics and Pseudorange Measurement Model

Each of the M SOPs will be assumed to emanate from a spatially-stationary terrestrial transmitter. The state vector of the m^{th} SOP $\boldsymbol{x}_{\text{sop},m}$ is defined as $\boldsymbol{x}_{\text{sop},m} \triangleq \left[{}^{e}\boldsymbol{r}_{\text{sop},m}^{\mathsf{T}},\, \boldsymbol{x}_{\text{clk,sop},m}^{\mathsf{T}}\right]^{\mathsf{T}} \in \mathbb{R}^5$, where ${}^{e}\boldsymbol{r}_{\text{sop},m} \in \mathbb{R}^3$ is its 3-D position state and $\boldsymbol{x}_{\text{clk,sop},m} \triangleq \left[c\delta t_{\text{sop},m},\, c\dot{\delta} t_{\text{sop},m}\right]^{\mathsf{T}} \in \mathbb{R}^2$ is its clock states, where $\delta t_{\text{sop},m}$ is the clock bias and $\dot{\delta} t_{\text{sop},m}$ is the clock drift. The SOP's discrete-time dynamics are modeled as

$$\boldsymbol{x}_{\text{sop},m}\,(k+1) = \mathbf{F}_{\text{sop}}\,\boldsymbol{x}_{\text{sop},m}(k) + \boldsymbol{w}_{\text{sop},m}(k), \quad k = 1, 2, \ldots, \tag{4.10}$$

$$\boldsymbol{x}_{\text{sop},m} = \left[{}^{e}\boldsymbol{r}_{\text{sop},m}^{\mathsf{T}},\, \boldsymbol{x}_{\text{clk,sop},m}^{\mathsf{T}}\right]^{\mathsf{T}}, \quad \mathbf{F}_{\text{sop}} = \text{diag}\left[\mathbf{I}_{3\times 3},\, \mathbf{F}_{\text{clk}}\right],$$

where $\boldsymbol{w}_{\text{sop},m}$ is the process noise, which is modeled as a discrete-time zero-mean white noise sequence with covariance $\mathbf{Q}_{\text{sop},m} = \text{diag}\left[\mathbf{0}_{3\times 3},\, \mathbf{Q}_{\text{clk,sop},m}\right]$, with $\mathbf{Q}_{\text{clk,sop},m}$ having identical structure to $\mathbf{Q}_{\text{clk,r}}$ in (4.7), except that $S_{\tilde{w}_{\delta t_{\text{r}}}}$ and $S_{\tilde{w}_{\dot{\delta} t_{\text{r}}}}$ are replaced with SOP clock-specific spectra $S_{\tilde{w}_{\delta t_{\text{sop},m}}}$ and $S_{\tilde{w}_{\dot{\delta} t_{\text{sop},m}}}$, respectively, where $S_{\tilde{w}_{\delta t_{\text{sop},m}}} \approx \frac{h_{0,\text{sop},m}}{2}$ and $S_{\tilde{w}_{\dot{\delta} t_{\text{sop},m}}} \approx 2\pi^2 h_{-2,\text{sop},m}$.

The pseudorange observation made by the vehicle-mounted receiver on the m^{th} SOP, after discretization and mild approximations discussed in [74], is related to the receiver's and

SOP's states by

$$z_{\text{sop},m}(j) = \|{}^{e}\boldsymbol{r}_b(j) - {}^{e}\boldsymbol{r}_{\text{sop},m}\|_2 + c \cdot [\delta t_r(j) - \delta t_{\text{sop},m}(j)] + v_{\text{sop},m}(j), \tag{4.11}$$

where $v_{\text{sop},m}$ is the measurement noise, which is modeled as a discrete-time zero-mean white Gaussian sequence with variance $\sigma^2_{\text{sop},m}$.

4.3.2 Framework Overview

The SOP-aided INS framework illustrated in Fig. 4.1 operates both with and without GNSS signals. To this end, the framework operates in one of two modes: (i) mapping mode when GNSS pseudoranges are available and (ii) radio SLAM mode when GNSS pseudoranges are unavailable. This subsection describes why special care must be taken when transitioning between GNSS-available and GNSS-unavailable modes and how the transition is performed.

In contrast to a traditional tightly-coupled GNSS-aided INS, the SOP-aided INS has the added complexity of having to deal with the unknown, dynamic, and stochastic states of SOPs. These states are estimated simultaneously with $\boldsymbol{x}_{\text{gnss,ins}}$, i.e., the EKF estimates the augmented state vector $\boldsymbol{x} \in \mathbb{R}^{18+5M}$, defined as

$$\boldsymbol{x} \triangleq \left[\, \boldsymbol{x}^{\mathsf{T}}_{\text{gnss,ins}},\, \boldsymbol{x}^{\mathsf{T}}_{\text{sop},1},\, \ldots,\, \boldsymbol{x}^{\mathsf{T}}_{\text{sop},M} \,\right]^{\mathsf{T}}. \tag{4.12}$$

Note that the EKF estimates absolute state values instead of state errors, which is another common approach when formulating an EKF for an INS [119]. While GNSS signals are available, $\boldsymbol{x}$ is estimated by the EKF in the mapping mode using the measurement set

$$\boldsymbol{z} = \left[\boldsymbol{z}^{\mathsf{T}}_{\text{gnss}},\, \boldsymbol{z}^{\mathsf{T}}_{\text{sop}}\right]^{\mathsf{T}}, \quad \boldsymbol{z}_{\text{gnss}} = \left[z_{\text{gnss},1}, \ldots,\, z_{\text{gnss},N}\right]^{\mathsf{T}},$$

$$\boldsymbol{z}_{\text{sop}} = \left[z_{\text{sop},1}, \ldots, z_{\text{sop},M}\right]^{\mathsf{T}}.$$

When GNSS signals become unavailable, the measurement set reduces to

$$\boldsymbol{z}' = \boldsymbol{z}_{\text{sop}}.$$

In [123], it was shown that $\boldsymbol{x}$ is stochastically unobservable during GNSS-unavailable modes; specifically, the EKF simultaneously estimating $\boldsymbol{x}_{\text{clk},r}$ and $\boldsymbol{x}_{\text{clk,sop},m}$ using $\boldsymbol{z}'$ produces unbounded clock error estimation uncertainties. For this reason, the SOP-aided INS framework transitions from the mapping mode to the radio SLAM mode, by modifying the state vector to resolve observability issues. The transition between the mapping and the radio SLAM modes is developed next to properly initialize the estimates, corresponding estimation uncertainties, and cross-correlations, so that a seamless transition takes place between GNSS-available and GNSS-unavailable modes.

To develop this transition, first note that during the radio SLAM mode, $\boldsymbol{z}_{\text{gnss}}$ is no longer available. Therefore, instead of estimating $\boldsymbol{x}_{\text{clk},r}$ and $\{\boldsymbol{x}_{\text{clk,sop},m}\}_{m=1}^{M}$ individually, the relative clock states between the receiver and each SOP, denoted $\boldsymbol{\Delta}\hat{\boldsymbol{x}}_{\text{clk},m} \triangleq \boldsymbol{x}_{\text{clk,r}} - \boldsymbol{x}_{\text{clk,sop},m}$, $m = 1, 2, \ldots, M$, will be estimated. As such, the state vector to be estimated is modified from (4.12) to become

$$\boldsymbol{x}' = \left[\boldsymbol{x}_{\text{imu}}^{\mathsf{T}}, \boldsymbol{x}'_{\text{sop},1}{}^{\mathsf{T}}, \ldots, \boldsymbol{x}'_{\text{sop},M}{}^{\mathsf{T}}\right]^{\mathsf{T}}, \tag{4.13}$$

where $\boldsymbol{x}'_{\text{sop},m} \triangleq \left[{}^{e}\boldsymbol{r}_{\text{sop},m}^{\mathsf{T}}, \boldsymbol{\Delta}\boldsymbol{x}_{\text{clk},m}^{\mathsf{T}}\right]^{\mathsf{T}}$, $m = 1, 2, \ldots, M$. At the moment of transition from GNSS-available to GNSS-unavailable, an estimate of the new state vector $\boldsymbol{x}'$ and the corresponding estimation error covariance $\mathbf{P}'$ are initialized from the latest produced estimate $\hat{\boldsymbol{x}}$ and its corresponding estimation error covariance $\mathbf{P}$ using

$$\hat{\boldsymbol{x}}' = \mathbf{T}\hat{\boldsymbol{x}}, \qquad \mathbf{P}' = \mathbf{M}\mathbf{P}\mathbf{M}^{\mathsf{T}},$$

$$\mathbf{T} = \begin{bmatrix} \mathbf{T}_{\text{gnss,ins}} & \mathbf{0}_{16\times5} & \cdots & \mathbf{0}_{16\times5} \\ \mathbf{T}_{\text{clk,r}} & \mathbf{T}_{\text{sop}} & \cdots & \mathbf{0}_{5\times5} \\ \vdots & \vdots & \ddots & \vdots \\ \mathbf{T}_{\text{clk,r}} & \mathbf{0}_{5\times5} & \cdots & \mathbf{T}_{\text{sop}} \end{bmatrix},$$

$$\mathbf{M} = \begin{bmatrix} \mathbf{M}_{\text{gnss,ins}} & \mathbf{0}_{15\times5} & \cdots & \mathbf{0}_{15\times5} \\ \mathbf{M}_{\text{clk,r}} & \mathbf{T}_{\text{sop}} & \cdots & \mathbf{0}_{5\times5} \\ \vdots & \vdots & \ddots & \vdots \\ \mathbf{M}_{\text{clk,r}} & \mathbf{0}_{5\times5} & \cdots & \mathbf{T}_{\text{sop}} \end{bmatrix},$$

$$\mathbf{T}_{\text{gnss,ins}} \triangleq \left[\mathbf{I}_{16\times16},\, \mathbf{0}_{16\times2}\right], \quad \mathbf{T}_{\text{clk,r}} \triangleq \begin{bmatrix} \mathbf{0}_{3\times16} & \mathbf{0}_{3\times2} \\ \mathbf{0}_{2\times16} & \mathbf{I}_{2\times2} \end{bmatrix},$$

$$\mathbf{T}_{\text{sop}} \triangleq \begin{bmatrix} \mathbf{0}_{3\times3} & \mathbf{0}_{3\times2} \\ \mathbf{0}_{2\times3} & -\mathbf{I}_{2\times2} \end{bmatrix},$$

$$\mathbf{M}_{\text{gnss,ins}} \triangleq \left[\mathbf{I}_{15\times15},\, \mathbf{0}_{15\times2}\right], \quad \mathbf{M}_{\text{clk,r}} \triangleq \begin{bmatrix} \mathbf{0}_{3\times15} & \mathbf{0}_{3\times2} \\ \mathbf{0}_{2\times15} & \mathbf{I}_{2\times2} \end{bmatrix}.$$

Notice that $\mathbf{P}$ and $\mathbf{P}'$ has one less dimension than $\hat{\boldsymbol{x}}$ and $\hat{\boldsymbol{x}}'$, respectively. This is due to the IMU's orientation estimation error being represented by a three-axis error angle vector, denoted $\tilde{\boldsymbol{\theta}} \in \mathbb{R}^3$, which has one less dimension than the estimate of ${}^{b}_{e}\bar{\boldsymbol{q}}$, denoted ${}^{b}_{e}\hat{\bar{\boldsymbol{q}}} \in \mathbb{R}^4$. The vector $\tilde{\boldsymbol{\theta}}$ is related to ${}^{b}_{e}\bar{\boldsymbol{q}}$, and ${}^{b}_{e}\hat{\bar{\boldsymbol{q}}}$ through

$${}^{b}_{e}\bar{\boldsymbol{q}} = {}^{b}_{e}\hat{\bar{\boldsymbol{q}}} \otimes \tilde{\bar{\boldsymbol{q}}}, \quad \tilde{\bar{\boldsymbol{q}}} = \left[\frac{1}{2}\tilde{\boldsymbol{\theta}}^{\mathsf{T}},\, \sqrt{1 - \frac{1}{4}\tilde{\boldsymbol{\theta}}^{\mathsf{T}}\tilde{\boldsymbol{\theta}}}\right]^{\mathsf{T}}, \tag{4.14}$$

where $\otimes$ denotes quaternion product. This error representation is common when estimating quaternions, since $\tilde{\bar{\boldsymbol{q}}}$ is an over-determined representation of the orientation error. Hence, the estimation error covariance associated with $\tilde{\bar{\boldsymbol{q}}}$ would be singular. To avoid singularity, the covariance associated with $\tilde{\boldsymbol{\theta}}$ is maintained instead.

To summarize, the two modes of operation are:

- **Mapping mode:** estimates $\boldsymbol{x}$ using the measurement set $\boldsymbol{z}$.
- **Radio SLAM mode:** estimates $\boldsymbol{x}'$ using the measurement set $\boldsymbol{z}'$.

The EKF time update and measurement update for each mode are provided next.

4.3.3 EKF Time Update

The time update should be adjusted according to the current operation mode to account for the state transformation from (4.12) to (4.13).

Time Update Equations for Mapping mode

During the mapping mode, the EKF produces the time update estimate of $\boldsymbol{x}(k+1)$, denoted $\hat{\boldsymbol{x}}(k+1|j) \triangleq \mathbb{E}[\boldsymbol{x}(k+1)|\{\boldsymbol{z}(i)\}_{i=1}^{j}]$, and an associated prediction error covariance $\mathbf{P}(k+1|j)$, where $k \geq j$, and j is the last time-step an INS-aiding source was available. The time update equations for each component of (4.12) are provided next. The time update of $\boldsymbol{x}_{\text{imu}}$ is produced using $\boldsymbol{z}_{\text{imu}}$ through the INS illustrated in Fig. 4.3. The discrete-time linearized equations to produce the one-step time update $\hat{\boldsymbol{x}}_{\text{imu}}$ are provided in Appendix A.5. The receiver's one-step clock state time update follows from (4.6) and is given by

$$\hat{\boldsymbol{x}}_{\text{clk,r}}(k+1|j) = \mathbf{F}_{\text{clk}}\hat{\boldsymbol{x}}_{\text{clk,r}}(k|j). \tag{4.15}$$

The SOPs' one-step state time update follows from (4.10) and is given by

$$\hat{\boldsymbol{x}}_{\text{sop},m}(k+1|j) = \mathbf{F}_{\text{sop}}\hat{\boldsymbol{x}}_{\text{sop},m}(k|j), \quad m = 1, \ldots, M. \tag{4.16}$$

Next, the one-step prediction error covariance is produced according to

$$\begin{aligned}
&\mathbf{P}(k+1|j) = \mathbf{F}(k)\mathbf{P}(k|j)\mathbf{F}^{\mathsf{T}}(k) + \mathbf{Q}(k), \qquad (4.17)\\
&\mathbf{F}(k) \triangleq \operatorname{diag}\left[\boldsymbol{\Phi}_{\text{imu}}(k+1,k),\, \mathbf{F}_{\text{clk}},\, \mathbf{F}_{\text{sop}},\, \ldots,\, \mathbf{F}_{\text{sop}}\right],\\
&\mathbf{Q}(k) \triangleq \operatorname{diag}\left[\mathbf{Q}_{\text{imu}}(k),\, \mathbf{Q}_{\text{clk},r},\, \mathbf{Q}_{\text{sop}},\, \ldots,\, \mathbf{Q}_{\text{sop}}\right],
\end{aligned}$$

where $\boldsymbol{\Phi}_{\text{imu}}$ and $\mathbf{Q}_{\text{imu}}$ are the discrete-time linearized INS state transition matrix and process noise covariance, respectively, which are provided in Appendix A.6.

Time Update Equations for Radio SLAM Mode

During the radio SLAM mode, the state time update has the same form as the mapping mode, except that (4.15) is omitted and the SOP state time update (4.16) is replaced with the SOP position and relative clock state time update, which is given by

$$\hat{\boldsymbol{x}}'_{\text{sop},m}(k+1|j) = \mathbf{F}_{\text{sop}}\hat{\boldsymbol{x}}'_{\text{sop},m}(k|j), \quad m = 1, \ldots, M.$$

The prediction error covariance $\mathbf{P}'(k+1|j)$ has the same form as (4.17), except that $\mathbf{F}$ is replaced with $\mathbf{F}' \triangleq \operatorname{diag}\left[\boldsymbol{\Phi}_{\text{imu}}, \mathbf{F}_{\text{sop}}, \ldots, \mathbf{F}_{\text{sop}}\right]$ and $\mathbf{Q}$ is replaced with $\mathbf{Q}' \triangleq \mathbf{M}\mathbf{Q}\mathbf{M}^{\mathsf{T}}$.

4.3.4 EKF Measurement Update

The measurement update should be adjusted according to the current operation mode to account for the change of measurement availability from $\boldsymbol{z}$ to $\boldsymbol{z}'$.

Measurement Update Equations for Mapping Mode

Assuming $\boldsymbol{z}(k+1)$ is available, the EKF measurement update step will produce $\hat{\boldsymbol{x}}(k+1|k+1)$. The standard EKF measurement update equations are slightly modified to map the 3-D orientation error correction to the 4-D quaternion state estimate. To avoid convoluting this section, the full set of EKF state measurement update equations to procude $\hat{\boldsymbol{x}}(k+1|k+1)$ are provided in Appendix A.7. Given a prediction error covariance $\mathbf{P}(k+1|j)$, the corresponding corrected error covariance is given by

$$\mathbf{P}(k+1|k+1) = \mathbf{P}(k+1|j) - \mathbf{K}(k+1)\mathbf{S}(k+1)\mathbf{K}^{\mathsf{T}}(k+1),$$

$$\mathbf{K}(k+1) \triangleq \mathbf{P}(k+1|j)\mathbf{H}^{\mathsf{T}}(k+1)\mathbf{S}^{-1}(k+1), \tag{4.18}$$

$$\mathbf{S}(k+1) \triangleq \mathbf{H}(k+1)\mathbf{P}(k+1)\mathbf{H}^{\mathsf{T}}(k+1) + \mathbf{R}(k+1), \tag{4.19}$$

where $\mathbf{H}$ is the measurement Jacobian and $\mathbf{R}$ is the measurement noise covariance of $\boldsymbol{z}$. In the mapping mode, i.e., $\boldsymbol{z} \triangleq \left[\boldsymbol{z}_{\text{gnss}}^{\mathsf{T}},\, \boldsymbol{z}_{\text{sop}}^{\mathsf{T}}\right]^{\mathsf{T}}$, the measurement Jacobian $\mathbf{H}$ is

$$\mathbf{H} = \left[\mathbf{H}_{\text{gnss}}^{\mathsf{T}},\, \mathbf{H}_{\text{sop}}^{\mathsf{T}}\right]^{\mathsf{T}},$$

$$\mathbf{H}_{\text{gnss}} = \begin{bmatrix} \mathbf{0}_{1\times 3} & \hat{\boldsymbol{l}}_{\text{gnss},1}^{\mathsf{T}} & \mathbf{0}_{1\times 9} & \boldsymbol{h}_{\text{clk}}^{\mathsf{T}} & \mathbf{0}_{1\times 5M} \\ \vdots & \vdots & \vdots & \vdots & \vdots \\ \mathbf{0}_{1\times 3} & \hat{\boldsymbol{l}}_{\text{gnss},N}^{\mathsf{T}} & \mathbf{0}_{1\times 9} & \boldsymbol{h}_{\text{clk}}^{\mathsf{T}} & \mathbf{0}_{1\times 5M} \end{bmatrix},$$

$$\mathbf{H}_{\text{sop}} = \begin{bmatrix} \mathbf{0}_{1\times 3} & \hat{\boldsymbol{l}}_{\text{sop},1}^{\mathsf{T}} & \mathbf{0}_{1\times 9} & \boldsymbol{h}_{\text{clk}}^{\mathsf{T}} & \hat{\boldsymbol{h}}_{\text{sop},1}^{\mathsf{T}} & \cdots & \mathbf{0} \\ \vdots & \vdots & \vdots & \vdots & \vdots & \ddots & \vdots \\ \mathbf{0}_{1\times 3} & \hat{\boldsymbol{l}}_{\text{sop},M}^{\mathsf{T}} & \mathbf{0}_{1\times 9} & \boldsymbol{h}_{\text{clk}}^{\mathsf{T}} & \mathbf{0} & \cdots & \hat{\boldsymbol{h}}_{\text{sop},M}^{\mathsf{T}} \end{bmatrix},$$

where $\hat{\boldsymbol{l}}_{\text{gnss},n} \triangleq \frac{{}^{e}\hat{\boldsymbol{r}}_b - {}^{e}\boldsymbol{r}_{\text{gnss},n}}{\|{}^{e}\hat{\boldsymbol{r}}_b - {}^{e}\boldsymbol{r}_{\text{gnss},n}\|}$, $\boldsymbol{h}_{\text{clk}} \triangleq [1,\, 0]^{\mathsf{T}}$, $\hat{\boldsymbol{l}}_{\text{sop},m} \triangleq \frac{{}^{e}\hat{\boldsymbol{r}}_b - {}^{e}\hat{\boldsymbol{r}}_{\text{sop},m}}{\|{}^{e}\hat{\boldsymbol{r}}_b - {}^{e}\hat{\boldsymbol{r}}_{\text{sop},m}\|}$, and $\boldsymbol{h}_{\text{sop},m} \triangleq \left[-\hat{\boldsymbol{l}}_{\text{sop},m}^{\mathsf{T}},\, -\boldsymbol{h}_{\text{clk}}^{\mathsf{T}}\right]^{\mathsf{T}}$.

Measurement Update Equations for Radio SLAM Mode

During the radio SLAM mode, the state and covariance update equations have the same form, except the measurement Jacobian is adjusted from $\mathbf{H}$ to $\mathbf{H}'$ to account for only SOP pseudoranges being available, i.e., $\boldsymbol{z}' = \boldsymbol{z}_{\text{sop}}$ and $\mathbf{R}$ is replaced with $\mathbf{R}'$, which is the measurement noise covariance of $\boldsymbol{z}'$. The adjusted measurement Jacobian is

$$\mathbf{H}' = \begin{bmatrix} \mathbf{0}_{1\times 3} & \hat{\boldsymbol{l}}_{\text{sop},1}^{\mathsf{T}} & \mathbf{0}_{1\times 9} & \boldsymbol{v}_{\text{sop},1}^{\mathsf{T}} & \cdots & \mathbf{0} \\ \vdots & \vdots & \vdots & \vdots & \ddots & \vdots \\ \mathbf{0}_{1\times 3} & \hat{\boldsymbol{l}}_{\text{sop},M}^{\mathsf{T}} & \mathbf{0}_{1\times 9} & \mathbf{0} & \cdots & \boldsymbol{v}_{\text{sop},M}^{\mathsf{T}} \end{bmatrix},$$

where $\boldsymbol{v}_{\text{sop},m} \triangleq \left[-\hat{\boldsymbol{l}}_{\text{sop},m}^{\mathsf{T}},\, \boldsymbol{h}_{\text{clk}}^{\mathsf{T}}\right]^{\mathsf{T}}$.

4.4 Simulation Study

This section presents simulation results demonstrating a UAV navigating via the tightly-coupled SOP-aided INS framework developed in Section 4.3. The SOP-aided INS is first compared against a traditional tightly-coupled GNSS-aided INS. Then, the performance of the SOP-aided INS is studied by varying the quantity and quality of exploited terrestrial SOPs.

4.4.1 Numerical Simulator Description

A numerical simulator was developed to generate:

- **"Ground truth" trajectory of the UAV:** The trajectory was generated using a six degrees of freedom (6DoF) kinematic model [119], which included a straight

segment with linear acceleration, a 5 degree pitching climb, a straight segment without acceleration, and four 60 degree banking turns, performed over a 200 second period. During the first 100 seconds of the trajectory, the UAV completes all maneuvers except for the last three banking turns, which are then completed during the remaining 100 seconds. This particular trajectory was chosen because it excites all 6DoF of the UAV, i.e., both horizontal and vertical directions and all three angles (roll, pitch, and yaw), allowing the SOP-aided INS to be studied under various maneuvers. The trajectory that the UAV traversed is illustrated in Fig. 4.4.

- **Gyroscope and accelerometer data:** This data was generated at 100 Hz according to (4.1) and (4.2), respectively, for a tactical-grade and a consumer-grade IMU. The random noise for each of the axes of the tactical-grade IMU was set to have a PSD of 10 deg $/\sqrt{\text{hr}}$ and 1000 $\mu\text{g}/\sqrt{\text{Hz}}$ for the gyroscope and accelerometer, respectively. The random noise for consumer-grade IMUs are typically stated in terms of total accumulated noise at the output of the sensor. Each axis of the consumer-grade IMU was set to have an accumulated noise of 0.3 deg /s and 2.5 mg for the gyroscope and accelerometer, respectively. The evolution of the biases were generated according to (4.3) and (4.4) using driving process noise with spectra set to $\mathbf{S}_{\boldsymbol{w}_{\text{gyr}}} \equiv 10^{-8} \cdot \mathbf{I}_{3\times 3}$ and $\mathbf{S}_{\boldsymbol{w}_{\text{acc}}} \equiv 10^{-8} \cdot \mathbf{I}_{3\times 3}$, respectively. These spectra are mapped online to the discrete-time noise covariances $\mathbf{Q}_{\boldsymbol{n}_{\text{gyr}}}$, $\mathbf{Q}_{\boldsymbol{n}_{\text{acc}}}$, $\mathbf{Q}_{\boldsymbol{w}_{\text{gyr}}}$, and $\mathbf{Q}_{\boldsymbol{w}_{\text{acc}}}$ through the equations provided in Appendix A.6.

- **GPS L1 C/A pseudoranges:** These pseudoranges were generated at 1 Hz according to (4.9), using satellite orbits produced from Receiver Independent Exchange (RINEX) files downloaded from a Continuously Operating Reference Station (CORS) server [124]. The GPS pseudorange measurement noise $\{v_{\text{gnss},n}(j)\}_{n=1}^{N}$ were set to be

independent with a measurement noise variance computed according to [125]

$$\sigma^2_{\text{gnss},n,j} = \frac{c^2 t_{\text{eml}} B_{\text{DLL}} T_c^2 \sigma_s^2}{2(C/N_0)_{n,j}} \left[1 + \frac{1}{T_{\text{CO}} (C/N_0)_{n,j}} \right], \tag{4.20}$$

where $t_{\text{eml}} \equiv 0.5$ chips is the early-minus-late correlator spacing, $B_{\text{DLL}} \equiv 0.05$ Hz is the delay lock loop (DLL) bandwidth, $T_c \equiv 1/(1.023 \times 10^6)$ s is the chip duration, $(C/N_0)_{n,j}$ (in Hz) is the time-varying received carrier-to-noise ratio, which was derived from the RINEX files, $\sigma_s \equiv 17$ is a scaling parameter to account for unmodeled errors, and $T_{CO} \equiv 10$ ms is the coherent integration time. Another common model often employed is the scaled C/N_0 - elevation model [126]. The receiver was set to be equipped with a typical temperature-compensated crystal oscillator (TCXO), with values specified in Table 4.1.

- **SOP pseudoranges:** These pseudoranges were generated at 5 Hz according to (4.11). The SOP pseudorange measurement noise $\{v_{\text{sop},m}(j)\}_{m=1}^{M}$ were set to be independent with a time-varying measurement noise variance which corresponds to code division multiple access (CDMA) signals, computed according to (4.20), except that $t_{\text{eml}} \equiv 1$, $\sigma^2_{\text{gnss},n,j}$ is replaced with $\sigma^2_{\text{sop},m,j}$, $T_c \equiv 1/(1.2288 \times 10^6)$, $\sigma_s \equiv 22$, $T_{CO} \equiv 1/37.5$ s, and the carrier-to-noise ratio $(C/N_0)_{n,j}$ is replaced with a time-varying log-distance path loss model [127]

$$\begin{aligned} (C/N_0)'_{m,j} &= P_0 - 10\gamma \cdot \log_{10}(d(j)/D_0), \\ (C/N_0)_{m,j} &= 10^{[(C/N_0)'_{m,j}/10]}, \end{aligned}$$

where $P_0 \equiv 56$ dB-Hz is a calibration carrier-to-noise ratio at a distance $D_0 \equiv 1400$ m, $d(j) \triangleq \|{}^e\boldsymbol{r}_b(j) - {}^e\boldsymbol{r}_{\text{sop},m}\|_2$, and $\gamma \equiv 2$ is the path loss exponent. The calibration values P_0 and D_0 are values commonly observed by the authors during experimental campaigns [25]. The SOP pseudorange measurement noise variance computation as-

sumes that the correlation function within the DLL is equivalent to GPS. This is a reasonable assumption for cellular CDMA signals when t_{eml} is between 0.8 and 1.25 chips. More sophisticated models are discussed in [128]. The SOP dynamics evolved according to (4.10). Each SOP was set to be equipped with a typical oven-controlled crystal oscillator (OCXO), with values specified in Table 4.1. The SOP transmitters' positions $\{{}^{e}\boldsymbol{r}_{\text{sop},m}\}_{m=1}^{4}$ were surveyed from cellular tower locations in downtown Los Angeles, California, USA.

4.4.2 Simulation Results: Tightly-coupled SOP-Aided INS vs. GNSS-Aided INS

To study the navigation performance of the tightly-coupled SOP-aided INS, it is compared against a tightly-coupled GNSS-aided INS during GNSS-available and GNSS-unavailable modes. The SOP-aided INS framework was assumed to be equipped with a consumer-grade IMU, while the GNSS-aided INS framework was assumed to be equipped with a tactical-grade IMU. For both frameworks, GPS pseudoranges were set to be available for $t \in [0, 100)$ seconds and unavailable for $t \in [100, 200]$ seconds. During the first 100 seconds, the inertial radio SLAM framework is in the mapping mode, which causes the estate estimates to begin to converge. This will be illustrated later in the results. The initial estimates (at $t = 0$ seconds) of the UAV's states were initialized with a random error drawn according to $\tilde{\boldsymbol{x}}_{\text{gnss,ins}}(0|0) \sim \mathcal{N}\left[\mathbf{0}_{17\times 1},\, \mathbf{P}_{\boldsymbol{x}_{\text{gnss,ins}}}(0|0)\right]$, where

$$\mathbf{P}_{\boldsymbol{x}_{\text{gnss,ins}}}(0|0) \triangleq \text{diag}\left[\mathbf{P}_{\boldsymbol{x}_{\text{imu}}}(0|0),\, \mathbf{P}_{\boldsymbol{x}_{\text{clk,r}}}(0|0)\right]$$

$$\mathbf{P}_{\boldsymbol{x}_{\text{imu}}}(0|0) \equiv \text{diag}\left[(10^{-2})\cdot\mathbf{I}_{3\times 3},\, 9\cdot\mathbf{I}_{3\times 3},\, \mathbf{I}_{3\times 3},\, (10^{-4})\cdot\mathbf{I}_{6\times 6}\right]$$

$$\mathbf{P}_{\boldsymbol{x}_{\text{clk,r}}}(0|0) \equiv \text{diag}\left[9,\, 1\right].$$

For the SOP-aided INS framework, the SOPs' state estimates were initialized according to $\hat{\boldsymbol{x}}_{\text{sop},m}(0|0) \sim \mathcal{N}\left[\boldsymbol{x}_{\text{sop},m}(0), \mathbf{P}_{\text{sop}}(0|0)\right]$, for $m = 1, \ldots, M$, with initial values $\boldsymbol{x}_{\text{sop},m}(0) \equiv \left[{}^{e}\boldsymbol{r}^{\mathsf{T}}_{\text{sop},m},\, 10^4, 10\right]^{\mathsf{T}}$, $\mathbf{P}_{\text{sop}}(0|0) \equiv (10^4) \cdot \text{diag}\left[\mathbf{I}_{3\times 3},\, 0.1,\, 0.01\right]$. Note that the estimate of the SOPs' states are initialized by drawing from a Gaussian distribution with a mean equal to the true states and a covariance to capture uncertainty. This initialization scheme is used in simulation to ensure consistent initial priors in the EKF. In practice, if the initial SOPs' states are completely unknown, then a small time-history of pseudoranges from the beginning of the run can be saved and processed through a batch filter to estimate these states. Then, the estimate and associated covariance of the batch filter can be used to initialize the EKF. As long as the vehicle is moving and has access to GPS, the position and clock states of the SOPs are observable [74, 123]. The simulated trajectory, SOP positions, the GPS cutoff location are illustrated in Fig. 4.4.

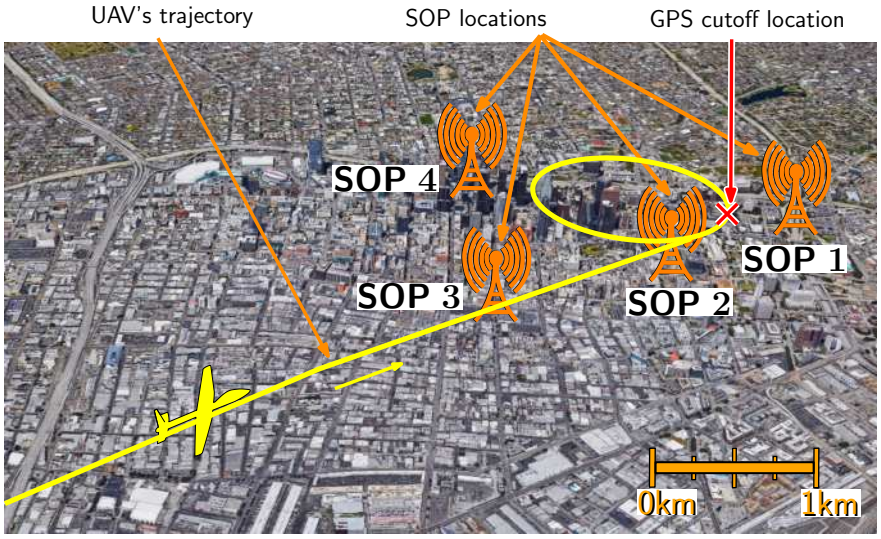

Figure 4.4: True trajectory the UAV traversed (yellow) and SOP locations (orange transmitters). The GPS cutoff location is marked with X.

Before the simulation results are presented, it is worth discussing the feasibility of the simulation scenario illustrated in Fig. 4.4. Notice that at some points during the UAV's trajectory, some of the SOPs are around 5 km from the UAV and have overlapping coverage areas with each other. In practice, towers typically transmit in all directions from three sets of antennas

that are spaced 120 degrees apart. Since SOP navigation receivers are not subscribers to the network (e.g., as a cell phone user is), the receiver is not limited to the artificial coverage areas that service provider user equipment impose to ensure that the device has optimal reception. A universal software radio peripheral (USRP) mounted to a vehicle can certainly sample and receive powerful signals from overlapping coverage areas, especially if they are flying in the air over the buildings. During several experiments conducted by the authors, powerful signals from more than 10 towers were simultaneously received, some of which were more than 6 km away from the receiver [129].

The resulting estimation error trajectories and corresponding ±three-standard deviation bounds ($\pm 3\sigma$) for the position of the UAV and SOP 1 are plotted in Fig. 4.5 and Fig. 4.6, respectively. The following may be concluded from Fig. 4.5 and Fig. 4.6. First, when GPS pseudoranges became unavailable at $t = 100$ seconds, the UAV's north, east, and down estimation error variance associated with the traditional GPS-aided INS begin to diverge unboundedly, as expected, whereas a bound can be established for the errors associated with the SOP-aided INS. Second, before GPS cutoff, the SOP-aided INS with a *consumer-grade* IMU yielded lower estimation error variances when compared to the traditional GPS-aided INS with a *tactical-grade* IMU; therefore, including SOP pseudoranges along with GPS pseudoranges to aid an INS may relax requirements on IMU quality. Third, the SOPs' north, east, and down estimation error variances suddenly reduce at approximately 65 seconds due to the UAV's left banking turn, causing a rapid change in the angle of the line-of-sight vector from the UAV to the SOP, which improves the estimability of the SOP's position. The uncertainty continues to reduce after GPS is cut off, indicating the SOPs' position states are stochastically observable in the radio SLAM mode. Fourth, the SOPs' position errors are consistent with the $\pm 3\sigma$ bounds, i.e., the produced error variances are correctly representing the estimation uncertainty. This can be seen visually in Fig. 4.7, which illustrates that the true position of SOP 1 is contained within the final 99^{th}–percentile uncertainty ellipsoid, which is centered at the final estimated position. Similar behavior was observed for SOPs 2, 3,

and 4 and after simulation runs using different realizations of process noise and measurement noise.

During these simulations it was assumed that pseudorange measurements from all four SOPs were available at 5 Hz, without interruption. If at any point in time pseudoranges become faulty from any of the SOPs, then the fault can be detected and the pseudoranges associated with that SOP should be temporarily excluded using a receiver autonomous integrity monitoring (RAIM) framework for SOPs [130]. The UAV's position errors and associated estimation uncertainty will increase when an SOP is excluded, since less measurements are available. The degradation in performance due to excluding a varying number of SOP's pseudoranges is studied in the next subsection.

The plots in Fig. 4.8(a)-(b) correspond to the estimation errors of the receiver's clock bias $c\delta t_{\mathrm{r}}$ and clock drift $c\dot{\delta}t_{\mathrm{r}}$, respectively, when GPS was available and the plots in Fig. 4.8(c)-(d) correspond to the estimation errors of SOP 1's clock bias $c\delta t_{\mathrm{sop},1}$ and clock drift $c\dot{\delta}t_{\mathrm{sop},1}$, respectively, while GPS was available. Fig. 4.8(e)-(f) correspond to the estimation errors of the relative bias $c\Delta\delta t_1$ and drift $c\Delta\dot{\delta}t_1$ between the UAV-mounted receiver and SOP 1 that were initialized when GPS pseudoranges became unavailable, as was described in Subsection 4.3.2. Note from Fig. 4.8(a)-(b) that including SOP pseudoranges along with GPS pseudoranges reduces the estimation uncertainty associated with $c\delta t_{\mathrm{r}}$ and $c\dot{\delta}t_{\mathrm{r}}$ compared to using GPS pseudoranges alone. Also note from Fig. 4.8(e)-(f), that the initialization scheme discussed in Subsection 4.3.2 produces consistent estimates of $c\Delta\delta t_1$ and drift $c\Delta\dot{\delta}t_1$ the moment GPS gets cut off and that these states are estimable during the GPS cut off period. Similar behavior has been observed through extensive experimental campaigns conducted by the authors [37,83,87]. In contrast, if $c\delta t_{\mathrm{r}}$, $c\dot{\delta}t_{\mathrm{r}}$ and $c\delta t_{\mathrm{sop},1}$, $c\dot{\delta}t_{\mathrm{sop},1}$ were estimated individually, their estimation errors would have diverged unboundedly [123].

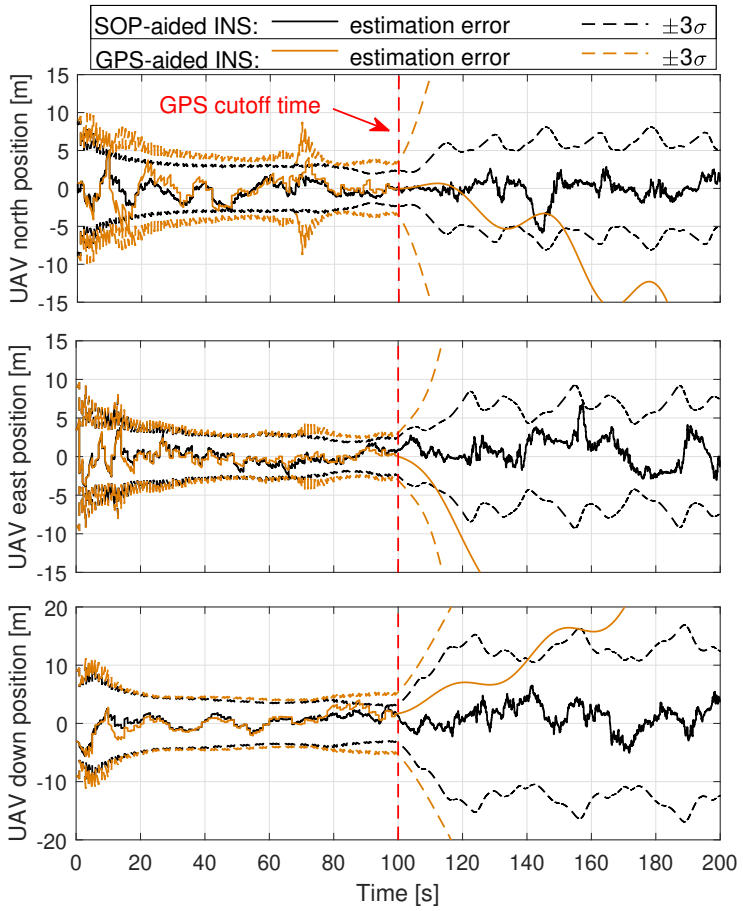

Figure 4.5: The resulting north, east, and down position errors for the UAV are illustrated for two frameworks. In both frameworks, the UAV had access to GPS pseudoranges for only the first 100 seconds while traversing the trajectory illustrated in Fig. 4.4, after which GPS pseudoranges were cut off. The GPS cutoff time is marked with a red dashed vertical line. The first framework used a tightly-coupled GPS-aided INS with a tactical-grade IMU (orange). In the second framework used an SOP-aided INS (black).

4.4.3 Performance Analysis

Several important factors affect the navigation performance when exploiting SOP pseudoranges to aid an INS. The main factors are: quantity of SOPs, quality of SOP-equipped oscillators, quality of receiver-equipped oscillator, receiver-to-SOP geometry, channel (e.g., line of sight conditions and multipath), and outliers due to unmodeled effects. In what follows, the performance sensitivity of the SOP-aided INS is studied by varying the quantity of SOPs and quality of their equipped oscillators using the environment illustrated in Fig. 4.4.

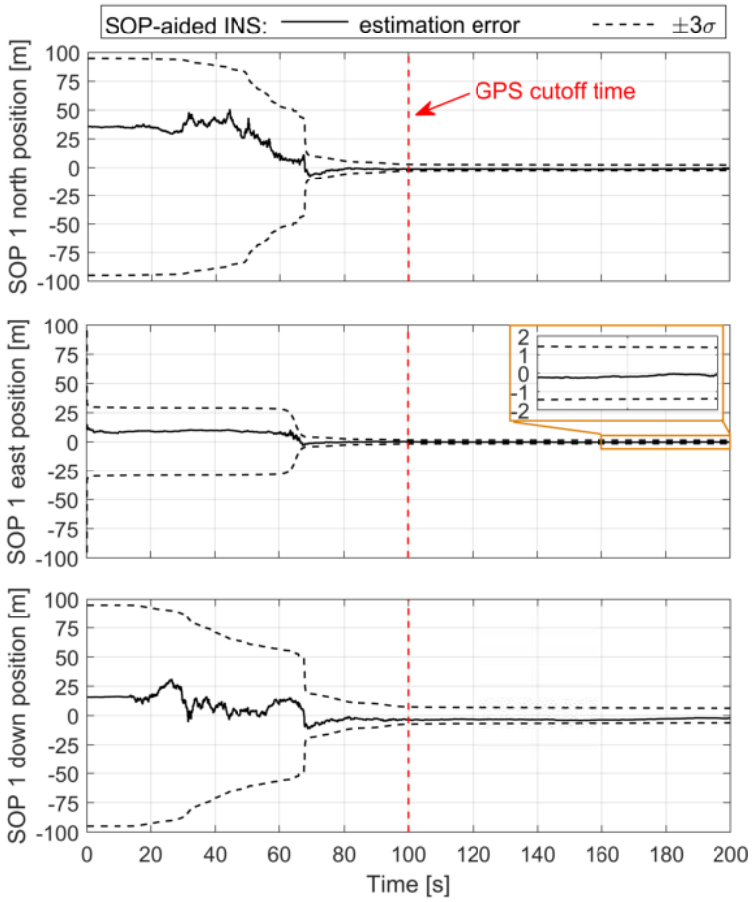

Figure 4.6: The resulting north, east, and down position errors and corresponding $\pm 3\sigma$ bounds (black) for SOP 1. The GPS cutoff time is marked with a red dashed vertical line.

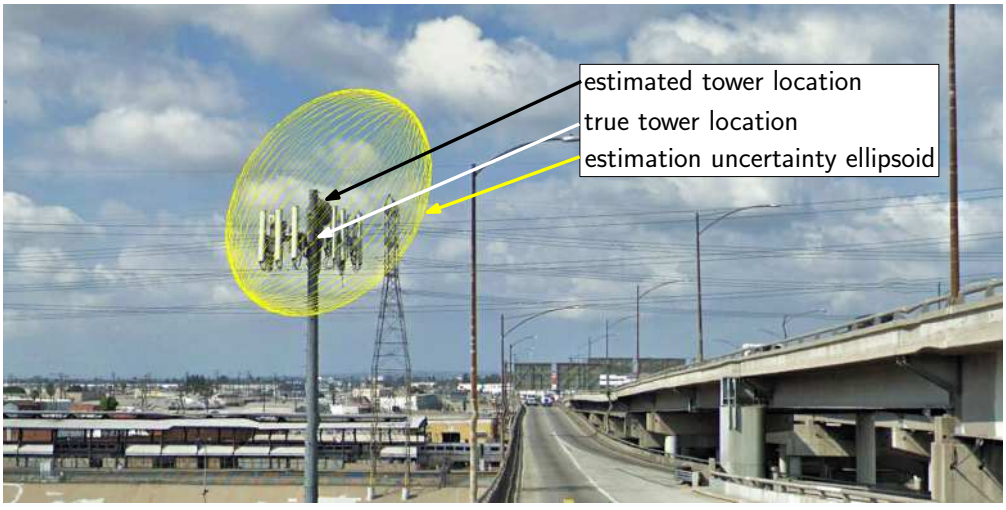

Figure 4.7: True position, final position estimate, and final 99^{th}–percentile uncertainty ellipsoid for SOP 1.

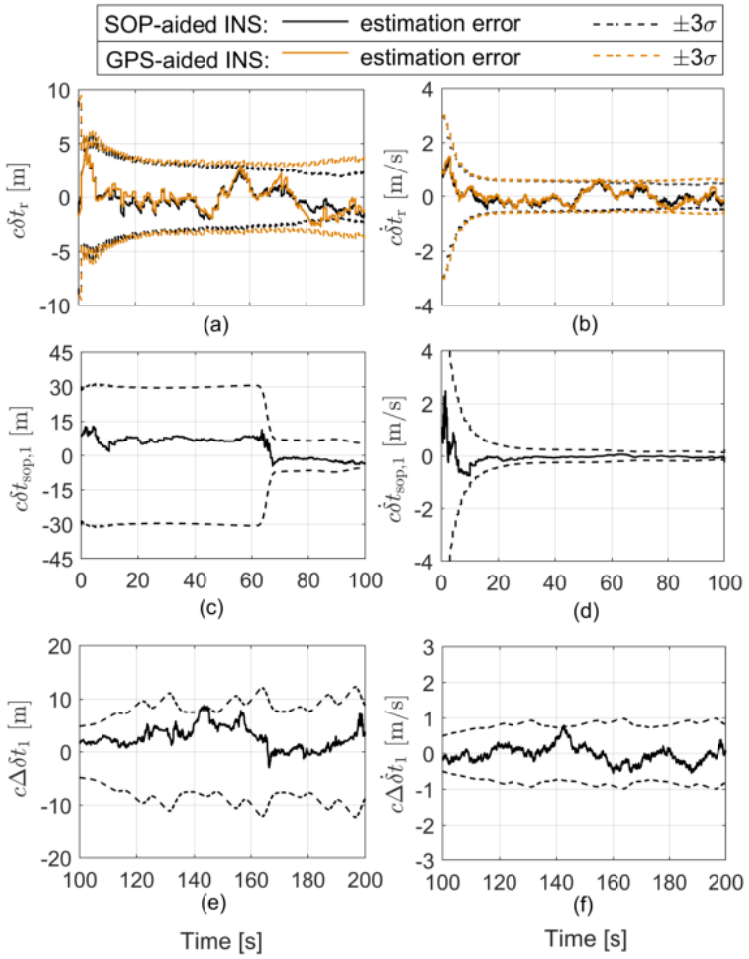

Figure 4.8: Estimation error trajectories and $\pm 3\sigma$ bounds for the clock states of the SOP-aided INS framework (black) and traditional GPS-aided INS (orange). (a) and (b) correspond to the receiver's clock bias $c\delta t_{\mathrm{r}}$ and clock drift $c\dot{\delta} t_{\mathrm{r}}$, respectively, while GPS was available and (c) and (d) correspond to SOP 1's clock bias $c\delta t_{\mathrm{sop},1}$ and clock drift $c\dot{\delta} t_{\mathrm{sop},1}$, respectively while GPS was available. (e) and (f) correspond to the relative bias $c\Delta\delta t_1$ and drift $c\Delta\dot{\delta} t_1$ between the UAV-mounted receiver and SOP 1 during the radio SLAM mode.

Varying Quantity of SOPs

To study the performance sensitivity of the SOP-aided INS framework for a varying number of SOPs, six separate simulation runs were conducted. The first four runs employed the SOP-aided INS with a consumer-grade IMU and $M = 1, \ldots, 4$ SOPs. The last two runs employed a traditional tightly-coupled GPS-INS and no SOPs ($M = 0$) with (i) a tactical-grade IMU and (ii) a consumer-grade IMU. Fig. 4.9 illustrates the resulting logarithm of

the determinant of the position estimation error covariance $\log\{\det[\mathbf{P}_{\boldsymbol{r}_b}(k|j)]\}$ for each run, which is related to the volume of the estimation uncertainty ellipsoid [54].

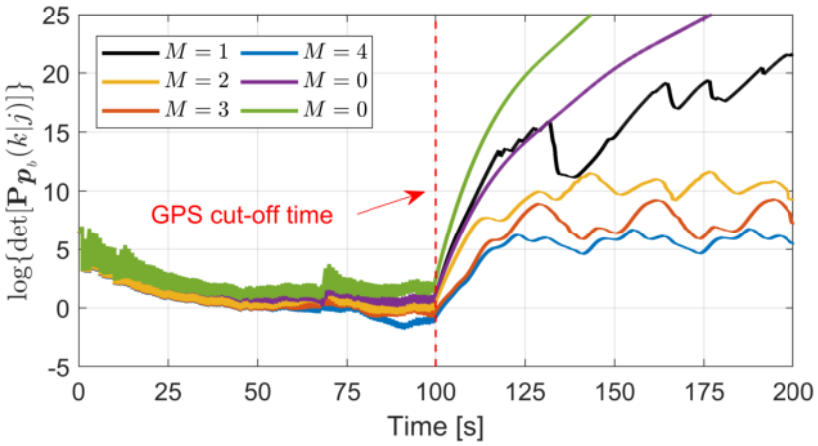

Figure 4.9: The logarithm of the determinant of the estimation error covariance of the UAV's position states $\log\{\det[\mathbf{P}_{\boldsymbol{r}_b}(k|j)]\}$. The two curves for $M = 0$ correspond to a tightly-coupled GPS-aided INS equipped with a tactical-grade IMU (purple) and consumer-grade IMU (green). The curves for $M = 1, 2, 3, 4$ correspond to the tightly-coupled SOP-aided INS with a consumer-grade IMU for a varying number of SOPs. The GPS cutoff time is marked with a red dashed vertical line.

The following may be concluded from Fig. 4.9. First, the estimation uncertainties produced by the SOP-aided INS are reduced when M is increased, and the sensitivity of the estimation uncertainty to varying M is captured by the distance between the $\log\{\det[\mathbf{P}_{\boldsymbol{r}_b}]\}$ trajectories. Second, although the SOP-aided INS used a *consumer-grade* IMU, the position estimation uncertainty for $M = 1, \ldots, 4$ was always lower than the position estimation uncertainty produced by a traditional tightly-coupled GPS-aided INS using a *tactical-grade* IMU. Third, the estimation uncertainties produced by the GPS-aided INS began to diverge unboundedly when GPS was cut off, whereas a bound may be specified for the uncertainties produced by the SOP-aided INS for $M = 1, \ldots, 4$.

Varying Quality of SOP Clocks

To study the performance sensitivity of the SOP-aided INS framework for a varying quality of SOP clocks, four simulation runs were conducted, where in each run all four SOPs were assumed to be equipped with the same clock quality: (i) worst TCXO, (ii) typical TCXO, (iii) typical OCXO, and (iv) best OCXO. In all runs, the UAV-mounted receiver was assumed to be equipped with a typical TCXO. The characterizing parameters of the four oscillator grades are tabulated in Table 4.1. The resulting 3σ bounds for exploiting four SOPs, which were assumed to all be equipped with a worst TCXO (black), typical TCXO (green), typical OCXO (blue), and best OCXO (purple), are plotted in Fig. 4.10. The four grades of oscillators considered and their characterizing parameters are tabulated in Table 4.1.

Table 4.1: Quality of SOP Clocks

Quality	**parameters** $\{\boldsymbol{h_{0,\mathrm{sop},m}}, \boldsymbol{h_{-2,\mathrm{sop},m}}\}$
Worst TCXO	$\{2.0 \times 10^{-19}, 2.0 \times 10^{-20}\}$
Typical TCXO	$\{9.4 \times 10^{-20}, 3.8 \times 10^{-21}\}$
Typical OCXO	$\{8.0 \times 10^{-20}, 4.0 \times 10^{-23}\}$
Best OCXO	$\{2.6 \times 10^{-22}, 4.0 \times 10^{-26}\}$

From Fig. 4.10 it may be concluded that while GPS was available, the sensitivity of the estimation performance to SOP clock quality was minimal. When GPS pseudoranges become unavailable, the estimation performance was significantly more sensitive to the SOP clock quality, and the sensitivity is captured by the distance between the 3σ trajectories. Although the uncertainty in the estimates were larger when SOPs were equipped with a worst TCXO, a bound may still be established.

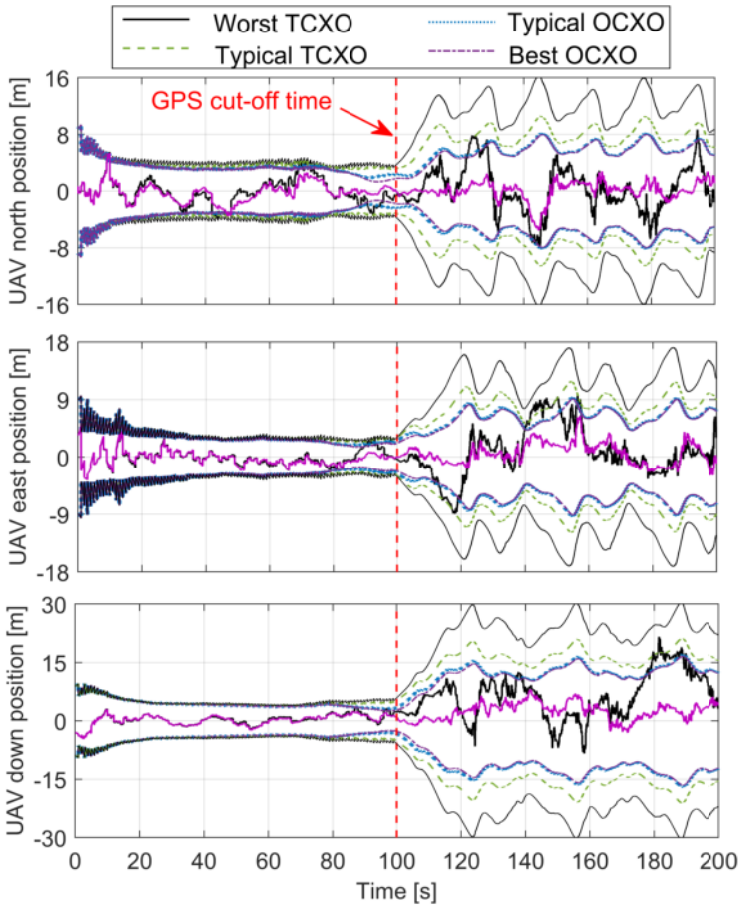

Figure 4.10: Estimation error trajectories and $\pm 3\sigma$ bounds for the UAV's north, east, and down position states with the tightly-coupled SOP-aided INS assuming all SOPs to be equipped with (i) worst TCXO (black), (ii) Typical TCXO (green), (iii) typical OCXO (blue), and (iv) best OCXO (purple). The GPS cutoff time is marked with a red dashed vertical line.

4.5 Experimental Demonstration

This section presents experimental results demonstrating a UAV navigating with the tightly-coupled SOP-aided INS framework using real IMU data, signals from three cellular SOP transmitters, and signals from 11 GPS satellites (when available). For a comparative analysis, results are also presented of the UAV navigating with a traditional tightly-coupled GPS-aided INS using the same IMU data and GPS signals. The following experiment was conducted by collecting data and then postprocessing the data in the lab. The experiment used an Autel Robotics UAV [131] equipped with:

- Tri-band (144/400/1200MHz) cellular omnidirectional antenna from Ettus Research [132].
- Consumer-grade L1 GPS active patch antenna from QGP Supply [133].
- Dual-channel USRP from Ettus Research [134], which was used to simultaneously downmix and sample cellular CDMA signals at 3.2 mega-samples per second (MSPS). Pseudoranges to three cellular SOPs were extracted from these samples at 5 Hz by processing them through the Multichannel Adaptive TRansceiver Information eXtractor (MATRIX) software-defined radio (SDR) [24,128], developed by the Autonomous Systems Perception, Intelligence, and Navigation (ASPIN) Laboratory at the University of California, Irvine.
- Proprietary consumer-grade IMU, developed by Autel Robotics. The Autel Robotics UAV allows access to raw IMU data, which were used for the time update at 100 Hz of the orientation, position, and velocity of the UAV as illustrated in Fig. 4.3. The IMU data is also coupled with altimeter and GPS data in the UAV's onboard navigation system to produce an integrated navigation solution. The UAV allows access to this navigation solution, which was used as the ground truth result with which the proposed tightly-coupled SOP-aided INS framework was compared.

Fig. 4.11 depicts the experimental software and hardware setup.

The UAV was commanded to traverse the trajectory plotted in Fig. 4.13(a), in which GPS was available for the first 50 seconds, then unavailable for the last 30 seconds. The SOP-aided INS framework was initialized with a state estimate given by

$$\hat{\boldsymbol{x}}(0|0) = \left[\hat{\boldsymbol{x}}_{\text{gnss,ins}}^{\mathsf{T}}(0|0), \hat{\boldsymbol{x}}_{\text{sop},1}^{\mathsf{T}}(0|0), \ldots, \hat{\boldsymbol{x}}_{\text{sop},3}^{\mathsf{T}}(0|0)\right]^{\mathsf{T}},$$

where the estimates of orientation ${}_{e}^{b}\hat{\boldsymbol{q}}(0|0)$, position ${}^{e}\hat{\boldsymbol{r}}_{b}(0|0)$, and velocity ${}^{e}\hat{\dot{\boldsymbol{r}}}_{b}(0|0)$ were set

to values parsed from the beginning of the UAV's navigation system log files, which were recorded during the trajectory, and the IMU biases $\hat{\boldsymbol{b}}_{\text{gyr}}$ and $\hat{\boldsymbol{b}}_{\text{acc}}$ were initialized by averaging 5 seconds of gravity-compensated IMU measurements while the vehicle was stationary and after the IMU had warmed up. The cellular SOP transmitters' initial state estimates were drawn according to $\hat{\boldsymbol{x}}_{\text{sop},m}(0|0) \sim \mathcal{N}\big(\big[{}^{e}\boldsymbol{r}_{\text{sop},m}^{\mathsf{T}}, \boldsymbol{x}_{\text{clk,sop},m}^{\mathsf{T}}(0)\big]^{\mathsf{T}}, \mathbf{P}_{\text{sop},m}(0|0)\big)$. The true transmitters' positions $\{{}^{e}\boldsymbol{r}_{\text{sop},m}\}_{m=1}^{3}$ were surveyed beforehand according to the framework described in [118] and verified using Google Earth. The initial clock bias and drift

$$\boldsymbol{x}_{\text{clk,sop},m}(0) = c\left[\delta t_{\text{sop},m}(0),\ \dot{\delta t}_{\text{sop},m}(0)\right]^{\mathsf{T}} \quad m = 1, \ldots, 3,$$

were solved for by using the initial set of cellular transmitter pseudoranges (4.11) according to

$$\begin{aligned} c\delta t_{\text{sop},m}(0) &= \|{}^{e}\boldsymbol{r}_{b}(0) - {}^{e}\boldsymbol{r}_{\text{sop},m}\| + c\delta t_{r}(0) - z_{\text{sop},m}(0), \\ c\dot{\delta t}_{\text{sop},m}(0) &= [\delta t_{\text{sop},m}(1) - \delta t_{\text{sop},m}(0)]/T, \end{aligned}$$

where $c\delta t_{\text{sop},m}(1) = \|{}^{e}\boldsymbol{r}_{b}(1) - {}^{e}\boldsymbol{r}_{\text{sop},m}\| + c\delta t_{r}(1) - z_{\text{sop},m}(1)$ and the receiver's clock bias $c\delta t_{r}(0)$ was provided by the GPS receiver while GPS was available.

The corresponding estimation error covariance was initialized according to

$$\begin{aligned} &\mathbf{P}(0|0) = \text{diag}\left[\mathbf{P}_{\text{gnss,ins}}(0|0), \mathbf{P}_{\text{sop},1}(0|0), \ldots, \mathbf{P}_{\text{sop},3}(0|0)\right], \\ &\mathbf{P}_{\boldsymbol{x}_{\text{gnss,ins}}}(0|0) \triangleq \text{diag}\left[\mathbf{P}_{\boldsymbol{x}_{\text{imu}}}(0|0),\ \mathbf{P}_{\boldsymbol{x}_{\text{clk,r}}}(0|0)\right] \\ &\mathbf{P}_{\boldsymbol{x}_{\text{imu}}}(0|0) \equiv \text{diag}\left[(10^{-1})\cdot\mathbf{I}_{3\times3},\ 9\cdot\mathbf{I}_{3\times3},\ \mathbf{I}_{3\times3},\ (10^{-4})\cdot\mathbf{I}_{6\times6}\right] \\ &\mathbf{P}_{\boldsymbol{x}_{\text{clk,r}}}(0|0) \equiv \text{diag}\left[0.1,\ 0.01\right] \\ &\mathbf{P}_{\text{sop},m}(0|0) \equiv 10^{4}\cdot\text{diag}\left[\mathbf{I}_{3\times3}, 0.3, 0.03\right], \quad m = 1, 2, 3. \end{aligned}$$

Signals may be acquired later in the run from SOPs that were not initialized in the EKF

while the receiver had access to GPS. Although this case is not considered in this experiment, it is worth mentioning here that a batch filter that uses pseudoranges collected over a short window of time may be used to initialize the estimates of the newly acquired SOP's in the absence of GPS [80]. To incorporate the uncertainty of the vehicle's position states, they may be added to the estimated vector and the INS-produced vehicle's position may be fed as measurements along with the SOP pseudoranges.

The process noise covariance of the receiver's clock $\mathbf{Q}_{\text{clk,r}}$ was set to correspond to a typical TCXO. The process noise covariances of the cellular transmitters' clocks were set to correspond to a typical OCXO, which is usually the case for cellular transmitters [15, 114]. The power spectral density matrices associated with the gyroscope and accelerometer noise were set to $\mathbf{S}_{\boldsymbol{n}_{\text{gyr}}} \equiv (7\times10^{-4})^2\cdot\mathbf{I}_{3\times3}$ and $\mathbf{S}_{\boldsymbol{n}_{\text{acc}}} \equiv (5\times10^{-4})^2\cdot\mathbf{I}_{3\times3}$, respectively. The power spectral density matrices associated with the gyroscope and accelerometer bias variations were set to $\mathbf{S}_{\boldsymbol{w}_{\text{gyr}}} \equiv (1\times10^{-4})^2\cdot\mathbf{I}_{3\times3}$ $\mathbf{S}_{\boldsymbol{w}_{\text{acc}}} \equiv (1\times10^{-4})^2\cdot\mathbf{I}_{3\times3}$, whose values were found empirically using raw IMU data. These spectra are mapped to the discrete-time noise covariances $\mathbf{Q}_{\boldsymbol{n}_{\text{gyr}}}$, $\mathbf{Q}_{\boldsymbol{n}_{\text{acc}}}$, $\mathbf{Q}_{\boldsymbol{w}_{\text{gyr}}}$, and $\mathbf{Q}_{\boldsymbol{w}_{\text{acc}}}$ online through the equations provided in Appendix A.6. The measurement noise variances $\{\sigma^2_{\text{sop},m}\}_{m=1}^3$ were computed according to (4.20), except that $\sigma^2_{\text{gnss},n,j}$ is replaced with $\sigma^2_{\text{sop},m,j}$, $T_c \equiv 1/(1.2288\times10^6)$, $\sigma_s \equiv 10$, $T_{CO} \equiv 1/37.5$ s, and the carrier-to-noise ratio C/N_0 produced by the MATRIX SDR for each SOP was used. The time history of C/N_0 for each SOP is illustrated in Fig. 4.12.

The UAV flew in the vicinity of three cellular SOPs with an initial uncertainty ellipsoid illustrated in Fig. 4.13(a). It can be seen in Fig. 4.13(b) that after the GPS cutoff point, the INS only solution (red) began to drift from the truth, resulting in a large final error. On the other hand, the tightly-coupled SOP-aided INS solution (green) prevented this drift by using the pseudoranges drawn from the three cellular SOPs, resulting in a significantly reduced final error. The north-east root mean squared error (RMSE) and final error for (i) GPS-aided INS framework after GPS cutoff (i.e., INS only) and (ii) SOP-aided INS framework

after GPS cutoff are summarized in Table. 4.2. The final estimated transmitter location and corresponding 95^{th}–percentile uncertainty ellipse for two of the SOP transmitters are shown in Fig. 4.13(c)-(d). The final localization errors for the three SOPs were 26.6, 19.6, and 59.1 m, respectively.

Note the following two points from these results. First, the final error of the UAV's position is smaller than the SOPs' position errors. Since the SOP-aided INS is EKF-based and the UAV has *a prior* knowledge of its state, the UAV's final position error can be smaller than the aiding sources' final position errors. The UAV's position error and uncertainty may grow in this time-window and the growth rate is dependent on IMU quality, the uncertainty in the SOPs' positions and clock states, and measurement quality. However, the pseudorange measurements from the SOPs are still significantly decreasing the error and uncertainty growth rate compared to an INS alone. Second, the relatively large estimation error of the third SOP is mostly attributed to a lower carrier-to-noise ratio compared to the other SOPs, which results in a higher measurement noise variance. Also, there were a small number of outliers in the pseudorange measurements that were not removed. To further enhance performance, these outliers may be detected and the SOP responsible for the outliers may be temporarily excluded using a RAIM approach for SOPs [130]. Despite not removing the small number of outlier pseudorange measurements, the final position error was smaller than the initial uncertainty and the position estimate was captured within the final estimation uncertainty ellipse.

Table 4.2: Experimental Estimation Errors after GPS cutoff

Estimation framework	**RMSE [m]**	**Final error [m]**
INS only	18.94	57.30
SOP-aided INS	5.84	9.59

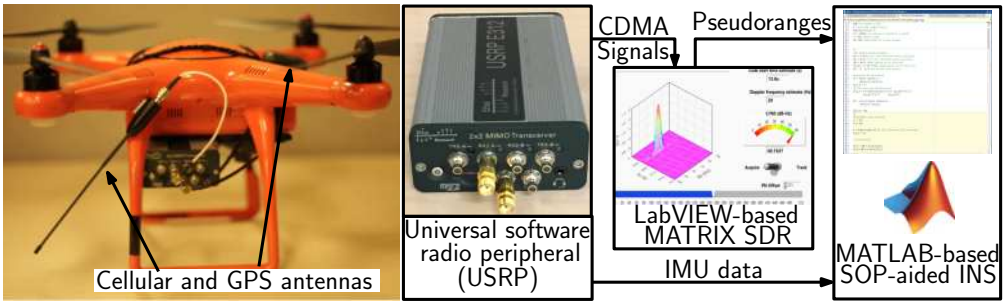

Figure 4.11: Experiment software and hardware setup.

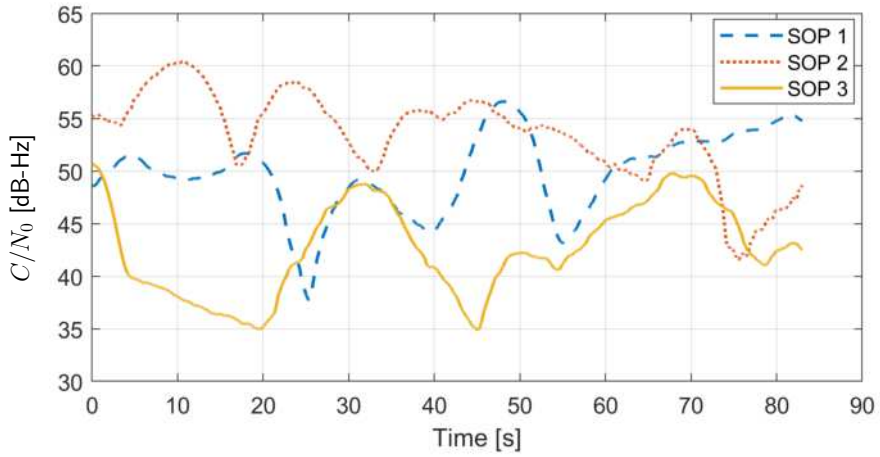

Figure 4.12: Time history of C/N_0 for SOP 1,2, and 3, produced by the MATRIX SDR.

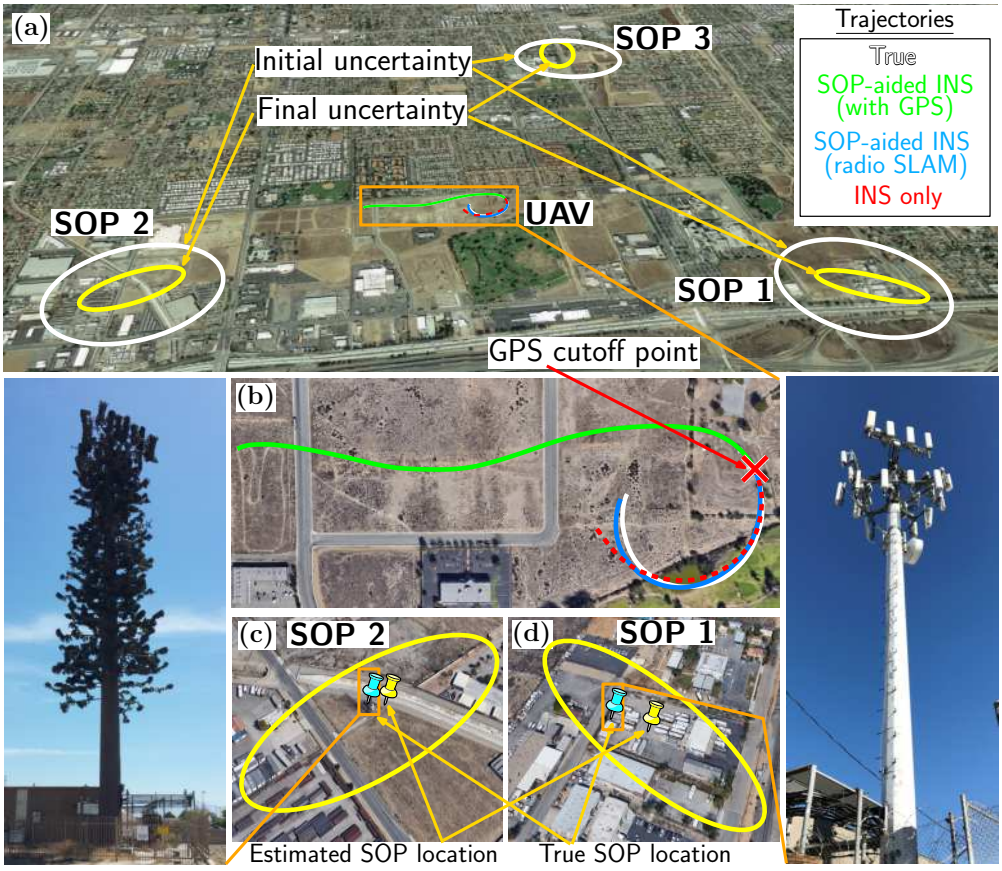

Figure 4.13: (a) Experimental environment showing the UAV's trajectory, cellular SOPs' locations, initial SOPs' position uncertainties, and final position uncertainties. (b) UAV's trajectory before and after GPS cutoff: (i) white: ground truth, (ii) green: SOP-aided INS before GPS cutoff, (iii) blue: SOP-aided INS after GPS cutoff, and (iv) red: GPS aided INS after GPS cutoff, i.e., INS only. (c) and (d) True and estimated SOP locations and corresponding final uncertainty ellipses.

Chapter 5

Information Fusion and Communication Strategies for Collaborative SOP-Aided Inertial Navigation

This chapter expands the radio SLAM concept that was used for SOP-aided INS developed and studied in the previous chapter by introducing collaboration and deals with the inherent burdens of communication between collaborators. Specifically, information and communication strategies are presented and studied for collaborating vehicles aiding their INSs with shared INS data and SOP pseudoranges. This chapter is organized as follows. Section 5.1 provides a high-level description of the communication and information fusion strategies that this chapter studies. Section 5.2 introduces new notation for the dynamics model of the SOPs and navigating vehicles as well as the receivers' measurement model. Section 5.3 describes the EKF-based CoRSLAM framework, an efficient method to communicate INS and SOP information between collaborators, and the TOA and TDOA information fusion

strategies. Section 5.4 compares the estimation performance of each fusion strategy. Section 5.7 develops an event-based communication scheme.

5.1 Problem Description

A high-level block diagram of the developed inertial CoRSLAM framework that enables a team of navigating vehicles to share INS data, GNSS pseudoranges, and SOP observables is illustrated in Fig. 5.1(a). During the time between measurement epochs, each vehicle uses its IMU data and clock models to perform an EKF time update and then packages INS information into $\mathbf{\Lambda}_n$ to share it with the other navigating vehicles. At each measurement epoch, receivers equipped on each vehicle produce pseudoranges to GNSS satellites (when GNSS signals are available) and observables to SOP emitters. This information is then sent to a local EKF measurement update step and is packaged into $\mathbf{\Lambda}_n$ along with the INS information. This chapter answers three questions regarding how the INS, GNSS, and SOP information should be shared between the navigating vehicles and fused in their navigation filters: 1) how should SOP observables be fused: (i) TOA or (ii) TDOA? 2) What INS information should be packed into $\mathbf{\Lambda}_n$ and communicated, so that consistent vehicle position estimates are produced while maintaining minimal communicated data? 3) When should $\mathbf{\Lambda}_n$ be transmitted: at a fixed-rate, i.e., at each measurement epoch, or using an event-based scheme, which closes τ only if a user-specified position estimation error constraint would be violated if τ remains open?

5.2 Model Description

In this section, the dynamics model of the SOP transmitters and the vehicles' states as well as the measurement models are provided. These models are used in the subsequent sections for

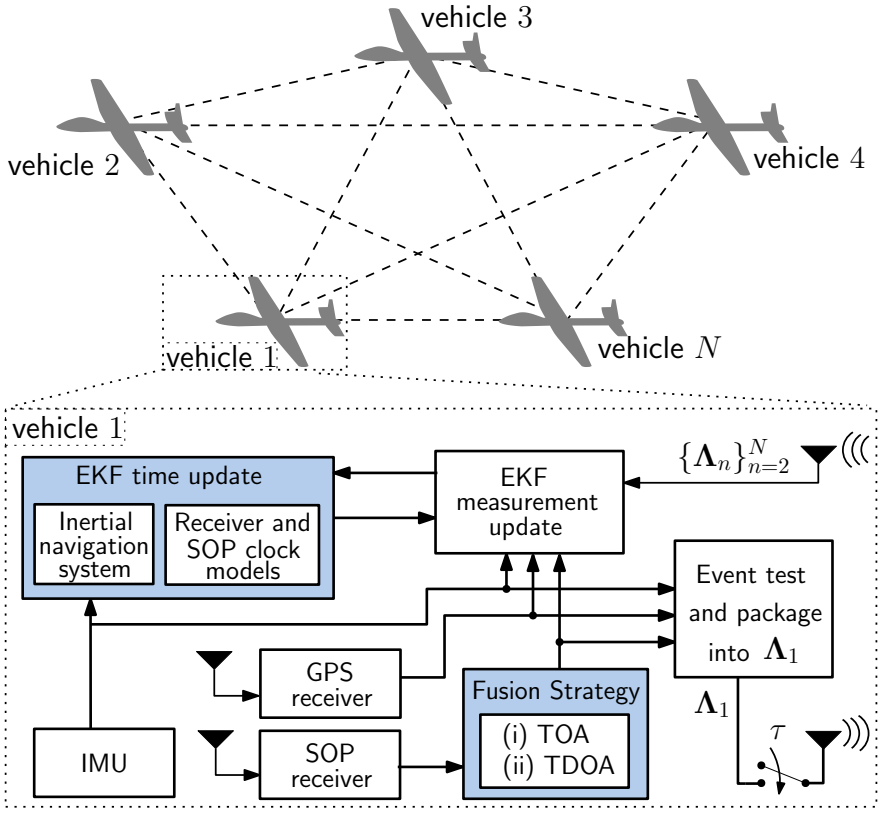

Figure 5.1: (a) A High-level diagram of an EKF-based collaborative INS aided by GNSS (when available) and SOP pseudoranges. The SOP pseudoranges are fused as either: (i) TOA or (ii) TDOA. This fusion takes place by packaging information into $\{\mathbf{\Lambda}_n\}_{n=1}^N$ and broadcasting them: (i) during every measurement epoch (i.e., at a fixed rate) or (ii) using an event-based strategy, which employs a mechanism to close τ only when needed.

the development of the EKF-based inertial CoRSLAM framework. New notation is defined in this chapter to deal with multiple navigating vehicles.

5.2.1 SOP Dynamics Model

Each SOP will be assumed to emanate from a spatially-stationary terrestrial transmitter, and its state vector will consist of its position states $\boldsymbol{r}_{\text{sop},m} \triangleq [x_{\text{sop},m},\, y_{\text{sop},m},\, z_{\text{sop},m}]^{\mathsf{T}} \in \mathbb{R}^3$ and clock error states $\boldsymbol{x}_{\text{clk,sop},m} \triangleq [c\delta t_{\text{sop},m},\, c\dot{\delta} t_{\text{sop},m}]^{\mathsf{T}} \in \mathbb{R}^2$, where c is the speed of light, $\delta t_{\text{sop},m}$ is the clock bias, $\dot{\delta} t_{\text{sop},m}$ is the clock drift, $m = 1, \ldots, M$, and M is the total number of SOPs.

The SOP's discretized dynamics are given by

$$\boldsymbol{x}_{\text{sop},m}\,(k{+}1) = \mathbf{F}_{\text{sop}}\,\boldsymbol{x}_{\text{sop},m}(k) + \boldsymbol{w}_{\text{sop},m}(k), \quad k = 1, 2, \ldots,$$

$$\mathbf{F}_{\text{sop}} = \begin{bmatrix} \mathbf{I}_{3\times 3} & \mathbf{0}_{3\times 2} \\ \mathbf{0}_{2\times 3} & \mathbf{F}_{\text{clk}} \end{bmatrix}, \qquad \mathbf{F}_{\text{clk}} = \begin{bmatrix} 1 & T \\ 0 & 1 \end{bmatrix}, \tag{5.1}$$

where T is the constant sampling interval, $\boldsymbol{x}_{\text{sop},m} = \left[\boldsymbol{r}^{\mathsf{T}}_{\text{sop},m},\, \boldsymbol{x}^{\mathsf{T}}_{\text{clk,sop},m}\right]^{\mathsf{T}} \in \mathbb{R}^5$, $\boldsymbol{w}_{\text{sop},m} \in \mathbb{R}^5$ is the process noise, which is modeled as a discrete-time zero-mean white noise sequence with covariance $\mathbf{Q}_{\text{sop},m} = \text{diag}\left[\mathbf{0}_{3\times 3},\, c^2\mathbf{Q}_{\text{clk,sop},m}\right]$, and

$$\mathbf{Q}_{\text{clk,sop},m} = \begin{bmatrix} S_{w_{\delta t_{\text{sop},m}}} T + S_{w_{\dot{\delta} t_{\text{sop},m}}} \frac{T^3}{3} & S_{w_{\dot{\delta} t_{\text{sop},m}}} \frac{T^2}{2} \\ S_{w_{\dot{\delta} t_{\text{sop},m}}} \frac{T^2}{2} & S_{w_{\dot{\delta} t_{\text{sop},m}}} T \end{bmatrix}.$$

The terms $S_{w_{\delta t_{\text{sop},m}}}$ and $S_{w_{\dot{\delta} t_{\text{sop},m}}}$ are the clock bias and drift process noise power spectra, respectively.

5.2.2 Vehicle Dynamics Model

The n^{th} navigating vehicle's state vector is $\boldsymbol{x}_{\text{r},n} = \left[\,\boldsymbol{x}^{\mathsf{T}}_{\text{ins},n},\, \boldsymbol{x}^{\mathsf{T}}_{\text{clk,r},n}\right]^{\mathsf{T}} \in \mathbb{R}^{18}$, where $\boldsymbol{x}_{\text{ins},n} \in \mathbb{R}^{16}$ is the INS's state vector, $\boldsymbol{x}_{\text{clk,r},n} \in \mathbb{R}^2$ is the navigating vehicle-mounted receiver's clock state vector, $n = 1, \ldots, N$, and N is the total number of navigating vehicles.

The INS 16-state vector is

$$\boldsymbol{x}_{\text{ins},n} = \left[{}^{b_n}_{g}\bar{\boldsymbol{q}}^{\mathsf{T}},\;\; \boldsymbol{r}^{\mathsf{T}}_{b_n},\;\; \dot{\boldsymbol{r}}^{\mathsf{T}}_{b_n},\;\; \boldsymbol{b}^{\mathsf{T}}_{\text{gyr},n},\;\; \boldsymbol{b}^{\mathsf{T}}_{\text{acc},n} \right]^{\mathsf{T}},$$

where ${}^{b_n}_{g}\bar{\boldsymbol{q}} \in \mathbb{R}^4$ is the 4-D unit quaternion vector, which represents the orientation of a body frame $\{b_n\}$ fixed at the n^{th} navigating vehicle with respect to a global frame $\{g\}$, e.g., the

Earth-centered Earth-inertial (ECI) frame [135]; $\boldsymbol{r}_{b_n} \in \mathbb{R}^3$ and $\dot{\boldsymbol{r}}_{b_n} \in \mathbb{R}^3$ are the 3-D position and velocity, respectively, of the navigating vehicle expressed in $\{g\}$; and $\boldsymbol{b}_{\text{gyr},n} \in \mathbb{R}^3$ and $\boldsymbol{b}_{\text{acc},n} \in \mathbb{R}^3$ are the gyroscope and accelerometer biases, respectively.

Receiver Clock State Dynamics

The n^{th} vehicle-mounted receiver's clock states will evolve according to

$$\boldsymbol{x}_{\text{clk},r_n}(k+1) = \mathbf{F}_{\text{clk}}\boldsymbol{x}_{\text{clk,r},n}(k) + \boldsymbol{w}_{\text{clk,r},n}(k), \tag{5.2}$$

where $\boldsymbol{w}_{\text{clk,r},n} \in \mathbb{R}^2$ is the process noise vector, which is modeled as a discrete-time zero-mean white noise sequence with covariance $\mathbf{Q}_{\text{clk,r},n}$, which has an identical form to $\mathbf{Q}_{\text{clk,sop},m}$, except that $S_{w_{\delta t_{\text{sop},m}}}$ and $S_{w_{\dot{\delta} t_{\text{sop},m}}}$ are now replaced with receiver-specific spectra $S_{w_{\delta t_{\text{r},n}}}$ and $S_{w_{\dot{\delta} t_{\text{r},n}}}$, respectively.

INS State Kinematics

The INS states will evolve in time according to

$$\boldsymbol{x}_{\text{ins},n}\,(k+1) = \boldsymbol{f}_{\text{ins}}\big[\,\boldsymbol{x}_{\text{ins},n}(k), {}^{b_n}\boldsymbol{\omega}(k), {}^{g}\boldsymbol{a}_{b_n}(k)\,\big]\,,$$

where $\boldsymbol{f}_{\text{ins}}$ is a vector-valued function of standard strapdown kinematic equations, which integrates the true 3-D rotational rate vector ${}^{b_n}\boldsymbol{\omega}$ in the body frame and the 3-D acceleration of the IMU ${}^{g}\boldsymbol{a}_{b_n}$ in the global frame to produce ${}^{b_n}_{g}\bar{\boldsymbol{q}}(k+1)$, $\boldsymbol{r}_{b_n}(k+1)$, and $\dot{\boldsymbol{r}}_{b_n}(k+1)$ and uses a velocity random walk model for the biases, which is given by

$$\boldsymbol{b}_{\text{gyr},n}(k+1) = \boldsymbol{b}_{\text{gyr},n}(k) + \boldsymbol{w}_{\text{gyr},n}(k), \tag{5.3}$$

$$\boldsymbol{b}_{\text{acc},n}(k+1) = \boldsymbol{b}_{\text{acc},n}(k) + \boldsymbol{w}_{\text{acc},n}(k), \tag{5.4}$$

where $\boldsymbol{w}_{\text{gyr},n}$ and $\boldsymbol{w}_{\text{acc},n}$ are process noise vectors that drive the in-run bias variation (or bias instability) and are modeled as white noise sequences with covariance $\mathbf{Q}_{\boldsymbol{w}_{\text{gyr}},n}$ and $\mathbf{Q}_{\boldsymbol{w}_{\text{acc}},n}$, respectively. In general, the function $\boldsymbol{f}_{\text{ins}}$ my take several forms, which depend on the chosen navigation frame and the INS error models employed. To simplify notation and the discussion throughout the chapter, this chapter develops an aided INS using an inertial frame (e.g., the ECI frame).

IMU Measurement Model

The IMU on the n^{th} navigating vehicle contains a triad-gyroscope and a triad-accelerometer, which produce measurements ${}^{n}\boldsymbol{z}_{\text{imu}} \triangleq \left[{}^{n}\boldsymbol{\omega}_{\text{imu}}^{\mathsf{T}},\ {}^{n}\boldsymbol{a}_{\text{imu}}^{\mathsf{T}}\right]^{\mathsf{T}}$ of the angular rate and specific force, which are modeled as

$$ {}^{n}\boldsymbol{\omega}_{\text{imu}}(k) = {}^{b_n}\boldsymbol{\omega}(k) + \boldsymbol{b}_{\text{gyr},n}(k) + \boldsymbol{n}_{\text{gyr},n}(k) \tag{5.5} $$

$$ \begin{aligned} {}^{n}\boldsymbol{a}_{\text{imu}}(k) =& \mathbf{R}\left[{}^{b_n}_{g}\bar{\boldsymbol{q}}(k)\right]\left({}^{g}\boldsymbol{a}_{b_n}(k) - {}^{g}\boldsymbol{g}_{n}(k)\right) + \boldsymbol{b}_{\text{acc},n}(k) \\ &+ \boldsymbol{n}_{\text{acc},n}(k), \end{aligned} \tag{5.6} $$

where $\mathbf{R}\left[{}^{b_n}_{g}\bar{\boldsymbol{q}}\right]$ is the equivalent rotation matrix of ${}^{b_n}_{g}\bar{\boldsymbol{q}}$, ${}^{g}\boldsymbol{g}_{n}$ is the acceleration due to gravity acting on the n^{th} navigating vehicle in the global frame, and $\boldsymbol{n}_{\text{gyr},n}$ and $\boldsymbol{n}_{\text{acc},n}$ are measurement noise vectors, which are modeled as zero-mean white noise sequences with covariances $\mathbf{Q}_{\boldsymbol{v}_{\text{gyr}},n}$ and $\mathbf{Q}_{\boldsymbol{v}_{\text{acc}},n}$, respectively.

5.2.3 Pseudorange Measurement Model

The pseudorange measurements made by the n^{th} receiver on the m^{th} SOP, after discretization and mild approximations discussed in [74], are modeled as

$$\begin{aligned} {}^{n}z_{\text{sop},m}(j) &= \|\boldsymbol{r}_{b_n}(j) - \boldsymbol{r}_{\text{sop},m}\|_2 \\ &\quad + c \cdot [\delta t_{\text{r},n}(j) - \delta t_{\text{sop},m}(j)] + {}^{n}v_{\text{sop},m}(j), \end{aligned} \tag{5.7}$$

where ${}^{n}v_{\text{sop},m}$ is the measurement noise, which is modeled as a discrete-time zero-mean white Gaussian sequence with variance ${}^{n}\sigma^2_{\text{sop},m}$ and $j \in \mathbb{N}$ represents the time index at which $\{{}^{n}z_{\text{sop},m}\}_{n=1}^{N}$ is available, which could be aperiodic. The pseudorange measurement made by the n^{th} receiver on the l^{th} GNSS SV, after compensating for ionospheric and tropospheric delays, is related to the navigating vehicle's states by

$$\begin{aligned} {}^{n}z_{\text{sv},l}(j) &= \|\boldsymbol{r}_{b_n}(j) - \boldsymbol{r}_{\text{sv},l}(j)\|_2 \\ &\quad + c \cdot [\delta t_{\text{r},n}(j) - \delta t_{\text{sv},l}(j)] + {}^{n}v_{\text{sv},l}(j), \end{aligned} \tag{5.8}$$

where ${}^{n}z_{\text{sv},l} \triangleq {}^{n}z'_{\text{sv},l} - c\delta t_{\text{iono}} - c\delta t_{\text{tropo}}$, δt_{iono} and δt_{tropo} are the ionospheric and tropospheric delays, respectively; ${}^{n}z'_{\text{sv},l}$ is the uncorrected pseudorange; ${}^{n}v_{\text{sv},l}$ is the measurement noise, which is modeled as a discrete-time zero-mean white Gaussian sequence with variance ${}^{n}\sigma^2_{\text{sv},l}$; and $l = 1, \ldots, L$, where L is the total number of GNSS SVs.

5.3 Collaborative Inertial Radio SLAM

In this section, the extended Kalman filter (EKF)-based inertial CoRSLAM framework illustrated in Fig. 5.1, that fuses either TOA or TDOA measurements from unknown SOPs and GNSS pseudoranges (if available) to aid each navigating vehicle's INS is presented and de-

scribed in detail. A method to efficiently share INS data between collaborators is discussed. The EKF time and measurement update equations are provided for the TOA and TDOA fusion strategies.

5.3.1 EKF-Based CoRSLAM Framework

In a CoRSLAM framework, the states of the SOPs are simultaneously estimated along with the states of the navigating vehicles. This can be achieved through an EKF with state vector

$$\boldsymbol{x} \triangleq \left[\boldsymbol{x}_{\mathrm{r},1}^{\mathsf{T}}, \ldots, \boldsymbol{x}_{\mathrm{r},N}^{\mathsf{T}}, \boldsymbol{x}_{\mathrm{sop},1}^{\mathsf{T}}, \ldots, \boldsymbol{x}_{\mathrm{sop},M}^{\mathsf{T}}\right]^{\mathsf{T}}.$$

The EKF produces an estimate, given by $\hat{\boldsymbol{x}}(k|j) \triangleq \mathbb{E}[\boldsymbol{x}(k)|\boldsymbol{Z}^j]$ of $\boldsymbol{x}(k)$, where $\mathbb{E}[\,\cdot\,|\,\cdot\,]$ is the conditional expectation operator, $\boldsymbol{Z}^j \triangleq \{\boldsymbol{z}(i)\}_{i=1}^{j}$, $\boldsymbol{z}$ is a vector of INS-aiding measurements (e.g., from GNSS or SOPs), $k \geq j$, and j is the last time-step an INS-aiding measurement was available.

Collaborating navigating vehicles that estimate common states using mutual observations traditionally fuse information (state estimates and/or observations) from each collaborator using one of two main architectures:

- **Centralized:** Each vehicle sends raw sensor data to a central fusion center, which estimates a common state vector and periodically sends the estimate to each vehicle. Centralized architectures produce the most consistent estimates, i.e., the EKF-produced estimation error covariance matches the covariance of the actual estimation error, since all inter-vehicle correlations are properly maintained. The drawback is in the large amount of raw sensor data that must be communicated to the central fusion center. Furthermore, the central fusion center is a single point of failure for the system.
- **Distributed:** Each vehicle estimates a copy of the state vector using its own sensor

data and then each vehicle shares and fuses these copies using covariance intersection (or one of its variants). Distributed architectures typically require less data transmission between collaborators, since raw sensor data is filtered locally at each vehicle. The drawback is in the difficulty of reaching consensus, i.e., in reaching agreement between the estimate copies, when inter-vehicle correlations are unknown. While covariance intersection techniques are used to fuse estimates with unknown inter-vehicle correlations, they typically produce overly conservative estimates, i.e., the EKF-produced estimation error covariance is larger than the actual covariance of the estimation error.

In contrast to traditional centralized and distributed approaches, the approach of the distributed CoRSLAM framework illustrated in Fig. 5.1 is for each navigating vehicle to monitor the entire state vector $\boldsymbol{x}$, but to distribute the INSs (the EKF time update step) amongst the navigating vehicles and to optimize what information is shared in $\boldsymbol{\Lambda}_n$ (TOA or TDOA from SOPs and what INS data) and how often $\boldsymbol{\Lambda}_n$ is transmitted for aiding corrections (the EKF update step). This approach eliminates a single point of failure, reduces the amount of transmitted data, and with the appropriate transmitted information in $\boldsymbol{\Lambda}_n$, the entire state vector $\boldsymbol{x}$ that is monitored at any particular vehicle will be brought into consensus with the state vector monitored at all other vehicles. The distributed CoRSLAM framework's operation is summarized in algorithm 3.

Algorithm 3 Distributed CoRSLAM Framework

Given: $\hat{\boldsymbol{x}}(j|j)$ and $\mathbf{P}_{\boldsymbol{x}}(j|j)$, each of the N vehicles conducts the following:
for $n = 1, \ldots, N$

- **Local Prediction:** Locally produce $\hat{\boldsymbol{x}}_{\mathrm{r},n}(k|j)$ using an INS and clock models and $\{\hat{\boldsymbol{x}}_{\mathrm{sop},m}(k|j)\}_{m=1}^{M}$ using SOP dynamics model.
- **Communication:** Package $\hat{\boldsymbol{x}}_{\mathrm{r}_n}(k|j)$, TOA (or TDOA) measurements, and INS data into $\boldsymbol{\Lambda}_n$ and transmit $\boldsymbol{\Lambda}_n$ if τ is closed.
- **Assimilation:** Unpackage $\{\boldsymbol{\Lambda}_i\}_{i=1}^{N} \backslash n$, assemble $\hat{\boldsymbol{x}}(k|j)$, and produce $\mathbf{P}_{\boldsymbol{x}}(k|j)$.
- **Correction:** Perform EKF measurement update to produce $\hat{\boldsymbol{x}}(k|k)$, and $\mathbf{P}_{\boldsymbol{x}}(k|k)$.

end for

In the following sections, the TOA and TDOA information fusion strategies are developed and compared. Both strategies have a common prediction (time update) step, which uses the on-board INS of each vehicle and clock models. Both strategies use GNSS pseudoranges as TOA measurements if they are available during the correction (measurement update) step. The distinction between these strategies is in how the SOP pseudoranges are fused to aid the navigating vehicles' on-board INSs: either TOA or TDOA with reference to selected SOPs.

5.3.2 Local Prediction

Each vehicle only locally produces a prediction of its own state vector $\hat{\boldsymbol{x}}_{\mathrm{r},n}(k|j)$ and of the SOPs' $\{\hat{\boldsymbol{x}}_{\mathrm{sop},m}(k|j)\}_{m=1}^{M}$. The full state prediction $\hat{\boldsymbol{x}}(k|j)$ and the corresponding prediction error covariance $\mathbf{P}_{\boldsymbol{x}}(k|j)$ become available locally during the assimilation step, which is described in Subsection 5.3.4.

State Prediction

To produce $\hat{\boldsymbol{x}}_{\mathrm{r},n}(k|j) = \left[\hat{\boldsymbol{x}}_{\mathrm{ins},n}^{\mathsf{T}}(k|j), \hat{\boldsymbol{x}}_{\mathrm{clk,r},n}^{\mathsf{T}}(k|j)\right]^{\mathsf{T}}$, the INS on-board the n^{th} navigating vehicle integrates ${}^{n}\boldsymbol{z}_{\mathrm{imu}}$ between aiding updates to produce a prediction of $\boldsymbol{x}_{\mathrm{ins},n}$. The one-step prediction is given by

$$\hat{\boldsymbol{x}}_{\mathrm{ins},n}(j+1|j) = \boldsymbol{f}_{\mathrm{ins}}[\,\hat{\boldsymbol{x}}_{\mathrm{ins},n}(j|j), {}^{n}\boldsymbol{z}_{\mathrm{imu}}(j+1)\,]\,, \tag{5.9}$$

where the function $\boldsymbol{f}_{\mathrm{ins}}$ contains standard INS equations, which depend on the navigation frame used, the mechanization type, and the INS error model used. which are described in [119,136]. Assuming there are κ time-steps between aiding updates, the navigating vehicle uses IMU data $\{{}^{n}\boldsymbol{z}_{\mathrm{imu}}(i)\}_{i=j}^{k}$ to recursively solve (5.9) to produce $\hat{\boldsymbol{x}}_{\mathrm{ins}_n}(k|j)$, where $k \equiv j+\kappa$. The vehicle-mounted receiver's κ-step clock state prediction follows from (5.2) and is given

by

$$\hat{\boldsymbol{x}}_{\mathrm{clk,r},n}(k|j) = \mathbf{F}_{\mathrm{clk}}^{\kappa} \hat{\boldsymbol{x}}_{\mathrm{clk,r},n}(j|j),$$

where

$$\mathbf{F}_{\mathrm{clk}}^{\kappa} \triangleq \begin{cases} \mathbf{I}_{2\times 2} & \kappa = 0 \\ \prod_{i=1}^{\kappa} \mathbf{F}_{\mathrm{clk}} & \kappa > 0. \end{cases}$$

The SOPs' κ-step state prediction, which follows from (5.1), is given by

$$\hat{\boldsymbol{x}}_{\mathrm{sop},m}(k|j) = \mathbf{F}_{\mathrm{sop}}^{\kappa} \hat{\boldsymbol{x}}_{\mathrm{sop},m}(j|j), \qquad m = 1, \ldots, M.$$

The location prediction for vehicle n is illustrated in Fig. 5.2.

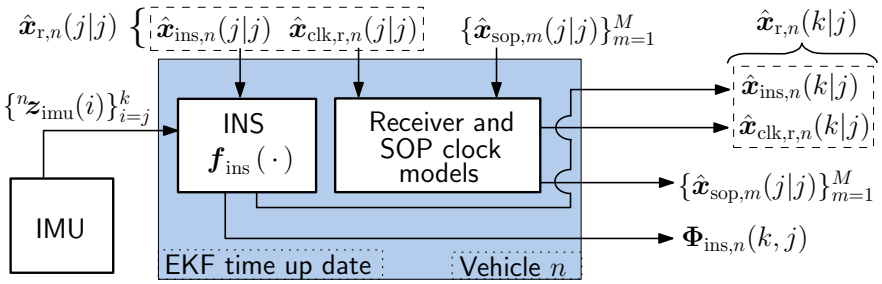

Figure 5.2: Local prediction for vehicle n. The inputs are IMU data $\{{}^{n}\boldsymbol{z}_{\mathrm{imu}}(i)\}_{i=j}^{k}$ and the current state estimates $\hat{\boldsymbol{x}}_{\mathrm{r},n}(j|j)$ and $\{\hat{\boldsymbol{x}}_{\mathrm{sop},m}(j|j)\}_{m=1}^{M}$. The outputs are the time updates $\hat{\boldsymbol{x}}_{\mathrm{r},n}(k|j)$ and $\{\hat{\boldsymbol{x}}_{\mathrm{sop},m}(k|j)\}_{m=1}^{M}$ and the Jacobian $\boldsymbol{\Phi}_{\mathrm{ins},n}(k,j)$.

Prediction Error Covariance

Although the prediction error covariance is not produced at this point in the algorithm, its computation is presented here to explain why it can not be produced until assimilation,

which is discussed in Subsection 5.3.4. The κ-step covariance prediction is given by

$$\mathbf{P}_{\boldsymbol{x}}(k|j) = \mathbf{F}(k,j)\mathbf{P}_{\boldsymbol{x}}(j|j)\mathbf{F}^{\mathsf{T}}(k,j) + \mathbf{Q}^{+}(k,j), \tag{5.10}$$

$$\mathbf{F}(k,j) \triangleq \text{diag}\left[\mathbf{F}_{\text{r},1}(k,j),\, \ldots,\, \mathbf{F}_{\text{r},N}(k,j),\, \mathbf{F}_{\text{sop}}^{\kappa},\, \ldots,\, \mathbf{F}_{\text{sop}}^{\kappa}\right],$$

$$\mathbf{F}_{\text{r},n}(k,j) \triangleq \text{diag}\left[\mathbf{\Phi}_{\text{ins},n}(k,j),\, \mathbf{F}_{\text{clk}}^{\kappa}\right],$$

$$\mathbf{\Phi}_{\text{ins},n}(k,j) \triangleq \prod_{i=j}^{k} \mathbf{\Phi}_{\text{ins},n}(i), \tag{5.11}$$

where $\mathbf{\Phi}_{\text{ins},n}(i)$ is the Jacobian of $\boldsymbol{f}_{\text{ins}}$ evaluated at $\hat{\boldsymbol{x}}_{\text{ins},n}(i|j)$. The structure of $\mathbf{\Phi}_{\text{ins},n}(i)$ is provided in Appendix A.6. The matrix $\mathbf{Q}^{+}(k,j)$ is the propagated process noise covariance, which has the form

$$\mathbf{Q}^{+}(k,j) \triangleq \text{diag}\big[\mathbf{Q}_{\text{r},1}^{+}(k,j), \ldots, \mathbf{Q}_{\text{r},N}^{+}(k,j), \\ \mathbf{Q}_{\text{sop},1}^{+}(k,j),\, \ldots,\, \mathbf{Q}_{\text{sop},M}^{+}(k,j)\big],$$

$$\mathbf{Q}_{\text{r},n}^{+}(k,j) \triangleq \sum_{i=j}^{k} \mathbf{F}_{\text{r},n}(i,j)\mathbf{Q}_{\text{r},n}(i)\mathbf{F}_{\text{r},n}^{\mathsf{T}}(i,j),$$

$$\mathbf{Q}_{\text{sop},m}^{+}(k,j) \triangleq \sum_{i=j}^{k} \mathbf{F}_{\text{sop}}^{(i-j)}\mathbf{Q}_{\text{sop},m}[\mathbf{F}_{\text{sop}}^{\mathsf{T}}]^{(i-j)},$$

where $\mathbf{Q}_{\text{r},n}(i) \triangleq \text{diag}\left[\mathbf{Q}_{\text{ins},n}(i),\, c^2\mathbf{Q}_{\text{clk,r},n}\right]$ and $\mathbf{Q}_{\text{ins},n}$ is the n^{th} navigating vehicle's discrete-time linearized INS process noise covariance. The structure of $\mathbf{Q}_{\text{ins},n}(i)$ is provided in Appendix A.6.

Note that, at this point in the algorithm the prediction error covariance (5.10) can not be computed at vehicle n, $\forall\, n \in \{1,\ldots,N\}$, since all matrices $\{\mathbf{\Phi}_{\text{ins},n}(k,j)\}_{n=1}^{N}$ are not available at each vehicle. In the next subsection, it is shown what INS information each vehicle transmits, so that (5.10) may be computed at each vehicle during the assimilation

step.

5.3.3 Vehicle-to-Vehicle Communication

To produce the prediction error covariance (5.10) at each vehicle, the state transition matrices $\{\mathbf{\Phi}_{\text{ins},n}(k,j)\}_{n=1}^{N}$ must be available. It can been seen in Appendix A.6 that the components of these matrices are a function of IMU data from each respective navigating vehicle. Therefore, two possible approaches to make $\{\mathbf{\Phi}_{\text{ins},n}(k,j)\}_{n=1}^{N}$ available to each vehicle are: 1) each vehicle communicates its raw IMU data or 2) each vehicle communicates the full matrix (5.11). On one hand, IMU data rates are typically between 100 Hz to 400 Hz, with 6 floating-point values per data sample. On the other hand, the matrix (5.11) is in $\mathbb{R}^{15\times 15}$, requiring the transmission of 225 floating-point values every EKF measurement update, which typically take place between 5 Hz to 10 Hz. These data rates make the transmission of raw accelerometer and gyroscope data or the matrix (5.11) undesirable for several reasons: (i) large communication bandwidth requirement, (ii) packet drops due to lossy communication channels, and (iii) privacy concerns.

To address this communication burden, instead of transmitting raw IMU data or the full matrix (5.11), a packet $\mathbf{\Lambda}_{\text{ins},n}$ containing minimal sufficient INS information to reconstruct an approximation of (5.11) with minimal degradation in performance is transmitted once per κ-step propagation. To derive the sufficient INS information to be communicated, the structure of (5.11) after a κ-step propagation is investigated. After carrying out κ successive

multiplications, the form of matrix (5.11) becomes approximately

$$\boldsymbol{\Phi}_{\text{ins},n}(k,j) \approx$$
$$\begin{bmatrix} \mathbf{I}_3 & \mathbf{0}_3 & \mathbf{0}_3 & \kappa T \mathbf{R}[\bar{\boldsymbol{q}}_{1,n}] & \mathbf{0}_3 \\ \lfloor \boldsymbol{v}_{1,n} \times \rfloor & \mathbf{I}_3 & \mathbf{I}_3 T & \boldsymbol{\Phi}_{1,n} & \frac{\kappa T^2}{2} \mathbf{R}[\bar{\boldsymbol{q}}_{2,n}] \\ \lfloor \boldsymbol{v}_{2,n} \times \rfloor & \mathbf{0}_3 & \mathbf{I}_3 & \boldsymbol{\Phi}_{2,n} & \kappa T \mathbf{R}[\bar{\boldsymbol{q}}_{1,n}] \\ \mathbf{0}_3 & \mathbf{0}_3 & \mathbf{0}_3 & \mathbf{I}_3 & \mathbf{0}_3 \\ \mathbf{0}_3 & \mathbf{0}_3 & \mathbf{0}_3 & \mathbf{0}_3 & \mathbf{I}_3 \end{bmatrix}, \tag{5.12}$$

where $\kappa = k - j$; $\lfloor \boldsymbol{v}_{1,n} \times \rfloor \in \mathbb{R}^{3\times 3}$ and $\lfloor \boldsymbol{v}_{2,n} \times \rfloor \in \mathbb{R}^{3\times 3}$ are skew symmetric matrices whose elements are defined from the vectors $\boldsymbol{v}_{1,n} \in \mathbb{R}^3$ and $\boldsymbol{v}_{2,n} \in \mathbb{R}^3$, respectively; the matrices $\mathbf{R}[\bar{\boldsymbol{q}}_{1,n}] \in \mathbb{R}^{3\times 3}$ and $\mathbf{R}[\bar{\boldsymbol{q}}_{2,n}] \in \mathbb{R}^{3\times 3}$ are rotation matrices; and $\boldsymbol{\Phi}_{1,n} \in \mathbb{R}^{3\times 3}$ and $\boldsymbol{\Phi}_{1,n} \in \mathbb{R}^{3\times 3}$ are arbitrarily structured matrices.

Note the following two properties of the structure (5.12). First, since $\lfloor \boldsymbol{v}_{1,n} \times \rfloor$ and $\lfloor \boldsymbol{v}_{2,n} \times \rfloor$ maintain a skew symmetric form, they can be transmitted using only three elements each. Second, the scaling pre-multiplying the matrices $\mathbf{R}[\bar{\boldsymbol{q}}_{1,n}]$ and $\mathbf{R}[\bar{\boldsymbol{q}}_{2,n}]$ is deterministic and only dependent on the IMU sampling period T and the number of iterations κ, therefore these matrices can be converted to quaternions $\bar{\boldsymbol{q}}_{1,n}$ and $\bar{\boldsymbol{q}}_{2,n}$ and then transmitted using only four elements each. From these properties, the sufficient INS information is found to be

$$\boldsymbol{\Lambda}_{\text{ins},n} \triangleq \{\boldsymbol{v}_{1,n}, \boldsymbol{v}_{2,n}, \bar{\boldsymbol{q}}_{1,n}, \bar{\boldsymbol{q}}_{2,n}, \boldsymbol{\Phi}_{1,n}, \boldsymbol{\Phi}_{2,n}\},$$

which only requires the transmission of 32 floating-point values every EKF measurement update. When EKF updates happen at the rate of SOP measurements T_{sop}, transmitting $\boldsymbol{\Lambda}_{\text{ins},n}$ instead of IMU data or the matrix (5.11) reduces the number of transmitted floating-

point values by at least

$$\left[1 - \frac{32}{\min(6 \times \frac{T_{\text{sop}}}{T_{\text{imu}}}, 225)}\right] \times 100\%,$$

where $\min(a, b)$ returns the smallest value between a and b. The tradeoff for significantly reducing the amount of communicated data is in positioning performance. Specifically, the vehicles' position estimation errors increase due to the approximation in (5.12), which arises due to the rotation matrices $\mathbf{R}[\bar{\boldsymbol{q}}_{1,n}]$ and $\mathbf{R}[\bar{\boldsymbol{q}}_{2,n}]$ deviating from true rotation matrices as T_{sop} increases. The increase in position error was shown to be minimal for typical values of T_{sop} and moderate probability of packet loss [37].

The INS information $\boldsymbol{\Lambda}_{\text{ins},n}$ is packaged inside of $\boldsymbol{\Lambda}_n$, along with other necessary information for each vehicle to produce an EKF update, and then is broadcasted by the n^{th} vehicle at the fixed rate of measurement epochs. The packet $\boldsymbol{\Lambda}_n$ is given by

$$\boldsymbol{\Lambda}_n(k) \triangleq \{\hat{\boldsymbol{x}}_{\text{ins},n}(k|j), \boldsymbol{\Lambda}_{\text{ins},n}(k,j), {}^n\boldsymbol{z}_{\text{sv}}(k), {}^n\boldsymbol{z}_{\text{sop}}(k)\}, \tag{5.13}$$

where ${}^n\boldsymbol{z}_{\text{sv}}$ and ${}^n\boldsymbol{z}_{\text{sop}}$ are GNSS and SOP pseudoranges, respectively, which are discussed further for each strategy in the following subsections.

5.3.4 Assimilation

Assuming a fully-connected graph, as in Fig. 5.1, the packets $\{\boldsymbol{\Lambda}_n(k)\}_{n=1}^N$ contain all components of the state prediction to assemble $\hat{\boldsymbol{x}}(k|j)$ and compute (5.10). To compute (5.10), the matrix $\mathbf{F}(k,j)$ is first assembled by using the information in $\{\boldsymbol{\Lambda}_{\text{ins},n}\}_{n=1}^N$. The vectors $\boldsymbol{v}_{1,n}$ and $\boldsymbol{v}_{2,n}$ are used to reconstruct the skew-symmetric matrices $\lfloor \boldsymbol{v}_{1,n} \times \rfloor$ and $\lfloor \boldsymbol{v}_{2,n} \times \rfloor$ in

(5.12) through

$$\lfloor \boldsymbol{a}\times \rfloor = \begin{bmatrix} 0 & -a_3 & a_2 \\ a_3 & 0 & -a_1 \\ -a_2 & a_1 & 0 \end{bmatrix}, \quad \boldsymbol{a} = \begin{bmatrix} a_1 \\ a_2 \\ a_3 \end{bmatrix}.$$

The quaternions $\bar{\boldsymbol{q}}_{1,n}$ and $\bar{\boldsymbol{q}}_{2,n}$ are converted to rotation matrices through

$$\mathbf{R}[\bar{\boldsymbol{q}}] = \mathbf{I}_{3\times 3} - q_4 \lfloor \boldsymbol{q}\times \rfloor + 2\lfloor \boldsymbol{q}\times \rfloor^2,$$

where $\bar{\boldsymbol{q}} \triangleq [\boldsymbol{q},\, q_4,]^\mathsf{T} = [q_1,\, q_2,\, q_3,\, q_4,]^\mathsf{T}$ and q_4 is the real component of the quaternion. Each vehicle may now compute the EKF measurement update and the corresponding corrected estimation error covariance. In the following two subsections, the correction equations are developed for two information fusion strategies: (1) TOA and (2) TDOA with SOP referencing.

5.3.5 TOA Information Fusion Strategy

In this subsection, the EKF-based CoRSLAM measurement update for fusing TOA measurements from SOPs is described. Specifically, the correction to the estimation error $\tilde{\boldsymbol{x}}(k|k)$ is provided, since it will be compared with the estimation error of the TDOA fusion strategy, denoted $\tilde{\tilde{\boldsymbol{x}}}(k|k)$, in Section 5.4.

TOA Measurements

The EKF measurement update will correct the navigating vehicles' INS and clock errors given the measurement vector

$$\boldsymbol{z} \triangleq \left[\boldsymbol{z}_{\text{sv}}^{\mathsf{T}},\, \boldsymbol{z}_{\text{sop}}^{\mathsf{T}}\right]^{\mathsf{T}}, \tag{5.14}$$

$$\boldsymbol{z}_{\text{sv}} \triangleq \left[{}^{1}\boldsymbol{z}_{\text{sv}}^{\mathsf{T}}, \ldots, {}^{N}\boldsymbol{z}_{\text{sv}}^{\mathsf{T}}\right]^{\mathsf{T}}, \quad \boldsymbol{z}_{\text{sop}} \triangleq \left[{}^{1}\boldsymbol{z}_{\text{sop}}^{\mathsf{T}}, \ldots, {}^{N}\boldsymbol{z}_{\text{sop}}^{\mathsf{T}}\right]^{\mathsf{T}},$$

$${}^{n}\boldsymbol{z}_{\text{sv}} = \left[{}^{n}z_{\text{sv},1}, \ldots, {}^{n}z_{\text{sv},L}\right]^{\mathsf{T}}, \quad {}^{n}\boldsymbol{z}_{\text{sop}} = \left[{}^{n}z_{\text{sop},1}, \ldots, {}^{n}z_{\text{sop},M}\right]^{\mathsf{T}}.$$

The correction equations are described next for: GNSS availability ($L > 0$) and GNSS unavailability ($L = 0$).

TOA Correction Equations

Given a prediction error $\tilde{\boldsymbol{x}}(k|j)$, the error correction and corresponding corrected error covariance are given by

$$\tilde{\boldsymbol{x}}(k|k) = \tilde{\boldsymbol{x}}(k|j) - \mathbf{L}(k)\mathbf{S}^{-1}(k)\boldsymbol{\nu}(k),$$

$$\mathbf{P}_{\boldsymbol{x}}(k|k) = \mathbf{P}_{\boldsymbol{x}}(k|j) - \mathbf{L}(k)\mathbf{S}^{-1}(k)\mathbf{L}^{\mathsf{T}}(k), \tag{5.15}$$

$$\mathbf{L}(k) \triangleq \mathbf{P}_{\boldsymbol{x}}(k|j)\mathbf{H}^{\mathsf{T}}(k), \tag{5.16}$$

$$\mathbf{S}(k) \triangleq \mathbf{H}(k)\mathbf{L}(k) + \mathbf{R}(k), \tag{5.17}$$

$$\boldsymbol{\nu}(k) \triangleq \boldsymbol{z}(k) - \hat{\boldsymbol{z}}(k|j), \tag{5.18}$$

where $\hat{\boldsymbol{z}}(k|j)$ is a vector containing the predicted GNSS pseudoranges and the predicted SOP TOA measurement set. The matrix $\mathbf{H}$ is the measurement Jacobian and has the form

$$\mathbf{H} = \begin{bmatrix} \mathbf{H}_{\text{sv,r}} & \mathbf{0}_{NL\times 5M} \\ \mathbf{H}_{\text{sop,r}} & \mathbf{H}_{\text{sop}} \end{bmatrix}, \ \mathbf{H}_{\text{sv,r}} \triangleq \text{diag}\left[{}^{1}\mathbf{H}_{\text{sv,r}}, \ldots, {}^{N}\mathbf{H}_{\text{sv,r}}\right],$$

$${}^{n}\mathbf{H}_{\text{sv},r} = \begin{bmatrix} \mathbf{0}_{1\times 3} & {}^{n}\hat{\mathbf{1}}_{\text{sv},1}^{\mathsf{T}} & \mathbf{0}_{1\times 9} & \boldsymbol{h}_{\text{clk}}^{\mathsf{T}} \\ \vdots & \vdots & \vdots & \vdots \\ \mathbf{0}_{1\times 3} & {}^{n}\hat{\mathbf{1}}_{\text{sv},L}^{\mathsf{T}} & \mathbf{0}_{1\times 9} & \boldsymbol{h}_{\text{clk}}^{\mathsf{T}} \end{bmatrix},$$

$$\mathbf{H}_{\text{sop,r}} \triangleq \text{diag}\left[{}^{1}\mathbf{H}_{\text{sop,r}}, \ldots, {}^{N}\mathbf{H}_{\text{sop,r}}\right],$$

where ${}^{n}\mathbf{H}_{\text{sop,r}}$ has the same structure as ${}^{n}\mathbf{H}_{\text{sv,r}}$, except ${}^{n}\hat{\mathbf{1}}_{\text{sv},l}^{\mathsf{T}}$ is replaced with ${}^{n}\hat{\mathbf{1}}_{\text{sop},m}^{\mathsf{T}}$,

$$\mathbf{H}_{\text{sop}} \triangleq \left[{}^{1}\mathbf{H}_{\text{sop}}^{\mathsf{T}}, \ldots, {}^{N}\mathbf{H}_{\text{sop}}^{\mathsf{T}}\right]^{\mathsf{T}},$$

$${}^{n}\mathbf{H}_{\text{sop}} = \text{diag}\left[{}^{n}\mathbf{H}_{\text{sop},1}, \ldots, {}^{n}\mathbf{H}_{\text{sop},M}\right],$$

$${}^{n}\hat{\mathbf{1}}_{\text{sv},l} \triangleq \frac{\hat{\boldsymbol{r}}_{b_n} - \boldsymbol{r}_{\text{sv},l}}{\|\hat{\boldsymbol{r}}_{b_n} - \boldsymbol{r}_{\text{sv},l}\|}, \quad {}^{n}\hat{\mathbf{1}}_{\text{sop},m} \triangleq \frac{\hat{\boldsymbol{r}}_{b_n} - \hat{\boldsymbol{r}}_{\text{sop},m}}{\|\hat{\boldsymbol{r}}_{b_n} - \hat{\boldsymbol{r}}_{\text{sop},m}\|},$$

$${}^{n}\mathbf{H}_{\text{sop},m} \triangleq \left[-{}^{n}\hat{\mathbf{1}}_{\text{sop},m}^{\mathsf{T}}, \ -\boldsymbol{h}_{\text{clk}}^{\mathsf{T}}\right], \quad \boldsymbol{h}_{\text{clk}} \triangleq [1, \ 0]^{\mathsf{T}},$$

and $\mathbf{R}$ is the measurement noise covariance. Note that $\mathbf{R}$ is not necessarily diagonal, since there are no assumptions made on the measurement noise statistics, except that $\mathbf{R} \succ \mathbf{0}$.

Note that if GNSS pseudoranges become completely unavailable, i.e., $L = 0$ and $\boldsymbol{z} \equiv \boldsymbol{z}_{\text{sop}}$, the state and covariance correction are identical, except that the Jacobian is adjusted to account for GNSS SV pseudoranges no longer being available, specifically

$$\mathbf{H} \equiv [\mathbf{H}_{\text{sop},r}, \ \mathbf{H}_{\text{sop}}]. \tag{5.19}$$

5.3.6 TDOA with SOP Referencing Information Fusion Strategy

In this information fusion strategy, TDOA measurements are computed at each vehicle-mounted receiver by differencing the drawn pseudoranges with a selected reference SOP. The produced estimation error and covariance of $\boldsymbol{x}$ when TDOA measurements are used will be denoted $\tilde{\bar{\boldsymbol{x}}}$, and $\mathbf{P}_{\bar{\boldsymbol{x}}}$, respectively.

TDOA Measurements

Each navigating vehicle is free to select an arbitrary reference SOP, i.e., the SOP measurement set computed by the n^{th} navigating vehicle becomes

$$
\begin{aligned}
{}^{n}\bar{\boldsymbol{z}}_{\text{sop}}^{\mathsf{T}} &\triangleq \left[{}^{n}\bar{z}_{\text{sop},1}, \ldots, {}^{n}\bar{z}_{\text{sop},M}\right]^{\mathsf{T}}, \\
{}^{n}\bar{z}_{\text{sop},m} &\triangleq {}^{n}z_{\text{sop},m} - {}^{n}z_{\text{sop},\iota_n} \\
&= \|\boldsymbol{r}_{b_n}(j) - \boldsymbol{r}_{\text{sop},m}\|_2 - \|\boldsymbol{r}_{b_n}(j) - \boldsymbol{r}_{\text{sop},\iota_n}\|_2 \\
&\quad + c \cdot [\delta t_{\text{sop},m}(j) - \delta t_{\text{sop},\iota_n}(j)] \\
&\quad + {}^{n}v_{\text{sop},m}(j) - {}^{n}v_{\text{sop},\iota_n}(j),
\end{aligned}
\tag{5.20}
$$

where ι_n is the reference SOP number used by the n^{th} navigating vehicle and the SOP number $m \in \{1, \ldots, M\} \backslash \iota_n$. Each navigating vehicle replaces the SOP TOA measurements $\boldsymbol{z}_{\text{sop}}$ with the SOP TDOA measurements $\bar{\boldsymbol{z}}_{\text{sop}}$ in the transmitted packet (5.13). Note that since the SOP transmitters are *not synchronized*, the TDOA measurements (5.20) are parameterized by the clock biases of both transmitters; therefore, both of these biases must be estimated. This differs from traditional TDOA-based localization approaches that assume synchronized transmitters, which allow for these biases to cancel and to be removed from the estimator.

The measurement set available to each vehicle-mounted receiver in the TDOA fusion strategy

may be written in terms of the measurement set (5.14) of the TOA fusion strategy as

$$\bar{\boldsymbol{z}} \triangleq \begin{bmatrix} \boldsymbol{z}_{\text{sv}} \\ \bar{\boldsymbol{z}}_{\text{sop}} \end{bmatrix} = \begin{bmatrix} \mathbf{I}_{NL\times NL} & \mathbf{0}_{NL\times NM} \\ \mathbf{0}_{NM\times NL} & \mathbf{T} \end{bmatrix} \begin{bmatrix} \boldsymbol{z}_{\text{sv}} \\ \boldsymbol{z}_{\text{sop}} \end{bmatrix} \triangleq \boldsymbol{\Xi}\boldsymbol{z} \tag{5.21}$$

where $\mathbf{I}_{NL\times NL}$ is an $NL \times NL$ identity matrix and $\mathbf{T}$ is the difference operator matrix that maps $\boldsymbol{z}_{\text{sop}}$ to $\bar{\boldsymbol{z}}_{\text{sop}}$, which has the form

$$\mathbf{T} = \text{diag}\left[\mathbf{T}_{\iota_1}, \ldots \mathbf{T}_{\iota_N}\right], \tag{5.22}$$

$$\mathbf{T}_{\iota_n} = \begin{bmatrix} 1 & \ldots & 0 & -1 & 0 & \ldots & 0 \\ \vdots & \ddots & \vdots & \vdots & \vdots & \ddots & \vdots \\ 0 & \ldots & 1 & -1 & 0 & \ldots & 0 \\ 0 & \ldots & 0 & -1 & 1 & \ldots & 0 \\ \vdots & \ddots & \vdots & \vdots & \vdots & \ddots & \vdots \\ 0 & \ldots & 0 & -1 & 0 & \ldots & 1 \end{bmatrix}, \tag{5.23}$$

where the column of "-1" resides in column ι_n. The structure of the prediction error covariance $\mathbf{P}_{\bar{\boldsymbol{x}}}(k|j)$ is not dependent on the fusion strategy; therefore, has the same form as (5.10). The correction equations are summarized next.

TDOA Correction Equations

Given a prediction error $\tilde{\bar{\boldsymbol{x}}}(k|j)$, the error correction and corresponding corrected error covariance are given by:

$$\tilde{\bar{\boldsymbol{x}}}(k|k) = \tilde{\bar{\boldsymbol{x}}}(k|j) - \bar{\mathbf{L}}(k)\bar{\mathbf{S}}^{-1}\bar{\boldsymbol{\nu}}(k), \tag{5.24}$$

$$\mathbf{P}_{\bar{\boldsymbol{x}}}(k|k) = \mathbf{P}_{\bar{\boldsymbol{x}}}(k|j) - \bar{\mathbf{L}}(k)\bar{\mathbf{S}}^{-1}(k)\bar{\mathbf{L}}^{\mathsf{T}}(k), \tag{5.25}$$

$$\bar{\mathbf{L}}(k) \triangleq \mathbf{P}_{\bar{\boldsymbol{x}}}(k|j)\bar{\mathbf{H}}^{\mathsf{T}}(k) \tag{5.26}$$

$$\bar{\mathbf{S}}(k) \triangleq \bar{\mathbf{H}}(k)\bar{\mathbf{L}}(k) + \bar{\mathbf{R}}(k) \tag{5.27}$$

$$\bar{\boldsymbol{\nu}}(k) \triangleq \bar{\boldsymbol{z}}(k) - \hat{\bar{\boldsymbol{z}}}(k|j), \tag{5.28}$$

where $\hat{\bar{\boldsymbol{z}}}(k|j)$ is the predicted GNSS pseudoranges and SOP TDOA measurement set and $\bar{\mathbf{H}}$ is the corresponding measurement Jacobian, which is related to $\mathbf{H}$ through

$$\bar{\mathbf{H}} \triangleq \begin{bmatrix} \mathbf{I}_{NL\times NL} & \mathbf{0}_{NL\times NM} \\ \mathbf{0}_{NM\times NL} & \mathbf{T} \end{bmatrix} \begin{bmatrix} \mathbf{H}_{\mathrm{sv},r} & \mathbf{0}_{NL\times 5M} \\ \mathbf{H}_{\mathrm{sop},r} & \mathbf{H}_{\mathrm{sop}} \end{bmatrix}.$$

The measurement noise covariance is given by $\bar{\mathbf{R}} = \boldsymbol{\Xi}\mathbf{R}\boldsymbol{\Xi}^{\mathsf{T}}$.

Note that if GNSS pseudoranges become completely unavailable ($L = 0$), i.e., $\bar{\boldsymbol{z}} \equiv \bar{\boldsymbol{z}}_{\mathrm{sop}}$, the state and covariance corrections are identical to when $L > 0$, except that the dimension of $\mathbf{I}_{NL\times NL}$ reduces to zero, modifying the measurement Jacobian to take the form

$$\bar{\mathbf{H}} = \mathbf{T}\mathbf{H}, \tag{5.29}$$

where $\mathbf{H}$ is the measurement Jacobian (5.19) from the TOA fusion strategy when $L = 0$.

5.4 Strategy Performance Comparison

In this section, the estimation performance of the two information fusion strategies presented in Section 5.3 are studied. First, it is shown that the TDOA estimation performance is invariant to the SOP reference selection. Then, it is shown that the TOA strategy yields less than or equal estimation error covariance corresponding to the navigating vehicles' positions than the TDOA strategy.

5.4.1 TDOA SOP Reference Selection

In this subsection, it is shown that the estimation error and error covariance are invariant to the choice of the SOP reference, which is summarized in Theorem 5.4.1.

Theorem 5.4.1. *Consider an environment comprising N receivers and M unknown SOPs with arbitrary: (i) receiver and SOP clock qualities (i.e., arbitrary process noise covariances $\{\mathbf{Q}_{\text{clk,r},n}\}_{n=1}^{N}$ and $\{\mathbf{Q}_{\text{clk,sop},m}\}_{m=1}^{M}$), (ii) geometric configurations, and (iii) measurement noise covariance (i.e., $\mathbf{R} \succ \mathbf{0}$, but not necessarily diagonal). The EKF-based CoRSLAM yields an estimation error and corresponding estimation error covariance that are invariant to each receiver's SOP reference selection.*

Proof. The proof will only consider GNSS unavailability periods ($L = 0$), i.e., $\bar{\boldsymbol{z}} \equiv \bar{\boldsymbol{z}}_{\text{sop}}$. The proof can be straightforwardly extended to GNSS availability ($L > 0$). Given $\tilde{\bar{\boldsymbol{x}}}(k|j)$, the

correction $\tilde{\tilde{\boldsymbol{x}}}(k|k)$ can be computed from (5.24). Substituting (5.29) into (5.26)-(5.28) gives

$$\begin{aligned}
\bar{\mathbf{L}}(k) &= \mathbf{P}_{\boldsymbol{x}}(k|j)\mathbf{H}^{\mathsf{T}}(k)\mathbf{T}^{\mathsf{T}} \\
&= \mathbf{L}(k)\mathbf{T}^{\mathsf{T}}, && (5.30) \\
\bar{\mathbf{S}}(k) &= \mathbf{T}\mathbf{H}(k)\mathbf{L}(k)\mathbf{T}^{\mathsf{T}} + \mathbf{T}\mathbf{R}(k)\mathbf{T}^{\mathsf{T}} \\
&= \mathbf{T}\mathbf{S}(k)\mathbf{T}^{\mathsf{T}}, && (5.31) \\
\bar{\boldsymbol{\nu}}(k) &= \mathbf{T}\boldsymbol{z}(k) - \mathbf{T}\hat{\boldsymbol{z}}(k|j) \\
&= \mathbf{T}\boldsymbol{\nu}(k). && (5.32)
\end{aligned}$$

Substituting (5.30)-(5.32) into (5.24) yields

$$\begin{aligned}
\tilde{\tilde{\boldsymbol{x}}}(k|k) = &\tilde{\tilde{\boldsymbol{x}}}(k|j) - \mathbf{L}(k)\mathbf{T}^{\mathsf{T}} \\
&\cdot [\mathbf{T}\mathbf{S}(k)\mathbf{T}^{\mathsf{T}}]^{-1}\mathbf{T}\boldsymbol{\nu}(k). && (5.33)
\end{aligned}$$

Recall that $\mathbf{T}$ is the difference operator, which computes the TDOA measurements when the n^{th} receiver references the drawn pseudoranges with respect to an arbitrary SOP number ι_n and has the block diagonal structure (5.22).

Next, consider the block of $\mathbf{T}$ that corresponds to the n^{th} receiver, which can be written as

$$\mathbf{T}_{\iota_n} = \mathbf{J}_{\iota_n} - \boldsymbol{v}\boldsymbol{e}_{\iota_n}^{\mathsf{T}}, \tag{5.34}$$

where $\mathbf{J}_{\iota_n} \in \mathbb{R}^{[(M-1)\times M]}$ is formed by removing the ι_n^{th} row from an identity matrix,

$$\boldsymbol{v} \triangleq [1, \ldots, 1]^{\mathsf{T}} \in \mathbb{R}^{(M-1)},$$

and $\boldsymbol{e}_{\iota_n}$ denotes the ι_n^{th} standard basis vector of appropriate dimension consisting of a 1 in the ι_n^{th} element and zeros elsewhere. From (5.34), it is easy to verify that $\mathbf{T}_{\iota_n} \in \mathbb{R}^{[(M-1)\times M]}$

is full row-rank and that $\mathbf{1} \triangleq \left[\boldsymbol{v}^{\mathsf{T}}, 1\right]^{\mathsf{T}}$ is a basis for the null space of $\mathbf{T}_{\iota_n}$; therefore,

$$\begin{aligned}\mathbf{0} = \mathbf{T}_{\iota_n}\mathbf{1} &= \sum_{i=1}^{M} \mathbf{T}_{\iota_n}\boldsymbol{e}_i \\ \Rightarrow -\sum_{\substack{i=1 \\ i\neq q}}^{M} \boldsymbol{t}_{\iota_n,i} &= \boldsymbol{t}_{\iota_n,q}, \quad \forall\, q \in [1,\ldots,M],\end{aligned} \tag{5.35}$$

where $\boldsymbol{t}_{\iota_n,i} \triangleq \mathbf{T}_{\iota_n}\boldsymbol{e}_i$ and $\boldsymbol{t}_{\iota_n,q} \triangleq \mathbf{T}_{\iota_n}\boldsymbol{e}_q$ denote the i^{th} and q^{th} column of $\mathbf{T}_{\iota_n}$, respectively. Partitioning $\mathbf{T}_{\iota_n}$ into columns yields

$$\begin{aligned}\mathbf{T}_{\iota_n} &= [\boldsymbol{t}_{\iota_n,1},\ldots,\boldsymbol{t}_{\iota_n,M}] \\ &= [\mathbf{T}_{\iota_n,1:M-1}, \boldsymbol{t}_{\iota_n,M}]\,,\end{aligned} \tag{5.36}$$

where $\mathbf{T}_{\iota_n,1:M-1}$ denotes the matrix consisting of the columns $\boldsymbol{t}_{\iota_n,1}$ through $\boldsymbol{t}_{\iota_n,M-1}$. Substituting the left side of (5.35) for $q \equiv M$ into the last column of (5.36) gives

$$\mathbf{T}_{\iota_n} = \left[\mathbf{T}_{\iota_n,1:M-1}, -\sum_{i=1}^{M-1} \boldsymbol{t}_{\iota_n,i}\right]. \tag{5.37}$$

Next, consider the difference operator matrix

$$\mathbf{T}' = \text{diag}\left[\mathbf{T}_{\iota'_1},\ldots\mathbf{T}_{\iota'_N}\right], \tag{5.38}$$

which forms the set of TDOA measurements when the n^{th} receiver uses SOP ι'_n as its reference, where $\iota'_n \in [1,\ldots,M]$. Proceeding in a similar manner that was used to write $\mathbf{T}_{\iota_n}$ as (5.37), it is straight forward to show that $\mathbf{T}_{\iota'_n}$ can be written as

$$\mathbf{T}_{\iota'_n} = \left[\mathbf{T}_{\iota'_n,1:M-1}, -\sum_{i=1}^{M-1} \boldsymbol{t}_{\iota'_n,i}\right]. \tag{5.39}$$

Note that since $\mathbf{T}_{\iota_n}$ and $\mathbf{T}_{\iota'_n}$ are full row-rank, the matrices $\mathbf{T}_{\iota_n,1:M-1}$ and $\mathbf{T}_{\iota'_n,1:M-1}$ are

square and invertible; therefore, there exists a matrix $\mathbf{E}_n$, such that

$$\mathbf{T}_{\iota'_n,1:M-1} = \mathbf{E}_n^{-1}\mathbf{T}_{\iota_n,1:M-1}. \tag{5.40}$$

From (5.40), the columns of $\mathbf{T}_{\iota'_n,1:M-1}$ are related to the columns of $\mathbf{T}_{\iota_n,1:M-1}$ through

$$\boldsymbol{t}_{\iota'_n,i} = \mathbf{E}_n^{-1}\boldsymbol{t}_{\iota_n,i}, \quad i = 1,\ldots,M-1. \tag{5.41}$$

Substituting the right side of (5.40) and (5.41) into the right side of (5.39) yields

$$\begin{aligned}\mathbf{T}_{\iota'_n} &= \left[\mathbf{E}_n^{-1}\mathbf{T}_{\iota_n,1:M-1}, -\mathbf{E}_n^{-1}\sum_{i=1}^{M-1}\boldsymbol{t}_{\iota_n,i}\right] \\ &= \mathbf{E}_n^{-1}\mathbf{T}_{\iota_n}.\end{aligned} \tag{5.42}$$

The relationship between $\mathbf{T}'$ and $\mathbf{T}$ can be found by substituting (5.42) into (5.38) for $n = 1,\ldots,N$, which gives

$$\begin{aligned}\mathbf{T}' &= \operatorname{diag}\left[\mathbf{E}_1^{-1}\mathbf{T}_{\iota_1},\ldots,\mathbf{E}_N^{-1}\mathbf{T}_{\iota_N}\right] \\ &= \mathbf{E}^{-1}\mathbf{T},\end{aligned} \tag{5.43}$$

where $\mathbf{E}^{-1} \triangleq \operatorname{diag}\left[\mathbf{E}_1^{-1},\ldots,\mathbf{E}_N^{-1}\right]$. Solving (5.43) for $\mathbf{T}$ and substituting into (5.33) gives

$$\begin{aligned}\tilde{\tilde{\boldsymbol{x}}}(k|k) =& \tilde{\tilde{\boldsymbol{x}}}(k|j) - \mathbf{L}(k)\mathbf{T}'^{\mathsf{T}}\mathbf{E}^{\mathsf{T}} \\ &\cdot [\mathbf{E}\mathbf{T}'\mathbf{S}(k)\mathbf{T}'^{\mathsf{T}}\mathbf{E}^{\mathsf{T}}]^{-1}\mathbf{E}\mathbf{T}'\boldsymbol{\nu}(k) \\ =& \tilde{\tilde{\boldsymbol{x}}}(k|j) - \mathbf{L}(k)\mathbf{T}'^{\mathsf{T}}\mathbf{E}^{\mathsf{T}} \\ &\cdot \mathbf{E}^{-\mathsf{T}}[\mathbf{T}'\mathbf{S}(k)\mathbf{T}'^{\mathsf{T}}]^{-1}\mathbf{E}^{-1}\mathbf{E}\mathbf{T}'\boldsymbol{\nu}(k) \\ =& \tilde{\tilde{\boldsymbol{x}}}'(k|k),\end{aligned} \tag{5.44}$$

where $\tilde{\tilde{\boldsymbol{x}}}'(k|k)$ is the estimation error correction when the difference operator matrix $\mathbf{T}'$ is

used. The last step in (5.44) follows from $\tilde{\bar{\boldsymbol{x}}}(k|j) = \tilde{\bar{\boldsymbol{x}}}'(k|j)$, since they only depend on IMU data, making (5.44) take the same form as (5.33), except that $\mathbf{T}$ is replaced with $\mathbf{T}'$.

Next, consider the EKF Riccati equation, which governs the time-evolution of the estimation error covariance

$$\begin{aligned}\mathbf{P}_{\bar{\boldsymbol{x}}}(j+\kappa|j) =& \mathbf{F}\big\{\mathbf{P}_{\bar{\boldsymbol{x}}}(j|j-\kappa) - \mathbf{P}_{\bar{\boldsymbol{x}}}(j|j-\kappa)\bar{\mathbf{H}}^{\mathsf{T}}(j) \\ & \cdot \left[\bar{\mathbf{H}}(j)\mathbf{P}_{\bar{\boldsymbol{x}}}(j|j-\kappa)\bar{\mathbf{H}}^{\mathsf{T}}(j) + \bar{\mathbf{R}}(j)\right]^{-1} \\ & \cdot \bar{\mathbf{H}}(j)\mathbf{P}_{\bar{\boldsymbol{x}}}(j|j-\kappa)\big\}\mathbf{F}^{\mathsf{T}} + \mathbf{Q}^{+}(j+\kappa, j),\end{aligned}$$

where the time arguments $(j+\kappa, j)$ have been dropped from $\mathbf{F}$ to simplify the notation. Substituting (5.29) into $\bar{\mathbf{H}}$ and using the relationship found in (5.42) gives

$$\begin{aligned}&\mathbf{P}_{\bar{\boldsymbol{x}}}(j+\kappa|j) \\ &= \mathbf{F}\big\{\mathbf{P}_{\bar{\boldsymbol{x}}}(j|j-\kappa) - \mathbf{P}_{\bar{\boldsymbol{x}}}(j|j-\kappa)\mathbf{H}^{\mathsf{T}}(j)\mathbf{T}^{\mathsf{T}} \\ &\quad \cdot \left[\mathbf{T}\mathbf{H}(j)\mathbf{P}_{\bar{\boldsymbol{x}}}(j|j-\kappa)\mathbf{H}^{\mathsf{T}}(j)\mathbf{T}^{\mathsf{T}} + \mathbf{T}\mathbf{R}(j)\mathbf{T}^{\mathsf{T}}\right]^{-1} \\ &\quad \cdot \mathbf{T}\mathbf{H}(j)\mathbf{P}_{\bar{\boldsymbol{x}}}(j|j-\kappa)\big\}\mathbf{F}^{\mathsf{T}} + \mathbf{Q}^{+}(j+\kappa, j) \\ &= \mathbf{F}\big\{\mathbf{P}_{\bar{\boldsymbol{x}}}(j|j-\kappa) - \mathbf{P}_{\bar{\boldsymbol{x}}}(j|j-\kappa)\mathbf{H}^{\mathsf{T}}(j)\mathbf{T}'^{\mathsf{T}}\mathbf{E}^{\mathsf{T}} \\ &\quad \cdot \mathbf{E}^{-\mathsf{T}}\left[\mathbf{T}'\mathbf{H}(j)\mathbf{P}_{\bar{\boldsymbol{x}}}(j|j-\kappa)\mathbf{H}^{\mathsf{T}}(j)\mathbf{T}'^{\mathsf{T}} + \mathbf{T}'\mathbf{R}(j)\mathbf{T}'^{\mathsf{T}}\right]^{-1}\mathbf{E}^{-1} \\ &\quad \cdot \mathbf{E}\mathbf{T}'\mathbf{H}(j)\mathbf{P}_{\bar{\boldsymbol{x}}}(j|j-\kappa)\big\}\mathbf{F}^{\mathsf{T}} + \mathbf{Q}^{+}(j+\kappa, j) \\ &= \mathbf{P}_{\bar{\boldsymbol{x}}'}(j+\kappa|j),\end{aligned}$$

where $\mathbf{P}_{\bar{\boldsymbol{x}}'}(j+\kappa|j)$ is the prediction error covariance when the difference operator matrix $\mathbf{T}'$ is used. □

5.4.2 TOA Versus TDOA

In this subsection, it is shown that fusing TOA measurements from unknown SOPs produces a less than or equal (in a positive semi-definite sense) position estimation error covariance matrix for each navigating vehicle than fusing TDOA.

Theorem 5.4.2. *Consider an environment comprising N receivers and M unknown SOPs with arbitrary: (i) receiver and SOP clock qualities (i.e., arbitrary clock process noise covariances $\{\mathbf{Q}_{\text{clk,r},n}\}_{n=1}^{N}$ and $\{\mathbf{Q}_{\text{clk,sop},m}\}_{m=1}^{M}$), (ii) geometric configurations, and (iii) measurement noise covariance (i.e., $\mathbf{R} \succ \mathbf{0}$, but not necessarily diagonal). The EKF-based CoRSLAM that fuses pseudoranges with a TOA fashion yields a less than or equal (in a positive semi-definite sense) position estimation error covariance for each of the navigating vehicles than a TDOA fashion.*

Proof. Define the correction (measurement update) estimation error covariance associated with the n^{th} receiver's position for fusing TOA measurements at time-step k as

$$\mathbf{P}_{\boldsymbol{r}_{b_n}}(k|k) \triangleq \boldsymbol{\Upsilon}_n \mathbf{P}_{\boldsymbol{x}}(k|k) \boldsymbol{\Upsilon}_n^{\mathsf{T}} \tag{5.45}$$

and the correction (measurement update) estimation error covariance associated with the n^{th} receiver's position for fusing TDOA measurements at time-step k as

$$\mathbf{P}_{\bar{\boldsymbol{r}}_{b_n}}(k|k) \triangleq \boldsymbol{\Upsilon}_n \mathbf{P}_{\bar{\boldsymbol{x}}}(k|k) \boldsymbol{\Upsilon}_n^{\mathsf{T}}, \tag{5.46}$$

where

$$\boldsymbol{\Upsilon}_n \triangleq \left[\mathbf{0}_{3\times\gamma_{n,1}}, \mathbf{I}_{3\times 3}, \mathbf{0}_{3\times\gamma_{n,2}}\right],$$

$\gamma_{n,1} \triangleq 17n-14$, and $\gamma_{n,2} \triangleq 17(N-n)+5M-11$. Substituting (5.15) and (5.25) into $\mathbf{P}_{\boldsymbol{x}}(k|k)$

and $\mathbf{P}_{\bar{\boldsymbol{x}}}(k|k)$ in (5.45) and (5.46), respectively, and differencing yields

$$\begin{aligned}
&\mathbf{P}_{\bar{\boldsymbol{r}}_{b_n}}(k|k) - \mathbf{P}_{\boldsymbol{r}_{b_n}}(k|k) \\
&= \boldsymbol{\Upsilon}_n \left[\mathbf{L}(k)\mathbf{S}^{-1}(k)\mathbf{L}^{\mathsf{T}}(k) - \bar{\mathbf{L}}(k)\bar{\mathbf{S}}^{-1}(k)\bar{\mathbf{L}}^{\mathsf{T}}(k)\right] \boldsymbol{\Upsilon}_n^{\mathsf{T}}.
\end{aligned} \tag{5.47}$$

Note that the prediction error covariances $\mathbf{P}_{\boldsymbol{x}}(k|j)$ and $\mathbf{P}_{\bar{\boldsymbol{x}}}(k|j)$ are only a function of the IMU data, making them independent of the information fusion type, i.e., $\mathbf{P}_{\boldsymbol{x}}(k|j) = \mathbf{P}_{\bar{\boldsymbol{x}}}(k|j)$; therefore, they have canceled and did not appear in (5.47). Substituting (5.30) and (5.31) into (5.47) gives

$$\begin{aligned}
&\mathbf{P}_{\bar{\boldsymbol{r}}_{b_n}}(k|k) - \mathbf{P}_{\boldsymbol{r}_{b_n}}(k|k) \\
&\quad= \boldsymbol{\Upsilon}_n \big[\mathbf{L}(k)\mathbf{S}^{-1}(k)\mathbf{L}^{\mathsf{T}}(k) \\
&\qquad - \mathbf{L}(k)\mathbf{T}^{\mathsf{T}} \left(\mathbf{T}\mathbf{S}(k)\mathbf{T}^{\mathsf{T}}\right)^{-1} \mathbf{T}^{\mathsf{T}}\mathbf{L}^{\mathsf{T}}(k)\big] \boldsymbol{\Upsilon}_n^{\mathsf{T}} \\
&\quad= \boldsymbol{\Upsilon}_n \mathbf{L}(k) \big[\mathbf{S}^{-1}(k) - \mathbf{T} \left(\mathbf{T}\mathbf{S}(k)\mathbf{T}^{\mathsf{T}}\right)^{-1} \mathbf{T}^{\mathsf{T}}\big] \mathbf{L}^{\mathsf{T}}(k) \boldsymbol{\Upsilon}_n^{\mathsf{T}}.
\end{aligned} \tag{5.48}$$

Define the matrices

$$\mathbf{A}(k) \triangleq \mathbf{S}_c(k)\mathbf{T}^{\mathsf{T}} \in \mathbb{R}^{NM \times N(M-1)}, \tag{5.49}$$

$$\mathbf{B}_n(k) \triangleq \boldsymbol{\Upsilon}_n \mathbf{L}(k) \mathbf{S}_c^{-1}(k) \in \mathbb{R}^{3 \times NM}, \quad n = 1, \ldots, N, \tag{5.50}$$

where $\mathbf{S}_c$ is the Cholesky decomposition of $\mathbf{S}$, i.e., $\mathbf{S} = \mathbf{S}_c\mathbf{S}_c^{\mathsf{T}}$. Since $\mathbf{S}$ is symmetric positive definite, $\mathbf{S}_c$ is unique and invertible. Substituting (5.49) and (5.50) into (5.48) yields

$$\begin{aligned}
&\mathbf{P}_{\bar{\boldsymbol{r}}_{b_n}}(k|k) - \mathbf{P}_{\boldsymbol{r}_{b_n}}(k|k) \\
&= \mathbf{B}_n(k) \left[\mathbf{I}_{NM \times NM} - \mathbf{A}(k) \left[\mathbf{A}^{\mathsf{T}}(k)\mathbf{A}(k)\right]^{-1} \mathbf{A}^{\mathsf{T}}(k)\right] \mathbf{B}_n^{\mathsf{T}}(k),
\end{aligned} \tag{5.51}$$

where $\mathbf{I}_{NM\times NM}$ is a $NM \times NM$ identity matrix. Define the matrix

$$\mathbf{\Omega}(k) \triangleq \mathbf{A}(k)\left[\mathbf{A}^{\mathsf{T}}(k)\mathbf{A}(k)\right]^{-1}\mathbf{A}^{\mathsf{T}}(k). \tag{5.52}$$

Substituting (5.52) into (5.51) gives

$$\mathbf{P}_{\bar{\boldsymbol{r}}_{b_n}}(k|k) - \mathbf{P}_{\boldsymbol{r}_{b_n}}(k|k) = \mathbf{B}_n(k)\mathbf{M}(k)\mathbf{B}_n^{\mathsf{T}}(k), \tag{5.53}$$

where $\mathbf{M}(k) \triangleq \mathbf{I}_{NM\times NM} - \mathbf{\Omega}(k)$. Note that,

(i) The matrix $\mathbf{\Omega} \in \mathbb{R}^{NM\times NM}$ is an orthogonal projection matrix, since it satisfies $\mathbf{\Omega}^2 = \mathbf{\Omega} = \mathbf{\Omega}^{\mathsf{T}}$. It has $N(M-1)$ eigenvalues of ones and N eigenvalues of zeros, since $\text{rank}(\mathbf{\Omega}) = \text{rank}(\mathbf{A}) = N(M-1)$. Therefore, $\mathbf{\Omega}$ is positive semi-definite.

(ii) The matrix $\mathbf{M}$ is also an orthogonal projection matrix, and its eigenvalues consist of N ones and $N(M-1)$ zeros [137]; therefore, it is positive semi-definite.

It follows from (ii) that

$$\mathbf{B}_n(k)\mathbf{M}(k)\mathbf{B}_n^{\mathsf{T}}(k) \succeq \mathbf{0}. \tag{5.54}$$

From (5.53) and (5.54), it can be concluded that

$$\mathbf{P}_{\bar{\boldsymbol{r}}_{b_n}}(k|k) \succeq \mathbf{P}_{\boldsymbol{r}_{b_n}}(k|k). \tag{5.55}$$

□

5.5 Simulation Results: TOA Versus TDOA

This section presents simulation results evaluating Theorem and Theorem established above.

5.5.1 Simulation Environment and Settings

The simulation environment consists of $N = 4$ UAV-mounted receivers and $M = 6$ SOP transmitters. The receiver's were set to have GPS available for the first 50 seconds of their trajectory and then unavailable for the remaining portion of the trajectory. SOP pseudo-ranges were available for their entire trajectories. The simulated UAV trajectories, SOP emitters' positions, and the UAVs' positions at the time GPS was set to become unavailable are illustrated in Fig. 5.3. The following describes the methods used to produce the simulated data.

UAVs' Trajectories

The UAVs' simulated trajectories were generated using a standard six degree of freedom (6DoF) kinematic model for airplanes [119]. Each vehicle performed the same maneuvers, which included the following segments conducted in succession over a 200 second period: 10 second straight and level linear acceleration along the direction of travel; 5 degree pitching climb for 30 seconds; 22 second straight and level linear velocity, while rolling to 60 degrees; five 60 degree left-banking turns. These trajectory segments were chosen because they collectively excite all 6DoF of the UAVs, i.e., both horizontal and vertical directions and all three angles (roll, pitch, and yaw), allowing the TOA and TDOA information fusion strategies to be studied under various maneuvers.

IMU Data

The gyroscope and accelerometer data were generated at 100 Hz using the simulated vehicles' accelerations and rotation rates through equations (5.6) and (5.5), respectively. The evolution of each vehicle's gyroscope and accelerometer biases were generated according to equations (5.3) and (5.4), using driving process noise with spectra $\mathbf{S}_{\boldsymbol{w}_{\text{gyr}},n} \equiv 10^{-8} \cdot \mathbf{I}_{3\times 3}$ and $\mathbf{S}_{\boldsymbol{w}_{\text{acc}},n} \equiv 10^{-8} \cdot \mathbf{I}_{3\times 3}$, respectively. The power of the corrupting white noise was set to correspond to a consumer-grade IMU. IMUs of this quality typically state the noise values in terms of accumulated noise. Each axis of the IMU was set to have an accumulated noise of 0.3 deg /s and 2.5 milligravities for the gyroscope and accelerometer, respectively. These spectra are mapped online to the discrete-time noise covariances $\mathbf{Q}_{\boldsymbol{n}_{\text{gyr}},n}$, $\mathbf{Q}_{\boldsymbol{n}_{\text{acc}},n}$, $\mathbf{Q}_{\boldsymbol{w}_{\text{gyr}},n}$, and $\mathbf{Q}_{\boldsymbol{w}_{\text{acc}},n}$ through the equations provided in Appendix A.6.

Receiver Clock

Each UAV-mounted receiver was set to be equipped with a TCXO, with clock process noise parameters $\{h_{0,r_n}, h_{-2,r_n}\}_{n=1}^{4} = \{9.4 \times 10^{-20}, 3.8 \times 10^{-21}\}$.

GPS Pseudoranges

GPS L1 C/A pseudoranges were generated at 1 Hz according to equation (5.8). The position of each GPS SV was generated by producing their orbits using Receiver Independent Exchange (RINEX) files downloaded on October 22, 2016 from a Continuously Operating Reference Station (CORS) server [124]. Eleven satellites were set to be available ($L = 11$) for $t \in [0, 50)$ seconds, and unavailable ($L = 0$) for $t \in [50, 200]$ seconds. The GPS pseudorange measurement noise terms were set to be independent from each other with measurement

noise variance computed according to [125]

$$ {}^{n}\sigma^2_{\text{sv},l} = \frac{c^2 t_{\text{eml}} B_{\text{DLL}} T_c^2}{2^n (C/N_0)_l} \left[1 - \frac{1}{T_{\text{CO}}{}^{n}(C/N_0)_l} \right], \tag{5.56} $$

where $t_{\text{eml}} \equiv 1$ chip, which is the early-minus-late correlator spacing, $B_{\text{DLL}} \equiv 0.05$ Hz is the delay lock loop bandwidth, $T_c \equiv 1/(1.023 \times 10^6)$ s is the chip duration and ${}^{n}(C/N_0)_l \equiv 2.512 \times 10^4$ Hz (equivalent to 44 dB-Hz) is the received carrier-to-noise ratio. The point at which GPS was cut off is illustrated as a red 'X' in Fig. 5.3.

SOP Pseudoranges

Pseudoranges were generated to the SOPs at 5 Hz according to equation (5.7). The evolution of each SOPs clock bias was modeled according to the dynamics discussed in Subsection 5.2.1, using parameters that correspond to a typical oven-controlled crystal oscillator (OCXO), with $\{h_{0,\text{sop},m}, h_{-2,\text{sop},m}\}_{m=1}^{6} = \{8 \times 10^{-20}, 4 \times 10^{-23}\}$. The SOP emitters' positions $\{\boldsymbol{r}_{\text{sop},m}\}_{m=1}^{6}$ were surveyed from cellular tower locations in downtown Los Angeles, California, USA. The SOP pseudorange measurement noise terms were set to be independent with a time-vary measurement noise variance using (5.56), except that ${}^{n}\sigma^2_{\text{sv},l}$ was replaced with ${}^{n}\sigma^2_{\text{sv},m}(j)$, $T_c \equiv 1/(1.2288 \times 10^6)$ s and ${}^{n}(C/N_0)_l$ is replaced with a time-varying log-distance path loss model [127]

$$ {}^{n}(C/N_0)'_m(j) = P_0 - 10 \cdot \log_{10}(d(j)/D_0), $$
$$ {}^{n}(C/N_0)_m(j) = 10^{[{}^{n}(C/N_0)'_m(j)/10]}, $$

where $P_0 \equiv 56$ dB-Hz is a calibration carrier-to-noise ratio at a distance $D_0 \equiv 1400$ m and $d(j) \triangleq \|\boldsymbol{r}_{b_n}(j) - \boldsymbol{r}_{\text{sop},m}(j)\|_2$. The calibration values P_0 and D_0 are values commonly observed by the authors during experimental campaigns [25].

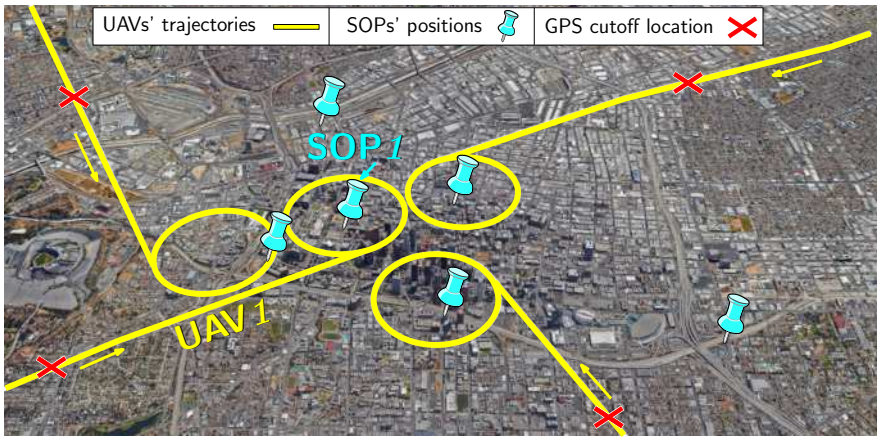

Figure 5.3: True trajectories the UAVs traversed (yellow), SOP emitters' positions (blue pins), and the UAVs' positions at the time GPS was cut off (red).

5.5.2 EKF-based CoRSLAM Filter Initialization

The initial estimates (at $t = 0$ seconds) of the UAVs' states were initialized by drawing a random error vector from a multivariate normal distribution and then applying the error to the "ground truth" state at $t = 0$. This initialization method is used instead of directly drawing the state estimate to deal with the quaternion initialization, which requires special handling. This method is described in the next three steps. First, the random error for each UAV was drawn according to

$$\tilde{\boldsymbol{x}}_{\mathrm{r},n}(0|0) \sim \mathcal{N}\left[\mathbf{0}_{17\times 1},\, \mathbf{P}_{\boldsymbol{x}_{\mathrm{r},n}}(0|0)\right]$$

$$\mathbf{P}_{\boldsymbol{x}_{\mathrm{r},n}}(0|0) \triangleq \mathrm{diag}\left[\mathbf{P}_{\boldsymbol{x}_{\mathrm{ins},n}}(0|0),\, \mathbf{P}_{\boldsymbol{x}_{\mathrm{clk,r}}}(0|0)\right]$$

$$\mathbf{P}_{\boldsymbol{x}_{\mathrm{ins},n}}(0|0) \equiv \mathrm{diag}\left[(10^{-2})\cdot\mathbf{I}_{3\times 3},\, 9\cdot\mathbf{I}_{3\times 3},\, \mathbf{I}_{3\times 3},\, (10^{-4})\cdot\mathbf{I}_{6\times 6}\right]$$

$$\mathbf{P}_{\boldsymbol{x}_{\mathrm{clk,r},n}}(0|0) \equiv \mathrm{diag}\left[9,\, 1\right],$$

were $\boldsymbol{a} \sim \mathcal{N}(\boldsymbol{\mu}, \mathbf{C})$ indicates that $\boldsymbol{a}$ is normally distributed with mean $\boldsymbol{\mu}$ and covariance $\mathbf{C}$. Second, to produce the initial quaternion estimate, the angle error $\boldsymbol{\theta} \in \mathbb{R}^3$, which are the first three elements of $\tilde{\boldsymbol{x}}_{\mathrm{r},n}$, are mapped to the error quaternion $\tilde{\boldsymbol{q}}_n \in \mathbb{R}^4$, which are then applied to the true state according to the equations shown in equation 4.14. Third, to produce initial

estimates of the remaining states, the remaining error components of $\tilde{\boldsymbol{x}}_{\mathrm{r},n}$ are applied to the true states as standard additive error.

The SOPs' state estimates were initialized according to $\hat{\boldsymbol{x}}_{\mathrm{sop},m}(0|0) \sim \mathcal{N}\left[\boldsymbol{x}_{\mathrm{sop},m}(0), \mathbf{P}_{\mathrm{sop}}(0|0)\right]$, for $m = 1, \ldots, M$, where $\boldsymbol{x}_{\mathrm{sop},m}(0) \equiv \left[\boldsymbol{r}_{\mathrm{sop},m}^{\mathsf{T}},\, 10^4, 10\right]^{\mathsf{T}}$, $\mathbf{P}_{\mathrm{sop}}(0|0) \equiv (10^4)\cdot\mathrm{diag}\left[\mathbf{I}_{3\times 3}\, 0.1,\, 0.01\right]$. This initialization scheme is used in simulation to ensure consistent initial priors in the EKF. In practice, if the initial SOPs' states are completely unknown, then a random position for each SOP may be drawn in the vicinity of the UAVs with a large enough uncertainty to encompass all possible points that a signal could be received from. The clock states may be initialized to zero with a large uncertainty. As long as there are enough vehicle's or the vehicles are moving, the position and clock states of the SOPs are observable [74].

5.5.3 TOA Versus TDOA Performance Comparison

This subsection evaluates the information fusion strategies (i) TOA and (ii) TDOA with SOP referencing, by comparing the resulting position estimation uncertainty of the UAVs produced by the EKF for each strategy. Errors for a traditional tightly-coupled GPS-aided INS are also provided for a comparative analysis. Fig. 5.4 shows the resulting estimation error trajectories and corresponding ± 3 times the EKF-produced estimation error standard deviations ($\pm 3\sigma$) for both strategies for the north, east, and down position states for UAV 1 and SOP 1. Fig. 5.5 illustrates the logarithm of the determinant of the estimation error covariance of the same UAV's position states, $\log\left\{\det\left[\mathbf{P}_{\boldsymbol{r}_{b_1}}\right]\right\}$, which is related to the volume of the uncertainty ellipsoid. Note that, TDOA measurements were produced using SOP 2 as the reference selection. The results were identical for choosing any other SOP as a reference, as expected from Theorem 5.4.1.

The following performance comparison may be concluded from these plots. First, the errors associated with the collaborative SOP-aided INS, regardless of the CoRSLAM information

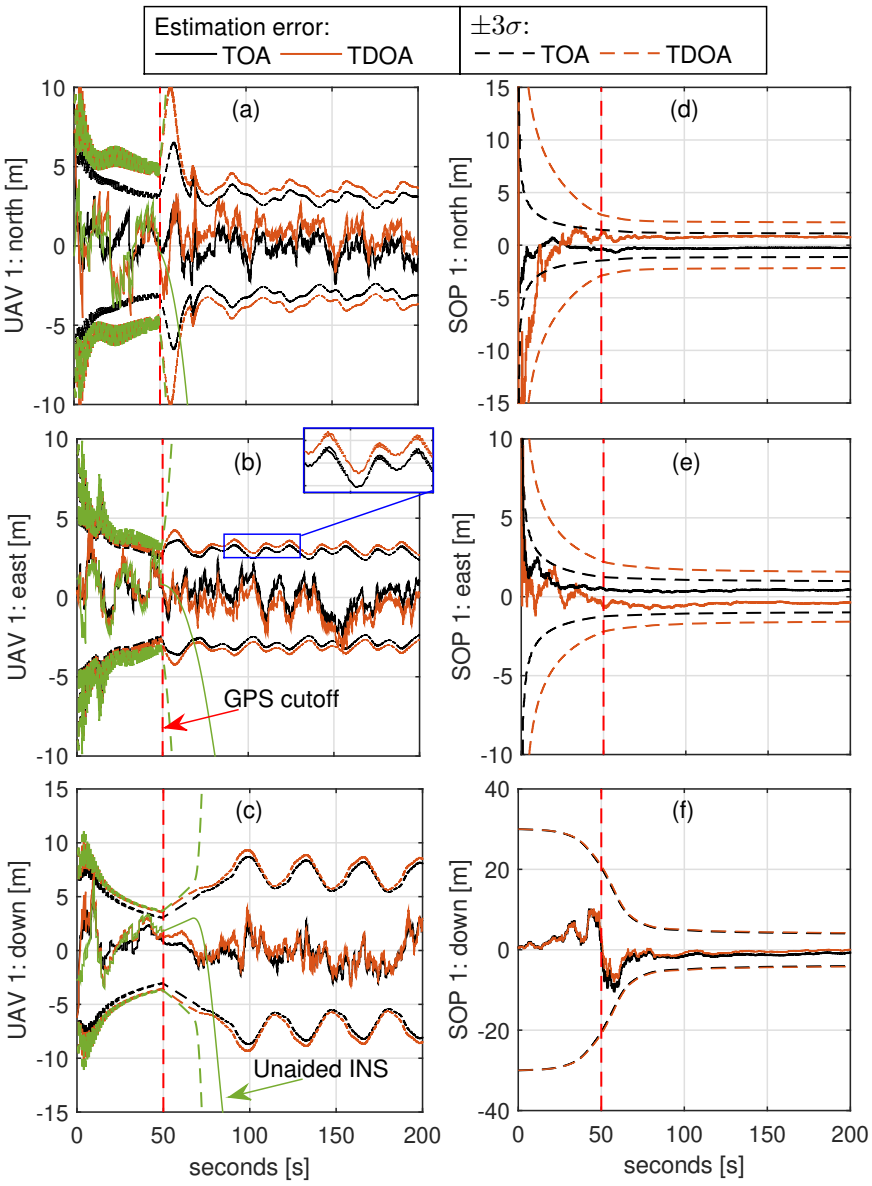

Figure 5.4: Estimation error trajectories and $\pm 3\sigma$ bounds for the (1) TOA and (2) TDOA with SOP referencing information fusion strategies for the environment depicted in Fig. 5.3. (a)-(c) Correspond to UAV 1 north, east, and down position errors, respectively. (d)-(f) Correspond to SOP 1 north, east, and down position errors, respectively. The red dotted line marks the time GPS pseudoranges were set to become unavailable ($L = 0$).

fusion strategy, remained bounded after GPS was cut off, whereas the errors associated with an unaided INS began to expectedly diverge. This indicates that if navigating vehicles are sharing and fusing INS information and pseudoranges drawn from SOPs with uncertain states, requirements on their INSs may be relaxed. That is, the cost of the navigation system can be reduced, since lower grade IMUs may still meet positioning accuracy requirements.

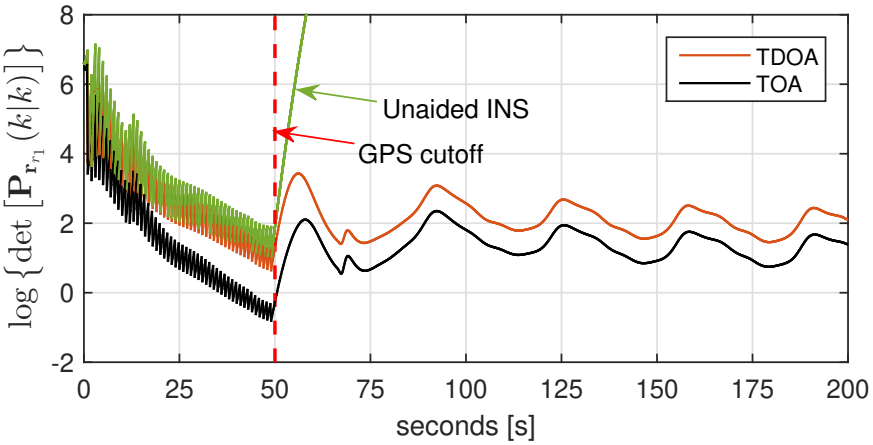

Figure 5.5: The logarithm of the determinant of the position estimation error covariance of UAV 1 for the environment depicted in Fig. 5.3.

Second, the TOA information fusion strategy consistently produced lower estimation error variances compared to the TDOA information fusion strategy in all coordinate directions. This indicates that the UAV's position uncertainty in any coordinate direction at any given time is less when SOP TOA measurements are shared and fused. Equivalently, the size of the uncertainty ellipsoid of the UAV's position states will be smaller if TOA is used and the difference in size is captured by the distance between in the $\log\left\{\det\left[\mathbf{P}_{\boldsymbol{r}_{b_1}}(k|k)\right]\right\}$ curves illustrated in Fig. 5.5. Note that these are representative results. Similar behavior of the estimation error uncertainties in the position states was reported for the other UAVs and SOPs and during simulation runs with different realizations of measurement and process noise. These findings support Theorem 5.4.2 established above.

5.6 Event-Based Information Fusion

In this section, an event-based information transmission scheme, which aims to minimize the amount of communicated data between collaborators, subject to a specified constraint on the vehicles' position estimation errors is developed.

5.6.1 Problem Formulation

Objective

The objective of the event-based information fusion scheme is to minimize the rate at which the data packets $\{\mathbf{\Lambda}_n\}_{n=1}^N$ are broadcasted by the navigating vehicles, while maintaining a specified estimation performance constraint. The performance constraint is defined such that the norm of any vehicle's position estimation error $\tilde{\boldsymbol{r}}_{b_n}$ remain below a specified maximum threshold $\xi_{\max}$ with probability p. Two norms are considered: $\|\tilde{\boldsymbol{r}}_{b_n}\|_2$ and $\|\tilde{\boldsymbol{r}}_{b_n}\|_\infty$, where $\|\boldsymbol{a}\|_q$ is the q-norm of vector $\boldsymbol{a}$. Formally, the performance constraint to be maintained is

$$\Pr\left[\|\tilde{\boldsymbol{r}}_{b_n}\|_q \leq \xi_{\max}\right] \geq p, \quad n = 1, \ldots, N, \tag{5.57}$$

where $\Pr[A]$ denotes the probability of event A and q is user-specified to be $q \equiv 2$ or $q \equiv \infty$.

Approach

In contrast to all vehicles transmitting $\{\mathbf{\Lambda}_n\}_{n=1}^N$ at a fixed rate, which is the rate at which measurements are made; in the event-based scheme, $\{\mathbf{\Lambda}_n\}_{n=1}^N$ are transmitted only if (5.57) would be violated, if transmission of $\{\mathbf{\Lambda}_n\}_{n=1}^N$ does not occur. Since the position estimation error *is not* available to the navigating vehicles, an online test is formulated using each vehicle's position estimation error covariance $\mathbf{P}_{\boldsymbol{r}_{b_n}}$, which *is* available to each vehicle via the EKF estimator, to check if (5.57) would be violated if transmission does not occur. In the next two subsections two separate tests are formulated: one corresponding to $\|\tilde{\boldsymbol{r}}_{b_n}\|_2$ and one corresponding to $\|\tilde{\boldsymbol{r}}_{b_n}\|_\infty$.

5.6.2 Two-Norm Test Formulation

Lemma 5.6.1. *Consider the performance constraint (5.57) with $q \equiv 2$ and a user specified p and $\xi_{\max}$. Testing if (5.57) is violated is equivalent to checking if*

$$\|\mathbf{P}_{\boldsymbol{r}_{r_n}}\|_2 \leq \frac{\xi_{\max}^2}{\eta_n}, \quad n = 1, \ldots, N, \tag{5.58}$$

is violated, where $\mathbf{P}_{\boldsymbol{r}_{r_n}}$ is the estimation error covariance associated with the n^{th} navigating vehicle, and η_n is the value of the inverse cumulative distribution function (cdf) of the Mahalanobis norm-squared of the estimation error $\|\tilde{\boldsymbol{r}}_{b_n}\|_{\text{M}}^2$ evaluated at p.

Proof. To formulate the test for (5.57) corresponding to $\|\tilde{\boldsymbol{r}}_{b_n}\|_2$, the Mahalanobis norm (or Mahalanobis distance) of the position estimation error for vehicle n, denoted $\|\tilde{\boldsymbol{r}}_{b_n}\|_{\text{M}}$, is used, which is given by

$$\|\tilde{\boldsymbol{r}}_{b_n}\|_{\text{M}}(k) = \sqrt{[\boldsymbol{r}_{b_n}(k) - \hat{\boldsymbol{r}}_{b_n}(k|k)]^{\mathsf{T}} \mathbf{P}_{\boldsymbol{r}_{b_n}}^{-1}(k|k)[\boldsymbol{r}_{b_n}(k) - \hat{\boldsymbol{r}}_{b_n}(k|k)]}. \tag{5.59}$$

In this context, the Mahalanobis norm provides a measure of how many standard deviations the true position is away from the estimated position. In what follows, it will be shown how $\|\tilde{\boldsymbol{r}}_{b_n}\|_{\text{M}}$ is related to the performance constraint (5.57), and how it leads to a simple test that each vehicle may perform to determine if $\{\boldsymbol{\Lambda}_n\}_{n=1}^N$ should be transmitted. Time dependency will be dropped in the sequel to simplify the notation.

Since the covariance $\mathbf{P}_{\boldsymbol{r}_{b_n}}$ is a real-valued, symmetric, positive definite matrix, it has an

eigendecomposition given by

$$\mathbf{P}_{\boldsymbol{r}_{b_n}} = \mathbf{U}_n \mathbf{D}_n \mathbf{U}_n^{\mathsf{T}}, \tag{5.60}$$
$$\mathbf{D} = \operatorname{diag}\left[\lambda_{n,1}, \lambda_{n,2}, \lambda_{n,3}\right],$$

where $\lambda_{n,i}$ is the i^{th} eigenvalue of $\mathbf{P}_{\boldsymbol{r}_{b_n}}$ and $\mathbf{U}_n$ is an orthogonal matrix whose i^{th} column is the i^{th} eigenvector of $\mathbf{P}_{\boldsymbol{r}_{b_n}}$. Substituting (5.60) into (5.59) and squaring both sides yields

$$\|\tilde{\boldsymbol{r}}_{b_n}\|_{\mathrm{M}}^2 = \boldsymbol{\xi}_n^{\mathsf{T}} \mathbf{D}_n^{-1} \boldsymbol{\xi}_n, \tag{5.61}$$

$$\boldsymbol{\xi}_n \triangleq \mathbf{U}^{\mathsf{T}} (\boldsymbol{r}_{b_n} - \hat{\boldsymbol{r}}_{b_n}). \tag{5.62}$$

The vector $\boldsymbol{\xi}_n = [\xi_{n,1}, \xi_{n,2}, \xi_{n,3}]^{\mathsf{T}}$ is the position estimation error $\tilde{\boldsymbol{r}}_{b_n}$ expressed in frame $\{g\}$, rotated by the orthogonal (rotation) matrix $\mathbf{U}^{\mathsf{T}}$ into a coordinate frame $\{f\}$, whose axes coincide with the principal axes of an ellipsoid. This ellipsoid is known as the probability concentration ellipsoid $\mathcal{E}$, which represents the probability p of the error $\boldsymbol{\xi}_n$ lying on or within the ellipsoid [80], where

$$p = \Pr\left(\|\tilde{\boldsymbol{r}}_{b_n}\|_{\mathrm{M}}^2 \leq \eta_n\right). \tag{5.63}$$

Given p and the distribution of $\|\tilde{\boldsymbol{r}}_{b_n}\|_{\mathrm{M}}^2$, the value η_n can be determined [138].

The principal axes of the confidence ellipsoid $\mathcal{E}$ are found by expanding the right side of (5.61) and substituting the expansion into the inequality $\|\tilde{\boldsymbol{r}}_{b_n}\|_{\mathrm{M}}^2 \leq \eta_n$ from (5.63), which gives

$$\frac{\xi_{n,1}^2}{\eta_n \lambda_{n,1}} + \frac{\xi_{n,2}^2}{\eta_n \lambda_{n,2}} + \frac{\xi_{n,3}^2}{\eta_n \lambda_{n,3}} \leq 1, \tag{5.64}$$

which is the equation of an ellipsoid with radii $\sqrt{\eta_n \lambda_{n,i}}$, for $i = 1, 2, 3$. The ellipsoid and the bounding constraint corresponding to $\|\tilde{\boldsymbol{r}}_{b_n}\|_2 \leq \xi_{\max}$ are illustrated as a 2-D example in Fig. 5.6.

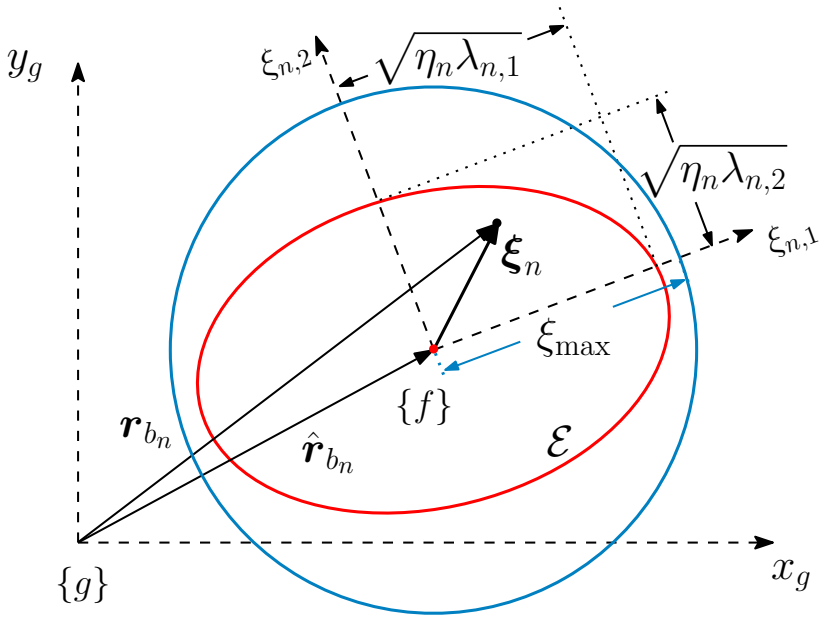

Figure 5.6: Probability concentration ellipse $\mathcal{E}$ with origin $\hat{\boldsymbol{r}}_{r_n}$ and radii $\sqrt{\eta_n \lambda_{n,i}}$, $i = 1, 2$.

Note that, although the value of $\boldsymbol{\xi}_n$ *is not available* to the navigating vehicle, the eigenvalues $\{\lambda_{n,i}\}_{i=1}^3$ and the specified probability p governing the size and shape of the ellipsoid $\mathcal{E}$ *are available* and upper-bound the "size" of $\boldsymbol{\xi}_n$. Specifically, $\|\boldsymbol{\xi}_n\|_2$ is bounded by the major axis of $\mathcal{E}$, which is given by

$$\max_{\mathcal{E}} \|\boldsymbol{\xi}_n\|_2 = \max_{\mathcal{E}} \|\tilde{\boldsymbol{r}}_{b_n}\|_2 = \sqrt{\eta_n \lambda_{\max}[\mathbf{P}_{\boldsymbol{r}_{b_n}}]}, \tag{5.65}$$

where $\max_{\mathcal{E}} d$ denotes the maximum value of d in set $\mathcal{E}$, $\lambda_{\max}[\mathbf{X}]$ denotes the maximum eigenvalue of $\mathbf{X}$, and $\|\tilde{\boldsymbol{r}}_{b_n}\|_2 = \|\boldsymbol{\xi}\|_2$ has been used, which holds since the 2-norm is invariant under coordinate frame rotation. Since the error constraint $\xi_{\max}$ is also invariant under coordinate frame rotation, the problem boils down to checking if the major axis of the

ellipsoid $\mathcal{E}$ is less than $\xi_{\max}$, i.e.,

$$\sqrt{\eta_n \lambda_{\max}[\mathbf{P}_{\boldsymbol{r}_{b_n}}]} \leq \xi_{\max}. \tag{5.66}$$

Finally, noting that $\lambda_{\max}[\mathbf{P}_{\boldsymbol{r}_{b_n}}] = \|\mathbf{P}_{\boldsymbol{r}_{b_n}}\|_2$ for covariance matrices and by solving (5.66) in terms of the specified constraints, the test simplifies to checking the violation of

$$\|\mathbf{P}_{\boldsymbol{r}_{r_n}}\|_2 \leq \frac{\xi_{\max}^2}{\eta_n}.$$

□

5.6.3 Infinity-Norm Test Formulation

Lemma 5.6.2. *Consider the performance constraint (5.57) with $q \equiv \infty$ and a user specified coordinate frame $\{g\}$, probability p, and maximum error $\xi_{\max}$. Testing if (5.57) is violated is equivalent to checking if*

$$\|\mathbf{P}_{\boldsymbol{r}_{r_n}}\|_{\max} \leq \frac{\xi_{\max}^2}{\eta_n}, \quad n = 1, \ldots, N, \tag{5.67}$$

is violated, where $\|\mathbf{X}\|_{\max}$ denotes the maximum norm of a matrix $\mathbf{X} \in \mathbb{R}^{d_1 \times d_2}$, which is given by

$$\|\mathbf{X}\|_{\max} \triangleq \max\{|\mathbf{X}_{ij}| \, | i = 1, \ldots, d_1, \, j = 1, \ldots, d_2\},$$

the matrix $\mathbf{P}_{\boldsymbol{r}_{r_n}}$ is the position estimation error covariance associated with the n^{th} navigating vehicle, and η_n is the value of the inverse cdf of the Mahalanobis norm-squared of the estimation error $\|\tilde{\boldsymbol{r}}_{b_n}\|_{\text{M}}^2$ evaluated at p.

Proof. The test formulation and the ∞-norm error constraint are coordinate frame dependent, since the ∞-norm is *not* invariant under coordinate frame rotations. Therefore, the coordinate frame $\{g\}$ in which the test is conducted is specified by the user along with $\xi_{\max}$ and p, (e.g., test if p is less than the probability that the maximum of the north, east, and down (NED) errors is less than $\xi_{\max}$). In contrast to the bounding circle (sphere in 3-D) associated with the constraint $\|\tilde{\boldsymbol{r}}_{b_n}\|_2 \leq \xi_{\max}$ in Fig. 5.6, the constraint $\|\tilde{\boldsymbol{r}}_{b_n}\|_\infty \leq \xi_{\max}$ is geometrically interpreted as a square (cube in 3-D), which is symmetric about the origin, with each of its sides a distance of $\xi_{\max}$ from the origin. Since the probability concentration ellipsoid $\mathcal{E}$ provides a bounding surface for which the estimation error is contained within for a specified probability p, a test will be formulated to check if $\mathcal{E}$ is contained within the cube corresponding to $\|\tilde{\boldsymbol{r}}_{b_n}\|_\infty \leq \xi_{\max}$.

The ellipsoid $\mathcal{E}$ expressed in $\{g\}$ is found by substituting (5.59) into the inequality $\|\tilde{\boldsymbol{r}}_{b_n}\|_{\mathrm{M}}^2 \leq \eta_n$ from (5.63), which gives

$$\frac{1}{\eta_n}\tilde{\boldsymbol{r}}_{b_n}^{\mathsf{T}}\mathbf{P}_{\tilde{\boldsymbol{r}}_{b_n}}^{-1}\tilde{\boldsymbol{r}}_{b_n} \leq 1. \tag{5.68}$$

The bounding cube is represented as a collection of six planes, defined by normal vectors $\pm\boldsymbol{n}_i$, $i = 1, 2, 3$, each of which is parallel to the corresponding unit vectors that define the coordinate frame $\{g\}$, e.g., $\boldsymbol{n}_2$ corresponds to the y_g direction and is parallel to $\boldsymbol{e}_2$, where $\boldsymbol{e}_i \in \mathbb{R}^3$ is the standard unit basis vector, containing a one in the i^{th} position and zeros elsewhere. Given the constraint $\xi_{\max}$, the i^{th} plane, denoted $\mathcal{P}_i$, is given by

$$\boldsymbol{n}_i^{\mathsf{T}}\tilde{\boldsymbol{r}}_{b_n} - \xi_{\max} = 0. \tag{5.69}$$

If the ellipsoid $\mathcal{E}$ extends beyond the plane $\mathcal{P}_i$, an intersecting ellipse $\mathcal{E}_i \triangleq \mathcal{E} \cap \mathcal{P}_\alpha$ will exist. The relationship between $\mathcal{E}$, $\mathcal{P}_i$, and $\mathcal{E}_i$ for $i = 2$ are illustrated in Fig. 5.7.

Since $\mathcal{E}$ and the bounding cube are both symmetric about the origin of $\{g\}$, it suffices to

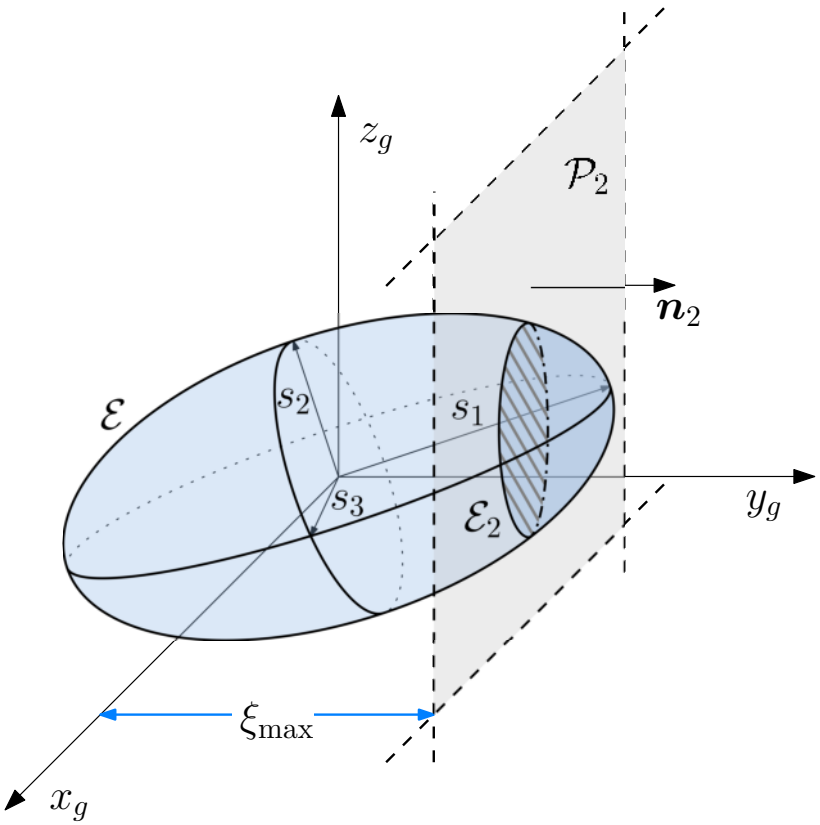

Figure 5.7: Probability concentration ellipsoid $\mathcal{E}$ with radii $s_\alpha \triangleq \sqrt{\eta_n \lambda_{n,\alpha}}$, $\alpha = 1, 2, 3$, and plane $\mathcal{P}_2$, representing one of six surfaces of the cube constraint. If $\mathcal{E}$ intersects the cube constraint at plane $\mathcal{P}_2$, then the ellipse $\mathcal{E}_2$ exists.

test if $\exists \mathcal{E}_i$, for only the three positive directions to determine if $\mathcal{E}$ is contained within the bounding cube. In what follows, the test for a general i^{th} plane is formulated. The points on and within the intersecting ellipse $\mathcal{E}_i$ represents the solution space that satisfies both (5.68) and (5.69). The expression for this solution space is found using the next steps. First, the i^{th} parallel vectors are set equal to each other, i.e., $\boldsymbol{n}_i \equiv \boldsymbol{e}_i$, which gives

$$\boldsymbol{e}_i^{\mathsf{T}} \tilde{\boldsymbol{r}}_{b_n} = \xi_{\max}, \tag{5.70}$$

which equates the i^{th} element of $\tilde{\boldsymbol{r}}_{b_n}$ to $\xi_{\max}$. Second, (5.70) is substituted into (5.68). For convenience in the remainder of the test formulation, $\tilde{\boldsymbol{r}}_{b_n}$ will be arranged to place $\xi_{\max}$ to the first element of a vector and the remaining elements will follow in $\boldsymbol{u}_i$. The matrix $\mathbf{P}^{-1}_{\tilde{\boldsymbol{r}}_{b_n}}$ is modified accordingly, so that the i^{th} diagonal element is placed into the top-left

element, denoted β_i and the corresponding cross-correlation elements are permutated into vector $\boldsymbol{b}_i \in \mathbb{R}^2$, and the remaining elements are placed into $\mathbf{A} \in \mathbb{R}^{2\times 2}$. These permutations are performed using a permutation matrix $\mathbf{N}_i$ through

$$\boldsymbol{y}_i \triangleq \mathbf{N}_i \tilde{\boldsymbol{r}}_{b_n} = \begin{bmatrix} \xi_{\max} \\ \boldsymbol{u}_i \end{bmatrix}, \quad \mathbf{Y}_i \triangleq \mathbf{N}_i \mathbf{P}^{-1}_{\tilde{\boldsymbol{r}}_{b_n}} \mathbf{N}_i^{\mathsf{T}} = \begin{bmatrix} \beta_i & \boldsymbol{b}_i^{\mathsf{T}} \\ \boldsymbol{b}_i & \mathbf{A}_i \end{bmatrix},$$

$$\mathbf{N}_i \triangleq \begin{bmatrix} \boldsymbol{e}_i^{\mathsf{T}} \\ \boldsymbol{G}_i \end{bmatrix}, \quad \mathbf{G}_i = \begin{bmatrix} \boldsymbol{e}_{\alpha\backslash i}^{\mathsf{T}} \\ \boldsymbol{e}_{\alpha+1\backslash i}^{\mathsf{T}} \end{bmatrix}, \quad \alpha = 1, 2, 3.$$

Noting the properties of permutation matrices

$$\mathbf{N}_i \mathbf{N}_i^{\mathsf{T}} = \mathbf{N}_i^{\mathsf{T}} \mathbf{N}_i = \mathbf{I}_{3\times 3},$$

the ellipsoid equation in (5.68) may be rewritten as

$$\boldsymbol{y}_i^{\mathsf{T}} \mathbf{Y}_i \boldsymbol{y}_i = \begin{bmatrix} \xi_{\max} \\ \boldsymbol{u}_i \end{bmatrix}^{\mathsf{T}} \begin{bmatrix} \beta_i & \boldsymbol{b}_i^{\mathsf{T}} \\ \boldsymbol{b}_i & \mathbf{A}_i \end{bmatrix} \begin{bmatrix} \xi_{\max} \\ \boldsymbol{u}_i \end{bmatrix} \leq \eta_n. \tag{5.71}$$

To check if there is a feasible solution to (5.71), the left side of the inequality is minimized over the remaining variables $\boldsymbol{u}_i$ and then the optimal value is compared with the right side of the inequality. Since $\mathbf{P}^{-1}_{\boldsymbol{r}_{b_n}} \succ \mathbf{0}$, then $\mathbf{A} = \mathbf{G}_\alpha \mathbf{P}^{-1}_{\boldsymbol{r}_{b_n}} \mathbf{G}^{\mathsf{T}} \succ \mathbf{0}$, making this a convex optimization problem with a known optimal value, which is given by [103]

$$\inf_{\boldsymbol{u}} \begin{bmatrix} \xi_{\max} \\ \boldsymbol{u}_i \end{bmatrix}^{\mathsf{T}} \begin{bmatrix} \beta_i & \boldsymbol{b}_i^{\mathsf{T}} \\ \boldsymbol{b}_i & \mathbf{A}_i \end{bmatrix} \begin{bmatrix} \xi_{\max} \\ \boldsymbol{u}_i \end{bmatrix} = \xi_{\max}^2 \mathbf{S}_i, \tag{5.72}$$

where $\mathbf{S}_i$ is the Schur complement of $\mathbf{A}_i$, which is equal to

$$\mathbf{S}_i = \beta_i - \boldsymbol{b}_i^{\mathsf{T}} \mathbf{A}_i^{-1} \boldsymbol{b}_i. \tag{5.73}$$

Checking if $\exists \mathcal{E}_i$ for $i = 1, 2, 3$ to determine if $\mathcal{E}$ is intersecting the bounding cube is equivalent to checking if $\mathbf{S}_i^{-1} \geq \xi_{\max}^2/\eta_n$. Conversely, checking if $\nexists \mathcal{E}_i$ for $i = 1, 2, 3$ to determine if $\mathcal{E}$ is contained within the bounding cube is equivalent to checking if

$$\mathbf{S}_i^{-1} < \frac{\xi_{\max}^2}{\eta_n} \quad \text{for} \quad i = 1, 2, 3. \tag{5.74}$$

Note that the Schur complement $\mathbf{S}_i$ is non-singular, since $\mathbf{P}_{\boldsymbol{r}_{b_n}}^{-1} \succ \mathbf{0}$ [103].

The number of tests in (5.74) can be reduced from three to one by testing only $\max_i \mathbf{S}_i^{-1}$. Conveniently, this value is equal to the maximum entry of $\mathbf{P}_{\boldsymbol{r}_{b_n}}$. To see this, consider the matrix block inversion property of the Schur complement [103]

$$\begin{bmatrix} \beta_i & \boldsymbol{b}_i^{\mathsf{T}} \\ \boldsymbol{b}_i & \mathbf{A}_i \end{bmatrix}^{-1} = \begin{bmatrix} \mathbf{S}_i^{-1} & -\mathbf{S}_i^{-1}\boldsymbol{b}_i^{\mathsf{T}}\mathbf{A}_i^{-1} \\ -\mathbf{A}_i^{-1}\mathbf{b}_i\mathbf{S}_i^{-1} & \mathbf{A}_i^{-1} + \mathbf{A}_i^{-1}\boldsymbol{b}_i\mathbf{S}_i^{-1}\boldsymbol{b}_i^{\mathsf{T}}\mathbf{A}_i^{-1} \end{bmatrix}. \tag{5.75}$$

The left side of (5.75) is

$$\mathbf{Y}_i^{-1} = \mathbf{N}_i \mathbf{P}_{\tilde{\boldsymbol{r}}_{b_n}} \mathbf{N}_i^{\mathsf{T}}. \tag{5.76}$$

From (5.75) one can deduce that $\mathbf{S}_i^{-1}$ is equal to the top-left element of $\mathbf{Y}_i^{-1}$. From (5.76) one can conclude that the top-left element of $\mathbf{Y}_i^{-1}$ is equal to the i^{th} diagonal element of $\mathbf{P}_{\tilde{\boldsymbol{r}}_{b_n}}$, since permutations conducted on the inverse of a matrix correspond to permutations conducted on the matrix itself. Finally, since the largest elements of a symmetric positive definite matrix are the diagonal elements, it suffices to check the largest element of the matrix. Therefore, the test to determine if the performance constraint (5.57) with $q \equiv \infty$ will be violated, boils down to each vehicle checking

$$\|\mathbf{P}_{\boldsymbol{r}_{r_n}}\|_{\max} \leq \frac{\xi_{\max}^2}{\eta_n}.$$

□

5.7 Simulation Results: Event-Based Information Fusion

In this section, simulation results are presented demonstrating the event-based information transmission scheme.

If the test (5.58) or (5.67) fails for any vehicle, the vehicle whose test fails requests all vehicles to transmit their $\{\mathbf{\Lambda}_n\}_{n=1}^N$, and subsequently all vehicles perform an EKF correction upon receiving the communicated packets from other vehicles. An event-trigger threshold on the EKF-produced 3σ error standard deviations of the vehicles' position states, over which the transmission of $\{\mathbf{\Lambda}_n\}_{n=1}^N$ is requested, can be found by taking the square root of (5.58), which yields

$$3\sigma \leq 3\frac{\xi_{\max}}{\sqrt{\eta_n}}. \tag{5.77}$$

In the next subsection, the pdf of $\|\tilde{\boldsymbol{r}}_{b_n}\|_{\mathrm{M}}^2$ is characterized in order to compute η_n using the inverse cumulative distribution function (cdf) on (5.63).

5.7.1 Mahalanobis Norm-Squared Distribution Characterization

To determine the pdf of $\|\tilde{\boldsymbol{r}}_{b_n}\|_{\mathrm{M}}^2$, 5×10^4 Monte Carlo runs were conducted using the environment illustrated in Fig 4.4. The value of $\|\tilde{\boldsymbol{r}}_{b_n}\|_{\mathrm{M}}^2$ was recorded for each run for $n = 1, \ldots, N$. The same simulation settings described in Subsection 5.5.1 were used, except each run used a different initial state estimate and different realizations of process and measurement noise.

GPS was set to be available for $t \in [0, 50)$ seconds with $L = 11$ and unavailable ($L = 0$) for $t \in [50, 200]$ seconds. Fig. 5.8 illustrates the Monte Carlo runs histogram of $\|\tilde{\boldsymbol{r}}_{b_n}\|^2_{\mathrm{M}}$ for UAV 1, from which it is deduced that the pdf follows a gamma distribution given by

$$p(\|\tilde{\boldsymbol{r}}_{b_n}\|^2_{\mathrm{M}}; s, \theta) = \frac{1}{\Gamma(s)\theta^s}(\|\tilde{\boldsymbol{r}}_{b_n}\|^2_{\mathrm{M}})^{s-1} e^{\frac{-\|\tilde{\boldsymbol{r}}_{b_n}\|^2_{\mathrm{M}}}{\theta}},$$

where s and θ are the shape and scale parameter of the gamma distribution, respectively, and Γ is the complete gamma function, which is given by

$$\Gamma(z) = \int_0^\infty x^{z-1} e^{-x} dx.$$

A maximum likelihood estimator was employed to find the parameters s and θ [139]. During GPS availability ($L = 11$), the parameters were found to be $\{s, \theta\} \approx \{3/2, 2\}$, which is equivalent to a Chi-squared distribution, with three DoF. During GPS unavailability ($L = 0$), the parameters were found to be $\{s, \theta\} \approx \{3/2, 2.63\}$. The estimated pdf for the GPS availability period is also plotted in Fig. 5.8(b) to show the shift in the pdf's scale parameter when GPS becomes unavailable.

It is important to note that during GPS unavailability the shape and scale parameters $\{s, \theta\}$ depend on the environment (e.g., number of SOPs and geometric distribution of SOPs). However, in a practical scenario the parameters $\{s, \theta\}$ may be determined online when GPS is still available. To do this, the following procedure may be used. First, in addition to the EKF running that has access to GPS, a parallel EKF is run with GPS fictitiously cut off. Second, the estimated UAVs' positions using SOPs only (GPS unavailability) are differenced with the GPS produced position estimates in order to calculate a time history of $\tilde{\boldsymbol{r}}_{b_n}$, $n = 1, \ldots, N$. Third, the time history $\tilde{\boldsymbol{r}}_{b_n}$ is downsampled to make the signal white. Forth, the distribution of $\|\tilde{\boldsymbol{r}}_{b_n}\|^2_{\mathrm{M}}$ is characterized by passing the downsampled signal through a maximum likelihood estimator for a gamma distribution [139].

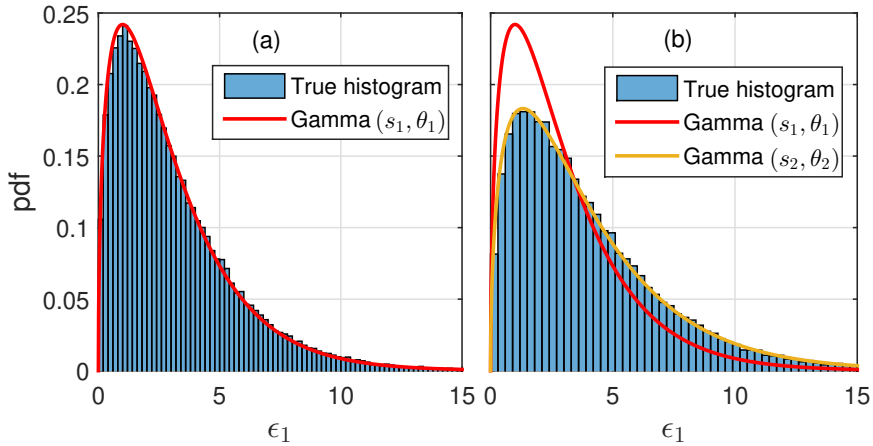

Figure 5.8: (a) Histogram of $\|\tilde{\boldsymbol{r}}_{b_1}\|^2_{\mathrm{M}}$ during GPS availability ($L = 11$) and gamma distribution with parameters $s_1 = 3/2$ and $\theta_1 = 2$ and (b) histogram of $\|\tilde{\boldsymbol{r}}_{b_1}\|^2_{\mathrm{M}}$ during GPS unavailability ($L = 0$) and gamma distribution with parameters $s_2 = 3/2$ and $\theta_2 = 2.63$.

5.7.2 Event-Based Versus Fixed-Rate

In this subsection, simulation results are presented to demonstrate the event-based communication scheme discussed in this section and to compare its resulting estimation performance and corresponding communication rate with a fixed-rate communication scheme.

To this end, the same environment illustrated in Fig. 4.4 was simulated using the settings described in subsection 5.5.1. GPS was set to be available for $t \in [0, 50)$ seconds, and unavailable for $t \in [50, 200]$ seconds. Two EKF-CoRSLAM estimators were run to estimate the UAVs' trajectories. The only difference between the estimators is in when the communication and correction step is performed: (i) fixed-rate, when measurements are made or (ii) event-based, when any UAV violates (5.58) or (5.67).

Each estimator was initialized according to the procedure discussed in subsection 5.5.2. For the event-based run, the two-norm ($q = 2$) test in (5.58) was employed, where the constraints specified on the UAVs' position estimates were set to be $\xi_{\max} \equiv 10$ m with a confidence probability $p \equiv 0.999$. Using this p and the shape and scale parameters found in Subsection 5.7.1, the inverse cdf of (5.63) evaluated to $\eta_1 \approx 16.27$ and $\eta_1 \approx 21.37$ for the GPS availability and unavailability periods, respectively. Plugging these values into (5.58) yields

$\|\mathbf{P}_{\boldsymbol{r}_{b_1}}(k|j)\|_2 \leq 6.15$ and $\|\mathbf{P}_{\boldsymbol{r}_{b_1}}(k|j)\|_2 \leq 4.68$ for the GPS available and unavailable periods, respectively. The infinity-norm ($q = \infty$) test in (5.67) was also employed on the UAVs' east, north, and down position covariance during a separate run. Plugging the above values into (5.67) yields $\|\mathbf{P}_{\boldsymbol{r}_{b_1}}(k|j)\|_{\max} \leq 6.15$ and $\|\mathbf{P}_{\boldsymbol{r}_{b_1}}(k|j)\|_{\max} \leq 4.68$ for the GPS available and unavailable periods, respectively.

To visualize the reduction of the transmitted data, the accumulation of transmitted data was recorded for each scheme by summing the number of transmitted bits each time a packet transmit occurred. The size of the packet in bits was found by summing the number of values in (5.13) and setting each value to be a 32-bit float data type, as described in [37]. For a comparative analysis, the accumulation of transmitted data for transmitting raw IMU data was also recorded.

Fig. 5.9 shows the resulting east, north, and down errors and corresponding $\pm 3\sigma$ bounds of UAV 1 along with the $\pm 3\sigma$ bound event-trigger thresholds (5.77) during GPS unavailability. To avoid convoluting the plot, only results for the test in (5.58) are shown in Fig. 5.9, since it was found that the resulting EKF plots were very similar to using the two-norm ($q = \infty$) test in (5.67). This is due to the dominate vertical uncertainties, which make $\|\mathbf{P}_{\boldsymbol{r}_{b_1}}(k|j)\|_2 \cong \|\mathbf{P}_{\boldsymbol{r}_{b_1}}(k|j)\|_{\max}$. Fig. 5.10 shows the resulting $\log\left\{\det\left[\mathbf{P}_{\boldsymbol{r}_{b_1}}(k|j)\right]\right\}$ for using the fixed rate and event-based communication schemes. The resulting accumulation of transmitted data for each scheme is illustrated in Fig. 5.11. Similar plots were noted for the other three UAVs.

The following may be concluded from these plots. First, note from Fig. 5.9 that the estimation uncertainties associated with the event-based communication scheme are consistently larger than the ones produced by the fixed-rate scheme. This is due to skipped measurement updates when the test (5.58) is satisfied. Second, it can be seen that the UAV's position uncertainties reduce when the errors approach the trigger threshold, which causes all UAVs to transmit their data packets and perform an EKF update. The threshold is triggered only

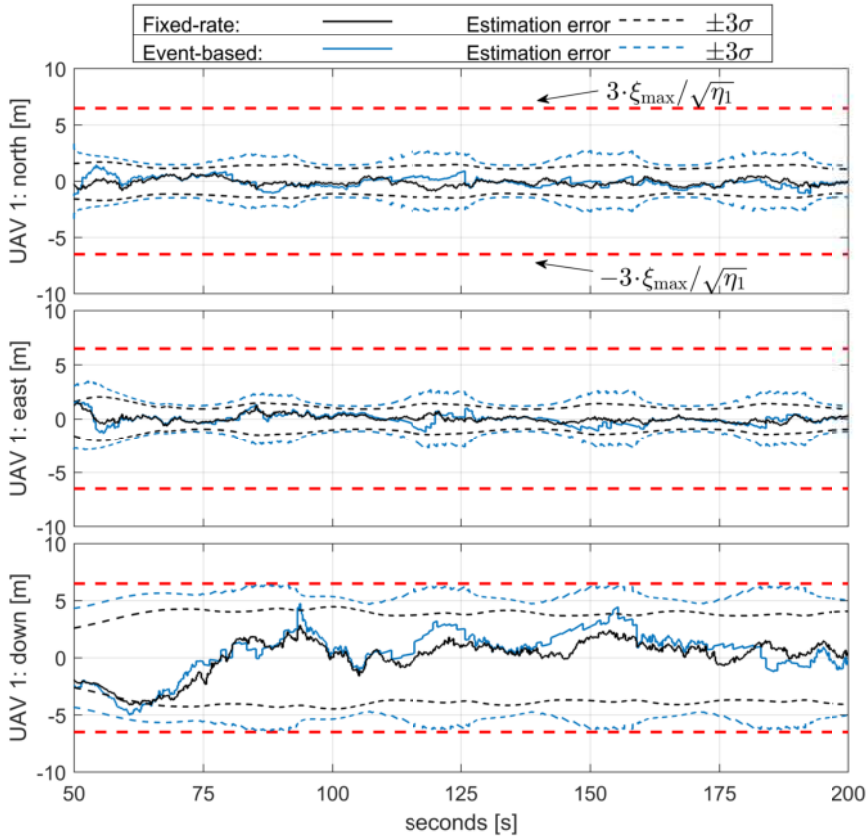

Figure 5.9: Resulting north, east, and down errors and corresponding $\pm 3\sigma$ bounds for UAV 1 for the event-based and fixed-rate communication schemes.

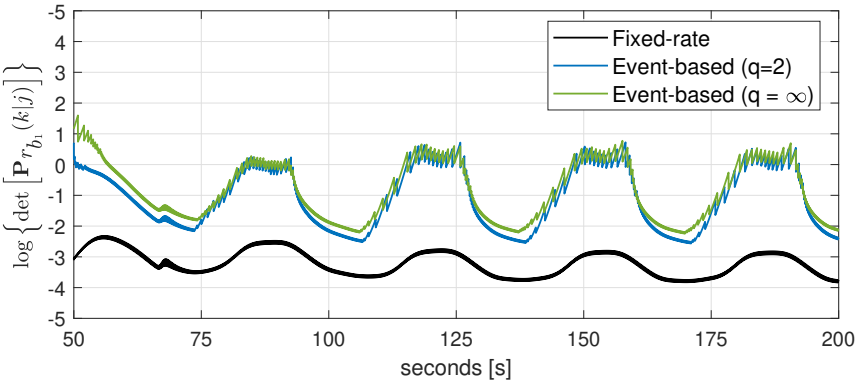

Figure 5.10: The resulting logarithm of the determinant of the estimation error covariance for the position states of UAV 1 for the event-based and fixed-rate communication schemes, as well as the event-trigger threshold.

by the UAVs' vertical uncertainty, which is expected due to the large vertical dilution of precision due to all of the SOPs residing under the UAVs. Third, the degradation in estimation performance by skipping these measurements is captured by the distance between

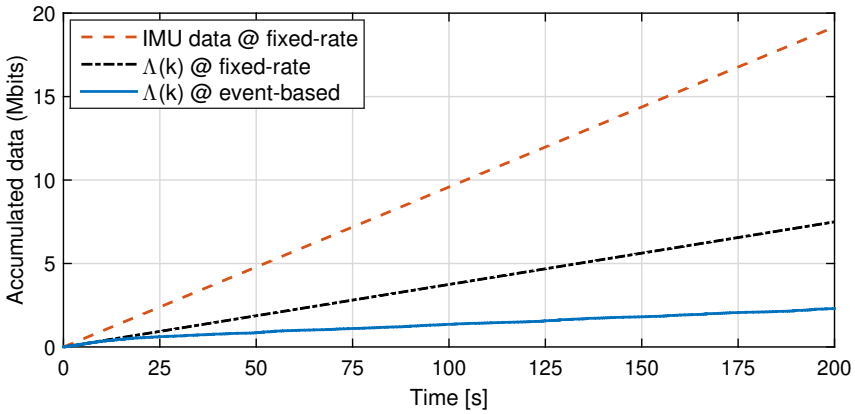

Figure 5.11: Accumulation of the communicated data for transmitting IMU data, transmitting the packet $\mathbf{\Lambda}$ at a fixed-rate, and transmitting the packet $\mathbf{\Lambda}$ using the event-based communication scheme.

the corresponding $\pm 3\sigma$ bounds in Fig. 5.9 and by $\log\left\{\det\left[\mathbf{P}_{\boldsymbol{r}_{b_1}}(k|j)\right]\right\}$ curves in Fig. 5.10. Fourth, the similarity between using (5.58) and (5.67) for event triggering is seen by comparing the $\log\left\{\det\left[\mathbf{P}_{\boldsymbol{r}_{b_1}}(k|j)\right]\right\}$ curves in Fig. 5.10. Finally, from Fig. 5.11, the following accumulation of transmitted data for each communication strategy was determined: 6.46 MB for transmitting $\mathbf{\Lambda}$ at a fixed rate and 3.06 MB for transmitting $\mathbf{\Lambda}$ using the event-based scheme. Therefore, although using the event-based strategy to transmit $\mathbf{\Lambda}$ causes a small increase in position uncertainty, the accumulated transmitted data is reduced by 52.6% compared to transmitting $\mathbf{\Lambda}$ using fixed-rate scheme. Transmitting raw IMU data at a fixed-rate accumulated 18.6 MB of transmitted data. The event-based communication strategy reduces the required amount of transmitted data by 83.6% compared to transmitting raw IMU data.

5.8 Experimental Demonstration

This section presents an experimental demonstration of the TOA and TDOA information fusion strategies discussed in Section 5.3 and the event-based communication scheme developed in Section 5.7 using two UAVs equipped with consumer-grade IMUs and software-defined radios (SDRs).

5.8.1 Hardware and Software Setup

The hardware and software setup was identical for the results presented in Subsection 5.8.3 and Subsection 5.8.4. A Consumer-grade L1 GPS active patch antenna [133] and a an omnidirectional cellular antenna [132] were mounted on each UAV to acquire and track GPS signals and multiple cellular transmitters, respectively, whose signals were modulated through code division multiple access (CDMA). The GPS and cellular signals were simultaneously downmixed and synchronously sampled via two-channel Ettus® E312 universal software radio peripherals (USRPs). These front-ends fed their data to the Multichannel Adaptive TRansceiver Information eXtractor (MATRIX) SDR, which produced pseudorange measurements from all GPS L1 C/A signals in view and three cellular transmitters [128]. The IMU data was sampled from the UAVs' on-board proprietary navigation system, which was developed by Autel Robotics®. Fig. 5.12 depicts the hardware and software setup.

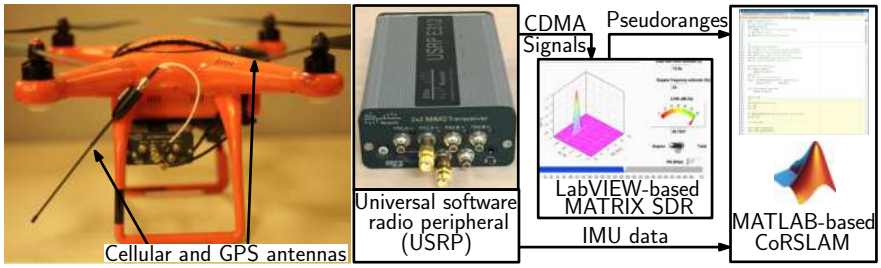

Figure 5.12: Experiment hardware setup.

5.8.2 CoRSLAM Initialization and Settings

The CoRSLAM framework was initialized using the same following procedure for each of the two results presented in the subsequent subsections. The state vector estimate was initialized according to

$$\hat{\boldsymbol{x}}(0|0) = \left[\hat{\boldsymbol{x}}_{\mathrm{r},1}^{\mathsf{T}}(0|0), \hat{\boldsymbol{x}}_{\mathrm{r},2}^{\mathsf{T}}(0|0), \hat{\boldsymbol{x}}_{\mathrm{sop},1}^{\mathsf{T}}(0|0), \ldots, \hat{\boldsymbol{x}}_{\mathrm{sop},3}^{\mathsf{T}}(0|0)\right]^{\mathsf{T}},$$

where the estimates of each UAV's orientation ${}^{b_n}_{g}\hat{\bar{\boldsymbol{q}}}(0|0)$, position $\hat{\boldsymbol{r}}_{b_n}(0|0)$, and velocity $\hat{\dot{\boldsymbol{r}}}_{b_n}(0|0)$ were set to values parsed from the beginning of the UAV's navigation system log files, which were recorded during the trajectory, and the IMU biases $\hat{\boldsymbol{b}}_{\text{gyr},n}$ and $\hat{\boldsymbol{b}}_{\text{acc},n}$ were initialized by averaging 5 seconds of gravity-compensated IMU measurements while the vehicles were stationary and after their IMUs had warmed up. The cellular SOP transmitters' initial state estimates were drawn according to $\hat{\boldsymbol{x}}_{\text{sop},m}(0|0) \sim \mathcal{N}\big(\big[\boldsymbol{r}^{\mathsf{T}}_{\text{sop},m}, \boldsymbol{x}^{\mathsf{T}}_{\text{clk,sop},m}(0)\big]^{\mathsf{T}}, \mathbf{P}_{\text{sop},m}(0|0)\big)$. The true transmitters' positions $\{\boldsymbol{r}_{\text{sop},m}\}_{m=1}^{3}$ were surveyed beforehand according to the framework described in [118] and verified using Google Earth. The initial clock bias and drift

$$\boldsymbol{x}_{\text{clk,sop},m}(0) = c\left[\delta t_{\text{sop},m}(0),\, \dot{\delta t}_{\text{sop},m}(0)\right]^{\mathsf{T}} \quad m = 1, \ldots, 3,$$

were solved for by using the initial set of cellular transmitter pseudoranges using equation (5.7) according to

$$\begin{aligned} c\delta t_{\text{sop},m}(0) &= \|\boldsymbol{r}_{b_n}(0) - \boldsymbol{r}_{\text{sop},m}\| + c\delta t_{\text{r},n}(0) - z_{\text{sop},m}(0), \\ c\dot{\delta t}_{\text{sop},m}(0) &= [c\delta t_{\text{sop},m}(1) - c\delta t_{\text{sop},m}(0)]/T, \end{aligned}$$

where $c\delta t_{\text{sop},m}(1) = \|\boldsymbol{r}_{b_n}(1) - \boldsymbol{r}_{\text{sop},m}\| + c\delta t_{\text{r},n}(1) - {}^{n}z_{\text{sop},m}(1)$ and the receiver's clock bias $c\delta t_{\text{r},n}(0)$ and $c\delta t_{\text{r},n}(1)$ was provided by the GPS receiver while GPS was available.

The corresponding estimation error covariance was initialized according to

$$\mathbf{P}_{\boldsymbol{x}}(0|0) = \text{diag}\left[\mathbf{P}_{\boldsymbol{x}_{\text{r}}}(0|0), \mathbf{P}_{\boldsymbol{x}_{\text{sop},1}}(0|0), \ldots, \mathbf{P}_{\boldsymbol{x}_{\text{sop},3}}(0|0)\right],$$

$$\mathbf{P}_{\boldsymbol{x}_{\text{r}}}(0|0) = \text{diag}\left[\mathbf{P}_{\boldsymbol{x}_{\text{r},1}}(0|0), \mathbf{P}_{\boldsymbol{x}_{\text{r},2}}(0|0)\right],$$

$$\mathbf{P}_{\boldsymbol{x}_{\text{r},n}}(0|0) \triangleq \text{diag}\left[\mathbf{P}_{\boldsymbol{x}_{\text{imu},n}}(0|0),\, \mathbf{P}_{\boldsymbol{x}_{\text{clk,r},n}}(0|0)\right]$$

$$\mathbf{P}_{\boldsymbol{x}_{\text{imu},n}}(0|0) \equiv \text{diag}\left[(0.1)\cdot\mathbf{I}_{3\times3},\, 9\cdot\mathbf{I}_{3\times3},\, \mathbf{I}_{3\times3},\, (10^{-4})\cdot\mathbf{I}_{6\times6}\right]$$

$$\mathbf{P}_{\boldsymbol{x}_{\text{clk,r},n}}(0|0) \equiv \text{diag}\left[0.1,\, 0.01\right] \quad n = 1, 2,$$

$$\mathbf{P}_{\text{sop},m}(0|0) \equiv 10^3 \cdot \text{diag}\left[\mathbf{I}_{3\times3}, 0.3, 0.03\right], \quad m = 1, 2, 3.$$

The process noise covariance of the receiver's clock $\mathbf{Q}_{\text{clk,r},n}$ was set to correspond to a typical TCXO. The process noise covariances of the cellular transmitters' clocks were set to correspond to a typical OCXO, which is usually the case for cellular transmitters [15, 114]. The power spectral density matrices associated with the gyroscope and accelerometer noise were set to $\mathbf{S}_{\boldsymbol{n}_{\text{gyr}}} \equiv (7\times10^{-4})^2\cdot\mathbf{I}_{3\times3}$ and $\mathbf{S}_{\boldsymbol{n}_{\text{acc}}} \equiv (5\times10^{-4})^2\cdot\mathbf{I}_{3\times3}$, respectively. The power spectral density matrices associated with the gyroscope and accelerometer bias variations were set to $\mathbf{S}_{\boldsymbol{w}_{\text{gyr}}} \equiv (1\times10^{-4})^2\cdot\mathbf{I}_{3\times3}$ $\mathbf{S}_{\boldsymbol{w}_{\text{acc}}} \equiv (1\times10^{-4})^2\cdot\mathbf{I}_{3\times3}$, whose values were found empirically using raw IMU data. The measurement noise variances $\{{}^n\sigma^2_{\text{sop},m}\}_{m=1}^3$ for UAV $n = 1$ and $n = 2$ were time-varying, and calculated according to (5.56) , except that $t_{\text{eml}} \equiv 1$, ${}^n\sigma^2_{\text{sv},l,j}$ is replaced with ${}^n\sigma^2_{\text{sop},m,j}$, $T_c \equiv 1/(1.2288\times10^6)$, $\sigma_s \equiv 10$, $T_{CO} \equiv 1/37.5$ s, and the carrier-to-noise ratios $\{{}^n(C/N_0)_{m,j}\}_{m=1}^3$, $n = 1, 2$, are replaced with the received carrier-to-noise ratio estimated by the MATRIX SDR, which are plotted in Fig. 5.13.

5.8.3 Experimental Results: TOA Versus TDOA

Experimental results are presented for three frameworks: (i) CoRSLAM with TOA information fusion, (ii) CoRSLAM with TDOA information fusion, and (iii) for comparative

analysis, a traditional GPS-aided INS. The UAVs traversed the white trajectories plotted in Figs. 5.14(c)–(d), in which GPS was available for the first 50 seconds then unavailable for the last 30 seconds. The north-east root mean squared errors (RMSE) and final errors for all three frameworks for the UAVs are summarized in Table. 5.1. The final estimated transmitter location and corresponding 99^{th}-percentile north-east uncertainty ellipse for two of the transmitters are shown in Fig. 5.14(b) and Fig. 5.14(e). The final localization errors for the three transmitters were 9.0, 7.9, and 52.8 m, respectively. Note that the relatively large estimation error of SOP 3 is primarily attributed to relatively large measurement noise compared to the measurement noise associated with SOP 1 and SOP 2. Upon investigation of Fig. 5.13, it can be seen that the received C/N_0 from SOP 3 at UAV 1 and UAV 2 was lower compared to the C/N_0 from SOP 1 and 2, most of the time. The lower C/N_0 maps to larger estimation error variance, according to (5.56). The larger measurement variance resulted in a larger final estimation error ellipse, which contained the true position of SOP 3.

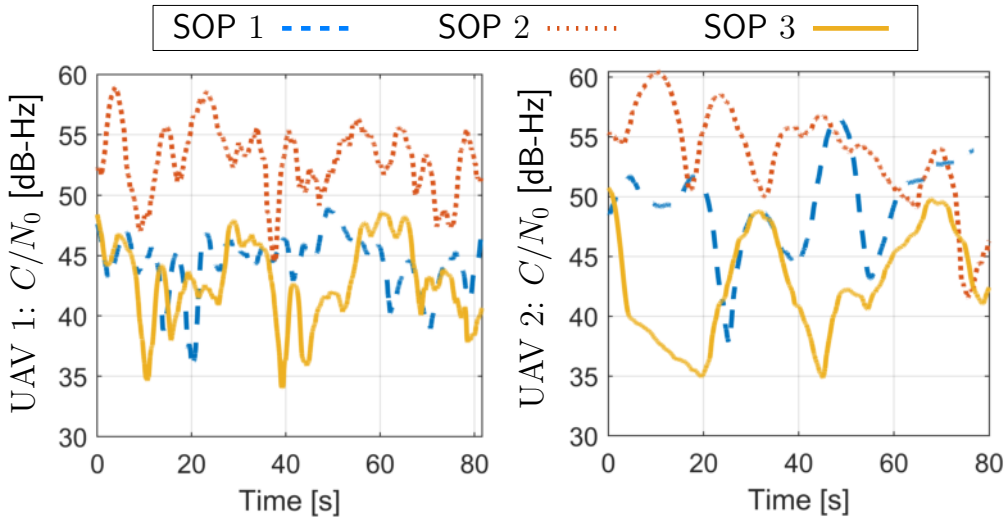

Figure 5.13: Time history of received C/N_0 for UAV 1 and UAV 2 from SOP 1,2, and 3, produced by the MATRIX SDR.

Table 5.1: Estimation Errors: TOA Versus TDOA

Framework	**GPS-aided INS**		**CoRSLAM-TOA**		**CoRSLAM-TDOA**	
Vehicle	UAV 1	UAV 2	UAV 1	UAV 2	UAV 1	UAV 2
RMSE (m)	21.5	18.9	3.1	4.2	3.3	4.4
Final Error (m)	57.3	54.7	4.3	6.0	4.4	6.2

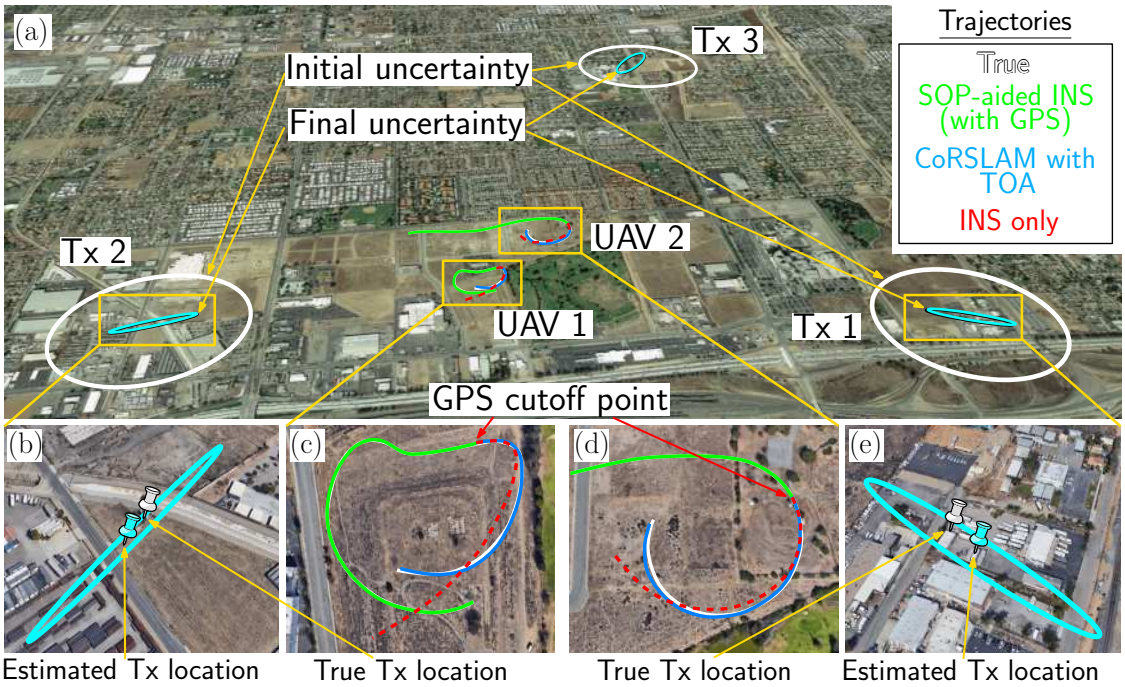

Figure 5.14: (a) Experimental environment with three cellular SOPs and two UAVs. (b)-(e) Mapping and navigation results for CoRSLAM with TOA information fusion.

5.8.4 Experimental Results: Event-Based Communication

Two transmission strategies were studied: (i) event-based using (5.58) with $\xi_{\max} \equiv 20$ m and $p \equiv 0.95$, and for a comparative analysis, (ii) fixed-rate where τ is closed periodically with a period of 0.2 s. For each of the two transmission schemes, the traversed UAV trajectories were estimated using the TOA information fusion strategy. The estimated trajectories using each transmission scheme for UAV 1 and UAV 2 are plotted in Fig. 5.15 (a) and (b), respectively. The north-east final errors for each communication scheme for the UAVs are summarized in Table. 5.2. The final estimated transmitter location and corresponding 99^{th}-percentile north-east uncertainty ellipse of SOP 1 for each communication strategy are

plotted in Fig. 5.15 (c). From the plots in Fig. 5.15, one can note a slight degradation in UAV localization performance, however the specified constraints p and $\xi_{\max}$ were maintained. Moreover, the fixed-rate communication strategy required the transmission of 8.38 Mbits, whereas the event-based reduced the transmission to 1.90 Mbits, a 77.3% reduction.

Table 5.2: Estimation Errors: Fixed-rate Versus Event-based Communication

Scheme	**Fixed-rate**		**Event-based**	
Vehicle	UAV 1	UAV 2	UAV 1	UAV 2
Final Error (m)	4.3	6.0	6.71	8.01

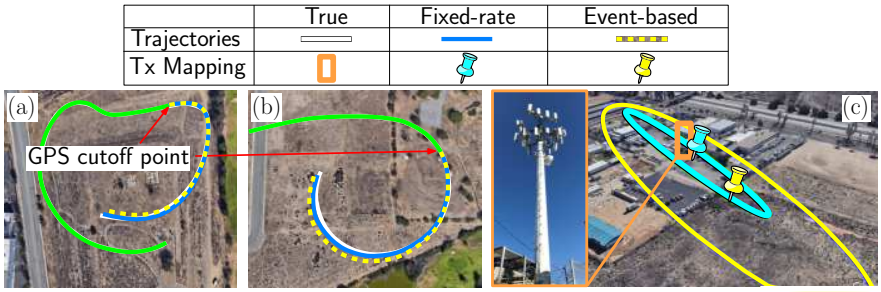

Figure 5.15: (a)-(b) UAV navigation results for fixed-rate (blue solid) and event-based (yellow dashed) information fusion. (c) Mapping results for Tx 1 using fixed-rate (blue) and event-based (yellow) information fusion.

Chapter 6

Dissertation Conclusions and Main Takeaways

This dissertation studied optimal mapping of SOPs and the exploitation of SOPs for aided inertial navigation.

In chapter 2, where optimal collaborative mapping of terrestrial SOPs was studied. First, the optimal placement of a receiver to an environment comprising one SOP and N pre-deployed receivers with a random initial distribution was considered. Three optimization problems were formulated and compared: minimizing the GDOP, maximizing the determinant of the inverse of the GDOP matrix, and maximizing the area of a polygon inscribed in the unit circle whose vertices are the endpoints of unit LOS vectors from the SOP to the receivers. It was shown that the area maximization problem is piecewise-concave with a simple analytical solution. Next, the optimal receiver placement problem was extended to an environment comprising an arbitrary number of SOPs. A novel optimization criterion was proposed for this scenario, namely, the sum of logarithms of polygon areas. It was demonstrated that while the classical GDOP and determinant optimization problems do not posses any useful

convexity properties, the proposed optimization criterion (i) yields a family of convex programs and guarantees a global optimal solution and (ii) allows for executing the solver of the family of convex programs in parallel. This chapter also derived the optimal mapping performance of a single SOP as a function of time and number of receivers in the environment and demonstrated the theoretical optimal mapping performance numerically and experimentally.

Next, this dissertation considered simultaneously mapping and navigating with SOPs. In chapter 3, the stochastic observability of a simultaneous receiver localization and transmitter mapping problem was studied. It was demonstrated that the system is stochastically unobservable when the clock biases of both a receiver and unknown transmitters are simultaneously estimated and that their associated estimation error variances will diverge. The divergence rate of a sequence lower-bounding the diverging variances was derived and shown to reach a steady-state that only depends on the receiver's clock quality. Despite the stochastically unobservable clock biases, simulation and experimental results demonstrated bounded localization errors of a UAV navigating via radio SLAM for 130 seconds without GPS.

Chapter 4 developed and studied an SOP-aided INS framework. The performance of the framework was compared against a traditional tightly-coupled GNSS-aided INS integration strategy and the performance sensitivity was studied by varying the quantity and quality of exploited SOPs. The SOP-aided INS was shown to possess several advantages over the GNSS-aided INS. When GNSS signals are available, incorporating ambient terrestrial SOPs produces a more accurate navigation solution compared to using GNSS alone. A bound could be established on the estimation errors in the absence of GNSS. The SOP-aided INS may relax requirements on IMU quality. For example, using a consumer-grade IMU was shown to produced estimation uncertainties lower than a traditional tightly-coupled GNSS-aided INS using a tactical-grade IMU when two, three, or four SOPs were exploited. Furthermore, it was shown that SOPs equipped with low-quality oscillators may serve as effective INS-aiding

sources to establish a bound on INS errors in the absence of GNSS. Moreover, experimental results demonstrated a vehicle navigating with the SOP-aided INS framework in the absence of GNSS, which yielded an RMSE reduction of 59.9% when compared to an unaided INS.

Chapter 5 developed and studied two information fusion strategies for navigating vehicle's to collaboratively aid their INS's with SOPs: TOA measurements and TDOA measurements with SOP referencing. It was proven analytically that using TOA measurements from SOPs with unknown positions and unknown and unsynchronized clock biases results in a smaller or equal navigating vehicle's position estimation error covariance than using TDOA measurements, regardless of the selected SOP reference. An approach to share INS data between navigating vehicles in a distributed fashion was discussed, which significantly reduces the amount of data that is required to be transmitted to perform the EKF measurement update. Simulation and experimental results were presented to demonstrate these fusion strategies.

Moreover, an event-based communication scheme using each vehicles' position estimation error covariance was developed, which aims to reduces the accumulated shared data between collaborators while maintaining a specified constraint on each vehicle's positioning error. The inequalities (5.58) and (5.67) provide simple tests to determine if the specified constraints will be violated and trigger communication. Given the probability density function (pdf) of $\|\tilde{\boldsymbol{r}}_{b_n}\|^2_{\mathrm{M}}$, the inverse cdf of (5.63) may be used to find the η_n that satisfies a specified p. The pdf of $\|\tilde{\boldsymbol{r}}_{b_n}\|^2_{\mathrm{M}}$ is characterized, leading to a simple online test that each navigating vehicle could perform independently to determine whether $\boldsymbol{\Lambda}_n$ should be transmitted. Simulation and experimental results were presented to compare the event-based scheme with a fixed-rate scheme.

Bibliography

[1] CB Insights, "40+ corporations working on autonomous vehicles," 2019.

[2] D. Gettinger, "Summary of drone spending in the FY 2019 defense budget request," *Center for the Study of the Drone at Bard College, New York, NY*.

[3] J. Du and M. Barth, "Next-generation automated vehicle location systems: Positioning at the lane level," *IEEE Transactions on Intelligent Transportation Systems*, vol. 9, no. 1, pp. 48–57, March 2008.

[4] Y. Jenie, E. van Kampen, J. Ellerbroek, and J. Hoekstra, "Safety assessment of a UAV CD&R system in high density airspace using Monte Carlo simulations," *IEEE Transactions on Intelligent Transportation Systems*, vol. 19, no. 8, pp. 2686–2695, August 2018.

[5] J. Farrell and M. Barth, *Aided Navigation: GPS with High Rate Sensors*. New York: McGraw-Hill, 2008.

[6] I. Skog and P. Handel, "In-car positioning and navigation technologies - a survey," *IEEE Transactions on Intelligent Transportation Systems*, vol. 10, no. 1, pp. 4–21, March 2009.

[7] A. Soloviev, "Tight coupling of GPS, INS, and laser for urban navigation," *IEEE Transactions on Aerospace and Electronic Systems*, vol. 46, no. 4, pp. 1731–1746, October 2010.

[8] A. Hata and D. Wolf, "Feature detection for vehicle localization in urban environments using a multilayer Lidar," *IEEE Transactions on Intelligent Transportation Systems*, vol. 17, no. 2, pp. 420–429, February 2016.

[9] M. Li and A. Mourikis, "High-precision, consistent EKF-based visual-inertial odometry," *International Journal of Robotics Research*, vol. 32, no. 6, pp. 690–711, May 2013.

[10] C. Rose, J. Britt, J. Allen, and D. Bevly, "An integrated vehicle navigation system utilizing lane-detection and lateral position estimation systems in difficult environments for GPS," *IEEE Transactions on Intelligent Transportation Systems*, vol. 15, no. 6, pp. 2615–2629, 2014.

[11] M. Maaref and Z. Kassas, "Ground vehicle navigation in GNSS-challenged environments using signals of opportunity and a closed-loop map-matching approach," *IEEE Transactions on Intelligent Transportation Systems*, pp. 1–16, June 2019.

[12] J. Petit, B. Stottelaar, M. Feiri, and F. Kargl, "Remote attacks on automated vehicles sensors: Experiments on camera and lidar," *Black Hat Europe*, vol. 11, 2015.

[13] J. Raquet and R. Martin, "Non-GNSS radio frequency navigation," in *Proceedings of IEEE International Conference on Acoustics, Speech and Signal Processing*, March 2008, pp. 5308–5311.

[14] L. Merry, R. Faragher, and S. Schedin, "Comparison of opportunistic signals for localisation," in *Proceedings of IFAC Symposium on Intelligent Autonomous Vehicles*, September 2010, pp. 109–114.

[15] K. Pesyna, Z. Kassas, J. Bhatti, and T. Humphreys, "Tightly-coupled opportunistic navigation for deep urban and indoor positioning," in *Proceedings of ION GNSS Conference*, September 2011, pp. 3605–3617.

[16] Z. Kassas, "Collaborative opportunistic navigation," *IEEE Aerospace and Electronic Systems Magazine*, vol. 28, no. 6, pp. 38–41, 2013.

[17] Z. Kassas, "Analysis and synthesis of collaborative opportunistic navigation systems," Ph.D. dissertation, The University of Texas at Austin, USA, 2014.

[18] J. McEllroy, "Navigation using signals of opportunity in the AM transmission band," Master's thesis, Air Force Institute of Technology, Wright-Patterson Air Force Base, Ohio, USA, 2006.

[19] S. Fang, J. Chen, H. Huang, and T. Lin, "Is FM a RF-based positioning solution in a metropolitan-scale environment? A probabilistic approach with radio measurements analysis," *IEEE Transactions on Broadcasting*, vol. 55, no. 3, pp. 577–588, September 2009.

[20] A. Popleteev, "Indoor positioning using FM radio signals," Ph.D. dissertation, University of Trento, Italy, 2011.

[21] V. Moghtadaiee and A. Dempster, "Indoor location fingerprinting using FM radio signals," *IEEE Transactions on Broadcasting*, vol. 60, no. 2, pp. 336–346, June 2014.

[22] C. Yang, T. Nguyen, and E. Blasch, "Mobile positioning via fusion of mixed signals of opportunity," *IEEE Aerospace and Electronic Systems Magazine*, vol. 29, no. 4, pp. 34–46, April 2014.

[23] C. Yang and T. Nguyen, "Tracking and relative positioning with mixed signals of opportunity," *NAVIGATION, Journal of the Institute of Navigation*, vol. 62, no. 4, pp. 291–311, December 2015.

[24] Z. Kassas, J. Khalife, K. Shamaei, and J. Morales, "I hear, therefore I know where I am: Compensating for GNSS limitations with cellular signals," *IEEE Signal Processing Magazine*, pp. 111–124, September 2017.

[25] J. Khalife and Z. Kassas, "Navigation with cellular CDMA signals – part II: Performance analysis and experimental results," *IEEE Transactions on Signal Processing*, vol. 66, no. 8, pp. 2204–2218, April 2018.

[26] J. del Peral-Rosado, J. López-Salcedo, F. Zanier, and G. Seco-Granados, "Position accuracy of joint time-delay and channel estimators in LTE networks," *IEEE Access*, vol. 6, no. 25185–25199, p. April, 2018.

[27] K. Shamaei and Z. Kassas, "LTE receiver design and multipath analysis for navigation in urban environments," *NAVIGATION, Journal of the Institute of Navigation*, vol. 65, no. 4, pp. 655–675, December 2018.

[28] M. Rabinowitz and J. Spilker, Jr., "A new positioning system using television synchronization signals," *IEEE Transactions on Broadcasting*, vol. 51, no. 1, pp. 51–61, March 2005.

[29] P. Thevenon, S. Damien, O. Julien, C. Macabiau, M. Bousquet, L. Ries, and S. Corazza, "Positioning using mobile TV based on the DVB-SH standard," *NAVIGATION, Journal of the Institute of Navigation*, vol. 58, no. 2, pp. 71–90, 2011.

[30] J. Yang, X. Wang, M. Rahman, S. Park, H. Kim, and Y. Wu, "A new positioning system using DVB-T2 transmitter signature waveforms in single frequency networks," *IEEE Transactions on Broadcasting*, vol. 58, no. 3, pp. 347–359, September 2012.

[31] J. Khalife, Z. Kassas, and S. Saab, "Indoor localization based on floor plans and power maps: Non-line of sight to virtual line of sight," in *Proceedings of ION GNSS Conference*, September 2015, pp. 2291–2300.

[32] R. Faragher and R. Harle, "Towards an efficient, intelligent, opportunistic smartphone indoor positioning system," *NAVIGATION, Journal of the Institute of Navigation*, vol. 62, no. 1, pp. 55–72, 2015.

[33] Y. Zhuang, Z. Syed, Y. Li, and N. El-Sheimy, "Evaluation of two WiFi positioning systems based on autonomous crowdsourcing of handheld devices for indoor navigation," *IEEE Transactions on Mobile Computing*, vol. 15, no. 8, pp. 1982–1995, August 2016.

[34] K. Pesyna, Z. Kassas, and T. Humphreys, "Constructing a continuous phase time history from TDMA signals for opportunistic navigation," in *Proceedings of IEEE/ION Position Location and Navigation Symposium*, April 2012, pp. 1209–1220.

[35] D. Lawrence, H. Cobb, G. Gutt, M. OConnor, T. Reid, T. Walter, and D. Whelan, "Navigation from LEO: Current capability and future promise," *GPS World Magazine*, vol. 28, no. 7, pp. 42–48, July 2017.

[36] T. Reid, A. Neish, T. Walter, and P. Enge, "Broadband LEO constellations for navigation," *NAVIGATION, Journal of the Institute of Navigation*, vol. 65, no. 2, pp. 205–220, 2018.

[37] J. Morales and Z. Kassas, "A low communication rate distributed inertial navigation architecture with cellular signal aiding," in *Proceedings of IEEE Vehicular Technology Conference*, 2018, pp. 1–6.

[38] J. Morales, J. Khalife, and Z. Kassas, "Simultaneous tracking of Orbcomm LEO satellites and inertial navigation system aiding using Doppler measurements," in *Proceedings of IEEE Vehicular Technology Conference*, April 2019, pp. 1–6.

[39] C. Ardito, J. Morales, J. Khalife, A. Abdallah, and Z. Kassas, "Performance evaluation of navigation using LEO satellite signals with periodically transmitted satellite positions," in *Proceedings of ION International Technical Meeting Conference*, 2019, pp. 306–318.

[40] J. Khalife and Z. Kassas, "Receiver design for Doppler positioning with LEO satellites," in *Proceedings of IEEE International Conference on Acoustics, Speech and Signal Processing*, May 2019, pp. 5506–5510.

[41] J. Morales, J. Khalife, U. S. Cruz, and Z. Kassas, "Orbit modeling for simultaneous tracking and navigation using LEO satellite signals," in *Proceedings of ION GNSS Conference*, September 2019, pp. 2090–2099.

[42] Z. Kassas, J. Morales, and J. Khalife, "New-age satellite-based navigation – STAN: simultaneous tracking and navigation with LEO satellite signals," *Inside GNSS Magazine*, vol. 14, no. 4, pp. 56–65, 2019.

[43] J. Morales, J. Khalife, and Z. Kassas, "GNSS vertical dilution of precision reduction using terrestrial signals of opportunity," in *Proceedings of ION International Technical Meeting Conference*, January 2016, pp. 664–669.

[44] K. Dogancay, "UAV path planning for passive emitter localization," *IEEE Transactions on Aerospace and Electronic Systems*, vol. 48, no. 2, pp. 1150–1166, April 2012.

[45] Z. Kassas and U. Ozguner, "A nonlinear filter coupled with hospitability and synthetic inclination maps for in-surveillance and out-of-surveillance tracking," *IEEE Transactions on Systems, Man, and Cybernetics, Part C: Applications and Reviews*, vol. 40, no. 1, pp. 87–97, 2010.

[46] J. Kim and S. Sukkarieh, "Autonomous airborne navigation in unknown terrain environments," *IEEE Transactions on Aerospace and Electronic Systems*, vol. 40, no. 3, pp. 1031–1045, July 2004.

[47] Y. Oshman, "Optimal sensor selection strategy for discrete-time state estimators," *IEEE Transactions on Aerospace and Electronic Systems*, vol. 30, no. 2, pp. 307–314, 1994.

[48] W. Meng, L. Xie, and W. Xiao, "Optimal TDOA sensor-pair placement with uncertainty in source location," *IEEE Transactions on Vehicular Technology*, vol. 65, no. 11, pp. 9260–9271, January 2016.

[49] H. Zhang, "Two-dimensional optimal sensor placement," *IEEE Transactions on Systems, Man and Cybernetics*, vol. 25, no. 5, pp. 781–792, May 1995.

[50] D. Jourdan and N. Roy, "Optimal sensor placement for agent localization," in *Proceedings of IEEE/ION Position, Location, And Navigation Symposium*, April 2006, pp. 128–139.

[51] J. Isaacs, D. Klein, and J. Hespanha, "Optimal sensor placement for time difference of arrival localization," in *Proceedings of IEEE Conference on Decision and Control*, December 2009, pp. 7878–7884.

[52] C. Yang, L. Kaplan, E. Blasch, and M. Bakich, "Optimal placement of heterogeneous sensors for targets with Gaussian priors," *IEEE Transactions on Aerospace and Electronic Systems*, vol. 49, no. 3, pp. 1637–1653, July 2013.

[53] Z. Kassas and T. Humphreys, "Motion planning for optimal information gathering in opportunistic navigation systems," in *Proceedings of AIAA Guidance, Navigation, and Control Conference*, August 2013, pp. 4551–4565.

[54] Z. Kassas, A. Arapostathis, and T. Humphreys, "Greedy motion planning for simultaneous signal landscape mapping and receiver localization," *IEEE Journal of Selected Topics in Signal Processing*, vol. 9, no. 2, pp. 247–258, March 2015.

[55] Z. Kassas and T. Humphreys, "Receding horizon trajectory optimization in opportunistic navigation environments," *IEEE Transactions on Aerospace and Electronic Systems*, vol. 51, no. 2, pp. 866–877, April 2015.

[56] P. Massat and K. Rudnick, "Geometric formulas for dilution of precision calculations," *NAVIGATION, Journal of the Institute of Navigation*, vol. 37, no. 4, pp. 379–391, 1990.

[57] N. Levanon, "Lowest GDOP in 2-D scenarios," *IEE Proceedings Radar, Sonar and Navigation*, vol. 147, no. 3, pp. 149–155, 2000.

[58] I. Sharp, K. Yu, and Y. Guo, "GDOP analysis for positioning system design," *IEEE Transactions on Vehicular Technology*, vol. 58, no. 7, pp. 3371–3382, 2009.

[59] N. Blanco-Delgado and F. Nunes, "Satellite selection method for multi-constellation GNSS using convex geometry," *IEEE Transactions on Vehicular Technology*, vol. 59, no. 9, pp. 4289–4297, November 2010.

[60] S. Martinez and F. Bullo, "Optimal sensor placement and motion coordination for target tracking," *Automatica*, vol. 42, no. 4, pp. 661–668, April 2006.

[61] W. Meng, L. Xie, and W. Xiao, "Optimality analysis of sensor-source geometries in heterogeneous sensor networks," *IEEE Transactions on Wireless Communications*, vol. 12, no. 4, pp. 1958–1967, April 2013.

[62] J. Spilker, Jr., *Global Positioning System: Theory and Applications*. Washington, D.C.: American Institute of Aeronautics and Astronautics, 1996, ch. 5: Satellite Constellation and Geometric Dilution of Precision, pp. 177–208.

[63] A. Bishop, B. Fidan, B. Anderson, K. Dogancay, and P. Pathirana, "Optimality analysis of sensor-target localization geometries," *Automatica*, vol. 46, pp. 479–492, 2010.

[64] N. Blanco-Delgado, F. Nunes, and G. Seco-Granados, "Relation between GDOP and the geometry of the satellite constellation," in *International Conference on Localization and GNSS*, June 2011, pp. 175–180.

[65] J. Morales and Z. Kassas, "Optimal receiver placement for collaborative mapping of signals of opportunity," in *Proceedings of ION GNSS Conference*, September 2015, pp. 2362–2368.

[66] D. Moreno-Salinas, A. Pascoal, and J. Aranda, "Optimal sensor placement for multiple target positioning with range-only measurements in two-dimensional scenarios," *Sensors*, vol. 13, no. 8, pp. 10 674–10 710, 2013.

[67] A. Dempster and E. Cetin, "Interference localization for satellite navigation systems," *Proceedings of the IEEE*, vol. 104, no. 6, pp. 1318–1326, 2016.

[68] M. Psiaki and T. Humphreys, "GNSS spoofing and detection," *Proceedings of the IEEE*, vol. 104, no. 6, pp. 1258–1270, June 2016.

[69] H. Durrant-Whyte and T. Bailey, "Simultaneous localization and mapping: part I," *IEEE Robotics & Automation Magazine*, vol. 13, no. 2, pp. 99–110, June 2006.

[70] J. Andrade-Cetto and A. Sanfeliu, "The effects of partial observability when building fully correlated maps," *IEEE Transactions on Robotics*, vol. 21, no. 4, pp. 771–777, August 2005.

[71] T. Vida-Calleja, M. Bryson, S. Sukkarieh, A. Sanfeliu, and J. Andrade-Cetto, "On the observability of bearing-only SLAM," in *Proceedings of IEEE Internartional Conference on Robotics and Automation*, vol. 1, April 2007, pp. 4114–4118.

[72] Z. Wang and G. Dissanayake, "Observability analysis of SLAM using Fisher information matrix," in *Proceedings of IEEE International Conference on Control, Automation, Robotics, and Vision*, vol. 1, December 2008, pp. 1242–1247.

[73] M. Bryson and S. Sukkarieh, "Observability analysis and active control for airborne SLAM," *IEEE Transactions on Aerospace and Electronic Systems*, vol. 44, no. 1, pp. 261–280, January 2008.

[74] Z. Kassas and T. Humphreys, "Observability analysis of collaborative opportunistic navigation with pseudorange measurements," *IEEE Transactions on Intelligent Transportation Systems*, vol. 15, no. 1, pp. 260–273, February 2014.

[75] V. Bageshwar, D. Gebre-Egziabher, W. Garrard, and T. Georgiou, "Stochastic observability test for discrete-time Kalman filters," *Journal of Guidance, Control, and Dynamics*, vol. 32, no. 4, pp. 1356–1370, July 2009.

[76] H. Chen, *Recursive Estimation and Control for Stochastic Systems*. New York: Wiley, 1985, p. 237.

[77] Y. Baram and T. Kailath, "Estimability and regulability of linear systems," *IEEE Transactions on Automatic Control*, vol. 33, no. 12, pp. 1116–1121, December 1988.

[78] K. Reif, S. Gunther, E. Yaz, and R. Unbehauen, "Stochastic stability of the discrete-time extended Kalman filter," *IEEE Transactions on Automatic Control*, vol. 44, no. 4, pp. 714–728, April 1999.

[79] K. Reif, S. Gunther, E. Yaz, and R. Unbehauen, "Stochastic stability of the continuous-time extended Kalman filter," *IEE Proceedings - Control Theory and Applications*, vol. 147, no. 1, pp. 45–52, January 2000.

[80] Y. Bar-Shalom, X. Li, and T. Kirubarajan, *Estimation with Applications to Tracking and Navigation*. New York, NY: John Wiley & Sons, 2002.

[81] A. Liu, "Stochastic observability, reconstructibility, controllability, and reachability," Ph.D. dissertation, University of California, San Diego, USA, 2011.

[82] C. Yang and A. Soloviev, "Simultaneous localization and mapping of emitting radio sources-SLAMERS," in *Proceedings of ION GNSS Conference*, September 2015, pp. 2343–2354.

[83] J. Morales, P. Roysdon, and Z. Kassas, "Signals of opportunity aided inertial navigation," in *Proceedings of ION GNSS Conference*, September 2016, pp. 1492–1501.

[84] C. Yang and A. Soloviev, "Covariance analysis of spatial and temporal effects of collaborative navigation," *NAVIGATION, Journal of the Institute of Navigation*, vol. 61, no. 3, pp. 213–225, 2014.

[85] "U.S. Department of Transportation, Intelligent Transportation Systems - Dedicated Short Range Communications," https://www.its.dot.gov/factsheets/pdf/JPO_HowCVWork.pdf.

[86] J. Morales and Z. Kassas, "Tightly-coupled inertial navigation system with signals of opportunity aiding," *IEEE Transactions on Aerospace and Electronic Systems*, 2019, submitted.

[87] J. Morales and Z. Kassas, "Distributed signals of opportunity aided inertial navigation with intermittent communication," in *Proceedings of ION GNSS Conference*, September 2017, pp. 2519–2530.

[88] D. Shin and T. Sung, "Comparisons of error characteristics between TOA and TDOA positioning," *IEEE Transactions on Aerospace and Electronic Systems*, vol. 38, no. 1, pp. 307–311, January 2002.

[89] T. Sathyan, M. Hedley, and M. Mallick, "An analysis of the error characteristics of two time of arrival localization techniques," in *Proceedings of International Conference on Information Fusion*, July 2010, pp. 1–7.

[90] R. Kaune, "Accuracy studies for TDOA and TOA localization," in *Proceedings of International Conference on Information Fusion*, July 2012, pp. 408–415.

[91] J. Morales and Z. Kassas, "Information fusion strategies for collaborative radio SLAM," in *Proceedings of IEEE/ION Position Location and Navigation Symposium*, April 2018, pp. 1445–1454.

[92] H. Mokhtarzadeh and D. Gebre-Egziabher, "Cooperative inertial navigation," *NAVIGATION, Journal of the Institute of Navigation*, vol. 61, no. 2, pp. 77–94, 2014.

[93] N. Alam, A. Kealy, and A. Dempster, "Cooperative inertial navigation for GNSS-challenged vehicular environments," *IEEE Transactions on Intelligent Transportation Systems*, vol. 14, no. 3, pp. 1370–1379, September 2013.

[94] Q. Liu, Z. Wang, and X. He, *Stochastic Control and Filtering over Constrained Communication Networks. Studies in Systems, Decision and Control.* Springer, 2019, ch. 7: Event-Based Recursive Distributed Filtering, pp. 117–134.

[95] Y. Yilmax, G. Moustakides, and X. Wang, "Spectrum sensing via event-triggered sampling," in *Proceedings of Asilomar Conference on Signals, Systems, and Computers*, 2011, pp. 1420–1424.

[96] C. Yang, L. Shi, and W. Ma, "A study of estimation and communication tradeoff using an event-based approach," in *Proceedings of Asilomar Conference on Signals, Systems and Computers*, 2013, pp. 32–36.

[97] D. Shi, T. Chen, and L. Shi, "Event-triggered maximum likelihood state estimation," *Automatica*, vol. 50, no. 1, pp. 247–254, 2014.

[98] S. Trimpe and R. D'Andrea, "Event-based state estimation with variance-based triggering," *IEEE Transactions on Automatic Control*, vol. 59, no. 12, pp. 3266–3281, December 2014.

[99] J. Morales and Z. Kassas, "Event-based communication strategy for collaborative navigation with signals of opportunity," in *Proceedings of Asilomar Conference on Signals, Systems and Computers*, November 2018, pp. 548–553.

[100] A. Thompson, J. Moran, and G. Swenson, *Interferometry and Synthesis in Radio Astronomy*, 2nd ed. John Wiley & Sons, 2001.

[101] D. Uciński, *Optimal Measurement Methods for Distributed Parameter System Identification*. CRC Press, 2005.

[102] J. Spilker, Jr., *Global Positioning System: Theory and Applications*. Washington, D.C.: American Institute of Aeronautics and Astronautics, 1996, ch. 2: Overview of GPS Operation and Design, pp. 57–119.

[103] S. Boyd and L. Vandenberghe, *Convex Optimization*. Cambridge University Press, 2004.

[104] A. Engle, *Problem-solving strategies*, 1st ed. Springer New York, 1998.

[105] R. Graham, D. Knuth, and O. Patashnik, *Concrete Mathematics: A Foundation for Computer Science*. Addison-Wesley Publishing Co., 1994.

[106] T. Humphreys, J. Bhatti, T. Pany, B. Ledvina, and B. O'Hanlon, "Exploiting multicore technology in software-defined GNSS receivers," in *Proceedings of ION GNSS Conference*, September 2009, pp. 326–338.

[107] J. Khalife, K. Shamaei, and Z. Kassas, "A software-defined receiver architecture for cellular CDMA-based navigation," in *Proceedings of IEEE/ION Position, Location, and Navigation Symposium*, April 2016, pp. 816–826.

[108] R. Roy and T. Kailath, "ESPRIT-estimation of signal parameters via rotational invariance techniques," *IEEE Transactions on Acoustics, Speech, and Signal Processing*, vol. 37, no. 7, pp. 984–995, July 1989.

[109] B. Fleury, M. Tschudin, R. Heddergott, D. Dahlhaus, and K. Pedersen, "Channel parameter estimation in mobile radio environments using the SAGE algorithm," *IEEE Journal on Selected Areas in Communications*, vol. 17, no. 3, pp. 434–450, 1999.

[110] P. Brockwell and R. Davis, *Introduction to Time Series and Forecasting*, 3rd ed. Springer, 2016.

[111] C. Chatfield, *Time-series Forecasting*. CRC Press, 2000.

[112] C. Ansley, W. Spivey, and W. Wrobleski, "On the structure of moving average processes," *Journal of Econometrics*, vol. 6, no. 1, pp. 121–134, July 1976.

[113] S. Narla, "The evolution of connected vehicle technology: From smart drivers to smart cars to... self-driving cars," *Institute of Transportation Engineers Journal*, vol. 83, no. 7, pp. 21–26, 2013.

[114] Z. Kassas, V. Ghadiok, and T. Humphreys, "Adaptive estimation of signals of opportunity," in *Proceedings of ION GNSS Conference*, September 2014, pp. 1679–1689.

[115] X. Li and V. Jilkov, "Survey of maneuvering target tracking. Part I: Dynamic models," *IEEE Transactions on Aerospace and Electronic Systems*, vol. 39, no. 4, pp. 1333–1364, 2003.

[116] J. Mendel, *Lessons in Estimation Theory for Signal Processing, Communications, and Control*, 2nd ed. Prentice Hall, 1995.

[117] Z. Kassas, J. Morales, K. Shamaei, and J. Khalife, "LTE steers UAV," *GPS World Magazine*, vol. 28, no. 4, pp. 18–25, April 2017.

[118] J. Morales and Z. Kassas, "Optimal collaborative mapping of terrestrial transmitters: receiver placement and performance characterization," *IEEE Transactions on Aerospace and Electronic Systems*, vol. 54, no. 2, pp. 992–1007, April 2018.

[119] P. Groves, *Principles of* GNSS*, Inertial, and Multisensor Integrated Navigation Systems*, 2nd ed. Artech House, 2013.

[120] M. Braasch, "Inertial navigation systems," in *Aerospace Navigation Systems*. John Wiley & Sons, Ltd, 2016.

[121] D. Gebre-Egziabher, "What is the difference between 'loose', 'tight', 'ultra-tight' and 'deep' integration strategies for INS and GNSS," *Inside GNSS*, pp. 28–33, January 2007.

[122] R. Brown and P. Hwang, *Introduction to Random Signals and Applied Kalman Filtering*, 3rd ed. John Wiley & Sons, 2002.

[123] J. Morales and Z. Kassas, "Stochastic observability and uncertainty characterization in simultaneous receiver and transmitter localization," *IEEE Transactions on Aerospace and Electronic Systems*, vol. 55, no. 2, pp. 1021–1031, April 2019.

[124] R. Snay and M. Soler, "Continuously operating reference station (CORS): history, applications, and future enhancements," *Journal of Surveying Engineering*, vol. 134, no. 4, pp. 95–104, November 2008.

[125] M. Braasch and A. van Dierendonck, "GPS receiver architectures and measurements," *Proceedings of the IEEE*, vol. 87, no. 1, pp. 48–64, January 1999.

[126] S. Tay and J. Marais, "Weighting models for GPS pseudorange observations for land transportation in urban canyons," in *Proceedings of the European Workshop on GNSS Signals and Signal Processing*, December 2014.

[127] J. Liberti and T. Rappaport, "A geometrically based model for line-of-sight multipath radio channels," in *Proceedings of IEEE Vehicular Technology Conference*, vol. 2, April 1996, pp. 844–848.

[128] J. Khalife, K. Shamaei, and Z. Kassas, "Navigation with cellular CDMA signals – part I: Signal modeling and software-defined receiver design," *IEEE Transactions on Signal Processing*, vol. 66, no. 8, pp. 2191–2203, April 2018.

[129] J. Khalife, K. Shamaei, S. Bhattacharya, and Z. Kassas, "Centimeter-accurate UAV navigation with cellular signals," in *Proceedings of ION GNSS Conference*, September 2018, pp. 2321–2331.

[130] M. Maaref and Z. Kassas, "Measurement characterization and autonomous outlier detection and exclusion for ground vehicle navigation with cellular signals," *IEEE Transactions on Intelligent Vehicles*, 2019, accepted.

[131] "Autel Robotics," https://auteldrones.com.

[132] "Ettus Research tri-band antenna," https://www.ettus.com/product/details/VERT400.

[133] QGP Supply, "GPS active antenna," 2020.

[134] "National Instruments universal software radio peripheral-2954R."

[135] M. Shuster, "A survey of attitude representations," *The Journal of the Astronautical Sciences*, vol. 41, no. 4, pp. 439–517, October 1993.

[136] J. Farrell and M. Barth, *The Global Positioning System and Inertial Navigation*. New York: McGraw-Hill, 1998.

[137] T. Amemiya, *Advanced Econometrics*. Cambridge, Massachusetts: Harvard University Press, 1985, p. 460.

[138] D. Torrieri, "Statistical theory of passive location systems," *IEEE Transactions on Aerospace and Electronic Systems*, vol. 20, no. 2, pp. 183–198, March 1983.

[139] S. Choi and R. Wette, "Maximum likelihood estimation of the parameters of the gamma distribution and their bias," *Technometrics*, vol. 11, no. 4, pp. 683–690, 1969.

Appendix A

Appendices

A.1 Derivation of the Area Optimization Function (2.16)

The resulting area ${}^{m}A\left({}^{m}\phi_{N+1}\right)$ for the m^{th} SOP after placing the $(N+1)^{\text{st}}$ is

$$ {}^{m}A\left({}^{m}\phi_{N+1}\right) = {}^{m}A_{N} + \Delta^{m}A\left({}^{m}\phi_{N+1}\right), \tag{A.1} $$

where ${}^{m}A_{N}$ is the area created by the pre-deployed receivers and $\Delta^{m}A\left({}^{m}\phi_{N+1}\right)$ is the change in area from introducing the $(N+1)^{\text{st}}$ receiver, and is given by

$$ \begin{aligned} &\Delta^{m}A\left({}^{m}\phi_{N+1}\right) = \\ &\quad \frac{1}{2}\left[\sin({}^{m}\phi_{N+1} - {}^{m}\phi_{n}) + \sin({}^{m}\theta_{n} - {}^{m}\phi_{N+1} + {}^{m}\phi_{n})\right. \\ &\quad \left. - \sin({}^{m}\theta_{n})\right]. \end{aligned} \tag{A.2} $$

Using the angle difference identity for the sine function, $\sin(\alpha-\beta) = \sin\alpha\cos\beta - \cos\alpha\sin\beta$, (A.2) can be rewritten as

$$\begin{aligned}
&\Delta^m A\,({}^m\phi_{N+1}) = \\
&\quad \frac{1}{2}\{[\sin({}^m\phi_{N+1})\cos({}^m\phi_n) - \cos({}^m\phi_{N+1})\sin({}^m\phi_n)] \\
&\quad + [\sin({}^m\theta_n + {}^m\phi_n)\cos({}^m\phi_{N+1}) \\
&\quad - \cos({}^m\theta_n + {}^m\phi_n)\sin({}^m\phi_{N+1})] - \sin({}^m\theta_n)\}\,.
\end{aligned} \tag{A.3}$$

The optimization function (A.1) can be parameterized by the candidate additional receiver position $\boldsymbol{r}_{N+1}$ by substituting the equality $[\cos({}^m\phi_n),\, \sin({}^m\phi_n)]^{\mathsf{T}} = \frac{\boldsymbol{r}_{r_n} - \hat{\boldsymbol{r}}_{s_m}}{\|\boldsymbol{r}_{r_n} - \hat{\boldsymbol{r}}_{s_m}\|}$ into (A.3) and substituting the result into (A.1), giving

$$\begin{aligned}
&{}^m A\,(\boldsymbol{r}_{N+1}) = \\
&\quad \frac{1}{2}\left\{ \frac{(x_{r_{N+1}} - \hat{x}_{s_m})}{\|\boldsymbol{r}_{r_n} - \hat{\boldsymbol{r}}_{s_m}\|}\,[\sin({}^m\theta_n + {}^m\phi_n) - \sin({}^m\phi_n)] \right. \\
&\quad + \frac{(y_{r_{N+1}} - \hat{y}_{s_m})}{\|\boldsymbol{r}_{r_n} - \hat{\boldsymbol{r}}_{s_m}\|}\,[\cos({}^m\phi_n) - \cos({}^m\theta_n + {}^m\phi_n)] \\
&\quad \left. - \sin({}^m\theta_n)\right\} + {}^m A_N.
\end{aligned} \tag{A.4}$$

Note that since ${}^m A_N$ is independent of $\boldsymbol{r}_{N+1}$, it may be omitted from the optimization problem. Its values can be computed off-line if desired.

A.2 Equations of the Polyhedra Constraints (2.16)

The direction of the l^{th} halfspace forming the polyhedron S_k is defined by the outward normal vector $-\boldsymbol{p}_{l,k}$, which is determined by the position of the n^{th} pre-deployed receiver and the position estimate of the m^{th} SOP, specifically

$$\boldsymbol{p}_{l,k} = \pm \left[-\frac{(y_{r_{N+1}} - \hat{y}_{s_m})}{\|\boldsymbol{r}_{r_n} - \hat{\boldsymbol{r}}_{s_m}\|}, \frac{(x_{r_{N+1}} - \hat{x}_{s_m})}{\|\boldsymbol{r}_{r_n} - \hat{\boldsymbol{r}}_{s_m}\|} \right]^{\mathsf{T}}. \tag{A.5}$$

The corresponding halfspace's offset from the origin of $\{f_1\}$ is

$$q_{l,k} = y_{r_n} - \frac{(\hat{y}_{s_m} - y_{r_n})}{(\hat{x}_{s_m} - x_{r_n})} \cdot x_{r_n}. \tag{A.6}$$

A.3 Derivation of Equation (2.22)

Given the pseudorange observations z_n defined in (2.3), define

$$\begin{aligned} \bar{z}_n(k) &\triangleq \|\boldsymbol{r}_{r_n}(k) - \boldsymbol{r}_s\| + c\delta t_{r_n}(k) - z_n(k) \\ &= c\delta t_s(k) - v_n(k). \end{aligned} \tag{A.7}$$

The clock bias δt_s can be removed by a single difference of (A.7) in time and substituting for the SOP's DT clock bias dynamics $c\delta t_s(k+1) = c\delta t_s(k) + cT\dot{\delta t}_s(k) + w_{\delta t_s}(k)$, yielding

$$\begin{aligned} \gamma_n(k+1) &\triangleq \bar{z}_n(k+1) - \bar{z}_n(k) \\ &= c\delta t_s(k+1) - c\delta t_s(k) - [v_n(k+1) - v_n(k)] \\ &= cT\dot{\delta t}_s(k) + w_{\delta t_s}(k) - [v_n(k+1) - v_n(k)]. \end{aligned} \tag{A.8}$$

The clock drift $\delta\dot{t}_s$ can be removed by a single difference of (A.8) in time and substituting for the SOP's clock drift dynamics $c\delta\dot{t}_s(k) = c\delta\dot{t}_s(k-1) + w_{\dot{\delta}t_s}(k-1)$, which yields

$$\begin{aligned}
\lambda_n(k+1) &\triangleq \gamma_n(k+1) - \gamma_n(k) \\
&= cT[\delta\dot{t}_s(k) - \delta\dot{t}_s(k-1)] + [w_{\delta t_s}(k) - w_{\delta t_s}(k-1)] \\
&- [v_n(k+1) - 2v_n(k) + v_n(k-1)] \\
&= Tw_{\dot{\delta}t_s}(k-1) + w_{\delta t_s}(k) - w_{\delta t_s}(k-1) \\
&- [v_n(k+1) - 2v_n(k) + v_n(k-1)].
\end{aligned}$$

Note that λ_n is the sum of three stationary sequences. For the sample ACF analysis conducted in this paper, each stationary sequence can be shifted to start with index k, giving

$$\lambda_n(k) = \lambda_{n,1}(k) + \lambda_{n,2}(k) + \lambda_{n,3}(k), \tag{A.9}$$

where $\lambda_{n,1}(k) \triangleq w_{\delta t_s}(k) - w_{\delta t_s}(k-1)$, $\lambda_{n,2}(k) \triangleq -[v_n(k) - 2v_n(k-1) + v_n(k-2)]$, and $\lambda_{n,3}(k) \triangleq Tw_{\dot{\delta}t_s}(k)$.

A.4 Derivation of Equation (2.23)

Equation (A.9) can be written as $\lambda_n(k) = \boldsymbol{\kappa}^{\mathsf{T}}\boldsymbol{y}(k)$ where

$$\boldsymbol{\kappa} \triangleq [\,1,\, T,\, -1,\, -1,\, 2,\, -1,\,]^{\mathsf{T}},$$

$$\boldsymbol{y}(k) \triangleq$$
$$\left[w_{\delta t_s}(k),\, w_{\dot{\delta}t_s}(k),\, w_{\delta t_s}(k-1),\, v_n(k),\, v_n(k-1),\, v_n(k-2)\right]^{\mathsf{T}}.$$

Assuming second-order ergodicity, i.e., for a sufficiently large number of samples L, the sample variance of λ_n, denoted $\text{var}_L(\lambda_n)$, is equal to the ensemble variance and is given by

$$\text{var}_L(\lambda_n) = \boldsymbol{\kappa}^\mathsf{T}\boldsymbol{\Sigma}\boldsymbol{\kappa}, \tag{A.10}$$

where $\boldsymbol{\Sigma} \triangleq \text{cov}(\boldsymbol{y}) = \text{diag}\left[c^2\mathbf{Q}_{\text{clk},s},\, c^2 b,\, \sigma_n^2\mathbf{I}_{3\times 3}\right]$ and $b \triangleq S_{\tilde{w}_{\delta t_s}}T + S_{\tilde{w}_{\dot{\delta} t_s}}\frac{T^3}{3}$ is the top left element of $\mathbf{Q}_{\text{clk},s}$. Finally, using (A.10) to solve for $\sigma_{r_n}^2$ gives

$$\begin{aligned} 6\sigma_{r_n}^2 &= \text{var}_L(\lambda_n) - c^2\left(2TS_{\tilde{w}_{\delta t_s}} + \frac{2}{3}T^3 S_{\tilde{w}_{\dot{\delta} t_s}}\right) \\ \Rightarrow \sigma_{r_n}^2 &= \frac{1}{6}\text{var}_L(\lambda_n) - \frac{1}{3}c^2 b. \end{aligned}$$

A.5 Time Update of the IMU State Vector (4.5)

The time update of $\boldsymbol{x}_{\text{imu}}$ is performed using ECEF strapdown mechanization equations.

A.5.1 Orientation Time Update

The orientation time update is given by

$${}^{b}_{e}\hat{\bar{\boldsymbol{q}}}(k+1|j) = {}^{b_{k+1}}_{b_k}\hat{\bar{\boldsymbol{q}}} \otimes {}^{b}_{e}\hat{\bar{\boldsymbol{q}}}(k|j), \tag{A.11}$$

where ${}^{b_{k+1}}_{b_k}\hat{\bar{\boldsymbol{q}}}$ represents an estimate of the rotation quaternion between the IMU's body frame at time k and $k+1$. The quaternion ${}^{b_{k+1}}_{b_k}\hat{\bar{\boldsymbol{q}}}$ is computed by integrating gyroscope rotation rate data $\boldsymbol{\omega}_{\text{imu}}(k)$ and $\boldsymbol{\omega}_{\text{imu}}(k+1)$ using a fourth order Runge-Kutta according to

$${}^{b_{k+1}}_{b_k}\hat{\bar{\boldsymbol{q}}} = \bar{\boldsymbol{q}}_0 + \frac{T}{6}\left(\boldsymbol{d}_1 + 2\boldsymbol{d}_2 + 2\boldsymbol{d}_3 + \boldsymbol{d}_4\right),$$

where

$$\boldsymbol{d}_1 = \frac{1}{2}\boldsymbol{\Omega}\left[{}^b\hat{\boldsymbol{\omega}}(k)\right]\bar{\boldsymbol{q}}_0, \quad \boldsymbol{d}_2 = \frac{1}{2}\boldsymbol{\Omega}\left[\bar{\boldsymbol{\omega}}\right]\cdot\left(\bar{\boldsymbol{q}}_0 + \frac{1}{2}T\boldsymbol{d}_1\right),$$

$$\boldsymbol{d}_3 = \frac{1}{2}\boldsymbol{\Omega}\left[\bar{\boldsymbol{\omega}}\right]\cdot\left(\bar{\boldsymbol{q}}_0 + \frac{1}{2}T\boldsymbol{d}_2\right),$$

$$\boldsymbol{d}_4 = \frac{1}{2}\boldsymbol{\Omega}\left[{}^b\hat{\boldsymbol{\omega}}(k+1)\right]\cdot\left(\bar{\boldsymbol{q}}_0 + T\boldsymbol{d}_3\right), \quad \bar{\boldsymbol{q}}_0 \triangleq \left[\,0,\,0,\,0,\,1\,\right]^{\mathsf{T}},$$

$$\bar{\boldsymbol{\omega}} \triangleq \frac{1}{2}\left[{}^b\hat{\boldsymbol{\omega}}(k) + {}^b\hat{\boldsymbol{\omega}}(k+1)\right] - {}^e_b\mathbf{R}^{\mathsf{T}}(k){}^e_i\boldsymbol{\omega},$$

where $\boldsymbol{\Omega}\left[\,\cdot\,\right] \in \mathbb{R}^{4\times 4}$ is given by

$$\boldsymbol{\Omega}\left[\boldsymbol{a}\right] \triangleq \begin{bmatrix} -\lfloor \boldsymbol{a}\times \rfloor & \boldsymbol{a} \\ -\boldsymbol{a}^{\mathsf{T}} & 0 \end{bmatrix}, \quad \boldsymbol{a} \triangleq \left[a_1, a_2, a_3\right]^{\mathsf{T}},$$

${}^b\hat{\boldsymbol{\omega}}(k)$ is the bias-compensated rotation rate measurement, which is computed according to

$${}^b\hat{\boldsymbol{\omega}}(k) = \boldsymbol{\omega}_{\text{imu}}(k) - \hat{\boldsymbol{b}}_{\text{gyr}}(k|j), \tag{A.12}$$

and ${}^e_i\boldsymbol{\omega} \triangleq [0,\,0,\,{}^e_i\omega]^{\mathsf{T}}$ is the rotation rate of the Earth, i.e., the rotation rate of the ECEF frame $\{e\}$ with respect to the ECI frame $\{i\}$. The value of ${}^e_i\omega$, according to the latest version of the world geodetic system (WGS 84), is ${}^e_i\omega = 7.292115 \times 10^{-5}$ rad/s.

A.5.2 Position and Velocity Time Update

Integrating IMU specific force data to perform a time update of the position and velocity in an ECEF coordinate frame introduces a centrifugal and Coriolis term due to the rotation rate of the Earth ${}^e_i\boldsymbol{\omega}$ [119]. Assuming that the variation of the Coriolis force is negligible

over the integration interval, the velocity time update is performed according to

$$
\begin{aligned}
{}^{e}\hat{\boldsymbol{r}}_b(k+1|j) = {}&{}^{e}\hat{\boldsymbol{r}}_b(k|j) + \frac{T}{2}\left[{}^{e}\hat{\boldsymbol{a}}(k) + {}^{e}\hat{\boldsymbol{a}}(k+1)\right] \\
&+ {}^{e}\boldsymbol{g}(k, {}^{e}\boldsymbol{r}_b(k))T - 2T\lfloor {}^{i}_{e}\boldsymbol{\omega}\times\rfloor {}^{e}\hat{\boldsymbol{r}}_b(k|j),
\end{aligned}
\tag{A.13}
$$

where ${}^{e}\hat{\boldsymbol{a}}$ and ${}^{b}\boldsymbol{a}$ are the transformed bias-compensated specific force and untransformed bias-compensated specific force, respectively, which are given by

$$
{}^{e}\hat{\boldsymbol{a}}(k) \triangleq \hat{\mathbf{R}}^{\mathsf{T}}(k) {}^{b}\hat{\boldsymbol{a}}(k),
\tag{A.14}
$$

$$
{}^{b}\boldsymbol{a}(k) = \hat{\boldsymbol{a}}_{\text{imu}}(k) - \hat{\boldsymbol{b}}_{\text{acc}}(k|j),
\tag{A.15}
$$

and $\hat{\mathbf{R}}(k) \triangleq \mathbf{R}\left[{}^{b}_{e}\hat{\boldsymbol{q}}(k|j)\right]$.

The position time update is performed according to

$$
\begin{aligned}
{}^{e}\hat{\boldsymbol{r}}_b(k+1|j) = {}&{}^{e}\hat{\boldsymbol{r}}_b(k|j) + \frac{T}{2}\left[{}^{e}\hat{\dot{\boldsymbol{r}}}_b(k+1|j) + {}^{b}\hat{\dot{\boldsymbol{r}}}(k|j)\right] \\
&- T^2\lfloor {}^{i}_{e}\boldsymbol{\omega}\times\rfloor {}^{e}\hat{\dot{\boldsymbol{r}}}_b(k|j).
\end{aligned}
\tag{A.16}
$$

A.5.3 Accelerometer and Gyroscope Bias Time Update

The time update of the biases $\boldsymbol{b}_{\text{gyr}}$ and $\boldsymbol{b}_{\text{acc}}$ follow from (4.1) and (4.2), respectively, giving

$$
\hat{\boldsymbol{b}}_{\text{gyr}}(k+1|j) = \hat{\boldsymbol{b}}_{\text{gyr}}(k|j),
$$

$$
\hat{\boldsymbol{b}}_{\text{acc}}(k+1|j) = \hat{\boldsymbol{b}}_{\text{acc}}(k|j).
$$

A.6 INS State Transition and Process Noise Covariance Matrices

The calculation of the discrete-time linearized INS state transition matrix $\mathbf{\Phi}_{\text{imu}}$ and process noise covariance $\mathbf{Q}_{\text{imu}}$ are performed using strapdown INS equations as described in [119,136]. The discrete-time linearized INS state transition matrix $\mathbf{\Phi}_{\text{imu}}$ is given by

$$\mathbf{\Phi}_{\text{imu}} = \begin{bmatrix} \mathbf{\Phi}_{\boldsymbol{qq}} & \mathbf{0}_{3\times3} & \mathbf{0}_{3\times3} & \mathbf{\Phi}_{\boldsymbol{qb}_{\text{gyr}}} & \mathbf{0}_{3\times3} \\ \mathbf{\Phi}_{\boldsymbol{rq}} & \mathbf{I}_{3\times3} & T\mathbf{I}_{3\times3} & \mathbf{\Phi}_{\boldsymbol{rb}_{\text{gyr}}} & \mathbf{\Phi}_{\boldsymbol{rb}_{\text{acc}}} \\ \mathbf{\Phi}_{\dot{\boldsymbol{r}}\boldsymbol{q}} & \mathbf{0}_{3\times3} & \mathbf{\Phi}_{\dot{\boldsymbol{r}}\dot{\boldsymbol{r}}} & \mathbf{\Phi}_{\dot{\boldsymbol{r}}\boldsymbol{b}_{\text{gyr}}} & \mathbf{\Phi}_{\dot{\boldsymbol{r}}\boldsymbol{b}_{\text{acc}}} \\ \mathbf{0}_{3\times3} & \mathbf{0}_{3\times3} & \mathbf{0}_{3\times3} & \mathbf{I}_{3\times3} & \mathbf{0}_{3\times3} \\ \mathbf{0}_{3\times3} & \mathbf{0}_{3\times3} & \mathbf{0}_{3\times3} & \mathbf{0}_{3\times3} & \mathbf{I}_{3\times3} \end{bmatrix},$$

where

$$\mathbf{\Phi}_{\boldsymbol{qq}} = \mathbf{I}_{3\times3} - T\lfloor {}^{e}_{i}\boldsymbol{\omega}\times\rfloor, \quad \mathbf{\Phi}_{\dot{\boldsymbol{r}}\dot{\boldsymbol{r}}} = \mathbf{I}_{3\times3} - 2T\lfloor {}^{e}_{i}\boldsymbol{\omega}\times\rfloor$$

$$\mathbf{\Phi}_{\boldsymbol{qb}_{\text{gyr}}} = -\frac{T}{2}\left[\hat{\mathbf{R}}^{\mathsf{T}}(k+1) + \hat{\mathbf{R}}^{\mathsf{T}}(k)\right],$$

$$\mathbf{\Phi}_{\dot{\boldsymbol{r}}\boldsymbol{q}} = -\frac{T}{2}\left\lfloor\left[{}^{e}\hat{\boldsymbol{a}}(k) + {}^{e}\hat{\boldsymbol{a}}(k+1)\right]\times\right\rfloor, \quad \mathbf{\Phi}_{\boldsymbol{rq}} = \frac{T}{2}\mathbf{\Phi}_{\dot{\boldsymbol{r}}\boldsymbol{q}},$$

$$\mathbf{\Phi}_{\dot{\boldsymbol{r}}\boldsymbol{b}_{\text{gyr}}} = -\frac{T}{2}\lfloor {}^{e}\hat{\boldsymbol{a}}(k)\times\rfloor\,\mathbf{\Phi}_{\boldsymbol{qb}_{\text{gyr}}}, \quad \mathbf{\Phi}_{\dot{\boldsymbol{r}}\boldsymbol{b}_{\text{acc}}} = \mathbf{\Phi}_{\boldsymbol{qb}_{\text{gyr}}},$$

$$\mathbf{\Phi}_{\boldsymbol{rb}_{\text{gyr}}} = \frac{T}{2}\mathbf{\Phi}_{\dot{\boldsymbol{r}}\boldsymbol{b}_{\text{gyr}}}, \quad \mathbf{\Phi}_{\boldsymbol{rb}_{\text{acc}}} = \frac{T}{2}\mathbf{\Phi}_{\dot{\boldsymbol{r}}\boldsymbol{b}_{\text{acc}}}.$$

The discrete-time linearized INS process noise covariance $\mathbf{Q}_{\text{imu}}$ is given by

$$\mathbf{Q}_{\text{imu}} = \frac{T}{2}\mathbf{\Phi}_{\text{imu}}^{\mathsf{T}}\mathbf{N}_c\mathbf{\Phi}_{\text{imu}} + \mathbf{N}_c,$$

where

$$\mathbf{N}_c = \mathrm{diag}\big[\mathbf{S}_{\boldsymbol{n}_{\mathrm{gyr}}},\, \mathbf{0}_{3\times3},\, \mathbf{S}_{\boldsymbol{n}_{\mathrm{acc}}},\, \mathbf{S}_{\boldsymbol{w}_{\mathrm{gyr}}},\, \mathbf{S}_{\boldsymbol{w}_{\mathrm{acc}}}\big]\,,$$

where $\mathbf{S}_{\boldsymbol{n}_{\mathrm{gyr}}} = T\mathbf{Q}_{\boldsymbol{n}_{\mathrm{gyr}}}$ and $\mathbf{S}_{\boldsymbol{n}_{\mathrm{acc}}} = T\mathbf{Q}_{\boldsymbol{n}_{\mathrm{acc}}}$ are the PSD matrices of the gyroscope's and accelerometer's random noise, respectively, and $\mathbf{S}_{\boldsymbol{w}_{\mathrm{gyr}}} = \mathbf{Q}_{\boldsymbol{n}_{\boldsymbol{w}_{\mathrm{gyr}}}}/T$ and $\mathbf{S}_{\boldsymbol{w}_{\mathrm{acc}}} = \mathbf{Q}_{\boldsymbol{w}_{\mathrm{acc}}}/T$ are the PSD matrices of the gyroscope's and accelerometer's bias variation, respectively.

A.7 EKF State Measurement Update Equations

The standard EKF equations are modified to deal with the 3-D orientation error correction, which contains one less dimension than the 4-D orientation quaternion estimate, as described in Subsection 4.3.2. To this end, the state estimate is separated into two parts according to $\hat{\boldsymbol{x}} \triangleq \left[{}^{b}_{e}\hat{\boldsymbol{q}}^{\mathsf{T}}, \hat{\boldsymbol{y}}^{\mathsf{T}}\right]^{\mathsf{T}}$, where ${}^{b}_{e}\hat{\boldsymbol{q}} \in \mathbb{R}^4$ is the orientation quaternion estimate and $\hat{\boldsymbol{y}} \in \mathbb{R}^{14+5M}$ is a vector containing the remaining estimates of $\boldsymbol{x}$. Next, the EKF correction vector $\breve{\boldsymbol{x}}(k+1)$, which is to be applied to the current state prediction $\hat{\boldsymbol{x}}(k+1|j)$ to produce the EKF state measurement update $\hat{\boldsymbol{x}}(k+1|k+1)$, is computed according to

$$\breve{x}(k+1) \triangleq \begin{bmatrix} \breve{\boldsymbol{\theta}}(k+1) \\ \breve{\boldsymbol{y}}(k+1) \end{bmatrix} = \begin{bmatrix} \boldsymbol{\Lambda}_{\boldsymbol{\theta}}\mathbf{K}(k+1)\boldsymbol{\nu}(k+1|j) \\ \boldsymbol{\Lambda}_{\boldsymbol{y}}\mathbf{K}(k+1)\boldsymbol{\nu}(k+1|j) \end{bmatrix},$$

where $\breve{\boldsymbol{\theta}} \in \mathbb{R}^3$ is the orientation correction, $\breve{\boldsymbol{y}} \in \mathbb{R}^{14+5M}$ is a vector containing the remaining corrections,

$$\boldsymbol{\Lambda}_{\boldsymbol{\theta}} \triangleq \big[\mathbf{I}_{3\times3}, \mathbf{0}_{3\times(14+5M)}\big]\,,$$

$$\boldsymbol{\Lambda}_{\boldsymbol{y}} \triangleq \big[\mathbf{0}_{(14+5M)\times3}, \mathbf{I}_{(14+5M)\times(14+5M)}\big]\,,$$

$\boldsymbol{\nu}(k+1|j) \triangleq \boldsymbol{z}(k+1) - \hat{\boldsymbol{z}}(k+1|j)$ is the measurement residual, and $\mathbf{K}$ and $\mathbf{S}$ are defined in (4.18) and (4.19), respectively. Finally, the EKF state measurement update $\boldsymbol{x}(k+1|k+1)$ is computed by applying $\breve{\boldsymbol{\theta}}(k+1)$ to ${}^{b}_{e}\hat{\boldsymbol{q}}(k+1|j)$ through (4.14), and applying $\breve{\boldsymbol{y}}(k+1)$ to $\boldsymbol{y}(k+1|j)$ using the standard EKF additive update equation, giving

$$\hat{\boldsymbol{x}}(k+1|k+1) =$$
$$\begin{bmatrix} {}^{b}_{e}\hat{\boldsymbol{q}}(k+1|j) \otimes \left[\frac{1}{2}\breve{\boldsymbol{\theta}}^{\mathsf{T}}(k+1), \sqrt{1 - \frac{1}{4}\breve{\boldsymbol{\theta}}^{\mathsf{T}}(k+1)\breve{\boldsymbol{\theta}}(k+1)}\right]^{\mathsf{T}} \\ \hat{\boldsymbol{y}}(k+1|j) + \breve{\boldsymbol{y}}(k+1) \end{bmatrix}.$$